Time-Dependent CP Violation Measurements in Neutral B Meson to Double-Charm Decays at the Japanese Belle Experiment

Zur Erlangung des akademischen Grades eines

DOKTORS DER NATURWISSENSCHAFTEN

von der Fakultät für Physik des
Karlruher Instituts für Technologie (KIT)

genehmigte

DISSERTATION

von

Diplom-Physiker Markus Röhrken
aus Varel in Friesland

Tag der mündlichen Prüfung: 13. Juli 2012
Referent: Prof. Dr. M. Feindt, Institut für Experimentelle Kernphysik
Korreferent: Prof. Dr. G. Quast, Institut für Experimentelle Kernphysik

Im Andenken an Margarete und Bernd Röhrken.

Abstract

In the Standard Model of electroweak interactions, the effect of CP violation is caused by a single irreducible complex phase in the Cabibbo-Kobayashi-Maskawa quark-mixing matrix of the three fundamental fermion families. The Belle and BaBar Collaborations experimentally established the existence of CP violating phenomena in the B meson system. In particular, the parameter $\sin(2\beta)$, where $\beta = \arg\left[-V_{cd}V_{cb}^{*}/V_{td}V_{tb}^{*}\right]$, is determined precisely by the measurements of mixing-induced CP violation in $b \to c\bar{c}s$ transitions.

The decays of $B^0 \to D^+D^-$ and $B^0 \to D^{*\pm}D^{\mp}$ are caused by $b \to c\bar{c}d$ transitions. In the lowest order perturbation theory, the transitions are described by Cabibbo-disfavored amplitudes. In this order, the mixing-induced CP violation is $\sin(2\beta)$ and no direct CP violation is possible. Additionally, higher order $b \to d$ loop diagrams, so-called penguin-diagrams, can contribute to the decays. The amplitudes corresponding to these diagrams may contain weak phases that are different from the amplitudes at lowest order. The theoretical considerations with respect to possible deviations of the mixing-induced and the direct CP violation due to the penguin contributions are associated with significant, in particular hadronic uncertainties, but predict corrections that are negligibly small.

In the year 2007, the Belle Collaboration using a data set of 535×10^6 $B\bar{B}$ pairs found evidence of an extraordinary large direct CP violation in $B^0 \to D^+D^-$ decays: $\mathcal{C}^{\mathrm{dir}}_{D^+D^-} = -0.91 \pm 0.23\,(\mathrm{stat.}) \pm 0.06\,(\mathrm{syst.})$, corresponding to a 3.2σ deviation from zero. This deviation was neither confirmed by BaBar, nor it was observed in other $B^0 \to D^{*\pm}D^{(*)\mp}$ decays.

In this PhD thesis, the measurements of the branching fraction and the time-dependent CP violation in $B^0 \to D^+D^-$ decays based on the final data set of the Belle experiment are presented. Furthermore, the thesis comprises the corresponding measurements in $B^0 \to D^{*\pm}D^{\mp}$ decays to provide a direct comparison to a related decay.

The final Belle data set contains 772×10^6 $B\bar{B}$ pairs recorded on the $\Upsilon(4S)$-resonance at the asymmetric-energy KEKB e^+e^--collider. The $\Upsilon(4S)$-resonance is produced with a Lorentz boost of $\beta\gamma = 0.425$ along the e^--beam. The boosted center-of-mass frame allows the measurements of proper decay time differences of the produced B mesons. The neutral B mesons originating from decays of the $\Upsilon(4S)$-resonance are quantum-mechanically entangled and the states of the B mesons evolve coherently. The measurement of the time evolution allows the experimental determination of time-dependent CP violating asymmetries.

The measurements in $B^0 \to D^+D^-$ and $B^0 \to D^{*\pm}D^{\mp}$ decays are performed as so-called blind analyses. Only after the validation of the time-integrated and time-dependent measurements by a wide variety of cross-checks using Monte Carlo simulations and control samples, the $B^0 \to D^+D^-$ and $B^0 \to D^{*\pm}D^{\mp}$ data sets are unblinded and the measurements are performed.

The results of the measurements of branching fractions are

$$\mathcal{B}\left(B^0 \to D^+D^-\right) = \left(2.12 \pm 0.16\,(\mathrm{stat.}) \pm 0.18\,(\mathrm{syst.})\right) \times 10^{-4},$$
$$\mathcal{B}\left(B^0 \to D^{*\pm}D^{\mp}\right) = \left(6.14 \pm 0.29\,(\mathrm{stat.}) \pm 0.50\,(\mathrm{syst.})\right) \times 10^{-4}.$$

The results of the measurement of time-dependent CP violation in $B^0 \to D^+D^-$ decays

are

$$\mathcal{S}_{\mathrm{D^+D^-}} = -1.06\ ^{+0.21}_{-0.14}\ (\mathrm{stat.}) \pm 0.08\ (\mathrm{syst.}),$$
$$\mathcal{C}_{\mathrm{D^+D^-}} = -0.43 \pm 0.16\ (\mathrm{stat.}) \pm 0.05\ (\mathrm{syst.}).$$

This measurement excludes the conservation of CP symmetry in $\mathrm{B^0} \to \mathrm{D^+D^-}$ decays, equivalent to $\mathcal{S}_{\mathrm{D^+D^-}} = \mathcal{C}_{\mathrm{D^+D^-}} = 0$, at a confidence level of $1 - 2.7 \times 10^{-5}$ corresponding to a significance of 4.2σ.

The results of the measurement of time-dependent CP violation in $\mathrm{B^0} \to \mathrm{D^{*\pm}D^{\mp}}$ decays are

$$\mathcal{A}_{\mathrm{D^*D}} = +0.06 \pm 0.05\ (\mathrm{stat.}) \pm 0.02\ (\mathrm{syst.}),$$
$$\mathcal{S}_{\mathrm{D^*D}} = -0.78 \pm 0.15\ (\mathrm{stat.}) \pm 0.05\ (\mathrm{syst.}),$$
$$\mathcal{C}_{\mathrm{D^*D}} = -0.01 \pm 0.11\ (\mathrm{stat.}) \pm 0.04\ (\mathrm{syst.}),$$
$$\Delta\mathcal{S}_{\mathrm{D^*D}} = -0.13 \pm 0.15\ (\mathrm{stat.}) \pm 0.04\ (\mathrm{syst.}),$$
$$\Delta\mathcal{C}_{\mathrm{D^*D}} = +0.12 \pm 0.11\ (\mathrm{stat.}) \pm 0.03\ (\mathrm{syst.}).$$

This measurement excludes the conservation of CP symmetry in $\mathrm{B^0} \to \mathrm{D^{*\pm}D^{\mp}}$ decays, equivalent to $\mathcal{A}_{\mathrm{D^*D}} = \mathcal{S}_{\mathrm{D^*D}} = \mathcal{C}_{\mathrm{D^*D}} = 0$, at a confidence level of $1 - 6.8 \times 10^{-5}$ corresponding to a significance of 4.0σ.

In both decay modes, the CP violation is driven by mixing-induced CP violation. The results of the mixing-induced CP violation in $\mathrm{B^0} \to \mathrm{D^+D^-}$ and $\mathrm{B^0} \to \mathrm{D^{*\pm}D^{\mp}}$ decays are consistent with precision measurements in $\mathrm{b} \to \mathrm{c\bar{c}s}$ transitions. The current world average is $-\eta_{\mathrm{CP}}\mathcal{S} = \sin(2\beta) = 0.68 \pm 0.02$.

In comparison to the previous $\mathrm{B^0} \to \mathrm{D^+D^-}$ analysis by the Belle Collaboration in 2007, the center value of the direct CP violation reduces approximately by a factor of 2 and deviates instead of 3.2σ approximately 2.0σ from zero. In $\mathrm{B^0} \to \mathrm{D^{*\pm}D^{\mp}}$ decays, no direct CP violation is observed. The results suggest, that the extraordinary large direct CP violation in the previous $\mathrm{B^0} \to \mathrm{D^+D^-}$ analysis was caused by a statistical fluctuation in the data. The current experimental precision does not allow to prove significantly a non-zero direct CP violation at small center values. Therefore, further measurements are necessary to probe for possible penguin contributions in $\mathrm{b} \to \mathrm{c\bar{c}d}$ transitions.

The presented measurements in $\mathrm{B^0} \to \mathrm{D^+D^-}$ and $\mathrm{B^0} \to \mathrm{D^{*\pm}D^{\mp}}$ decays supersede the previous measurements by the Belle Collaboration and are more precise than all measurements performed by the Belle and BaBar Collaborations before.

The results of this PhD thesis have been published in

> M. Röhrken *et al.* (Belle Collaboration),
> "Measurements of Branching Fractions and Time-Dependent
> CP Violating Asymmetries in $\mathrm{B^0} \to \mathrm{D^{(*)\pm}D^{\mp}}$ Decays",
> Physical Review D **85**, 091106 (2012).

Zusammenfassung

Im Standard Modell der elektroschwachen Wechselwirkung wird der Effekt der CP-Verletzung durch eine einzige und irreduzible komplexe Phase in der Cabibbo-Kobayashi-Maskawa Quarkmischungsmatrix der drei fundamentalen Fermionfamilien verursacht. Die Belle and BarBar Kollaborationen haben die Existenz CP-verletzender Phänomene im System der B-Mesonen experimentell bestätigt. Insbesondere wurde der Parameter $\sin(2\beta)$, mit $\beta = \arg\left[-V_{cd}V^*_{cb}/V_{td}V^*_{tb}\right]$, durch Messungen der mischungsinduzierten CP-Verletzung in $b \to c\bar{c}s$ Übergängen mit hoher Präzision bestimmt.

Die Zerfälle $B^0 \to D^+D^-$ und $B^0 \to D^{*\pm}D^{\mp}$ werden durch $b \to c\bar{c}d$ Übergänge verursacht. In niedrigster Ordnung der Störungstheorie werden diese Übergänge durch Cabibbo-unterdrückte Amplituden beschrieben. In dieser Ordnung ist die mischungsinduzierte CP-Verletzung durch $\sin(2\beta)$ gegeben und es ist keine direkte CP-Verletzung möglich. Zusätzlich können in höherer Ordnung $b \to d$ Schleifendiagramme, sogenannte Pinguindiagramme, zu den Zerfällen beitragen. Die Amplituden dieser Diagramme können schwache Phasen beinhalten, die verschieden von den Amplituden in niedrigster Ordnung sind. Die theoretischen Überlegungen zu möglichen Abweichungen der mischungsinduzierten und der direkten CP-Verletzung durch die möglichen zusätzlichen Beiträge von Pinguinamplituden sind mit signifikanten, insbesondere hadronischen Unsicherheiten behaftet, sagen aber Korrekturen vorher, die vernachlässigbar gering sind.

Im Jahr 2007 fand die Belle Kollaboration unter Verwendung eines Datensatzes von 535×10^6 $B\bar{B}$-Paaren in $B^0 \to D^+D^-$ Zerfällen Evidenz für eine ungewöhnlich hohe direkte CP-Verletzung: $\mathcal{C}^{\mathrm{dir}}_{D^+D^-} = -0.91 \pm 0.23\,(\mathrm{stat.}) \pm 0.06\,(\mathrm{syst.})$, entsprechend einer 3.2σ Abweichung von Null. Diese Abweichung wurde weder von BaBar bestätigt, noch wurde sie in anderen $B^0 \to D^{*\pm}D^{(*)\mp}$ Zerfällen beobachtet.

In dieser Dissertation werden die Messungen des Verzweigungsverhältnisses und der zeitabhängigen CP-Verletzung in $B^0 \to D^+D^-$ Zerfällen mit dem finalen Belle Datensatz präsentiert. Darüberhinaus umfaßt die Dissertation die Messungen in $B^0 \to D^{*\pm}D^{\mp}$ Zerfällen, um einen direkten Vergleich zu einem verwandten Zerfall zu ermöglichen.

Der finale Belle Datensatz umfaßt 772×10^6 $B\bar{B}$-Paare, die auf der $\Upsilon(4S)$-Resonanz an dem asymmetrischen KEKB e^+e^--Beschleuniger aufgezeichnet wurden. Die $\Upsilon(4S)$-Resonanz wird mit einem Lorentzfaktor von $\beta\gamma = 0.425$ entlang des e^--Strahls erzeugt. Das bewegte Schwerpunktsystem erlaubt die Messung der Zerfallszeitdifferenzen der erzeugten B-Mesonen. Die neutralen B-Mesonen aus Zerfällen der $\Upsilon(4S)$-Resonanz sind quantenmechanisch verschränkt und die Zustände der B-Mesonen entwickeln sich zeitlich kohärent. Die Vermessung der zeitlichen Entwicklung erlaubt die experimentelle Bestimmung von zeitabhängigen CP-verletzenden Asymmetrien.

Die Messungen in $B^0 \to D^+D^-$ und in $B^0 \to D^{*\pm}D^{\mp}$ Zerfällen werden als sogenannte blinde Analysen durchgeführt. Erst nach Validierung der zeitintegrierten und zeitabhängigen Messungen durch eine Vielzahl von Tests unter Verwendung von Monte Carlo Simulationen und Kontrollkanälen werden die $B^0 \to D^+D^-$ und $B^0 \to D^{*\pm}D^{\mp}$ Datensätze geöffnet und die Messungen durchgeführt.

Die Ergebnisse der Messungen der Verzweigunsverhältnisse sind

$$\mathcal{B}\left(B^0 \to D^+D^-\right) = \left(2.12 \pm 0.16\,(\text{stat.}) \pm 0.18\,(\text{syst.})\right) \times 10^{-4},$$
$$\mathcal{B}\left(B^0 \to D^{*\pm}D^{\mp}\right) = \left(6.14 \pm 0.29\,(\text{stat.}) \pm 0.50\,(\text{syst.})\right) \times 10^{-4}.$$

Die Ergebnisse der Messung der zeitabhängiger CP-Verletzung in $B^0 \to D^+D^-$ Zerfällen sind

$$\begin{aligned} \mathcal{S}_{D^+D^-} &= -1.06\ {}^{+0.21}_{-0.14}\ (\text{stat.}) \pm 0.08\ (\text{syst.}), \\ \mathcal{C}_{D^+D^-} &= -0.43 \pm 0.16\ (\text{stat.}) \pm 0.05\ (\text{syst.}). \end{aligned}$$

Diese Messung schließt die Erhaltung der CP-Symmetrie in $B^0 \to D^+D^-$ Zerfällen, äquivalent zu $\mathcal{S}_{D^+D^-} = \mathcal{C}_{D^+D^-} = 0$, in einem Konfidenzintervall von $1 - 2.7 \times 10^{-5}$, entsprechend einer Signifikanz von 4.2σ, aus.

Die Ergebnisse der Messung der zeitabhängiger CP-Verletzung in $B^0 \to D^{*\pm}D^{\mp}$ Zerfällen sind

$$\begin{aligned} \mathcal{A}_{D^*D} &= +0.06 \pm 0.05\ (\text{stat.}) \pm 0.02\ (\text{syst.}), \\ \mathcal{S}_{D^*D} &= -0.78 \pm 0.15\ (\text{stat.}) \pm 0.05\ (\text{syst.}), \\ \mathcal{C}_{D^*D} &= -0.01 \pm 0.11\ (\text{stat.}) \pm 0.04\ (\text{syst.}), \\ \Delta\mathcal{S}_{D^*D} &= -0.13 \pm 0.15\ (\text{stat.}) \pm 0.04\ (\text{syst.}), \\ \Delta\mathcal{C}_{D^*D} &= +0.12 \pm 0.11\ (\text{stat.}) \pm 0.03\ (\text{syst.}). \end{aligned}$$

Diese Messung schließt die Erhaltung der CP-Symmetrie in $B^0 \to D^{*\pm}D^{\mp}$ Zerfällen, äquivalent zu $\mathcal{A}_{D^*D} = \mathcal{S}_{D^*D} = \mathcal{C}_{D^*D} = 0$, in einem Konfidenzintervall von $1 - 6.8 \times 10^{-5}$, entsprechend einer Signifikanz von 4.0σ aus.

In beiden Zerfällen wird die CP-Verletzung durch mischungsinduzierte CP-Verletzung verursacht. Die Ergebnisse der mischungsinduzierten CP-Verletzung in $B^0 \to D^+D^-$ und $B^0 \to D^{*\pm}D^{\mp}$ Zerfällen sind konsistent den Präzisionmessungen in $b \to c\bar{c}s$ Übergängen. Der aktuelle Weltmittelwert ist $-\eta_{CP}\mathcal{S} = \sin(2\beta) = 0.68 \pm 0.02$.

Im Vergleich zur vorherigen $B^0 \to D^+D^-$ Analyse der Belle Kollaboration aus dem Jahr 2007 ist der Zentralwert der direkten CP-Verletzung ungefähr halbiert und weicht anstatt um 3.2σ um ungefähr 2.0σ von Null ab. In $B^0 \to D^{*\pm}D^{\mp}$ Zerfällen wird keine direkte CP-Verletzung beobachtet. Dies legt den Schluß nahe, daß die ungewöhnlich hohe direkte CP-Verletzung der vorherigen $B^0 \to D^+D^-$ Analyse durch eine statistische Fluktuation in den Daten verursacht wurde. Die gegenwärtige experimentelle Präzision erlaubt es nicht eine von Null verschiedene direkte CP-Verletzung bei geringen Zentralwerten signifikant nachzuweisen. Daher sind weitere Messungen notwendig, um die möglichen Beiträge von Pinguinamplituden in $b \to c\bar{c}d$ Übergängen experimentell zu bestimmen.

Die neuen Messungen in $B^0 \to D^+D^-$ und $B^0 \to D^{*\pm}D^{\mp}$ Zerfällen ersetzen die bisherigen Messungen der Belle Kollaboration und sind präziser als alle bisherigen Messungen, die von den Belle und BaBar Kollaborationen zuvor durchgeführt wurden.

Die Ergebnisse dieser Dissertation wurden veröffentlicht in

> M. Röhrken *et al.* (Belle Collaboration),
> "Measurements of Branching Fractions and Time-Dependent
> CP Violating Asymmetries in $B^0 \to D^{(*)\pm}D^{\mp}$ Decays",
> Physical Review D **85**, 091106 (2012).

Contents

1 Introduction

The non-conservation of the symmetry under CP transformation, which is the combined operation of charge-conjugation C and parity-transformation P, is a phenomenon in particle physics of fundamental importance. The theoretical explanation of CP violation is closely related to the basic properties of the Standard Model of particle physics: the flavor structure, the number of fermion families and the mass hierarchy.

The violation of CP symmetry manifests itself in differences in CP-conjugated processes and thereby allows to distinguish unambiguously between matter and antimatter. According to the CPT theorem, all Lorentz-invariant local quantum field theories are assumed to conserve symmetry under the combined transformation of CP-conjugation and time-reversal T. Therefore, the violation of CP symmetry is equivalent to the violation of symmetry under time-reversal, and establishes an arrow of time on the microscopic level.

The violation of CP symmetry is experimentally observable in the study of weakly decaying mesons. In particular, neutral B mesons, bound states of heavy beauty- and light down-quarks, exhibit large CP violating effects. Many physical processes involving the time evolution and the decay of B mesons are driven by interference and loop effects, and thereby allow to test properties of the underlying quantum theory. Several dedicated particle accelerators and experiments were operated to create large numbers of B mesons and to study their properties in detail.

In this thesis, the unique properties of the Japanese B-factory experiment Belle such as the boosted center-of-mass system and the quantum-entanglement of B^0-$\bar{B}^0$ pairs produced by $\Upsilon(4S)$ decays are utilised to provide experimental evidence for the non-conservation of CP symmetry in the B meson system. The measurements presented in this thesis focus on decays of neutral B mesons to double-charm modes, in particular on $B^0 \to D^+D^-$ and $B^0 \to D^{*\pm}D^{\mp}$ decays. In the Standard Model, the effect of CP violation emerging in electroweak interactions is explained by the Kobayashi-Maskawa mechanism. Therefore, this thesis provides a test for fundamental properties of electroweak interactions.

In the following, important steps in the history of CP violation and the physics related to the study of b-hadrons, in particular of B mesons, are summarised. The historical introduction already anticipates essential physical phenomena and experimental features needed to perform the measurements presented in this thesis.

1.1 History of CP Violation and B Physics

In 1964, J.W. Cronin, V.L. Fitch *et al.* discovered the violation of CP symmetry in the kaon system [1]. In particular, they observed the decay of the long-living neutral kaon, which normally decays into a three pion final state with CP eigenvalue $\eta_{CP} = -1$, into two pions with the CP eigenvalue $\eta_{CP} = +1$,

$$K^0_L \rightarrow \pi^+\pi^-, \tag{1.1}$$

with a fraction of the decays at a level of 2×10^{-3}.

In subsequent measurements, the same effect has been observed in the charge asymmetry of semileptonic decays [2, 3], e.g.

$$\frac{\Gamma(K^0_L \rightarrow \pi^- e^+ \nu_e) - \Gamma(K^0_L \rightarrow \pi^+ e^- \nu_e)}{\Gamma(K^0_L \rightarrow \pi^- e^+ \nu_e) + \Gamma(K^0_L \rightarrow \pi^+ e^- \nu_e)} = \Big(+2.24 \pm 0.36\ (\text{stat.})\Big) \times 10^{-3}. \tag{1.2}$$

The effect of CP violation manifests itself in the inequality of the decay probabilities of the above CP-conjugated processes, and the more frequent decays to positrons than to electrons demonstrate how the effect allows to unambiguously distinguish between matter and antimatter.

The question how CP violation emerges in the interaction of quarks remained unanswered for one decade. In 1973, M. Kobayashi and T. Maskawa pointed out the possible occurrence of CP violation, if three families of quarks exist [4]. In this case, the quark mixing matrix contains a complex phase that is irreducible. Consequently, CP violating effects are caused by the interference of different charged current components in electroweak interactions. These theoretical considerations by Kobayashi and Maskawa are remarkable, because in 1973 only the three lightest quarks - the up-, down- and strange-quarks - were experimentally known.

In 1977, L. Lederman *et al.* performed measurements in proton-nucleus collisions,

$$\begin{aligned} p + \big\{\text{Cu}, \text{Pt}\big\} &\rightarrow X + \text{anything} \\ X &\rightarrow \mu^+\mu^-, \end{aligned}$$

and observed a narrow structure in the di-muon mass at approximately 9.5 GeV/c^2 [5]. They discovered the first hadron consisting of b-quarks: the $\Upsilon(1S)$-resonance, the lowest bound state of $b\bar{b}$-quarks with quantum numbers of $J^{PC} = 1^{--}$. Due to the quantum numbers, the $\Upsilon(1S)$ and other radially excited states can be directly produced in e^+e^--annihilations. In further experiments performed at the CESR e^+e^- storage ring, the CLEO and CUSB Collaborations observed the $\Upsilon(2S)$, $\Upsilon(3S)$ [6, 7] and the $\Upsilon(4S)$ [8, 9]. The $\Upsilon(4S)$ is of particular interest for B physics, because its mass is located directly above the threshold for $B\bar{B}$ meson pair production. In 1981, CLEO and CUSB observed the first B mesons originating from $\Upsilon(4S)$ decays [10, 11].

In 1983, the MAC and Mark II Collaborations, performing experiments at the PEP e^+e^- storage ring at SLAC, observed long lifetimes of hadrons containing b-quarks [12, 13]. For example, the MAC Collaboration reported from inclusive measurements of impact parameters a lifetime of

$$\tau_b = \Big[1.8 \pm 0.6\ (\text{stat.}) \pm 0.4\ (\text{syst.})\Big] \times 10^{-12}\,\text{s}. \tag{1.3}$$

In spite of the heavy mass of the b-quark, $m_b \approx 4.2\ \mathrm{GeV}/c^2$, the lifetimes of hadrons containing b-quarks turned out to be very long, e.g. significantly longer than that of less heavy hadrons composed of c-quarks. The long lifetime is caused by the suppression of inter-family transitions, equivalent to small elements V_{cb} and V_{ub} in the Cabibbo-Kobayashi-Maskawa quark mixing matrix. The observations by the MAC and Mark II Collaborations were an important motivation to look for new effects that can only emerge, if particles, in particular B mesons, live long enough.

In 1987, the ARGUS Collaboration, performing measurements at the DORIS e^+e^- storage ring at DESY, observed same-charge di-lepton events [14],

$$e^+e^- \rightarrow \Upsilon(4S) \rightarrow \left\{B^0B^0/\bar{B}^0\bar{B}^0\right\} \rightarrow X + l^{\pm}l^{\pm}, \tag{1.4}$$

The $B\bar{B}$ meson pairs originating from $\Upsilon(4S)$ decays are produced in an antisymmetric state. If one B meson decays as a B^0 at time t, the second B meson is necessarily a $\bar{B}^0$ at this instant of time. In absence of the possibility of a B^0 meson to change into its own antiparticle, $\bar{B}^0$, and vice versa, both leptons are expected to have opposite charges. Consequently, by observing same-charge di-lepton events ARGUS discovered B^0-$\bar{B}^0$ oscillations. In addition to the inclusive observation of same-charge di-lepton events, ARGUS was able to fully reconstruct one particular event as a $e^+e^- \rightarrow \Upsilon(4S) \rightarrow B^0B^0$ decay in the following decay chains:

$$\begin{aligned}
B_1^0 &\rightarrow D_1^{*-}\mu_1^+\nu_1 \\
&\qquad D_1^{*-} \rightarrow \bar{D}^0\pi_{1s}^- \\
&\qquad\qquad \bar{D}^0 \rightarrow K_1^+\pi_1^- \\
B_2^0 &\rightarrow D_2^{*-}\mu_2^+\nu_2 \\
&\qquad D_2^{*-} \rightarrow D^-\pi_s^0 \\
&\qquad\qquad D^- \rightarrow K_2^+\pi_2^-\pi_2^-
\end{aligned} \tag{1.5}$$

The fully reconstructed event and the assignment of the final state particles of the above decay chains is shown in Figure 1.1(a). In semileptonic decays of neutral B mesons, the positive (negative) charge of the lepton tags the neutral B mesons as a B^0 ($\bar{B}^0$). Therefore this event provides an illustrative example for the evidence of B^0-$\bar{B}^0$ oscillations.

ARGUS estimated the oscillation frequency to be approximately $0.5\,\mathrm{ps}^{-1}$ and the mixing probability to be $\chi = (17 \pm 5)\,\%$, indicating that B^0-$\bar{B}^0$ oscillations are a relatively large effect. Because the oscillations are caused by higher order electroweak interactions dominated by virtual top quark pairs, the ARGUS measurement provided evidence for a non-zero CKM element V_{td} and allowed to determine a lower bound on the top-quark mass of $m_t > 50\ \mathrm{GeV}/c^2$, suggesting the top-quark to be very heavy.

The implications of the long lifetime and the relatively large oscillation frequency of neutral B mesons on possible CP violating effects have already been pointed out early by I.I. Bigi and A.I. Sanda. In the same year 1987, they published a classical paper containing detailed theoretical considerations about how CP violation can manifest itself in B decays, and predicted certain decay modes to have large effects [15]. In Figure 1.1(b) two relevant passages of the article are shown. Most importantly, they demonstrated that CP violation can emerge in the decays of B^0 and $\bar{B}^0$ mesons to common final states. Particularly, the amplitudes in B^0 and

$\bar{B}^0$ decays are of comparable magnitude for decays to CP eigenstates, such as $B^0 \to J/\psi K^0_S$ and $B^0 \to D^+D^-$. In this case, the CP violating asymmetry is time-dependent and depends on the interplay of phases in the decay amplitudes and in the mixing. The mixing phase is $e^{-i\phi_M} = (V^*_{tb}V_{td})/(V_{tb}V^*_{td})$ and the result of a non-zero CKM element V_{td} by ARGUS raised the expectations of the so-called mixing-induced CP violation to be a large effect in B decays.

Furthermore, I.I. Bigi and A.I. Sanda demonstrated that the dynamics in the time evolution of two neutral B mesons produced with negative C-parity in an entangled state, e.g. as in $e^+e^- \to \Upsilon(4S) \to B^0\bar{B}^0$, depends on the proper decay time difference between both B mesons, $t_1 - t_2$, and not on their sum, $t_1 + t_2$ (see the emphasised minus signs in Equation 2.6 in Figure 1.1(b)). Consequently, the proper decay time difference between two B mesons in an $\Upsilon(4S)$ event needs to be measured to observe time-dependent CP violating asymmetries. Experimentally, the proper decay times of weakly decaying particles are estimated by the measurements of flight lengths. Up to that time, all storage rings operated on the $\Upsilon(4S)$-resonance were symmetric-energy e^+e^--colliders. At symmetric-energy colliders, the average decay length is only about 30 µm in laboratory frame: a distance too small to resolve the corresponding proper decay time differences by vertex detectors in collision experiments, even at the present day.

This situation resulted in the idea to build asymmetric-energy e^+e^--colliders [16]. The asymmetry in the energy of the beams causes the $\Upsilon(4S)$ to move in the laboratory frame and increases the spatial separation of the B meson decay vertices to about 200 µm on average. The translation of measurements of decay flight length differences into proper decay time differences by the known Lorentz boost of the $\Upsilon(4S)$ then allows to observe time-dependent CP violating asymmetries. Furthermore, the low branching fractions of relevant B decays, e.g. $\mathcal{B}\left(B^0 \to J/\psi K^0_S\right) \approx 4 \times 10^{-4}$, imposed high demands on the luminosity of future accelerators to perform measurements in feasible time periods. The accelerators are required to operate on instantaneous luminosities in the order of 10^{34} $cm^{-2}s^{-1}$, which is about three orders of magnitude higher than that of PEP, CESR and DORIS.

Two asymmetric-energy e^+e^--colliders, KEKB at KEK and PEP II at SLAC, were designed and constructed as high luminosity B-factories [17, 18]. For measurements at the B-factories, at KEKB the Belle experiment and at PEP II the BaBar experiment were designed and constructed [19, 20]. Both B-factory experiments were commissioned and started taking data in the year 1999.

In 2001, the Belle and BaBar Collaborations established CP violation in the B meson system. Confirming the predictions of I.I. Bigi and A.I. Sanda from 1987, Belle and BaBar observed mixing-induced CP violation in the time-dependent CP violating asymmetry of $B^0 \to (c\bar{c})\,K^0$ decays [21, 22]. For example, Belle reported the measurement of mixing-induced CP violation of

$$\sin(2\beta) = 0.99 \pm 0.14\ (\text{stat.}) \pm\ 0.06\ (\text{syst.}), \tag{1.6}$$

where β denotes one angle in the Unitarity Triangle and is sensitive to the mixing-phase in B^0-$\bar{B}^0$ oscillations. The proper decay time distributions of this measurement are shown in Figure 1.1(c). The measurements demonstrated that CP violation is a large effect in the B meson system, unlike in the kaon system. The discovery motivated to look for CP violation in a variety of other B decay modes.

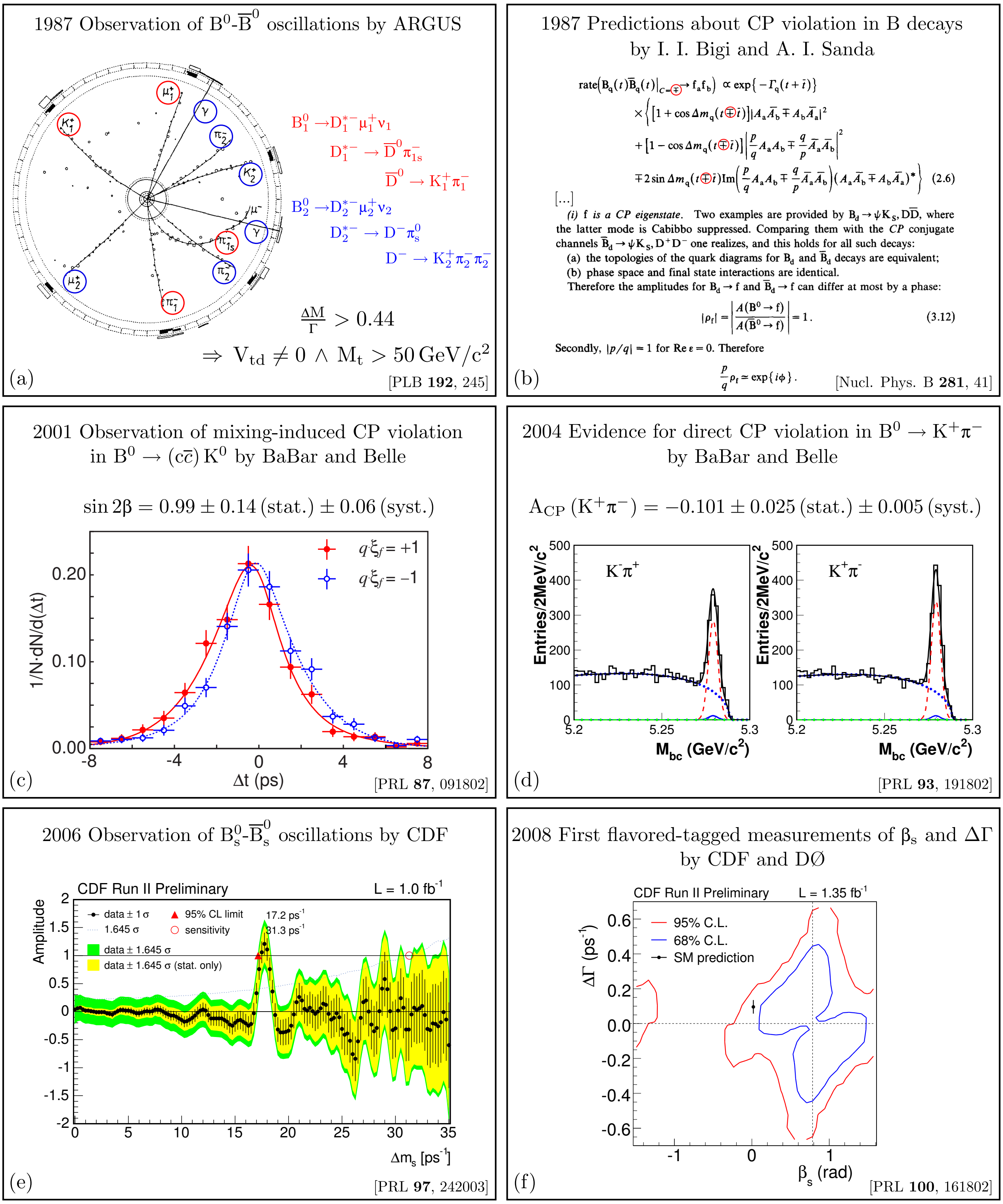

1987 Observation of B^0-$\overline{B}^0$ oscillations by ARGUS

$B_1^0 \to D_1^{*-}\mu_1^+\nu_1$

$D_1^{*-} \to \overline{D}^0\pi_{1s}^-$

$\overline{D}^0 \to K_1^+\pi_1^-$

$B_2^0 \to D_2^{*-}\mu_2^+\nu_2$

$D_2^{*-} \to D^-\pi_s^0$

$D^- \to K_2^+\pi_2^-\pi_2^-$

$$\frac{\Delta M}{\Gamma} > 0.44$$

$$\Rightarrow V_{td} \neq 0 \wedge M_t > 50\,\mathrm{GeV/c^2}$$

(a) [PLB **192**, 245]

1987 Predictions about CP violation in B decays by I. I. Bigi and A. I. Sanda

$$\begin{aligned}\mathrm{rate}\left(B_q(t)\overline{B}_q(t)\big|_{C=\enclose{circle}{\mp}} \to f_a f_b\right) &\propto \exp\{-\Gamma_q(t+\bar{t})\}\\ &\times\Big\{\left[1+\cos\Delta m_q(t\enclose{circle}{\mp}\bar{t})\right]|A_a\overline{A}_b \mp A_b\overline{A}_a|^2\\ &+\left[1-\cos\Delta m_q(t\enclose{circle}{\mp}\bar{t})\right]\left|\frac{p}{q}A_aA_b \mp \frac{q}{p}\overline{A}_a\overline{A}_b\right|^2\\ &\mp 2\sin\Delta m_q(t\enclose{circle}{\mp}\bar{t})\,\mathrm{Im}\left(\frac{p}{q}A_aA_b \mp \frac{q}{p}\overline{A}_a\overline{A}_b\right)\left(A_a\overline{A}_b \mp A_b\overline{A}_a\right)^*\Big\} \qquad (2.6)\end{aligned}$$

[...]

(i) f is a CP eigenstate. Two examples are provided by $B_d \to \psi K_S, D\overline{D}$, where the latter mode is Cabibbo suppressed. Comparing them with the *CP* conjugate channels $\overline{B}_d \to \psi K_S, D^+D^-$ one realizes, and this holds for all such decays:

(a) the topologies of the quark diagrams for B_d and $\overline{B}_d$ decays are equivalent;
(b) phase space and final state interactions are identical.

Therefore the amplitudes for $B_d \to f$ and $\overline{B}_d \to f$ can differ at most by a phase:

$$|\rho_f| = \left|\frac{A(B^0 \to f)}{A(\overline{B}^0 \to f)}\right| = 1. \qquad (3.12)$$

Secondly, $|p/q| = 1$ for $\mathrm{Re}\,\varepsilon = 0$. Therefore

$$\frac{p}{q}\rho_f \simeq \exp\{i\phi\}.$$

(b) [Nucl. Phys. B **281**, 41]

2001 Observation of mixing-induced CP violation in $B^0 \to (c\bar{c})\,K^0$ by BaBar and Belle

$$\sin 2\beta = 0.99 \pm 0.14\,(\mathrm{stat.}) \pm 0.06\,(\mathrm{syst.})$$

(c) [PRL **87**, 091802]

2004 Evidence for direct CP violation in $B^0 \to K^+\pi^-$ by BaBar and Belle

$$A_{CP}\,(K^+\pi^-) = -0.101 \pm 0.025\,(\mathrm{stat.}) \pm 0.005\,(\mathrm{syst.})$$

(d) [PRL **93**, 191802]

2006 Observation of B_s^0-$\overline{B}_s^0$ oscillations by CDF

(e) [PRL **97**, 242003]

2008 First flavored-tagged measurements of β_s and $\Delta\Gamma$ by CDF and DØ

(f) [PRL **100**, 161802]

Figure 1.1: Selection of milestones in the history of physics related to B mesons.

In 2004, the Belle and BaBar Collaborations found evidence for direct CP violation in $B^0 \to K^+\pi^-$ decays [23, 24]. For example, Belle reported an asymmetry of

$$A_{CP}\left(B^0 \to K^+\pi^-\right) = -0.101 \pm 0.025\ (\text{stat.}) \pm\ 0.005\ (\text{syst.}). \tag{1.7}$$

Direct CP violation manifests itself in an asymmetry in the occurrence of CP conjugated processes, as it is visible in the difference of signal yields for $B^0 \to K^+\pi^-$ and $\bar{B}^0 \to K^-\pi^+$ decays in Figure 1.1(d). The effect requires an interference between different amplitudes contributing to the decay. In particular, the direct CP violation in $B^0 \to K^+\pi^-$ decays is caused by large contributions of $b \to d$ penguin amplitudes.

Thus, the B-factory experiments were able to find direct CP violation in B decays in a short period of time at a level of 10^{-1}. These measurements can be compared to the kaon system, where the observation of direct CP violation took more than 30 years of experimental efforts, and was established at a level of 10^{-6} not until the year 1999 [25, 26].

A closely related particle to the B^0 meson is the B_s^0 meson. The particles differ only by the exchange of a down-quark to a strange-quark, and a variety of effects established in the B^0 system are expected to emerge in the B_s^0 system by similar mechanisms. At the Tevatron $p\bar{p}$-collider, the CDF and DØ Collaborations performed measurements in the B_s^0 system that paved the way for future experimental research.

In 2006, CDF observed B_s^0-$\bar{B}_s^0$ oscillations [27], and determined the oscillation frequency to be about 35-times higher than that of B^0 mesons, see Figure 1.1(e). The B-factory experiments are not able to resolve the time-dependence of particles involving such fast oscillations. The time-dependent measurements in the B_s^0 system require large Lorentz boosts as provided only by high energy hadron colliders.

In 2008, CDF and DØ performed the first flavor-tagged measurement of $\Delta\Gamma$ and β_s in $B_s^0 \to J/\psi\phi$ decays [28, 29]. The CDF result is shown in Figure 1.1(f). In analogy to the mixing-induced CP violation measurements by BaBar and Belle related to the angle β of the Unitarity Triangle, the measurements of the corresponding angle β_s are sensitive to the mixing phase in B_s^0-$\bar{B}_s^0$ oscillations, $e^{-i\phi_{M_s}} = (V_{tb}^* V_{ts})/(V_{tb} V_{ts}^*)$. Since the effect is much smaller than in the B^0 system, the observation of $\beta_s \neq 0$ requires further measurements by new experiments.

During the work to this thesis, the LHCb experiment, a new experiment dedicated to study B physics at the LHC pp-collider at CERN, started operation. In 2012, the LHCb Collaboration reported evidence for a time-integrated difference in the CP asymmetry between $D^0 \to K^-K^+$ and $D^0 \to \pi^-\pi^+$ decays of

$$\Delta A_{CP} = A_{CP}\left(D^0 \to K^-K^+\right) - A_{CP}\left(D^0 \to \pi^-\pi^+\right) = (-0.82 \pm 0.21\ (\text{stat.}) \pm 0.11\ (\text{syst.}))\%, \tag{1.8}$$

corresponding to a significance of 3.5σ [30]. This difference is sensitive to direct CP violation, and, if confirmed, provides the first evidence for CP violation in the charm sector.

Further experimental efforts will contribute to the understanding of the flavor structure of the Standard Model and, in addition to the kaon and B meson system, possibly establish the Kobayashi-Maskawa mechanism for the generation of CP violation in other systems of weakly decaying mesons.

1.2 Connection to Cosmological Problems

In fundamental cosmological questions, the phenomenon of CP violation is discussed as one ingredient to explain the dominance of matter over antimatter in the universe. In particular the observation of the primordial abundance of deuterium and the measurements of the cosmic microwave background indicate a cosmological baryon asymmetry of $\mathcal{O}(10^{-10})$ [31, 32].

In 1967, Andrei Sakharov proposed three necessary conditions needed to be satisfied to generate a baryon-antibaryon asymmetry from an initially symmetric state [33]. According to Sakharov, an excess of baryons over antibaryons can be developed by a dynamic mechanism in the hot model of the expanding universe, if there exist

- a deviation from thermal equilibrium in the early phase of the hot and dense universe,
- interactions violating the conservation of baryon number,
- differences between the probabilities of charge-conjugated processes, or expressed equivalently: the violation of C and CP symmetries.

The violation of CP symmetry has so far been observed only in electroweak interactions of quarks, in particular in decays of mesons. The CP violation generated by the Kobayashi-Maskawa mechanism is considered to be several magnitudes to small to generate the observed asymmetry in the universe by electroweak baryogenesis [34]. These findings are an important motivation to search for further sources of CP violation in nature.

2 Theoretical Foundations

2.1 CP Violation in the Standard Model of Particle Physics

In the Standard Model of particle physics, the theory of electromagnetic and weak interactions is unified by the Glashow-Weinberg-Salam (GWS) model [35, 36]. The GWS model describes the electroweak interactions by a gauge theory based on spontaneously broken symmetry groups

$$\mathrm{SU}(2)_\mathrm{L} \times \mathrm{U}(1)_\mathrm{Y} \xrightarrow{\mathrm{SSB}} \mathrm{U}(1)_\mathrm{em}. \tag{2.1}$$

The electroweak symmetry breaking is assumed to be caused by the Higgs mechanism which generates the $\mathrm{W}^\pm$ and Z^0 gauge boson masses and the masses of the fundamental fermions [37]. The effect of CP violation is closely related to the flavor structure, the mass hierarchy and the number of fermion families within the Standard Model.

In the following, the basic principles of the Standard Model of electroweak interactions and of the spontaneous symmetry breaking by the Higgs mechanism are briefly described. In addition, it will be demonstrated, how the Higgs field introduces complex couplings to the quark fields in the Yukawa interactions, and how the couplings give rise to CP violation in the charged-current interactions of quarks. The discussion neglects details of the leptonic sector and focuses on the electroweak interactions of quarks.

The fundamental fermions are organised into three families of quarks and leptons:

$$\begin{pmatrix} \mathrm{u} & \nu_\mathrm{e} \\ \mathrm{d} & \mathrm{e}^- \end{pmatrix}, \quad \begin{pmatrix} \mathrm{c} & \nu_\mu \\ \mathrm{s} & \mu^- \end{pmatrix} \quad \text{and} \quad \begin{pmatrix} \mathrm{t} & \nu_\tau \\ \mathrm{b} & \tau^- \end{pmatrix} \tag{2.2}$$

The families have identical gauge interactions, but differ in their flavor quantum numbers and masses. The quarks and leptons form doublets of left-handed and singlets of right-handed fields, denoted in the following by

$$\begin{pmatrix} \mathrm{u_j} & \nu_\mathrm{j} \\ \mathrm{d_j} & \mathrm{e_j} \end{pmatrix} \quad \to \quad \begin{pmatrix} \mathrm{u_{Lj}} \\ \mathrm{d_{Lj}} \end{pmatrix}, \quad \begin{pmatrix} \nu_\mathrm{Lj} \\ \mathrm{l_{Lj}} \end{pmatrix} \quad \text{and} \quad \mathrm{u_{Rj}}, \mathrm{d_{Rj}}, \mathrm{l_{Rj}} \qquad \text{for } \mathrm{j} \in \{1,2,3\}, \tag{2.3}$$

where the quark fields are given in the weak eigenstate basis and the index j specifies the family.

The Lagrangian invariant under gauge transformations involves dynamical terms for the quark fields and kinetic terms for the gauge fields B_μ and $\mathrm{W}^\mathrm{i}_\mu$,

$$\mathcal{L} = \left(\bar{\mathrm{u}}_\mathrm{Lj}, \bar{\mathrm{d}}_\mathrm{Lj}\right) \mathrm{i} \not{D} \begin{pmatrix} \mathrm{u_{Lj}} \\ \mathrm{d_{Lj}} \end{pmatrix} + \bar{\mathrm{u}}_\mathrm{Rj}\, \mathrm{i} \not{D}\, \mathrm{u_{Rj}} + \bar{\mathrm{d}}_\mathrm{Rj}\, \mathrm{i} \not{D}\, \mathrm{d_{Rj}} - \frac{1}{4} \mathrm{B}_{\mu\nu} \mathrm{B}^{\mu\nu} - \frac{1}{4} \mathrm{W}^\mathrm{i}_{\mu\nu} \mathrm{W}^{\mu\nu}_\mathrm{i}, \tag{2.4}$$

where the symbol $\not{D}$ is defined as $\not{D} := \gamma^\mu \mathrm{D}_\mu$. The covariant derivative D_μ introduces couplings of the gauge fields B_μ and W^i_μ to the quark fields, and can be expressed as

$$D_\mu = \partial_\mu - i g' Y B_\mu - i g T^a W^a_\mu, \tag{2.5}$$

where g' and g are the electroweak coupling constants, and T^a and Y are the generators of the $SU(2)_L$ and the $U(1)_Y$ symmetry groups that introduce the weak isospin and hypercharge.

In $U(1)$, the field strength tensor $B_{\mu\nu}$ is related to the gauge field by

$$B_{\mu\nu} = \partial_\mu B_\nu - \partial_\nu B_\mu, \tag{2.6}$$

and in $SU(2)$, the field strength tensors $W^i_{\mu\nu}$ are related to the gauge fields by

$$W^i_{\mu\nu} = \partial_\mu W^i_\nu - \partial_\nu W^i_\mu - g\,\varepsilon^{ijk} W^j_\mu W^k_\nu \qquad \text{for } i \in \{1,2,3\}. \tag{2.7}$$

The coupling constants g' and g are related to the Weinberg angle θ_W and the electric charge e by

$$g \sin\theta_W = g' \cos\theta_W = e, \tag{2.8}$$

which provides the unification of weak and electromagnetic interactions.

In this form the vector bosons corresponding to the gauge fields B_μ and W^i_μ are massless and cause long range weak interactions. Furthermore, the couplings are defined as real preventing CP violation to emerge in the interactions.

The Standard Model contains a single $SU(2)$ doublet of a scalar field, that is referred to as the Higgs field and defined by

$$\phi = \begin{pmatrix} \phi^+ \\ \phi^0 \end{pmatrix}. \tag{2.9}$$

The Lagrangian of the scalar field, given by

$$\mathcal{L}_{\text{Higgs}} = \left(D_\mu \phi\right)^\dagger D_\mu \phi - \mu^2 \phi^\dagger \phi - \lambda \left(\phi^\dagger \phi\right)^2, \tag{2.10}$$

is invariant under local $SU(2) \times U(1)$ transformations. The covariant derivative D_μ takes the same form as in Equation 2.5 and introduces the scalar hypercharge in a way that the ϕ^0 does not couple to the photon.

If the scalar field acquires a non-vanishing vacuum expectation value, for example expressed by

$$\langle 0|\phi|0\rangle = \frac{1}{\sqrt{2}} \begin{pmatrix} 0 \\ v \end{pmatrix} \qquad \text{with } \phi = \frac{1}{\sqrt{2}} e^{i \frac{\sigma^i}{2} \theta^i(x)} \begin{pmatrix} 0 \\ v + h(x) \end{pmatrix} \text{ and } v = \sqrt{-\frac{\mu^2}{\lambda}}, \tag{2.11}$$

then the $SU(2)_L \times U(1)_Y$ symmetry gets spontaneously broken down to the $U(1)_{em}$ subgroup, that remains symmetric with respect to the vacuum.

The non-vanishing vacuum expectation value causes the ground state to be degenerated and allows for massless scalar excitations that can be identified as Goldstone bosons. The Goldstone bosons can be eliminated by making use of the $SU(2)$ invariance of the Lagrangian and removing the dependence on θ^i in Equation 2.11 by rotations. In the so-called unitarity gauge, the kinetic term of the Lagrangian in Equation 2.10 adopts the form

$$\left(D_\mu\phi\right)^\dagger D_\mu\phi = \frac{1}{2}\left(\partial_\mu h\right)(\partial^\mu h) + \frac{1}{8}\left[\left(g'B_\mu - gW^3_\mu\right)^2 + g^2\left(W^1_\mu\right)^2 + g^2\left(W^2_\mu\right)^2\right](h+v)^2. \tag{2.12}$$

The non-vanishing vacuum expectation value of the scalar field gives rise to quadratic terms of the gauge fields and as a consequence the gauge bosons that correspond to these fields acquire a mass. The elimination of the Goldestone bosons can be considered as absorbing the degrees of freedom from the Goldstone bosons into the longitudinal components of the gauge bosons.

From the Higgs Lagrangian, the fields of three massive vector bosons can be constructed by combinations of the gauge fields B_μ and W^i_μ:

$$\begin{aligned} W^+_\mu &= \frac{1}{\sqrt{2}}\left(W^1_\mu - i\,W^2_\mu\right) \\ W^-_\mu &= \frac{1}{\sqrt{2}}\left(W^1_\mu + i\,W^2_\mu\right) \\ Z_\mu &= \frac{1}{\sqrt{g^2+g'^2}}\left(gW^3_\mu - g'B_\mu\right) \end{aligned} \tag{2.13}$$

The fields W^+_μ, W^-_μ and Z_μ can be identified as the heavy vector bosons W^+, W^- and Z^0 mediating weak interactions. Their masses are related by

$$M_{W^\pm} = M_{Z^0}\cos\theta_W = \frac{1}{2}gv. \tag{2.14}$$

The combination orthogonal to the Z_μ field,

$$A_\mu = \frac{1}{\sqrt{g^2+g'^2}}\left(g'W^3_\mu + gB_\mu\right), \tag{2.15}$$

has no mass term and can be identified as the photon.

The couplings of the fermions to the vector bosons can be expressed as the interactions of neutral and charged currents described by the Lagrangian

$$\mathcal{L}_{\text{int}} = \underbrace{eJ^\mu_{em}A_\mu + \frac{g}{\cos\theta_W}\left(J^\mu_Z - \sin^2\theta_W J^\mu_{em}\right)Z_\mu}_{\text{neutral current interaction (NC)}} \;-\; \underbrace{\frac{1}{\sqrt{2}}g\left(J^\mu_+W^-_\mu + J^\mu_-W^+_\mu\right)}_{\text{charged current interaction (CC)}}\;, \tag{2.16}$$

where the electromagnetic current J^μ_{em} is given by

$$J^\mu_{em} = \frac{2}{3}\bar{u}_{Lj}\gamma^\mu u_{Lj} - \frac{1}{3}\bar{d}_{Lj}\gamma^\mu d_{Lj} - \bar{l}_{Lj}\gamma^\mu l_{Lj}, \tag{2.17}$$

the neutral weak current J^μ_Z is given by

$$J^\mu_Z = \frac{1}{2}\left(\bar{u}_{Lj}\gamma^\mu u_{Lj} - \bar{d}_{Lj}\gamma^\mu d_{Lj} - \bar{l}_{Lj}\gamma^\mu l_{Lj} + \bar{\nu}_{Lj}\gamma^\mu \nu_{Lj}\right), \tag{2.18}$$

and the weak charged currents $J^{\mu}_{\pm}$ are given by

$$\begin{aligned} J^{\mu}_{+} &= \bar{u}_{Lj}\gamma^{\mu}d_{Lj} + l_{Lj}\gamma^{\mu}\nu_{Lj}, \\ J^{\mu}_{-} &= \bar{d}_{Lj}\gamma^{\mu}u_{Lj} + \nu_{Lj}\gamma^{\mu}l_{Lj}. \end{aligned} \tag{2.19}$$

The quark masses arise from the Yukawa interactions with the Higgs field. The Lagrangian of the Yukawa interaction involves the coupling of right-handed quark field singlets via the scalar field ϕ to left-handed quark field doublets and can be written as

$$\mathcal{L}_{\text{Yukawa}} = -Y^{d}_{ij}\left(\bar{u}_{Lj},\bar{d}_{Lj}\right)\begin{pmatrix} \phi^{+} \\ \phi^{0} \end{pmatrix} d_{Rj} - Y^{u}_{ij}\left(\bar{u}_{Lj},\bar{d}_{Lj}\right)\begin{pmatrix} \phi^{0*} \\ -\phi^{-} \end{pmatrix} u_{Rj}, \tag{2.20}$$

where the Yukawa couplings Y^d and Y^u are complex matrices for up-type and down-type quarks. If the scalar field ϕ acquires a non-vanishing vacuum expectation value, then the Yukawa interactions constitute mass terms for the quarks. In the unitarity gauge, the mass matrices M^u and M^d for the up-type and down-type quarks are proportional to the Yukawa couplings with the scale given by the vacuum expectation value v:

$$(M^{u})_{ij} = \frac{1}{\sqrt{2}}Y^{u}_{ij}v \qquad \text{and} \qquad \left(M^{d}\right)_{ij} = \frac{1}{\sqrt{2}}Y^{d}_{ij}v \tag{2.21}$$

The mass eigenstates of the quarks are determined from the diagonalisation of the mass matrices with the four unitary 3×3 matrices U^u_L, U^u_R, U^d_L and U^d_R,

$$\begin{pmatrix} m_u & 0 & 0 \\ 0 & m_c & 0 \\ 0 & 0 & m_t \end{pmatrix} = U^{u}_{L}M^{u}U^{u\dagger}_{R} \qquad \text{and} \qquad \begin{pmatrix} m_d & 0 & 0 \\ 0 & m_s & 0 \\ 0 & 0 & m_b \end{pmatrix} = U^{d}_{L}M^{d}U^{d\dagger}_{R}. \tag{2.22}$$

The matrices U^u_L, U^u_R, U^d_L and U^d_R transform the left-handed and right-handed quark fields from the weak eigenstate basis, denoted by u and d, to the mass eigenstate basis, denoted in the following by u^m and d^m:

$$\begin{aligned} u^{m}_{L} &= U^{u}_{L}u_{L} & \qquad d^{m}_{L} &= U^{d}_{L}d_{L} \\ u^{m}_{R} &= U^{u}_{R}u_{R} & \qquad d^{m}_{R} &= U^{d}_{R}d_{R} \end{aligned} \tag{2.23}$$

The Lagrangian describing the interactions of quarks with the gauge fields in Equation 2.16 can be written in terms of the quark mass eigenstates. The expressions for the neutral currents retain their form when applying the above transformations. This invariance of the neutral currents with respect to transformations from the weak to the mass eigenstate basis is the reason that no flavor changing neutral currents occur on tree-level and is the fundament of the Glashow-Iliopolus-Maiani (GIM) mechanism [38].

The charged currents expressed in the mass eigenstate basis are

$$\begin{aligned} J^{+}_{\mu} &= \bar{u}_{L}\gamma^{\mu}d_{L} = \bar{u}^{m}_{L}\gamma^{\mu}U^{u}_{L}U^{d\dagger}_{L}d^{m}_{L} = \bar{u}^{m}_{L}\gamma^{\mu}V_{CKM}d^{m}_{L} \\ J^{-}_{\mu} &= \bar{d}_{L}\gamma^{\mu}u_{L} = \bar{d}^{m}_{L}\gamma^{\mu}U^{d}_{L}U^{u\dagger}_{L}u^{m}_{L} = \bar{d}^{m}_{L}\gamma^{\mu}V^{\dagger}_{CKM}u^{m}_{L}, \end{aligned} \tag{2.24}$$

where $V_{CKM} = U^{u}_{L}U^{d\dagger}_{L}$ is the unitary 3×3 Cabibbo-Kobayashi-Masakawa (CKM) matrix. The

CKM matrix defines the couplings of the W± bosons to the quarks with definite masses in charged-currents interactions.

For the charged current interactions of quarks, the Lagrangian and the corresponding CP-conjugated Lagrangian expressed by the mass eigenstates of quarks and using the chirality operator $1-\gamma^5$ are

$$\begin{gathered}
\mathcal{L}_{\mathrm{int}}^{\mathrm{CC}} = -\frac{1}{\sqrt{2}} g \left[\left(\sum_{\mathrm{ij}} (\mathrm{V}_{\mathrm{CKM}})_{\mathrm{ij}} \, \bar{\mathrm{u}}_{\mathrm{i}}^{\mathrm{m}} \gamma^{\mu} \left(1-\gamma^5\right) \mathrm{d}_{\mathrm{j}}^{\mathrm{m}} \right) \mathrm{W}_{\mu}^{-} + \left(\sum_{\mathrm{ij}} (\mathrm{V}_{\mathrm{CKM}})_{\mathrm{ij}}^{*} \, \bar{\mathrm{d}}_{\mathrm{j}}^{\mathrm{m}} \gamma^{\mu} \left(1-\gamma^5\right) \mathrm{u}_{\mathrm{i}}^{\mathrm{m}} \right) \mathrm{W}_{\mu}^{+} \right] \\
\mathrm{CP} \Updownarrow \qquad (2.25) \\
\mathcal{L}_{\mathrm{int}}^{\mathrm{CC,CP}} = -\frac{1}{\sqrt{2}} g \left[\left(\sum_{\mathrm{ij}} (\mathrm{V}_{\mathrm{CKM}})_{\mathrm{ij}} \, \bar{\mathrm{d}}_{\mathrm{j}}^{\mathrm{m}} \gamma^{\mu} \left(1-\gamma^5\right) \mathrm{u}_{\mathrm{i}}^{\mathrm{m}} \right) \mathrm{W}_{\mu}^{+} + \left(\sum_{\mathrm{ij}} (\mathrm{V}_{\mathrm{CKM}})_{\mathrm{ij}}^{*} \, \bar{\mathrm{u}}_{\mathrm{i}}^{\mathrm{m}} \gamma^{\mu} \left(1-\gamma^5\right) \mathrm{d}_{\mathrm{j}}^{\mathrm{m}} \right) \mathrm{W}_{\mu}^{-} \right].
\end{gathered}$$

The above equations show, that the symmetry under CP transformations is only conserved in the charged-current interactions of quarks, if $(\mathrm{V}_{\mathrm{CKM}})_{\mathrm{ij}}^{*} = (\mathrm{V}_{\mathrm{CKM}})_{\mathrm{ij}}$ is satisfied. In 1973, Kobayashi and Maskawa demonstrated that the quark mixing matrix contains an irreducible complex phase, if there are at least three families of quarks [4]. The complex phase causes $(\mathrm{V}_{\mathrm{CKM}})_{\mathrm{ij}}^{*} \neq (\mathrm{V}_{\mathrm{CKM}})_{\mathrm{ij}}$ and is the only source of CP violation in the Standard Model. Because of its importance, the properties and the implications of the CKM matrix are explained in more detail in the next section.

2.2 The CKM Matrix and the Unitarity Triangle

In the charged-current interaction given by the Lagrangian in Equation 2.25, the physical up-type and down-type quarks with definite masses couple to the $W^{\pm}$ bosons according to the involved CKM elements as illustrated in Figure 2.1.

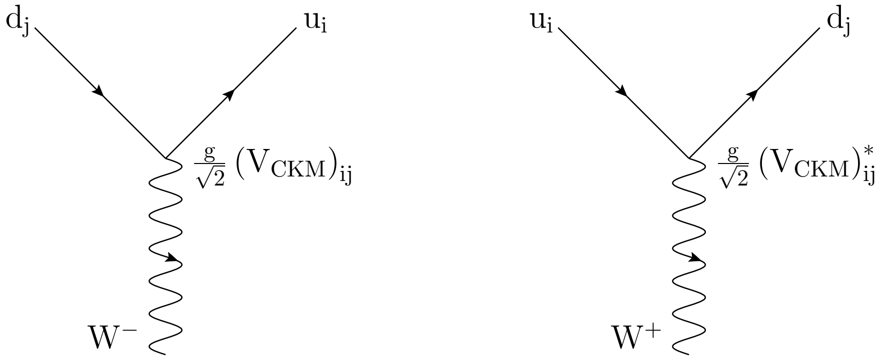

Figure 2.1: The couplings of up-type and down-type quarks to $W^{\pm}$ bosons in the mass eigenstate basis.

The CKM matrix relates the mass eigenstates of the down-type quarks to the corresponding weak eigenstates by

$$\begin{pmatrix} d \\ s \\ b \end{pmatrix}_{\substack{\text{weak}\\ \text{basis}}} = \begin{pmatrix} V_{ud} & V_{us} & V_{ub} \\ V_{cd} & V_{cs} & V_{cb} \\ V_{td} & V_{ts} & V_{tb} \end{pmatrix} \begin{pmatrix} d \\ s \\ b \end{pmatrix}_{\substack{\text{mass}\\ \text{basis}}} . \tag{2.26}$$

In general, a complex $N \times N$ matrix contains $2N^2$ real parameters. The unitarity of the CKM matrix, equivalent to

$$\sum_i (V_{CKM})_{ij} (V_{CKM})^*_{ik} = \delta_{jk} \qquad \text{and} \qquad \sum_j (V_{CKM})_{ij} (V_{CKM})^*_{kj} = \delta_{ik}, \tag{2.27}$$

reduces the number of independent real parameters to N^2.

The phases of the up-type and down-type quark fields can be arbitrarily rotated by the transformations

$$u_i \to e^{i\phi^u_i} u_i \qquad \text{and} \qquad d_j \to e^{i\phi^d_j} d_j. \tag{2.28}$$

When applying the above transformations to the CKM elements according to

$$(V_{CKM})_{ij} \to e^{-i\phi^u_i} (V_{CKM})_{ij} e^{i\phi^d_j}, \tag{2.29}$$

then $2N-1$ relative phases can be eliminated and therefore the matrix contains $(N-1)^2$ independent physical parameters. In general an orthogonal $N \times N$ matrix can be composed from $\frac{1}{2}N(N-1)$ independent rotation angles. Consequently, the CKM matrix can be constructed from

$$\underbrace{\frac{1}{2}N(N-1)}_{\text{angles}} + \underbrace{\frac{1}{2}(N-1)(N-2)}_{\text{phases}} = \underbrace{(N-1)^2}_{\text{total parameters}} \tag{2.30}$$

parameters [39].

In the case of two fermion families, the CKM matrix contains only one angle and no phase. This case would not allow for CP violation and is equivalent to the two family quark mixing described by the Cabibbo-Matrix [40],

$$V_{\mathrm{Cabibbo}} = \begin{pmatrix} \cos\theta_C & \sin\theta_C \\ -\sin\theta_C & \cos\theta_C \end{pmatrix}, \tag{2.31}$$

where $\sin\theta_C = |V_{us}| \approx 0.23$ and $\theta_C \approx 13°$ is the Cabibbo angle [41].

In the case of three fermion families as in the Standard Model, the CKM matrix is described by three angles and one complex phase. A representation in analogy to the Cabibbo matrix uses rotations with angles θ_{ij} between family i and j in the parameterisation

$$\mathbf{V}_{\mathrm{CKM}} = \begin{pmatrix} 1 & 0 & 0 \\ 0 & c_{23} & s_{23} \\ 0 & -s_{23} & c_{23} \end{pmatrix} \begin{pmatrix} c_{13} & 0 & s_{13}e^{-i\delta} \\ 0 & 1 & 0 \\ -s_{13}e^{i\delta} & 0 & c_{13} \end{pmatrix} \begin{pmatrix} c_{12} & s_{12} & 0 \\ -s_{12} & c_{12} & 0 \\ 0 & 0 & 1 \end{pmatrix} \tag{2.32}$$

$$= \begin{pmatrix} c_{12}c_{13} & s_{12}c_{13} & s_{13}e^{-i\delta} \\ -s_{12}c_{23} - c_{12}s_{23}s_{13}e^{i\delta} & c_{12}c_{23} - s_{12}s_{23}s_{13}e^{i\delta} & s_{23}c_{13} \\ s_{12}s_{23} - c_{12}c_{23}s_{13}e^{i\delta} & -c_{12}s_{23} - s_{12}c_{23}s_{13}e^{i\delta} & c_{23}c_{13} \end{pmatrix}, \tag{2.33}$$

where $c_{ij} = \cos\theta_{ij}$ and $s_{ij} = \sin\theta_{ij}$, and δ is the CP violating phase [42].

The experimental determination of the flavor structure revealed a strong hierarchy in the CKM matrix, which manifests itself in $s_{13} \ll s_{23} \ll s_{12} \ll 1$. The hierarchical structure becomes apparent in a representation in terms of the Wolfenstein parameters λ, A, ρ and η defined by the relations [43]

$$s_{12} = \lambda = \frac{|V_{us}|}{\sqrt{|V_{ud}|^2 + |V_{us}|^2}}, \qquad s_{23} = A\lambda^2, \qquad s_{13}\, e^{\delta} = A\lambda^3 (\rho + i\eta) = V^*_{ub}. \tag{2.34}$$

The expansion of the CKM elements in terms of powers of the parameter $\lambda \approx 0.23$ up to the order of three results in

$$\mathbf{V}_{\mathrm{CKM}} = \begin{pmatrix} 1 - \lambda^2/2 & \lambda & A\lambda^3 (\rho - i\eta) \\ -\lambda & 1 - \lambda^2/2 & A\lambda^2 \\ A\lambda^3 (1 - \rho - i\eta) & -A\lambda^2 & 1 \end{pmatrix} + \mathcal{O}\left(\lambda^4\right). \tag{2.35}$$

This representation reveals the hierarchical structure of the CKM matrix. The diagonal elements representing transitions within the same family are close to one. The transitions from the first to the second family are suppressed by a factor λ, the transitions from the second to the third family by a factor λ^2 and the transitions from the first to the third family by a factor λ^3. Furthermore, at this order of expansion the complex phase manifests itself in the CKM elements V_{td} and V_{ub}, which implies CP violation to be possibly sizeable in transitions involving b quarks.

The unitarity of the CKM matrix as expressed by Equation 2.27 results in the following six relations of vanishing CKM element combinations:

$$\underbrace{\mathbf{V}^*_{\mathrm{ud}}\mathbf{V}_{\mathrm{us}}}_{\mathcal{O}(\lambda)}+\underbrace{\mathbf{V}^*_{\mathrm{cd}}\mathbf{V}_{\mathrm{cs}}}_{\mathcal{O}(\lambda)}+\underbrace{\mathbf{V}^*_{\mathrm{td}}\mathbf{V}_{\mathrm{ts}}}_{\mathcal{O}(\lambda^5)}=\delta_{\mathrm{ds}}=0 \tag{2.36}$$

$$\underbrace{\mathbf{V}_{\mathrm{ud}}\mathbf{V}^*_{\mathrm{cd}}}_{\mathcal{O}(\lambda)}+\underbrace{\mathbf{V}_{\mathrm{us}}\mathbf{V}^*_{\mathrm{cs}}}_{\mathcal{O}(\lambda)}+\underbrace{\mathbf{V}_{\mathrm{ub}}\mathbf{V}^*_{\mathrm{cb}}}_{\mathcal{O}(\lambda^5)}=\delta_{\mathrm{uc}}=0 \tag{2.37}$$

$$\underbrace{\mathbf{V}^*_{\mathrm{us}}\mathbf{V}_{\mathrm{ub}}}_{\mathcal{O}(\lambda^4)}+\underbrace{\mathbf{V}^*_{\mathrm{cs}}\mathbf{V}_{\mathrm{cb}}}_{\mathcal{O}(\lambda^2)}+\underbrace{\mathbf{V}^*_{\mathrm{ts}}\mathbf{V}_{\mathrm{tb}}}_{\mathcal{O}(\lambda^2)}=\delta_{\mathrm{sb}}=0 \tag{2.38}$$

$$\underbrace{\mathbf{V}_{\mathrm{td}}\mathbf{V}^*_{\mathrm{cd}}}_{\mathcal{O}(\lambda^4)}+\underbrace{\mathbf{V}_{\mathrm{ts}}\mathbf{V}^*_{\mathrm{cs}}}_{\mathcal{O}(\lambda^2)}+\underbrace{\mathbf{V}_{\mathrm{tb}}\mathbf{V}^*_{\mathrm{cb}}}_{\mathcal{O}(\lambda^2)}=\delta_{\mathrm{ct}}=0 \tag{2.39}$$

$$\underbrace{\mathbf{V}_{\mathrm{td}}\mathbf{V}^*_{\mathrm{ud}}}_{\mathcal{O}(\lambda^3)}+\underbrace{\mathbf{V}_{\mathrm{ts}}\mathbf{V}^*_{\mathrm{us}}}_{\mathcal{O}(\lambda^3)}+\underbrace{\mathbf{V}_{\mathrm{tb}}\mathbf{V}^*_{\mathrm{ub}}}_{\mathcal{O}(\lambda^3)}=\delta_{\mathrm{ut}}=0 \tag{2.40}$$

$$\underbrace{\mathbf{V}_{\mathrm{ud}}\mathbf{V}^*_{\mathrm{ub}}}_{\mathcal{O}(\lambda^3)}+\underbrace{\mathbf{V}_{\mathrm{cd}}\mathbf{V}^*_{\mathrm{cb}}}_{\mathcal{O}(\lambda^3)}+\underbrace{\mathbf{V}_{\mathrm{td}}\mathbf{V}^*_{\mathrm{tb}}}_{\mathcal{O}(\lambda^3)}=\delta_{\mathrm{db}}=0 \tag{2.41}$$

The above relations can be interpreted geometrically as triangles in the complex plane. In the above equations, the order of side lengths in the triangles are specified in terms of the Wolfenstein parameter λ. The first four triangles have sides of very different lengths with ratios of $\lambda : \lambda^5 \approx 360$ and $\lambda^2 : \lambda^4 \approx 19$, and are therefore degenerate. The sides of the two last triangles all have a length in the order of λ^3 and consequently large internal angles in the order of 10°.

The six triangles corresponding to Equations 2.36 to 2.41 all have the same area which is half of the Jarlskog invariant J defined by [44]

$$\mathrm{J} = \pm\,\mathrm{Im}\left[\mathrm{V}_{\mathrm{ij}}\mathrm{V}_{\mathrm{kl}}\mathrm{V}^*_{\mathrm{il}}\mathrm{V}^*_{\mathrm{kj}}\right] \qquad \text{for } \mathrm{i} \neq \mathrm{k},\, \mathrm{l} \neq \mathrm{j}. \tag{2.42}$$

The Jarlskog invariant is a dimensionless and phase-convention independent measure of the size of CP violation in the Standard Model. The experimentally determined value is $\approx 3 \times 10^{-5}$ [45]. In combination with the quark masses, it leads to a neccessary condition for CP violation given by

$$-2\mathrm{J}\left(\mathrm{m}_{\mathrm{t}}^2-\mathrm{m}_{\mathrm{c}}^2\right)\left(\mathrm{m}_{\mathrm{c}}^2-\mathrm{m}_{\mathrm{u}}^2\right)\left(\mathrm{m}_{\mathrm{u}}^2-\mathrm{m}_{\mathrm{t}}^2\right)\left(\mathrm{m}_{\mathrm{b}}^2-\mathrm{m}_{\mathrm{s}}^2\right)\left(\mathrm{m}_{\mathrm{s}}^2-\mathrm{m}_{\mathrm{d}}^2\right)\left(\mathrm{m}_{\mathrm{d}}^2-\mathrm{m}_{\mathrm{b}}^2\right) \neq 0. \tag{2.43}$$

A non-vanishing value of the above relation is necessary for CP violation to emerge in the quark sector [39].

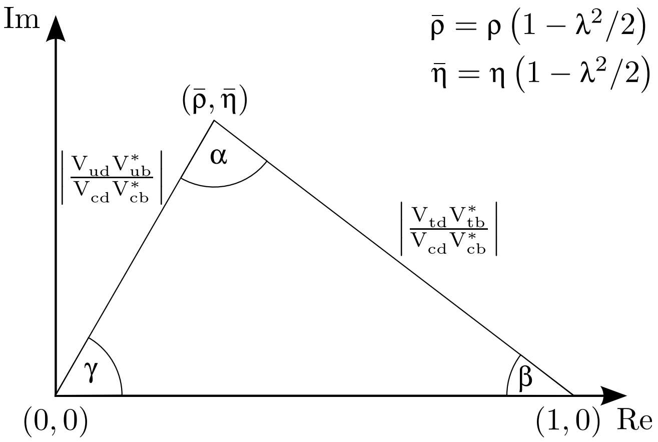

Figure 2.2: Illustration of the Unitarity Triangle in the complex plane.

Of particular interest for B physics is the triangle given by Equation 2.41, because each side is related to CKM elements describing b quark transitions as occurring in CKM-favored and CKM-suppressed B decays and in B^0-$\bar{B}^0$ oscillations. The so-called Unitarity Triangle arises by dividing each side by the experimentally best known side, which is $V_{cd}V_{cb}^*$. An illustration of the Unitarity Triangle and the definitions of the angles and sides is shown in Figure 2.2. The angles α, β and γ of the Unitarity Triangle, also often referred to as ϕ_2, ϕ_1, ϕ_3, are related to the CKM elements by

$$\alpha = \phi_2 = \arg\left(-\frac{V_{td}V_{tb}^*}{V_{ud}V_{ub}^*}\right), \tag{2.44}$$

$$\beta = \phi_1 = \arg\left(-\frac{V_{cd}V_{cb}^*}{V_{td}V_{tb}^*}\right), \tag{2.45}$$

$$\gamma = \phi_3 = \arg\left(-\frac{V_{ud}V_{ub}^*}{V_{cd}V_{cb}^*}\right). \tag{2.46}$$

One key objective of flavor physics, in particular of the Belle experiment, is to experimentally overconstrain the Unitarity Triangle by a large variety of independent measurements. The experimental determination of the angles α, β and γ of the Unitarity Triangle is closely related to the measurement of CP violation. The angle β is known at a precision better than 1° from time-dependent measurements of mixing-induced CP violation in $b \to c\bar{c}s$ transitions such as in $B^0 \to J/\psi K_S^0$ decays, see Section 2.6. The objective of the present analysis is the measurement of time-dependent CP violation in $b \to c\bar{c}d$ transitions, in particular in $B^0 \to D^+D^-$ and $B^0 \to D^{*\pm}D^{\mp}$ decays. The mixing-induced CP violation in $b \to c\bar{c}d$ transitions are closely related to the angle β and can be compared to the measurements in $b \to c\bar{c}s$ transitions.

The constraints on the Unitarity Triangle in the $\bar{\rho}\bar{\eta}$-plane at current experimental status are summarised in Figure 2.3. In total, the flavor part of the Standard Model as determined by constraints from the Unitarity Triangle performs well. Tight constraints come from the mentioned measurements of the angle β, from B^0-$\bar{B}^0$ and B_s^0-$\bar{B}_s^0$ oscillations measurements and from $|V_{ub}|$ measurements in semileptonic $b \to u$ transitions. In global fits, a few tensions persist which are related to measurements with large uncertainties and need to be confirmed.

The constraints on the Unitarity Triangle and on observables related to the CKM elements

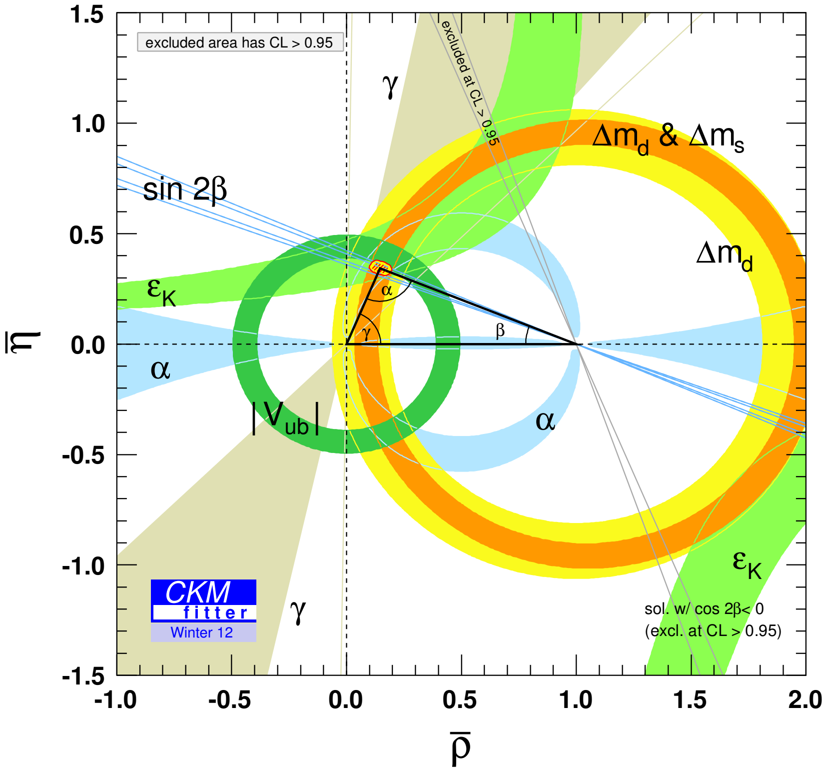

Figure 2.3: Constraints on the Unitarity Triangle in the $\bar{\rho}\bar{\eta}$-plane provided by the CKMfitter group [46].

from global fits of available measurements as obtained by the CKMfitter group and the UTfit Collaboration can be found in References [46, 47]. A general summary covering the experimental knowledge about the CKM matrix and the Unitarity Triangle can be found in Reference [45].

2.3 Time Evolution of Neutral Mesons

The time evolution of weakly decaying neutral mesons is characterised by the effect of particle-antiparticle oscillations. Particle-antiparticle oscillations emerge in different fields of high energy physics and have been experimentally established for neutrinos and neutral mesons. The theoretical explanations for the different kinds of oscillations have all in common that particles once produced with a definite flavor content, e.g. a B^0 or a ν_e, are not mass eigenstates of their particular system and evolve over time into mixtures of B^0 and $\bar{B}^0$ mesons or of ν_e, ν_μ and ν_τ neutrinos, respectively.

In the following, the theoretical formalism for the description of the time evolution and mixing of neutral mesons will be introduced with a focus on the B^0 system. The B^0 system is of special importance because the mixing introduces a phase that can give rise to large CP violating effects.

In the neutral meson sector, K^0-$\bar{K}^0$, D^0-$\bar{D}^0$, B^0-$\bar{B}^0$ and B_s^0-$\bar{B}_s^0$ oscillations are theoretically described as a 2-level quantum system coupled by higher order weak interactions.

A state that is initially a superposition of P^0 and $\bar{P}^0$ (with $P \in \{K, D, B, B_s\}$), e.g.

$$|\Psi(0)\rangle = a(0)\,|P^0\rangle + b(0)\,|\bar{P}^0\rangle, \tag{2.47}$$

evolves over time into a different mixture of P^0 and $\bar{P}^0$ and additionally contains contributions of all possible final decay states,

$$|\Psi(t)\rangle = a(t)\,|P^0\rangle + b(t)\,|\bar{P}^0\rangle + \sum_i c_i(t)\,|f_i\rangle. \tag{2.48}$$

The time scale of weak interactions that cause particle-antiparticle oscillations is much larger than that of strong or electromagnetic interactions. Following an approximation by Wigner and Weisskopf [48, 49], the time evolution is governed by a Schrödinger equation with an effective Hamiltonian that does not contain explicitly the couplings to the final states f_i:

$$i\frac{\partial}{\partial t}\begin{pmatrix} a(t) \\ b(t) \end{pmatrix} = \mathbf{H}\begin{pmatrix} a(t) \\ b(t) \end{pmatrix} \tag{2.49}$$

The effective Hamiltonian $\mathbf{H}$ is not Hermitian due to the possibility of decays of the particles. It is composed of a dispersive and an absorptive part:

$$\mathbf{H} = \mathbf{M} - \frac{i}{2}\mathbf{\Gamma} = \begin{pmatrix} M_{11} & M_{12} \\ M_{21} & M_{22} \end{pmatrix} - \frac{i}{2}\begin{pmatrix} \Gamma_{11} & \Gamma_{12} \\ \Gamma_{21} & \Gamma_{22} \end{pmatrix} \tag{2.50}$$

The diagonal elements of the mass matrix $\mathbf{M}$ and the decay matrix $\mathbf{\Gamma}$ correspond to flavor-conserving $P^0 \leftrightarrow P^0$ and $\bar{P}^0 \leftrightarrow \bar{P}^0$ transitions and the off-diagonal elements to flavor-changing $P^0 \rightarrow \bar{P}^0$ and $\bar{P}^0 \rightarrow P^0$ transitions. The matrices $\mathbf{M}$ and $\mathbf{\Gamma}$ are Hermitian inferring that $M_{12} = M_{21}^*$ and $\Gamma_{12} = \Gamma_{21}^*$. The invariance under CPT transformations requires $M_{11} = M_{22} =: M$ and $\Gamma_{11} = \Gamma_{22} =: \Gamma$.

The eigenstates of the Hamiltonian are

$$|P_{L,H}\rangle = p\,|P^0\rangle \mp q\,|\bar{P}^0\rangle, \tag{2.51}$$

where the complex coefficients p and q satisfy the normalisation condition $|p|^2 + |q|^2 = 1$ and are given by

$$\begin{aligned}\frac{q}{p} &= \pm\sqrt{\frac{M_{12}^* - \frac{i}{2}\Gamma_{12}^*}{M_{12} - \frac{i}{2}\Gamma_{12}}} \\ &\approx \pm\frac{M_{12}^*}{|M_{12}|}\left(1 - \frac{1}{2}\,\mathrm{Im}\,\frac{\Gamma_{12}}{M_{12}}\right). \end{aligned} \tag{2.52}$$

The corresponding eigenvalues are

$$\lambda_{L,H} = M - \frac{i}{2}\Gamma \pm \frac{q}{p}\left(M_{12} - \frac{i}{2}\Gamma_{12}\right). \tag{2.53}$$

$|P_{L,H}\rangle$ represent the physical light (L) and heavy (H) mass eigenstates with well-defined masses $M_{L,H}$ and decay widths $\Gamma_{L,H}$:

$$M_L = \mathrm{Re}(\lambda_L) \quad \text{and} \quad \Gamma_L = \mathrm{Im}(\lambda_L) \tag{2.54}$$

$$M_H = \mathrm{Re}(\lambda_H) \quad \text{and} \quad \Gamma_H = \mathrm{Im}(\lambda_H) \tag{2.55}$$

The time evolution of the mass eigenstates can be inferred from the Schrödinger equation:

$$|P_{L,H}(t)\rangle = e^{-i\mathbf{H}t}|P_{L,H}\rangle \tag{2.56}$$

$$= e^{-iM_{L,H}t}e^{-\frac{1}{2}\Gamma_{L,H}t}|P_{L,H}\rangle \tag{2.57}$$

The light and heavy eigenstate have a mass difference $\Delta M = M_H - M_L$ and a decay width difference $\Delta\Gamma = \Gamma_L - \Gamma_H$. Neglecting possible CP violation in mixing by assuming $|\frac{q}{p}| = 1$ the differences are given by $\Delta M = 2|M_{12}|$ and $\Delta\Gamma = 2|\Gamma_{12}|$.

The time evolution for flavor eigenstates can be expressed by the above relations. At time $t = 0$, pure neutral meson states $|P^0\rangle$ and $|\bar{P}^0\rangle$ (with $P \in \{K, D, B, B_s\}$) evolve as

$$|P^0(t)\rangle = \quad g_+(t)|P^0\rangle + \frac{q}{p}g_-(t)|\bar{P}^0\rangle \tag{2.58}$$

$$|\bar{P}^0(t)\rangle = \quad g_+(t)|\bar{P}^0\rangle + \frac{p}{q}g_-(t)|P^0\rangle, \tag{2.59}$$

where

$$g_+(t) = e^{-iMt}e^{-\Gamma t/2}\left[\ \cosh\left(\frac{\Delta\Gamma t}{4}\right)\cos\left(\frac{\Delta M t}{2}\right) - i\sinh\left(\frac{\Delta\Gamma t}{4}\right)\sin\left(\frac{\Delta M t}{2}\right)\right] \tag{2.60}$$

$$g_-(t) = e^{-iMt}e^{-\Gamma t/2}\left[-\sinh\left(\frac{\Delta\Gamma t}{4}\right)\cos\left(\frac{\Delta M t}{2}\right) + i\cosh\left(\frac{\Delta\Gamma t}{4}\right)\sin\left(\frac{\Delta M t}{2}\right)\right]. \tag{2.61}$$

The functions $g_+(t)$ and $g_-(t)$ have the following properties:

$$\left|g_\pm(t)\right|^2 = \frac{e^{-\Gamma t}}{2}\left[\ \cosh\left(\frac{\Delta\Gamma t}{2}\right) \pm \cos(\Delta M t)\right] \tag{2.62}$$

$$g_+^*(t)\,g_-(t) = \frac{e^{-\Gamma t}}{2}\left[-\sinh\left(\frac{\Delta\Gamma t}{2}\right) + i\sin(\Delta M t)\right] \tag{2.63}$$

From the above time evolution, the time-dependent decay rates of neutral mesons produced at $t = 0$ in a flavor eigenstate P^0 or $\bar{P}^0$ and decaying to the final state f can be determined. The time-dependent decay rates are proportional to the absolute square of the involved decay amplitudes:

$$\Gamma[P^0(t) \to f] \propto \left|\langle f | P^0(t) \rangle\right|^2 \tag{2.64}$$

$$\Gamma[\bar{P}^0(t) \to f] \propto \left|\langle f | \bar{P}^0(t) \rangle\right|^2 \tag{2.65}$$

The decay rates describing decays to the CP conjugated state $|\bar{f}\rangle = CP|f\rangle$ are:

$$\Gamma[P^0(t) \to \bar{f}] \propto \left|\langle \bar{f} | P^0(t) \rangle\right|^2 \tag{2.66}$$

$$\Gamma[\bar{P}^0(t) \to \bar{f}] \propto \left|\langle \bar{f} | \bar{P}^0(t) \rangle\right|^2 \tag{2.67}$$

For the following discussion, it is advantageous to define the decay amplitudes as

$$A_f := \langle f|\mathcal{H}|P^0\rangle, \qquad A_{\bar{f}} := \langle \bar{f}|\mathcal{H}|P^0\rangle, \qquad \bar{A}_f := \langle f|\mathcal{H}|\bar{P}^0\rangle \quad \text{and} \quad \bar{A}_{\bar{f}} := \langle \bar{f}|\mathcal{H}|\bar{P}^0\rangle, \tag{2.68}$$

and to introduce the following ratios defined by

$$\lambda_f := \frac{q}{p}\frac{\bar{A}_f}{A_f} \qquad \text{and} \qquad \lambda_{\bar{f}} := \frac{q}{p}\frac{\bar{A}_{\bar{f}}}{A_{\bar{f}}}. \tag{2.69}$$

By inserting the time evolution of the flavor eigenstates given by Equations 2.58 and 2.59 into Equations 2.64 to 2.67 and making use of the functions $g_+(t)$ and $g_-(t)$ defined in Equations 2.60 and 2.61, the time-dependent decay rates are proportional to the following expressions [50]:

$$\begin{aligned}\Gamma[P^0(t) \to f] \propto |A_f|^2 e^{-\Gamma t}\Bigg\{&\frac{1+|\lambda_f|^2}{2}\cosh\left(\frac{\Delta\Gamma}{2}t\right) + \frac{1-|\lambda_f|^2}{2}\cos(\Delta M t)\\ &-\mathrm{Re}(\lambda_f)\sinh\left(\frac{\Delta\Gamma}{2}t\right) - \mathrm{Im}(\lambda_f)\sin(\Delta M t)\Bigg\}\end{aligned} \tag{2.70}$$

$$\begin{aligned}\Gamma[\bar{P}^0(t) \to f] \propto |A_f|^2 \left|\frac{p}{q}\right|^2 e^{-\Gamma t}\Bigg\{&\frac{1+|\lambda_f|^2}{2}\cosh\left(\frac{\Delta\Gamma}{2}t\right) - \frac{1-|\lambda_f|^2}{2}\cos(\Delta M t)\\ &-\mathrm{Re}(\lambda_f)\sinh\left(\frac{\Delta\Gamma}{2}t\right) + \mathrm{Im}(\lambda_f)\sin(\Delta M t)\Bigg\}\end{aligned} \tag{2.71}$$

$$\begin{aligned}\Gamma[P^0(t) \to \bar{f}] \propto \left|\bar{A}_{\bar{f}}\right|^2 \left|\frac{q}{p}\right|^2 e^{-\Gamma t}\Bigg\{&\frac{1+\left|\lambda_{\bar{f}}\right|^{-2}}{2}\cosh\left(\frac{\Delta\Gamma}{2}t\right) - \frac{1-\left|\lambda_{\bar{f}}\right|^{-2}}{2}\cos(\Delta M t)\\ &-\mathrm{Re}\left(\frac{1}{\lambda_{\bar{f}}}\right)\sinh\left(\frac{\Delta\Gamma}{2}t\right) + \mathrm{Im}\left(\frac{1}{\lambda_{\bar{f}}}\right)\sin(\Delta M t)\Bigg\}\end{aligned} \tag{2.72}$$

$$\begin{aligned}\Gamma[\bar{P}^0(t) \to \bar{f}] \propto \left|\bar{A}_{\bar{f}}\right|^2 e^{-\Gamma t}\Bigg\{&\frac{1+\left|\lambda_{\bar{f}}\right|^{-2}}{2}\cosh\left(\frac{\Delta\Gamma}{2}t\right) + \frac{1-\left|\lambda_{\bar{f}}\right|^{-2}}{2}\cos(\Delta M t)\\ &-\mathrm{Re}\left(\frac{1}{\lambda_{\bar{f}}}\right)\sinh\left(\frac{\Delta\Gamma}{2}t\right) - \mathrm{Im}\left(\frac{1}{\lambda_{\bar{f}}}\right)\sin(\Delta M t)\Bigg\}\end{aligned} \tag{2.73}$$

The decay rates in Equation 2.70 to 2.73 allow to calculate the time evolution of any neutral weak decay process and are important not only for the mixing, but allow for interference effects that can give rise to CP violation as shown in Section 2.4. In the derivation of the decay rates no assumptions except the validity of the CPT theorem have been applied. Therefore the decay rates are applicable to any weakly decaying neutral meson P^0 or $\bar{P}^0$ (with $P \in \{K, D, B, B_s\}$).

For the oscillations of neutral mesons, the probabilities to observe an initially pure neutral meson P^0 at time $t > 0$ without mixing as a P^0 or with mixing as a $\bar{P}^0$ are given by

$$\begin{aligned} P_{\text{unmixed}}(t) = \left|\langle P^0 | P^0(t)\rangle\right|^2 &= \frac{1}{2} e^{-\Gamma t}\left[\cosh\left(\frac{\Delta\Gamma}{2} t\right) + \cos(\Delta M t)\right] \\ &= \frac{1}{2} e^{-\Gamma t}\left[\cosh(y\Gamma t) + \cos(x\Gamma t)\right] \end{aligned} \tag{2.74}$$

$$\begin{aligned} P_{\text{mixed}}(t) = \left|\langle P^0 | \bar{P}^0(t)\rangle\right|^2 &= \frac{1}{2}\left|\frac{q}{p}\right|^2 e^{-\Gamma t}\left[\cosh\left(\frac{\Delta\Gamma}{2} t\right) - \cos(\Delta M t)\right] \\ &= \frac{1}{2}\left|\frac{q}{p}\right|^2 e^{-\Gamma t}\left[\cosh(y\Gamma t) - \cos(x\Gamma t)\right], \end{aligned} \tag{2.75}$$

where $x := \frac{\Delta M}{\Gamma}$ and $y := \frac{\Delta\Gamma}{2\Gamma}$ are dimensionless parameters characterising the mixing of neutral mesons. In the case of a mass difference $\Delta M \neq 0$, the mixing is a consequence of $P^0 \leftrightarrow \bar{P}^0$ transitions. The case of a decay width difference $\Delta\Gamma \neq 0$ is equivalent to a difference in the lifetimes of the mass eigenstates and the mixing is a consequence of the disappearance of the shorter-lived eigenstate over time. Since the longer-lived eigenstate is a linear combination of P^0 and $\bar{P}^0$ states, an initially pure P^0 sample acquires a $\bar{P}^0$ component over time.

	K^0	D^0	B^0	B^0_s
Mean mass M (MeV/c^2)	497	1865	5279	5366
Mass difference ΔM ($\frac{\hbar}{\mathrm{ps}}$)	$(5.27 \pm 0.03) \times 10^{-3}$	$\left(25^{+5.9}_{-6.3}\right) \times 10^{-3}$	0.504 ± 0.004	17.77 ± 0.12
Lifetime τ_H (ps)	51160 ± 210	0.410 ± 0.002	1.519 ± 0.001	1.543 ± 0.060
τ_L (ps)	89.58 ± 0.05	0.410 ± 0.002	1.519 ± 0.001	1.408 ± 0.033
$x = \frac{\Delta M}{\Gamma}$	0.946	0.01	0.776	26.1
$y = \frac{\Delta\Gamma}{2\Gamma}$	0.997	0.01	< 0.01	0.05

Table 2.1: Summary of parameters characterising the mixing of K^0, D^0, B^0 and B^0_s mesons at current experimental status [51, 52, 53].

K^0-$\bar{K}^0$, D^0-$\bar{D}^0$, B^0-$\bar{B}^0$ and B^0_s-$\bar{B}^0_s$ oscillations have all been observed experimentally [51, 52, 53]. The current experimental status of the mixing parameters is summarised in Table 2.1 and the corresponding time-dependent mixing probabilities are shown in Figure 2.4.

The K^0-$\bar{K}^0$ system is characterised by a large difference in lifetimes. The decay of the almost CP-odd K^0_L to the CP-even $\pi\pi$ final state is suppressed by $\mathcal{O}\left(10^{-3}\right)$. Additionally, since $M_{\pi\pi\pi} \approx M_{K^0}$, the decay to $\pi\pi\pi$ is kinematically suppressed and as a consequence K^0_L mesons have a much larger lifetime than K^0_S mesons.

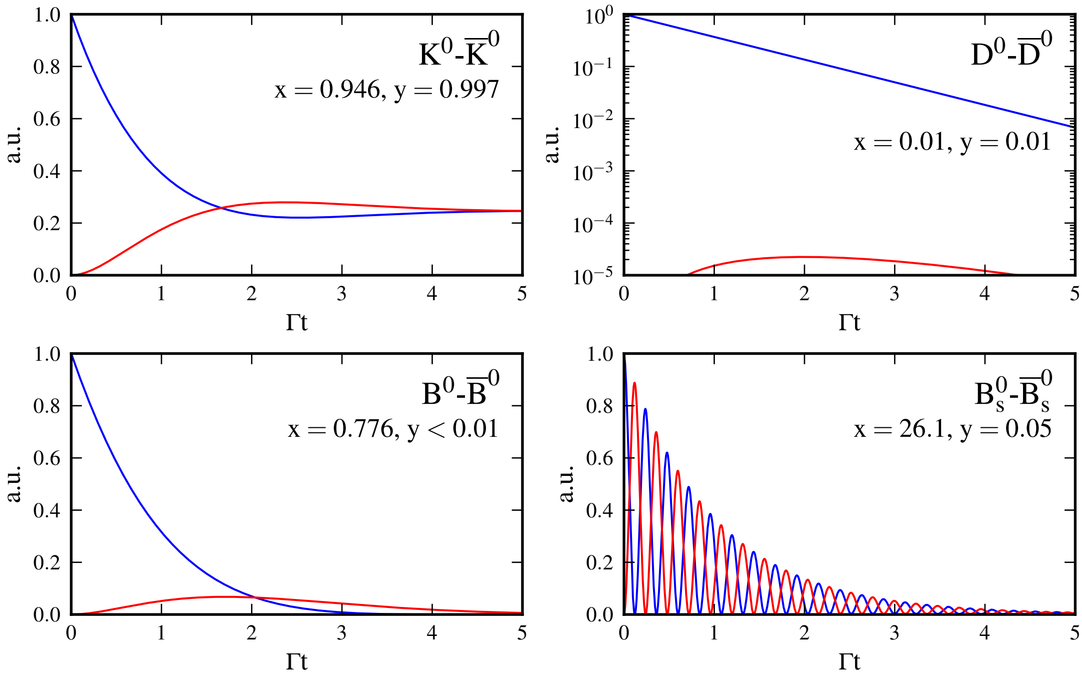

Figure 2.4: Distributions for the unmixed (blue) and mixed (red) probabilities in dependence on the proper decay time for initially pure meson samples in the K^0, D^0, B^0 and B_s^0 system. Please note the logarithmic scale for D^0 mesons.

Mixing in the D^0-$\bar{D}^0$ system is currently subject of intense experimental and theoretical research. The mixing can proceed via second order box diagrams of weak interactions or via intermediate states accessible to both D^0 and $\bar{D}^0$ mesons that can have effects on large distances. In the box diagrams, down-type quarks are exchanged and the b-quark contributions, which are due to their large invariant mass typically expected to lead to enhancements, are suppressed by very small CKM elements. The system is described in good approximation by only two generations and therefore GIM-cancellations contribute to further suppressions. As a consequence D^0-$\bar{D}^0$ mixing is a very small effect.

B^0-$\bar{B}^0$ and B_s^0-$\bar{B}_s^0$ oscillations are caused by second order box diagrams mediated by the exchange of two W bosons and two up-type quarks as shown in Figure 2.5.

The off-diagonal elements M_{12}^q ($q \in \{d, s\}$) calculated from the box diagrams are given by [54, 55]

$$M_{12}^q = -\frac{G_F^2 M_W^2 \eta_B M_{B_q} B_{B_q} f_{B_q}^2}{12\pi^2} S_0(M_t^2/M_W^2) \left(V_{tq}^* V_{tb}\right)^2 e^{i\left(\pi - \phi_{B_q}^{CP}\right)}, \tag{2.76}$$

where G_F is the Fermi constant, M_i the masses of the B_q mesons and the W bosons, η a perturbative QCD correction, B_{B_q} a non-perturbative parameter related to the involved hadronic matrix element $\langle \bar{B}_q^0 | (\bar{b}q)_{V-A} (b\bar{q})_{V-A} | B_q^0 \rangle$, f_{B_q} the B_q decay constant, $S_0(M_t^2/M_W^2)$ an Inami-Lin function describing the dependence on the top-quark mass, and $\phi_{B_q}^{CP}$ a convention dependent

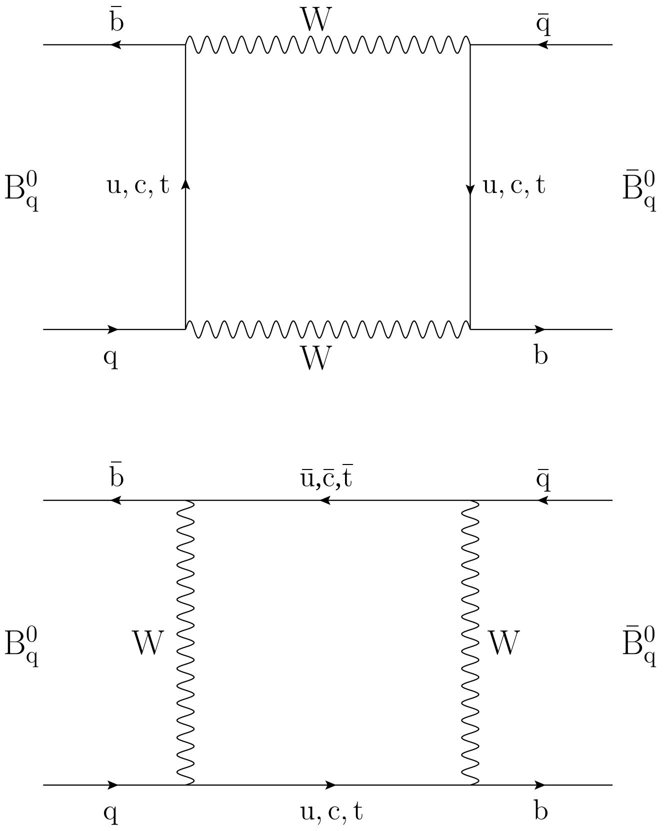

Figure 2.5: Second order electroweak box diagrams contributing to B_q^0-$\bar{B}_q^0$ oscillations ($q \in \{d, s\}$).

phase related to CP transformations on the B flavor eigenstates.

The off-diagonal elements M_{12} are dominated by the contributions of the internal top-quarks. Due to the quadratic dependence on the involved CKM element V_{tq}, the oscillation frequency ΔM is about 35-times higher in the B_s^0-$\bar{B}_s^0$ system with CKM element V_{ts} than in the B^0-$\bar{B}^0$ system with CKM element V_{td}.

M_{12} is related to Γ_{12} by

$$\frac{\Gamma_{12}}{M_{12}} \approx -\frac{3\pi}{2\,S_0(M_t^2/M_W^2)}\left(\frac{M_b^2}{M_W^2}\right) = \mathcal{O}(M_b^2/M_t^2) \ll 1 \tag{2.77}$$

The absorptive parts of the Hamiltonian Γ_{12} can give rise to differences in the decay width. The relative decay width differences $\frac{\Delta\Gamma}{\Gamma}$ of the mass eigenstates are given by

$$\frac{\Delta\Gamma}{\Gamma} \approx 16\pi^2 \frac{f_{B_q}^2}{M_{B_q}^2} |V_{cq}|^2. \tag{2.78}$$

In the B^0 system, the decay width difference is very small, $\frac{\Delta\Gamma}{\Gamma} \lesssim \mathcal{O}\left(10^{-2}\right)$, and cannot be resolved at present experiments. In the B_s^0 system, the decay width difference is, with $\frac{\Delta\Gamma}{\Gamma} \approx \mathcal{O}\left(10^{-1}\right)$, sizeable and results in significant different lifetimes of the mass eigenstates, which has been observed experimentally.

Comparing Equations 2.52 and 2.76, one finds that the phase of $\frac{q}{p}$ is given by the phase of

$$M_{12}^{q} = \left|M_{12}^{q}\right| e^{i\phi_{M}^{q}} \quad \text{with } \phi_{M}^{q} = \pi + 2\arg(V_{tq}^{*}V_{tb}) - \phi_{B_q}^{CP} = 2\beta_{(s)}\,, \tag{2.79}$$

where the convention dependent phase is set to $\phi_{B_q}^{CP} = \pi$. The phases of $\frac{q}{p}$ are directly related to the angle β_s for B_s^0 mesons and to the angle β in the unitarity triangle for B^0 mesons. The latter is, being approximately 21°, relatively large.

2.4 CP Violation in Meson Decays

As described in Sections 2.1 and 2.2, the effect of CP violation in the Standard Model of electroweak interactions is caused by a single irreducible complex phase in the CKM matrix. In weak decays of charged and neutral mesons, CP violation can manifest itself in three different categories: in the decay, in the mixing, and in the interference between mixing and decay. The three categories of CP violation are illustrated in Figure 2.6 and described in the following.

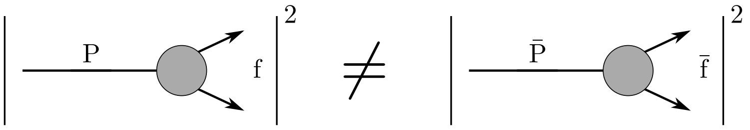

(a) CP violation in the decay ("direct CP violation")

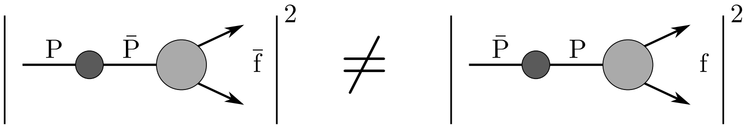

(b) CP violation in the mixing

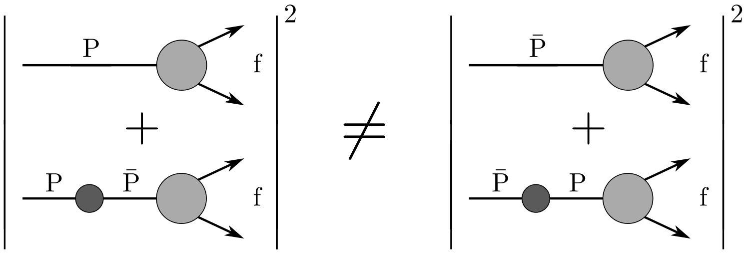

(c) CP violation in the interference between mixing and decay ("mixing-induced CP violation")

Figure 2.6: Three categories of CP violation in meson decays. The illustration has been adapted from Reference [39].

2.4.1 CP Violation in the Decay

If the magnitudes of the amplitudes of CP conjugated processes are different, equivalent to

$$\left|\bar{A}_{\bar{f}}/A_{f}\right| \neq 1, \tag{2.80}$$

then CP violation can occur in the decay. This category of CP violation is referred to as direct CP violation and is the only source of CP violation in decays of charged mesons. This category is illustrated in Figure 2.6(a).

The necessary conditions for direct CP violation are at least two contributing decay amplitudes with non-vanishing relative weak and strong phases. The weak phases originate from complex CKM elements and enter with opposite sign in A_f and $\bar{A}_{\bar{f}}$. The strong phases originate from hadronic effects, e.g. from rescattering of intermediate on-shell states. The strong phases need to be different for the amplitudes contributing to the decay. Since the strong interaction is invariant under CP transformations, the strong phases are the same for A_f and $\bar{A}_{\bar{f}}$.

The total amplitude of a decay and of its CP conjugated decay can be written as

$$A_f = \sum_j |a_j| e^{i\left(\delta_j + \phi_j\right)} \tag{2.81}$$

$$\text{and} \quad \bar{A}_{\bar{f}} = \sum_j |a_j| e^{i\left(\delta_j - \phi_j\right)}, \tag{2.82}$$

where a_j denotes single contributing amplitudes, and δ_j and ϕ_j are the associated strong and weak phases. The necessary condition for direct CP violation becomes apparent in the difference of the squared amplitudes,

$$|A_f|^2 - |\bar{A}_{\bar{f}}|^2 = 2 \sum_{i,j} |a_i||a_j| \sin(\delta_i - \delta_j) \sin(\phi_i - \phi_j). \tag{2.83}$$

Due to the interference, a non-vanishing value in the difference only exists, if the contributing amplitudes provide both: a non-trivial strong phase difference $\delta_i - \delta_j$ and a non-trivial weak phase difference $\phi_i - \phi_j$.

For direct CP violation, an asymmetry can be defined by

$$A_{CP} = \frac{\Gamma(P \to f) - \Gamma(\bar{P} \to \bar{f})}{\Gamma(P \to f) + \Gamma(\bar{P} \to \bar{f})} = \frac{1 - |\bar{A}_{\bar{f}}/A_f|^2}{1 + |\bar{A}_{\bar{f}}/A_f|^2} \propto \sin(\delta_i - \delta_j) \sin(\phi_i - \phi_j). \tag{2.84}$$

2.4.2 CP Violation in the Mixing

If the complex coefficients q and p differ by more than a phase, equivalent to

$$|q/p| \neq 1, \tag{2.85}$$

then CP violation occurs in the mixing. This category of CP violation is illustrated in Figure 2.6(b).

Consider flavor-specific decays satisfying

$$P^0 \to f \not\leftarrow \bar{P}^0 \quad \text{and} \quad P^0 \not\to \bar{f} \leftarrow \bar{P}^0, \tag{2.86}$$

equivalent to $|A_{\bar{f}}| = |\bar{A}_f| = 0$, and assume no direct CP violation by requiring $|A_f| = |\bar{A}_{\bar{f}}|$, then the forbidden $P^0 \to \bar{f}$ and $\bar{P}^0 \to f$ decays are only possible due to P^0-$\bar{P}^0$ oscillations. The asymmetry of the forbidden decays calculated from the time-dependent decay rates in Equations 2.71 and 2.72 can be expressed as

$$A_{fs} = \frac{\Gamma(\bar{P}^0(t) \to f) - \Gamma(P^0(t) \to \bar{f}))}{\Gamma(\bar{P}^0(t) \to f) + \Gamma(P^0(t) \to \bar{f}))} = \frac{1 - |q/p|^4}{1 + |q/p|^4}, \tag{2.87}$$

and is independent of time. A deviation of the asymmetry from zero and consequently a CP violation in the mixing corresponds to unequal mixing probabilities

$$|\langle \bar{P}^0|P(t)\rangle|^2 \neq |\langle P^0|\bar{P}(t)\rangle|^2. \tag{2.88}$$

2.4.3 CP Violation in the Interference between Mixing and Decay

In decays to final states f that are common to P^0 and $\bar{P}^0$, an interference between the decay without mixing, $P^0 \to f$, and the decay with mixing, $P^0 \to \bar{P}^0 \to f$, arises.

CP violation in the interference between mixing and decay occurs, if

$$\mathrm{Im}(\lambda_f) \neq 0, \qquad \text{with } \lambda_f = \frac{q}{p}\frac{\bar{A}_f}{A_f}. \tag{2.89}$$

This category of CP violation is referred to as mixing-induced CP violation and is illustrated in Figure 2.6(c). Mixing-induced CP violation can be observed by the time-dependent asymmetry $A_{CP}(t)$ of neutral mesons decaying into CP eigenstates f_{CP}, defined by

$$A_{CP}(t) = \frac{\Gamma(\bar{P}^0(t) \to f_{CP})) - \Gamma(P^0(t) \to f_{CP})}{\Gamma(\bar{P}^0(t) \to f_{CP})) + \Gamma(P^0(t) \to f_{CP})}. \tag{2.90}$$

The asymmetry calculated from the time-dependent decay rates in Equations 2.70 and 2.71 can be expressed as

$$A_{CP}(t) = \frac{\mathcal{S}_{CP}^{mix}\sin(\Delta Mt) - \mathcal{C}_{CP}^{dir}\cos(\Delta Mt)}{\cosh(\Delta\Gamma t/2) - \mathcal{A}_{\Delta\Gamma}\sinh(\Delta\Gamma t/2)}, \tag{2.91}$$

where

$$\mathcal{S}_{CP}^{mix} := \frac{2\,\mathrm{Im}(\lambda_{f_{CP}})}{1+|\lambda_{f_{CP}}|^2}, \qquad \mathcal{C}_{CP}^{dir} := \frac{1-|\lambda_{f_{CP}}|^2}{1+|\lambda_{f_{CP}}|^2}, \qquad \mathcal{A}_{\Delta\Gamma} := \frac{2\,\mathrm{Re}(\lambda_{f_{CP}})}{1+|\lambda_{f_{CP}}|^2}, \tag{2.92}$$

$$\text{and} \quad |\mathcal{S}_{CP}^{mix}|^2 + |\mathcal{C}_{CP}^{dir}|^2 + |\mathcal{A}_{\Delta\Gamma}|^2 = 1. \tag{2.93}$$

The parameters $\mathcal{S}_{CP}^{mix}$ and $\mathcal{C}_{CP}^{dir}$ measure mixing-induced and direct CP violation, respectively. The parameter $\mathcal{A}_{\Delta\Gamma}$ provides another observable in neutral meson systems with sizeable decay width difference $\Delta\Gamma$.

In the B^0 system, the decay width difference $\Delta\Gamma$ is negligible and the time-dependent CP asymmetry $A_{CP}(t)$ in Equation 2.91 can be rewritten as

$$A_{CP}(t) = \mathcal{S}_{CP}^{mix}\sin(\Delta Mt) - \mathcal{C}_{CP}^{dir}\cos(\Delta Mt). \tag{2.94}$$

The parameters $\mathcal{S}_{CP}^{mix}$ and $\mathcal{C}_{CP}^{dir}$ are experimentally accessible from the amplitudes of the sine and cosine oscillations in the proper decay times of flavor-tagged decays, see Section 2.5. If the amplitudes contributing to a decay all carry the same weak phase, then $|\mathcal{A}_{f_{CP}}| = |\bar{\mathcal{A}}_{f_{CP}}|$ and $|\lambda_{f_{CP}}| = 1$. As a consequence, no direct CP violation occurs and the mixing-induced CP violation,

$$\mathcal{S}_{CP}^{mix} = \mathrm{Im}(\lambda_f), \tag{2.95}$$

is directly related to the phases of the CKM elements involved in the mixing. These decays are referred to as golden modes. Because of its importance, the CP violation in $b \to c\bar{c}s$ transitions in the golden mode of $B^0 \to J/\psi K^0_S$ decays is discussed in Section 2.6.

The objective of the present analysis is the measurement of time-dependent CP violation in $B^0 \to D^+D^-$ and $B^0 \to D^{*\pm}D^{\mp}$ decays. These decays are mediated by $b \to c\bar{c}d$ transitions. As it will be discussed in Section 2.7, $b \to d$ penguin amplitudes that may have different weak phases can contribute to the decays and possibly result in $|\lambda_{f_{CP}}| \neq 1$. Consequently, in addition to mixing-induced CP violation that is expected to be similar to that in $b \to c\bar{c}s$ transitions, the penguin amplitudes might give rise to direct CP violation.

2.5 Coherent $B^0\bar{B}^0$ Mixing

At the Belle experiment, B mesons are produced by the asymmetric-energy KEKB e^+e^--collider via the decay of the $\Upsilon(4S)$-resonance. Neutral $B\bar{B}$ mesons originating from $\Upsilon(4S)$ decays are produced in an entangled state and evolve coherently. The decay of one of the B mesons as a B^0 or $\bar{B}^0$ determines the flavor of the second B meson to be opposite at the particular instant of time. This is a manifestation of the Einstein-Podolsky-Rosen (EPR) effect [56] and is important for the time-dependent CP violation measurements at the Belle experiment.

Starting from the two-body wave function describing the entangled $B^0\bar{B}^0$ state and applying the theory of the time evolution of neutral mesons from Section 2.3, the rate of the joint decay of both B mesons, the resulting CP asymmetries and the probability distributions needed for the time-dependent CP violation measurements in the present analysis are derived.

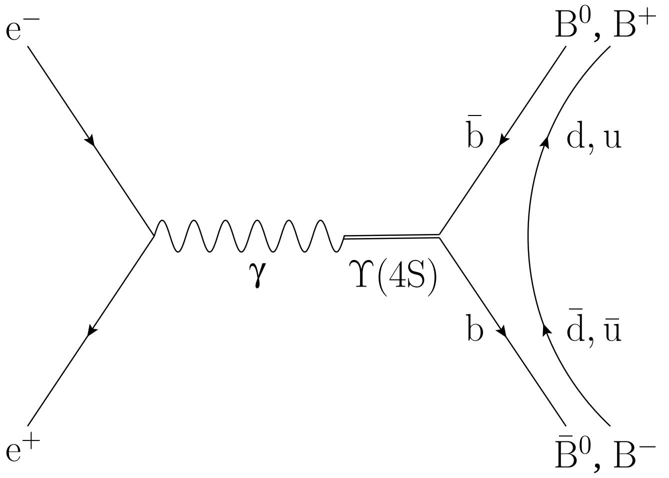

Figure 2.7: Illustration of the production mechanism of $B\bar{B}$ pairs via the decay of the $\Upsilon(4S)$-resonance at e^+e^--colliders.

The production mechanism of $B\bar{B}$ pairs over the $\Upsilon(4S)$ is shown in Figure 2.7. The $\Upsilon(4S)$ has the quantum numbers $J^{PC} = 1^{--}$. The decay of the $\Upsilon(4S)$ into $B\bar{B}$ pairs is a strong interaction process that conserves the quantum numbers. The B mesons are pseudoscalars and the $B^0\bar{B}^0$ state is produced with orbital angular momentum $L = 1$ in a P-wave configuration. The parity of the system is $P = (-1)^L = -1$ and requires the spatial part of the wave function of the $B^0\bar{B}^0$ state to be antisymmetric. The Bose-Einstein statistics requires the overall wave function to be symmetric. Consequently, the flavor part of the wave function, denoted in the following by Ψ, needs also to be antisymmetric and can be written as

$$|\Psi(t_1,t_2)\rangle = \frac{1}{\sqrt{2}}\Big(|B^0(t_1)\rangle|\bar{B}^0(t_2)\rangle - |\bar{B}^0(t_1)\rangle|B^0(t_2)\rangle\Big). \tag{2.96}$$

Considering one of the B mesons decays at time t_1 to the final state f_a and assume the second B meson decays at time t_2 to the final state f_b, then the joint amplitude can be expressed as

$$\langle f_a f_b|\Psi(t_1,t_2)\rangle = \frac{1}{\sqrt{2}}\Big(\langle f_a|B^0(t_1)\rangle\langle f_b|\bar{B}^0(t_2)\rangle - \langle f_a|\bar{B}^0(t_1)\rangle\langle f_b|B^0(t_2)\rangle\Big). \tag{2.97}$$

By defining the amplitudes

$$A_i := \langle f_i | B^0 \rangle \quad \text{and} \quad \bar{A}_i := \langle f_i | \bar{B}^0 \rangle, \tag{2.98}$$

and introducing the time evolution of the flavor eigenstates from Equations 2.58 and 2.59, the joint amplitude can be written as

$$\begin{aligned} \langle f_a f_b | \Psi(t_1,t_2) \rangle = \frac{1}{\sqrt{2}} \Big\{ & \big[g_+(t_1) g_+(t_2) - g_-(t_1) g_-(t_2) \big] \big(A_a \bar{A}_b - \bar{A}_a A_b \big) \\ & + \big[g_+(t_1) g_-(t_2) - g_-(t_1) g_+(t_2) \big] \Big(\frac{p}{q} A_a A_b - \frac{q}{p} \bar{A}_a \bar{A}_b \Big) \Big\}. \end{aligned} \tag{2.99}$$

The time-dependent decay rate is obtained from the absolute square of the joint amplitude. By substituting the functions $g_+(t)$ and $g_-(t)$ defined in Equations 2.60 and 2.61, the decay rate is given by [57]

$$\begin{aligned} \Gamma[\Psi(t_1,t_2) \to f_a f_b] &= \Big| \langle f_a f_b | \Psi(t_1,t_2) \rangle \Big|^2 \\ &= \frac{1}{2} e^{-\Gamma(t_1+t_2)} \Big\{ \big(|A_a|^2 + |\bar{A}_a|^2 \big) \big(|A_b|^2 + |\bar{A}_b|^2 \big) - 4 \,\mathrm{Re}\Big(\frac{q}{p} A_a^* \bar{A}_a \Big) \mathrm{Re}\Big(\frac{q}{p} A_b^* \bar{A}_b \Big) \\ &\quad - 2 \sin[\Delta M (t_1 - t_2)] \Big[\mathrm{Im}\Big(\frac{q}{p} A_a^* \bar{A}_a \Big) \big(|A_b|^2 - |\bar{A}_b|^2 \big) - \big(|A_a|^2 - |\bar{A}_a|^2 \big) \mathrm{Im}\Big(\frac{q}{p} A_b^* \bar{A}_b \Big) \Big] \\ &\quad - \cos[\Delta M (t_1 - t_2)] \Big[\big(|A_a|^2 - |\bar{A}_a|^2 \big) \big(|A_b|^2 - |\bar{A}_b|^2 \big) + 4 \,\mathrm{Im}\Big(\frac{q}{p} A_a^* \bar{A}_a \Big) \mathrm{Im}\Big(\frac{q}{p} A_b^* \bar{A}_b \Big) \Big] \Big\}. \end{aligned} \tag{2.100}$$

Equation 2.100 describes the time-dependent decay rate of an entangled $B^0\bar{B}^0$ pair produced by the $\Upsilon(4S)$ resonance and decaying to the final states f_a and f_b. Assuming CPT invariance and $|q/p| = 1$, the decay rate can be used to calculate the time-dependence of any neutral weak decay process.

The dynamics in the time evolution depends on the proper decay time difference of both B mesons, $t_1 - t_2$, and not on their sum, $t_1 + t_2$. This dependence is already implicitely included in the decay rates in the classic paper by I.I. Bigi and A.I. Sanda [15], predicting CP violation in the B meson system in 1987 (see the emphasised minus signs in Equation 2.6 in Figure 1.1(b)) and is the reason for the asymmetry in the energy of the beams at the KEKB e^+e^--collider. The asymmetry causes a Lorentz boost of the $\Upsilon(4S)$, and thereby increases the spatial separation of the B meson decay vertices. The translation of measurements of the decay flight length differences with the known Lorentz boost into proper decay time differences allows to observe time-dependent CP violation in the B meson system. The principle of the time-dependent CP violation measurements is illustrated in Figure 2.8.

Consider one of the neutral B mesons decays at time t_{CP} to a CP eigenstate f_{CP}, for example $B^0 \to D^+D^-$. Assuming the second B meson decays at time t_{tag} flavor-specific as a B^0 to f_{tag}, corresponding to $A_{tag} := A_b = \langle f_{tag} | B^0 \rangle$ and $\bar{A}_b = 0$. By introducing $\lambda_{f_{CP}}$ defined in Equati-

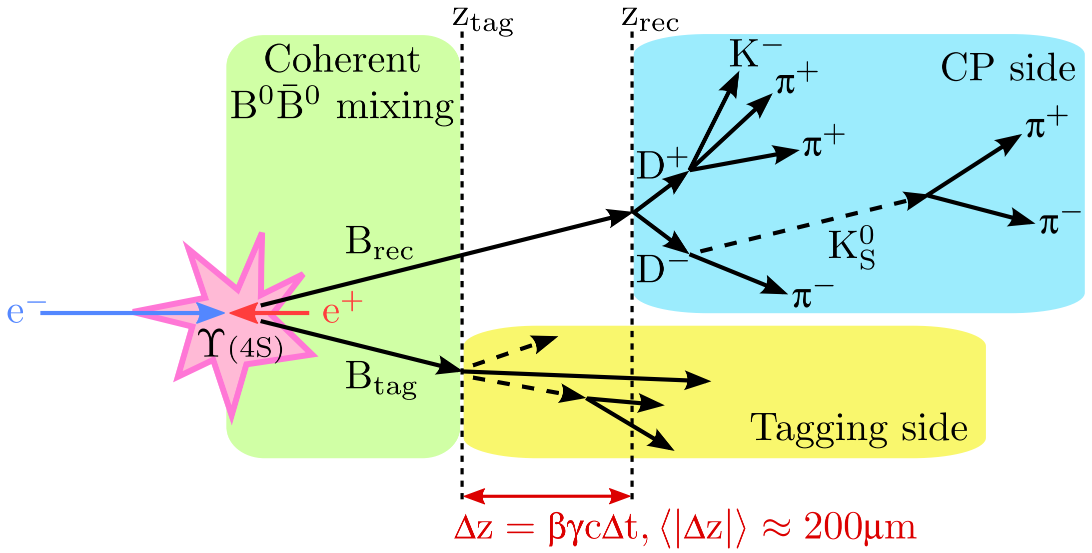

Figure 2.8: Principle of time-dependent CP violation measurements at the Belle experiment: Due to the asymmetric-energy of the e^+e^--collider, the $B^0\bar{B}^0$ pairs from $\Upsilon(4S)$ decays are produced with a Lorentz boost along the e^--beam. The neutral B mesons evolve coherently, until one B meson decays and determines by an EPR-like correlation the flavor of the second B meson to be opposite. The second B meson then oscillates independently and decays. For the time-dependent CP violation measurements, one B meson is reconstructed in a CP eigenstate, e.g. in $B^0 \rightarrow D^+D^-$, and the flavor of the other B meson is determined from its decay products. The measurements of the displaced decay vertices of the B mesons allow to translate the flight length difference Δz into a proper decay time difference Δt. The combination of the flavor information of the second B meson with the Δt measurement enables to measure the time-dependent CP violating asymmetry in Equation 2.103.

on 2.69, the time-dependent decay rate can be written as

$$\begin{aligned}\Gamma[\Psi\left(t_{CP},t_{tag}\right)\rightarrow f_{CP}f_{tag}] &= \left|\langle f_{CP}f_{tag}|\Psi\left(t_{CP},t_{tag}\right)\rangle\right|^2 \\ &= \frac{1}{2}e^{-\Gamma(t_{CP}+t_{tag})}|A_{CP}|^2\left|A_{tag}\right|^2\Big[(1+\left|\lambda_{f_{CP}}\right|^2) \\ &\quad -2\,\mathrm{Im}(\lambda_{f_{CP}})\sin[(\Delta M(t_{CP}-t_{tag})]-(1-\left|\lambda_{f_{CP}}\right|^2)\cos[(\Delta M(t_{CP}-t_{tag})]\Big].\end{aligned} \quad (2.101)$$

In the opposite case, if the second B meson decays at time t_{tag} flavor-specific as a $\bar{B}^0$ to $\bar{f}_{tag}$, corresponding to $A_{tag} := \bar{A}_b = \langle\bar{f}_{tag}|\bar{B}^0\rangle$ and $A_b = 0$, then the time-dependent decay rate can be written as

$$\begin{aligned}\Gamma[\Psi\left(t_{CP},t_{tag}\right)\rightarrow f_{CP}\bar{f}_{tag}] &= \left|\langle f_{CP}\bar{f}_{tag}|\Psi\left(t_{CP},t_{tag}\right)\rangle\right|^2 \\ &= \frac{1}{2}e^{-\Gamma(t_{CP}+t_{tag})}|A_{CP}|^2\left|A_{tag}\right|^2\Big[(1+\left|\lambda_{f_{CP}}\right|^2) \\ &\quad +2\,\mathrm{Im}(\lambda_{f_{CP}})\sin[(\Delta M(t_{CP}-t_{tag})]+(1-\left|\lambda_{f_{CP}}\right|^2)\cos[(\Delta M(t_{CP}-t_{tag})]\Big].\end{aligned} \quad (2.102)$$

Again, in the decay rates the time-dependence of the dynamics originates from the proper decay time differences, denoted in the following by $\Delta t = t_{CP} - t_{tag}$. The sine and cosine oscillations in the decay rates have opposite signs depending on whether the second B meson, referred to as B_{tag}, decays as a B^0 or as a $\bar{B}^0$. Furthermore, the amplitudes of the sine and cosine oscillations are sensitive to mixing-induced and direct CP violation observables.

The time-dependent CP asymmetry $A_{CP}(t)$ constructed from the time-dependent decay rates in Equations 2.101 and 2.102 is

$$\begin{aligned} A_{CP}(\Delta t) &= \frac{\Gamma\left[\Psi\left(t_{CP}, t_{tag}\right) \to f_{CP}\bar{f}_{tag}\right] - \Gamma\left[\Psi\left(t_{CP}, t_{tag}\right) \to f_{CP}f_{tag}\right]}{\Gamma\left[\Psi\left(t_{CP}, t_{tag}\right) \to f_{CP}\bar{f}_{tag}\right] + \Gamma\left[\Psi\left(t_{CP}, t_{tag}\right) \to f_{CP}f_{tag}\right]} \\ &= \mathcal{S}_{CP}^{mix} \sin(\Delta M \Delta t) - \mathcal{C}_{CP}^{dir} \cos(\Delta M \Delta t) . \end{aligned} \tag{2.103}$$

Compared to the time-dependent CP asymmetry introduced in Equation 2.94, one finds, that $A_{CP}(t)$ has the same form, but depends on the proper decay time difference Δt of two B mesons in an $\Upsilon(4S)$ event instead of the proper decay time of one B meson.

By integration over the experimentally not accessible sum of proper decay times, $t_{CP} + t_{tag}$, and by normalisation to the possible proper decay time difference interval of $-\infty < \Delta t < +\infty$, the probability to find in an $\Upsilon(4S)$ event one B meson decaying to a CP eigenstate f_{CP} and the other B meson decaying flavor-specific with a proper decay time difference Δt is

$$P(\Delta t, q) = \frac{1}{4\tau_{B^0}} e^{-|\Delta t|/\tau_{B^0}} \left[1 + q\left(\mathcal{S}_{CP}^{mix} \sin(\Delta m \Delta t) - \mathcal{C}_{CP}^{dir} \cos(\Delta m \Delta t)\right)\right], \tag{2.104}$$

where $q = +1$ (-1) represents the b-flavor charge, when the second B meson is tagged as B^0 $(\bar{B}^0)$.

In Figure 2.9 the distributions for B^0 and $\bar{B}^0$ tags and the corresponding CP asymmetries for three different scenarios of CP violation are shown.

- In the first scenario, a non-vanishing mixing-induced CP violation ($\mathcal{S} \neq 0$) with no direct CP violation ($\mathcal{C} = 0$) shifts and deforms the Δt distributions for B^0 (red) and $\bar{B}^0$ (blue) tags horizontally. The resulting time-dependent CP asymmetry follows a sine oscillation.

- In the second scenario, a non-vanishing direct CP violation ($\mathcal{C} \neq 0$) with no mixing-induced CP violation ($\mathcal{S} = 0$) shifts the Δt distributions vertically. The direct CP violation causes one decay to occur more or less frequently than that of its CP conjugated process. The resulting CP asymmetry follows a cosine oscillation.

- In the third scenario, a non-vanishing mixing-induced and a non-vanishing direct CP violation, ($\mathcal{S} \neq 0$ and $\mathcal{C} \neq 0$) are present. The Δt distributions are shifted and deformed both, horizontally and vertically, and the resulting CP asymmetry is a superposition of sine and cosine oscillations.

The CP violation measurements are performed at the Belle experiment as illustrated in Figure 2.8. One experimental difficulty is to resolve the proper decay time differences. Due to the low Lorentz boost, the resolution in the measurements of the decay flight length difference of

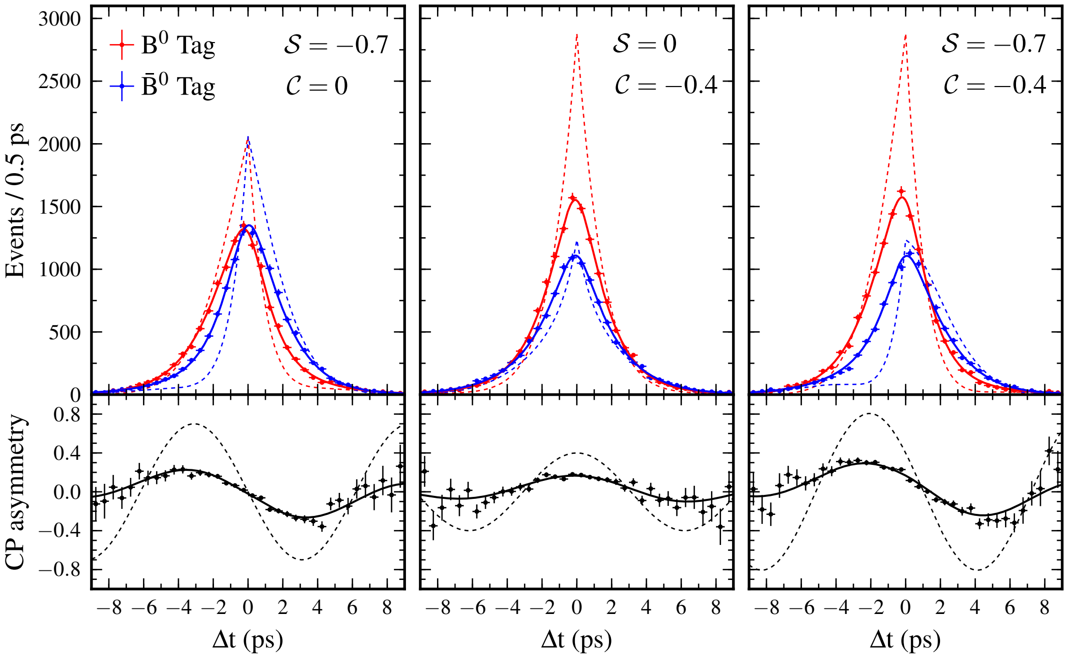

Figure 2.9: Theoretical (dashed lines) and experimental (solid lines) proper decay time difference distributions and the corresponding CP asymmetries for three different scenarios of mixing-induced CP violation $\mathcal{S}$ and direct CP violation $\mathcal{C}$.

the two B mesons is in the same order as the average flight length difference. The effect of the resolution is visible when comparing the theoretical (dashed lines) and experimental (solid lines) Δt distributions in Figure 2.9. In addition, the experimental assignment of the flavor of the B_{tag} meson from its decay products cannot be perfect. The uncertainties in the flavor tagging decision and possible mistags affect the measurement of the sine and cosine time-dependence and effectively result in a reduction of the measured amplitudes. This effect is visible in the time-dependent CP asymmetries in Figure 2.9: the amplitudes of the experimental oscillations are lower than the theoretical ones.

2.6 CP Violation in $\mathrm{b} \to \mathrm{c\bar{c}s}$ transitions

In the B meson system CP violation has been observed for the first time in $\mathrm{b} \to \mathrm{c\bar{c}s}$ transitions such as in $\mathrm{B}^0 \to \mathrm{J}/\psi \mathrm{K}^0_\mathrm{S}$ decays [22, 21]. This decay is referred to as the golden mode for the determination of the angle β of the Unitarity Triangle and is discussed in the following.

In $\mathrm{B}^0 \to \mathrm{J}/\psi \mathrm{K}^0_\mathrm{S}$ decays the J/ψ and the K^0_S are produced with orbital angular momentum of $\mathrm{L} = 1$ in a P-wave configuration. Neglecting the small CP violation in K^0-$\bar{\mathrm{K}}^0$ mixing, the K^0_S has like the J/ψ a CP eigenvalue of $+1$. In combination with the $(-1)^{\mathrm{L}=1} = -1$ contribution from the angular momentum, the $\mathrm{J}/\psi \mathrm{K}^0_\mathrm{S}$ final state has the CP eigenvalue $\eta_{\mathrm{CP}} = -1$.

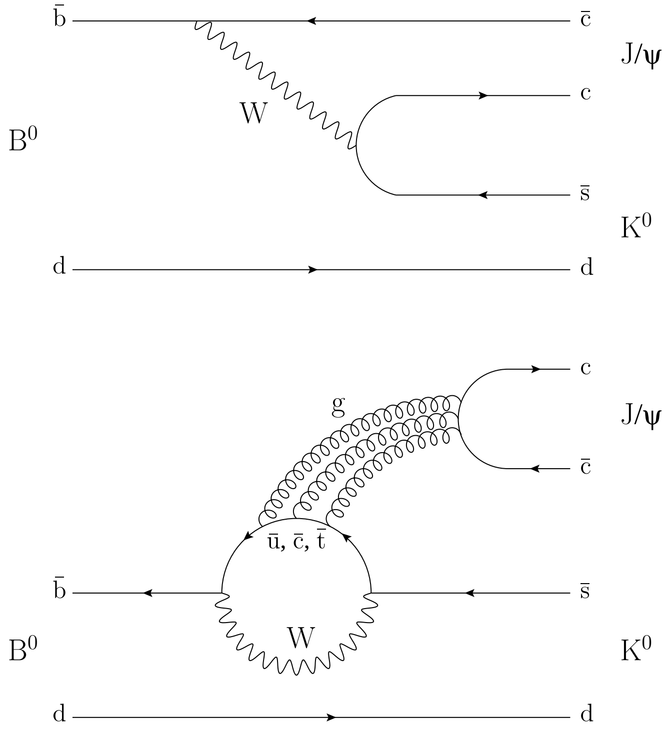

Figure 2.10: Tree-level (top) and penguin diagrams (bottom) contributing to $\mathrm{B}^0 \to \mathrm{J}/\psi \mathrm{K}^0_{\mathrm{S,L}}$ decays.

The tree-level and penguin diagrams contributing to $\mathrm{B}^0 \to \mathrm{J}/\psi \mathrm{K}^0_\mathrm{S}$ decays are shown in Figure 2.10. On tree-level, the decay is mediated by $\mathrm{b} \to \mathrm{c\bar{c}s}$ transitions that are color-suppressed due to the internal emission of a W boson. The penguin diagrams have an internal loop with virtual up-type quarks. The loops involving virtual $\bar{\mathrm{c}}$ and $\bar{\mathrm{t}}$ quarks have CKM elements of the same order as the transitions in the tree diagram and carry the same weak phase. In contrast, the loop involving virtual $\bar{\mathrm{u}}$ quarks, that could introduce a different weak phase via V_{ub}, is suppressed by a factor of λ^2, where $\lambda \approx 0.23$ refers to the expansion parameter in the Wolfenstein parameterisation. In the penguin diagrams, the $\mathrm{c\bar{c}}$ pair forming the J/ψ is created from gluons. Since the $\mathrm{c\bar{c}}$ pair has to be created in a color singlet state, it cannot be created from a single gluon. All above effects result in a high suppression of penguin amplitudes. No so-called penguin pollution and hence no direct CP violation are expected in $\mathrm{b} \to \mathrm{c\bar{c}s}$ transitions.

The mixing-induced CP violation in $B^0 \to J/\psi K^0_S$ decays can be estimated from the involved decay amplitudes and mixing-phases. The parameter $\lambda_{J/\psi K^0_S}$ defined in Equation 2.69 characterises the mixing-induced CP violation explained in Section 2.4.3. It depends on the ratio q/p which introduces the B mixing phase and the amplitudes of the CP conjugated decays. Since B^0 mesons decay to $J/\psi K^0$, but $\bar{B}^0$ mesons decay to $J/\psi \bar{K}^0$, the $J/\psi K^0_S$ final state involves K^0-$\bar{K}^0$ mixing and $\lambda_{J/\psi K^0_S}$ includes also the neutral kaon mixing phase. The parameter $\lambda_{J/\psi K^0_S}$ can then be expressed as

$$\begin{aligned}\lambda_{J/\psi K^0_S} &= \left(\frac{q}{p}\right)_{B^0} \frac{\bar{A}}{A} \left(\frac{q}{p}\right)_{K^0} \\ &= \eta_{CP} \frac{V^*_{tb} V_{td}}{V_{tb} V^*_{td}} \frac{V_{cb} V^*_{cs}}{V^*_{cb} V_{cs}} \frac{V^*_{cd} V_{cs}}{V_{cd} V^*_{cs}} \\ &= \eta_{CP} e^{-2i\beta},\end{aligned} \tag{2.105}$$

where β refers to the angle of the Unitarity Triangle defined in Equation 2.45.

Because of $\mathcal{S}^{\mathrm{mix}}_{J/\psi K^0_S} = -\eta_{CP} \sin(2\beta)$, the resulting time-dependent CP asymmetry in $B^0 \to J/\psi K^0_S$ decays is

$$A_{CP}(\Delta t) = -\eta_{CP} \sin(2\beta) \sin(\Delta M \Delta t). \tag{2.106}$$

Thus the angle β of the Unitarity Triangle can be determined by time-dependent CP asymmetry measurements of $B^0 \to J/\psi K^0_S$ decays. The same arguments also hold for other $b \to c\bar{c}s$ transitions, for example $B^0 \to J/\psi K^0_L$ decays with $\eta_{CP} = +1$.

The current world average of $\sin(2\beta)$ from $b \to c\bar{c}s$ transitions is

$$\sin(2\beta) = 0.68 \pm 0.02, \tag{2.107}$$

which corresponds to a value of $\beta = (21.4 \pm 0.8)^\circ$ [58]. Due to the high precision in $b \to c\bar{c}s$ transitions achieved by the B-factory experiments BaBar and Belle, the $\sin(2\beta)$ result provides a Standard Model reference and contributes to put tight constraints on the CKM metrology, e.g. on the Unitarity Triangle shown in Figure 2.3.

2.7 CP Violation in $b \to c\bar{c}d$ transitions

The Feynman diagrams contributing to $B^0 \to D^+D^-, D^{*+}D^-, D^{*-}D^+$ and $D^{*+}D^{*-}$ decays, referred to as neutral B meson to double-charm decays, are shown in Figure 2.11. On tree level, the decays are mediated by Cabibbo-disfavored, but color-allowed $b \to c\bar{c}d$ transitions. In addition to the tree-level diagrams, $b \to d$ penguin diagrams can contribute to the decays. The CKM elements of the penguin amplitudes are of the order of λ^3 as the tree-level amplitudes, but can carry different weak phases.

In contrast to $B^0 \to D^+D^-, D^{*+}D^-$ and $D^{*-}D^+$ decays, $B^0 \to D^{*+}D^{*-}$ is the decay of a pseudo-scalar meson to two vector mesons and involves a mixing of CP-even and CP-odd states which can be disentangled by an angular analysis. The measurements of $B^0 \to D^{*+}D^{*-}$ decays are not part of this work and have been carried out in parallel by the Belle Collaboration [59, 60]. The present analysis covers the measurement of branching fractions and time-dependent CP violation in $B^0 \to D^+D^-, D^{*+}D^-$ and $D^{*-}D^+$ decays. These decays are discussed in the following.

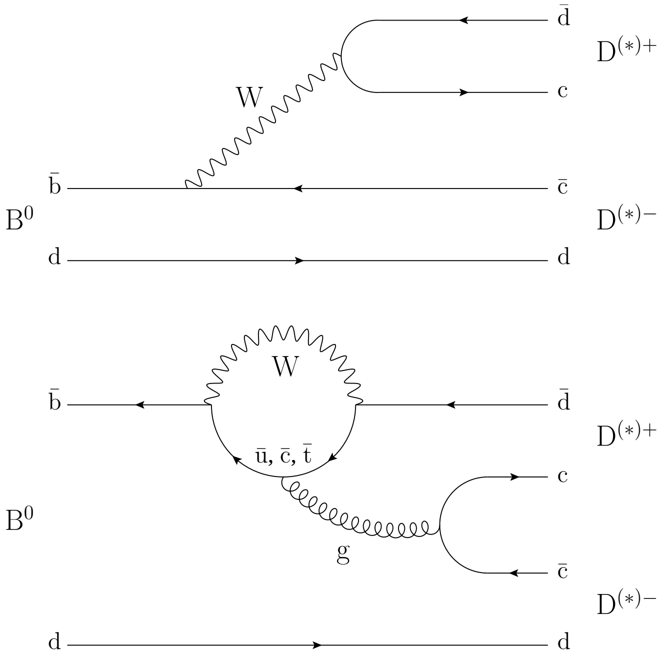

Figure 2.11: Tree-level (top) and penguin diagrams (bottom) contributing to $B^0 \to D^{(*)+}D^{(*)-}$ decays.

2.7.1 CP Violation in $B^0 \to D^+D^-$ Decays

The D^+D^- configuration is a CP eigenstate with eigenvalue $\eta_{CP} = +1$. The total decay amplitude of the $B^0 \to D^+D^-$ decay involves contributions from tree-level amplitudes (A_T) and penguin amplitudes (A_P^q with $q \in \{u, c, t\}$) and can be written as [61, 62]

$$A\left(B^0 \to D^+D^-\right) = \lambda_c^{(d)}\left(A_T + A_P^c\right) + \lambda_u^{(d)} A_P^u + \lambda_t^{(d)} A_P^t, \tag{2.108}$$

where $\lambda_q^{(d)} = V_{qd} V_{qb}^*$.

By introducing the relative strong phase δ and the relative weak phase γ between the decay amplitudes, the total decay amplitudes can be rewritten as

$$A\left(B^0 \to D^+D^-\right) = \mathcal{A}\left[1 - r e^{i(\delta+\gamma)}\right], \tag{2.109}$$

$$\bar{A}\left(B^0 \to D^+D^-\right) = \mathcal{A}\left[1 - r e^{i(\delta-\gamma)}\right], \tag{2.110}$$

where $\mathcal{A}$ refers to the CP conserving amplitude governed by the tree-level contributions and the ratio r measures the suppression of the penguin amplitudes with respect to the tree amplitude.

According to

$$\lambda_{D^+D^-} = e^{-2i\beta} \frac{\bar{A}\left(B^0 \to D^+D^-\right)}{A\left(B^0 \to D^+D^-\right)}, \tag{2.111}$$

the CP violation in $B^0 \to D^+D^-$ decays is determined by the expressions

$$\begin{aligned} \mathcal{S}_{D^+D^-}^{\text{mix}} = \frac{2\,\text{Im}\left(\lambda_{D^+D^-}\right)}{1+|\lambda_{D^+D^-}|^2} &= -\frac{\sin(2\beta) + 2r\cos(\delta)\sin(2\beta+\gamma) + r^2\sin\left[2\left(\beta+\gamma\right)\right]}{1+2r\cos(\delta)\cos(\gamma)+r^2} \\ &\approx -\sin(2\beta) - 2r\cos(2\beta)\cos(\delta)\sin(\gamma), \end{aligned} \tag{2.112}$$

$$\begin{aligned} \mathcal{C}_{D^+D^-}^{\text{dir}} = \frac{1-|\lambda_{D^+D^-}|^2}{1+|\lambda_{D^+D^-}|^2} &= -\frac{2r\sin(\delta)\sin(\gamma)}{1+2r\cos(\delta)\cos(\gamma)+r^2} \\ &\approx -2r\sin(\delta)\sin(\gamma). \end{aligned} \tag{2.113}$$

In the case of negligible penguin contributions, the mixing-induced CP violation in $B^0 \to D^+D^-$ decays is exactly $\mathcal{S}_{D^+D^-}^{\text{mix}} = -\sin(2\beta)$ and the direct CP violation vanishes. This case is equivalent to CP violation in the golden modes involving $b \to c\bar{c}s$ transitions such as in $B^0 \to J/\psi K_S^0$ decays discussed in Section 2.6.

In the case of sizeable penguin amplitudes, the mixing-induced CP violation is shifted with respect to $-\sin(2\beta)$ depending on the magnitude of the ratio r. Additionally, in combination with a non-vanishing relative strong phase a non-zero direct CP violation can emerge.

The calculation of the contributions of penguin amplitudes are associated with difficulties due to hadronic effects. The decays involve charm quarks in intermediate and final states which give rise to long-range interactions. This complicates certain theoretical approaches such as calculations based on factorization approximations. The current theoretical predictions on mixing-induced and direct CP violation in $B^0 \to D^+D^-$ decays are associated with large uncertainties. Standard Model conform model-dependent and model-independent predictions for the ratio r corresponding to the suppression of the penguin contributions range from values as low as 0.03 [63] to upper bounds of 0.3 [64, 65, 66]. Even larger contributions can be accommodated in extensions to the Standard Model [67].

CP violation in $b \to c\bar{c}d$ transitions has been previously studied by both, the Belle and the BaBar Collaborations. In 2007, Belle using a data set of 535×10^6 $B\bar{B}$ pairs has found evidence of a large direct CP violation in $B^0 \to D^+D^-$ decays: $\mathcal{C}_{D^+D^-}^{\text{dir}} = -0.91 \pm 0.23\,(\text{stat.}) \pm 0.06\,(\text{syst.})$, corresponding to a 3.2$\sigma$ deviation from zero [68]. This deviation has not been confirmed by BaBar and has not been observed in other $B^0 \to D^\pm D^{(*)\mp}$ decay modes [69, 70, 71]

The objective of the present analysis is the measurement of the branching fraction and time-dependent CP violation in $B^0 \to D^+D^-$ decays using the final Belle data set of 772×10^6 $B\bar{B}$ pairs. Furthermore, to provide a comparison to a directly related decay, the analysis covers additionally the measurement of $B^0 \to D^{*\pm}D^\mp$ decays.

2.7.2 CP Violation in $B^0 \to D^{*\pm}D^\mp$ Decays

The $B^0 \to D^{*\pm}D^\mp$ decays allow to probe independently from $B^0 \to D^+D^-$ decays for penguin effects in double-charm decays. Unlike D^+D^-, the $D^{*+}D^-$ and $D^{*-}D^+$ configurations are not CP eigenstates. Both states are accessible from B^0 and $\bar{B}^0$ decays with amplitudes of comparable magnitudes. Therefore an interference between direct decays and decays following B^0-$\bar{B}^0$ oscillations emerges, and mixing-induced and direct CP violation similar to that in $B^0 \to D^+D^-$ decays is expected.

The time-dependent decay rate for $B^0 \to D^{*\pm}D^\mp$ has four flavor-charge configurations and can be written as

$$f_{D^{*\pm}D^\mp}(\Delta t) = (1 \pm \mathcal{A}_{D^*D})\frac{e^{-|\Delta t|/\tau_{B^0}}}{8\tau_{B^0}}\left\{1 + q\left[\mathcal{S}_{D^{*\pm}D^\mp}\sin(\Delta m\Delta t) - \mathcal{C}_{D^{*\pm}D^\mp}\cos(\Delta m\Delta t)\right]\right\}. \quad (2.114)$$

Generally, the parameters $\mathcal{S}_{D^{*\pm}D^\mp}$ and $\mathcal{C}_{D^{*\pm}D^\mp}$ for the $D^{*+}D^-$ and $D^{*-}D^+$ configurations are not independent, but related by $\mathcal{S}_{D^{*\pm}D^\mp} = -\sqrt{1 - \mathcal{C}^2_{D^{*\pm}D^\mp}}\sin(2\beta_{\text{eff}} \pm \delta)$ [72]. The expression includes dependencies on the angle β, which can be modified by penguin contributions to the effective angle β_{eff}, and on the relative strong phase δ between $B^0 \to D^{*+}D^-$ and $B^0 \to D^{*-}D^+$ decay amplitudes.

The time- and flavor-integrated asymmetry $\mathcal{A}_{D^*D}$ is defined as

$$\mathcal{A}_{D^*D} = \frac{N_{D^{*+}D^-} - N_{D^{*-}D^+}}{N_{D^{*+}D^-} + N_{D^{*-}D^+}}, \quad (2.115)$$

and measures direct CP violation in $B^0 \to D^{*\pm}D^\mp$ decays.

The decay rate in Equation 2.114 can be expressed in an equivalent parameterisation given by [73]

$$\begin{aligned}
\mathcal{S}_{D^*D} &= \frac{1}{2}(\mathcal{S}_{D^{*+}D^-} + \mathcal{S}_{D^{*-}D^+}),\\
\mathcal{C}_{D^*D} &= \frac{1}{2}(\mathcal{C}_{D^{*+}D^-} + \mathcal{C}_{D^{*-}D^+}),\\
\Delta\mathcal{S}_{D^*D} &= \frac{1}{2}(\mathcal{S}_{D^{*+}D^-} - \mathcal{S}_{D^{*-}D^+}),\\
\Delta\mathcal{C}_{D^*D} &= \frac{1}{2}(\mathcal{C}_{D^{*+}D^-} - \mathcal{C}_{D^{*-}D^+}).
\end{aligned} \quad (2.116)$$

In this parameterisation, the decay rate of $B^0 \to D^{*\pm}D^{\mp}$ decays can be written as

$$\begin{aligned} f_{D^{*\pm}D^{\mp}}(\Delta t) = (1 \pm \mathcal{A}_{D^*D})\frac{e^{-|\Delta t|/\tau_{B^0}}}{8\tau_{B^0}} \\ \times\Big\{1 + q\Big[\Big(\mathcal{S}_{D^*D} \pm \Delta\mathcal{S}_{D^*D}\Big)\sin(\Delta m\Delta t) - \Big(\mathcal{C}_{D^*D} \pm \Delta\mathcal{C}_{D^*D}\Big)\cos(\Delta m\Delta t)\Big]\Big\}, \end{aligned} \quad (2.117)$$

where $\mathcal{S}_{D^*D}$ parameterises mixing-induced and $\mathcal{C}_{D^*D}$ flavor-dependent direct CP violation. The parameters $\Delta\mathcal{S}_{D^*D}$ and $\Delta\mathcal{C}_{D^*D}$ are not sensitive to CP violation. The parameter $\Delta\mathcal{S}_{D^*D}$ is related to the relative strong phase δ between the decay amplitudes and $\Delta\mathcal{C}_{D^*D}$ describes the asymmetry between the rates $\Gamma(B^0 \to D^{*+}D^-) + \Gamma(\bar{B}^0 \to D^{*-}D^+)$ and $\Gamma(B^0 \to D^{*-}D^+) + \Gamma(\bar{B}^0 \to D^{*+}D^-)$.

If the contributions of penguin amplitudes to $B^0 \to D^{*\pm}D^{\mp}$ decays are negligible, and the relative strong phase between the $B^0 \to D^{*+}D^-$ and $B^0 \to D^{*-}D^+$ decay amplitudes is zero and their magnitudes are the same, then

$$\mathcal{A}_{D^*D} = 0, \quad \mathcal{S}_{D^{*+}D^-} = \mathcal{S}_{D^{*-}D^+} = -\sin(2\beta), \quad \mathcal{C}_{D^{*+}D^-} = \mathcal{C}_{D^{*-}D^+} = 0, \quad (2.118)$$

or equivalent

$$\mathcal{A}_{D^*D} = 0, \quad \mathcal{S}_{D^*D} = -\sin(2\beta), \quad \mathcal{C}_{D^*D} = \Delta\mathcal{S}_{D^*D} = \Delta\mathcal{C}_{D^*D} = 0. \quad (2.119)$$

In this case, the time-dependent CP violating asymmetry in $B^0 \to D^{*\pm}D^{\mp}$ decays measures directly $-\sin(2\beta)$.

3 The Belle Experiment

3.1 The Υ-Resonances

The Υ-resonances are bound systems of b- and $\bar{b}$-quarks with quantum numbers of $J^{PC} = 1^{--}$ and can be produced directly in e^+e^--collisions. The experimental cross-section of e^+e^--annihilations in the region of the Υ-resonances is shown Figure 3.1. The decay widths of the three lowest $b\bar{b}$-states, the $\Upsilon(1S)$, $\Upsilon(2S)$ and $\Upsilon(3S)$, are relatively small and in the order of a few ten keV/c^2. The narrow widths of these resonances are an effect of the Okubo-Zweig-IIzuka (OZI) suppression of hadronic decays.

The fourth $b\bar{b}$-state, the $\Upsilon(4S)$, has a mass of 10.58 GeV/c^2, which is only 20 MeV/c^2 above the threshold for $B\bar{B}$ pair production. The $\Upsilon(4S)$ is a broad resonance with a width of approximately 20 MeV/c^2 and decays almost exclusively into $B^0\bar{B}^0$ and B^+B^- pairs. The $B^0\bar{B}^0$ pairs from $\Upsilon(4S)$ decays evolve coherently and allow for time-dependent CP asymmetry measurements. These unique properties led to the construction and commissioning of dedicated high luminosity e^+e^--colliders such as KEKB, that operate on the center-of-mass energy of the $\Upsilon(4S)$ as B-factories.

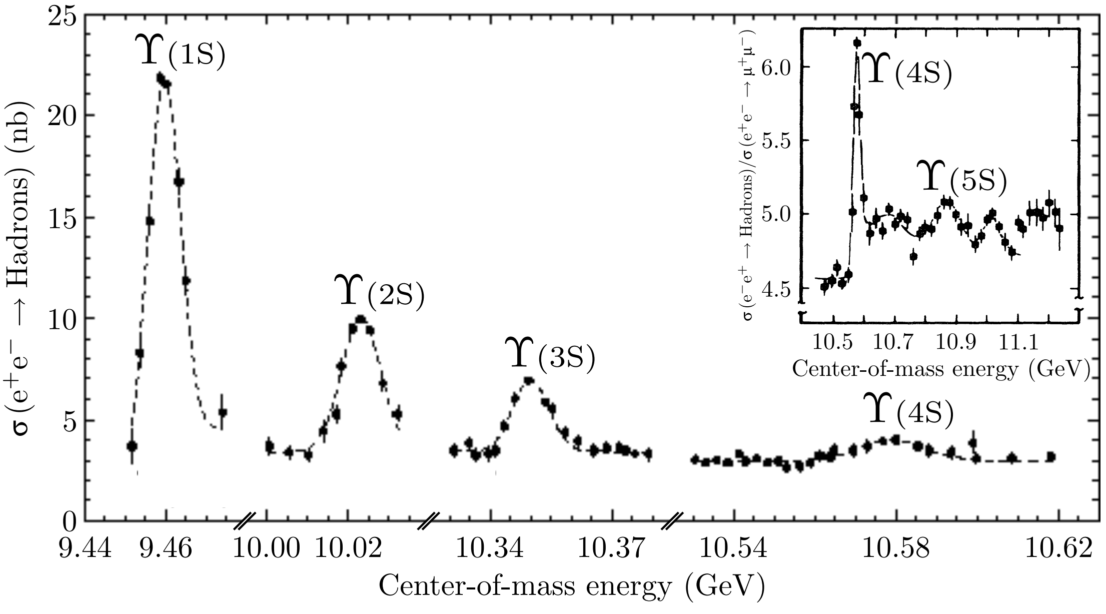

Figure 3.1: Cross-section of e^+e^--annihilations measured by CUSB and CLEO revealing the family of Υ-resonances [74, 75].

The $\Upsilon(5S)$ has a mass of 10.88 GeV/c^2. This is only approximately 300 MeV/c^2 higher than that of the $\Upsilon(4S)$, but it is located above a couple of further thresholds such as that for $B_s^0\bar{B}_s^0$ pair production. The $\Upsilon(5S)$ can decay into $B_{(s)}^{(*)}\bar{B}_{(s)}^{(*)}$ meson pairs, B meson pairs in association with pions or into other $b\bar{b}$-states.

The present analysis uses the final data set of $(772 \pm 11) \times 10^6\,B\bar{B}$ pairs recorded by the Belle detector and produced by KEKB on the $\Upsilon(4S)$. As shown in Figure 3.1, the cross-section of $e^+e^- \to \Upsilon(4S)$ is approximately 1 nb and the height of the peak is relatively small compared to the background. The background is caused by $e^+e^- \to q\bar{q}$ $(q \in \{u,d,s,c\})$ processes, that have a cross-section of approximately 3 nb. This background is referred to as continuum background. Depending on the particular analysis and the involved reconstructed decay modes, the continuum processes can give rise to a large source of background.

3.2 KEKB Accelerator

The KEKB accelerator is an asymmetric-energy e^+e^--collider designed to produce large numbers of $B\bar{B}$ pairs at a center-of-mass energy of $\sqrt{s} = 10.58\,\mathrm{GeV}$, corresponding to the mass of the the $\Upsilon(4S)$. The accelerator has been commissioned in 1998 and consists of two storage rings with a circumference of approximately 3 km and is located 11 m below ground, see Figure 3.2. The electrons and positrons have an energy of 8 GeV and 3.5 GeV, and are stored in bunches in the High Energy Ring (HER) and Low Energy Ring (LER), respectively. The two storage rings intercept at a single interaction point (IP) with a crossing angle of ±11 mrad.

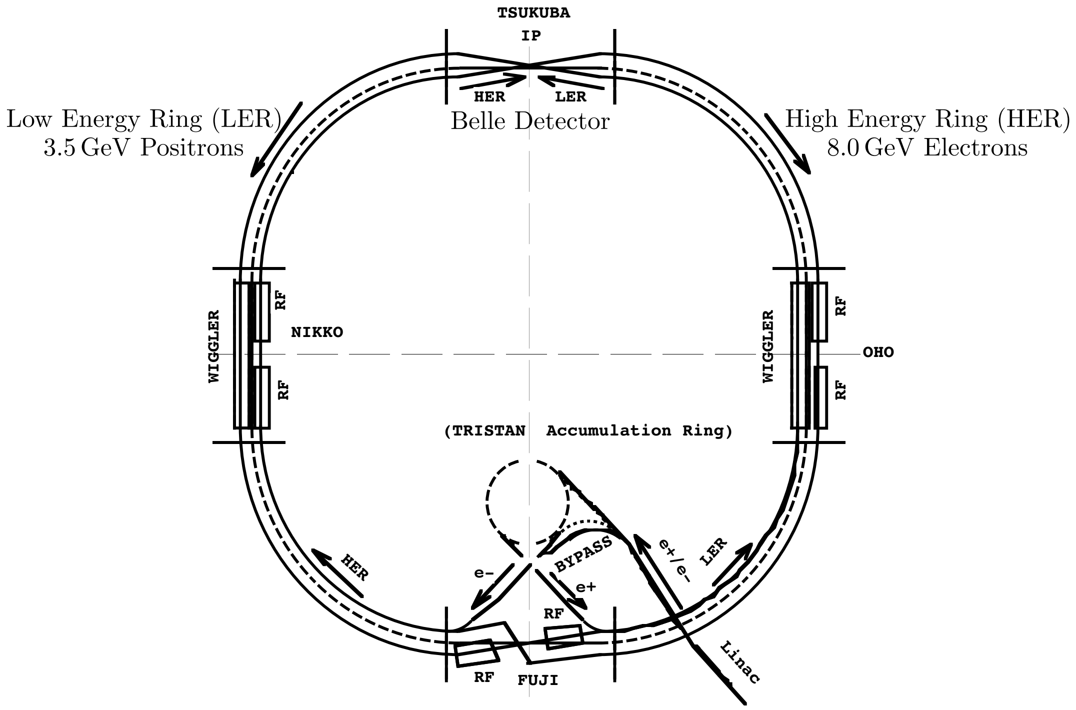

Figure 3.2: The KEKB accelerator [18].

The asymmetry in the energy of the KEKB collider corresponds to a Lorentz boost of $\beta\gamma = 0.425$ along the e^--beam direction in the laboratory reference system. The Lorentz boost causes a spatial separation of the decay vertices of the two produced B mesons and increases their average decay length difference from about $30\,\mu\mathrm{m}$, when produced symmetrically, to approximately 200 µm, which is an experimentally accessible distance for measurements. With the known boost, the decay length difference can be translated into a proper decay time difference, $\Delta t = \Delta z/\beta\gamma c$, and consequently allows for time-dependent measurements.

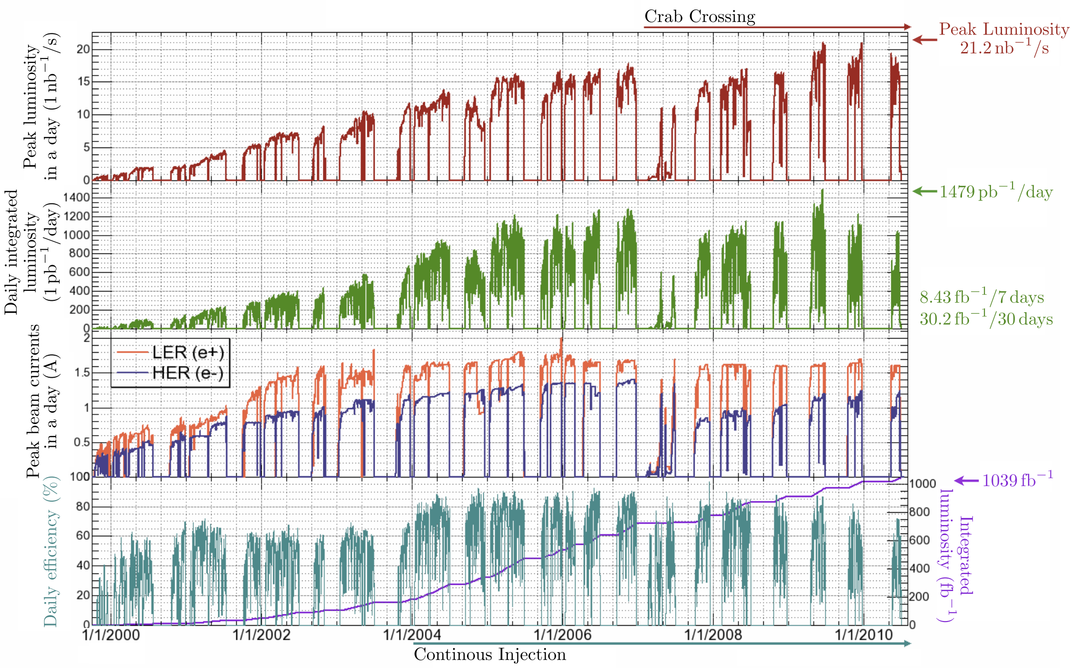

Figure 3.3: Luminosity of the KEKB accelerator and the Belle experiment between October 1999 and June 2010. The figure has been provided by the KEKB group.

The KEKB accelerator has been operated as a B-factory for the Belle experiment from October 1999 to June 2010. An overview of the achieved instantaneous and integrated luminosities in this period is shown in Figure 3.3. The KEKB accelerator was originally designed to achieve an instantaneous luminosity of $\mathcal{L} = 1.0 \times 10^{34}\,\mathrm{cm^{-2}s^{-1}}$, corresponding to a production rate of approximately $10\,B\bar{B}$ pairs per second. The accelerator received major upgrades during its lifetime, such as the installation of crab cavities, special superconducting RF cavities that kick the beams sideways to cause head-on collisions of the bunches at the interaction point. Due to the improvements in the operation and the design of the accelerator, KEKB exceeded the design luminosity and set various world records with peak luminosities as high as $2.1 \times 10^{34}\,\mathrm{cm^{-2}s^{-1}}$.

The Belle detector recorded an integrated luminosity of $711\,\mathrm{fb^{-1}}$, corresponding to $772 \times 10^6\,B\bar{B}$ pairs, produced by KEKB on the $\Upsilon(4S)$. Additionally, the KEKB accelerator was operated at different center-of-mass energies. For example, the Belle detector recorded $121\,\mathrm{fb^{-1}}$ on the $\Upsilon(5S)$, which allows for measurements in the B_s^0 system and for spectroscopy of $b\bar{b}$-states. In total, KEKB and the Belle experiment reached an integrated luminosity of more than $1\,\mathrm{ab^{-1}}$.

A detailed description of the design and operation of the KEKB accelerator is given in References [18, 76].

3.3 Belle Detector

The Belle detector is a multipurpose detector covering a solid angle of 4π around the interaction region and is optimised to perform time-dependent measurements using the asymmetric KEKB e^+e^--collider.

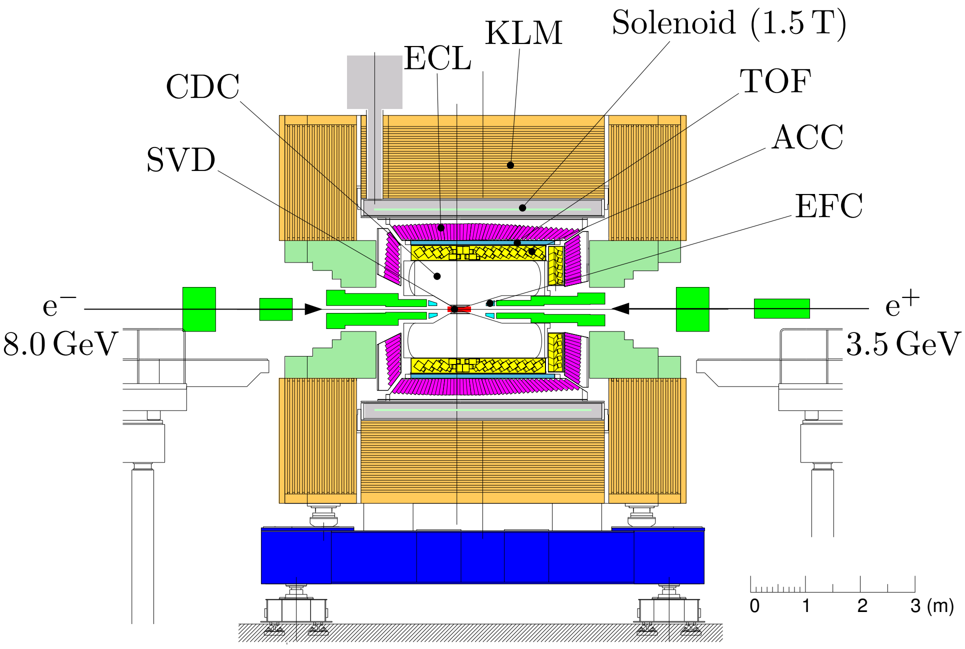

Figure 3.4: The Belle detector in a side view [77].

A schematic side view of the Belle detector is shown in Figure 3.4. The detector is equipped with a 1.5 T superconducting solenoid magnet with several subdetectors to detect and identify charged and neutral particles. The tracks of charged particles are reconstructed based on measurements of the silicon vertex detector (SVD) and of the central drift chamber (CDC). Electromagnetic showers are detected in arrays of CsI(TI) crystals of the electromagnetic calorimeter (ECL). In the extreme forward calorimeter (EFC), arrays of BGO crystals mask the beam to reduce the background for the CDC and are used as a luminosity monitor for the experiment. Muons and K_L^0 mesons are detected by arrays of resistive plate counters placed in the iron yoke that provides the magnetic flux return (KLM). In addition to measurements of specific energy loss in the CDC, particle identification is performed by measurements of aerogel threshold Čerenkov counters (ACC) and time-of-flight counters (TOF) located outside of the CDC.

The layout and the working principle of the individual components of the Belle detector are briefly described in the next sections. The descriptions and illustrations follow partly the technical publications in the given references, that contain further detailed information. The detector components important for the present analysis are the tracking system, the electromagnetic calorimeter and the systems for particle identification.

3.3.1 Beam Pipe

The interaction point is located at the crossing point of the e^-- and e^+-storage rings. It is surrounded by a beam pipe constructed as a double-wall cylinder composed of beryllium, see Figure 3.5. The walls of the beam pipe are with 0.5 mm as thin as possible to minimise multiple Coulomb scattering, which is a limiting effect on the z-vertex position measurements. The beam pipe is subject to beam-induced heating effects, that can be as high as a few hundred Watt and need an active cooling system to avoid negative effects on the surrounding silicon vertex detector. The 2.5 mm thick gap between the cylinders in the beam pipe is used as a channel for cooling by helium gas. The outer cylinder of the beam pipe is covered with a 20 µm thick gold film to reduce the background from synchrotron radiation. A detailed description of the beryllium beam pipe is given in Reference [77].

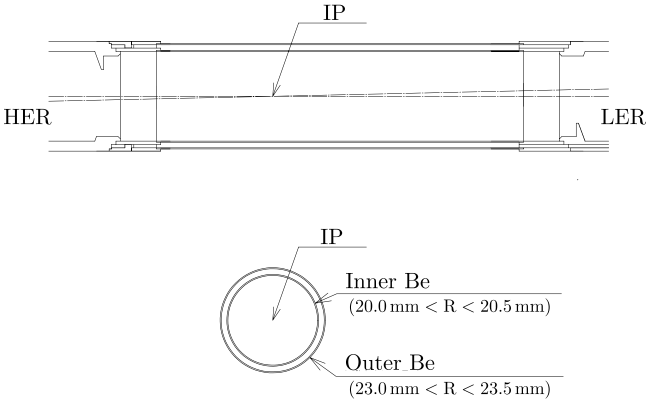

Figure 3.5: Layout of the beryllium beam pipe enclosing the interaction point at the first period of the Belle experiment from 1999 to 2003 [77].

3.3.2 Silicon Vertex Detector

The key objective of the Belle experiment and of the present analysis is the observation of time-dependent CP violation in neutral B decays. For such analyses, the decay length difference between two neutral B mesons originating from $\Upsilon(4S)$ decays needs to be measured at high precision. Due to the low Lorentz boost of the asymmetric-energy KEKB e^+e^--collider, the average decay length difference between the B mesons in z-direction is only approximately 200 µm. As a consequence, the silicon vertex detector (SVD) is required to have a high spatial resolution, capable to measure the difference in the z-vertex positions with a precision of approximately 100 µm.

The SVD is the innermost detector and is placed close to the interaction region outside of the cylindrical beryllium beam pipe. It has to resist high levels of radiation caused by the beam background. The SVD is subdivided into layers of different radii around the beam pipe. On each layer, ladders consisting of double-sided silicon strip detectors (DSSD) are mounted. The DSSDs provide depleted pn-junctions. Charged particles passing the junctions create electron and hole pairs along their trajectory. The created electrons and holes drift to the n^+ and p^+ strips on the surface of the DSSDs. The n^+ strips are aligned perpendicular and the p^+ strips are aligned along to the beam axis and therefore can provide measurements of charged tracks with respect to the $r\phi$ and z direction.

Two different vertex detectors have been operated in the Belle experiment:

The initial SVD, referred to as SVD1, has been operated from 1999 to 2003. The SVD1 detector has a barrel-only design and consists of three layers with radii of 30, 45.5, and 60.5 mm. It covers a polar angle of $23° < \theta < 139°$, corresponding to 86% of the full solid angle, and is equipped with 102 DSSDs. Each DSSD has 1280 sense strips and 640 read-out pads on opposite sides. The pitch of the strips is $42\,\mu$m in z direction and $25\,\mu$m in ϕ direction. The active size of the DSSD sensors is approximately $55 \times 33\,\text{mm}^2$.

The SVD was upgraded by an improved detector in 2003, referred to as SVD2. The upgraded detector is mounted closer to the beam pipe and has an improved coverage of the polar angle θ. The layout of the SVD2 detector is shown in Figure 3.6. It has four layers with radii of 20, 43.5, 70, and 88.0 mm and covers a polar angle of $17° < \theta < 150°$ corresponding to 93% of the full solid angle. It is equipped with 246 DSSDs. Two different kinds of DSSDs with strip pitches between 50 and $75\,\mu$m are used. The sensors of the DSSDs have a size of $28.4 \times 79.6\,\text{mm}^2$ in the first three layers and a size of $34.9 \times 76.4\,\text{mm}^2$ in the fourth layer.

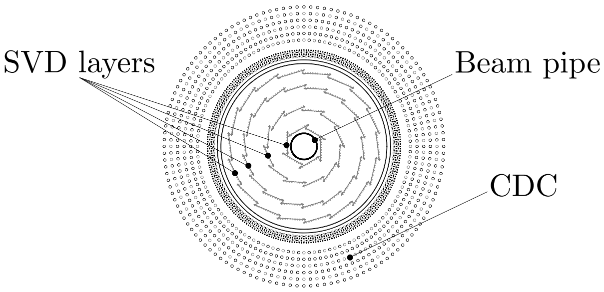

(a) SVD2 front view

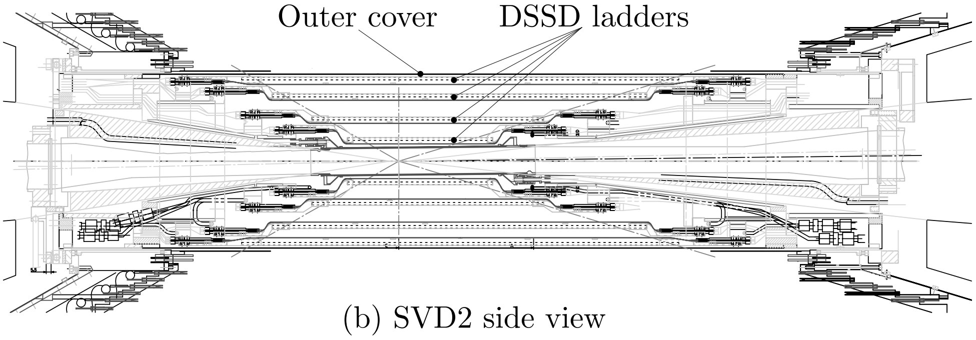

(b) SVD2 side view

Figure 3.6: The SVD2 detector operated at the Belle experiment from 2003 to 2010 [78].

The performance of the SVD can be quantified by the resolution of impact parameter measurements. The impact parameter of charged tracks is defined as the distance of closest approach to the interaction point. In general, the impact parameter resolution is different in $r\phi$ and in z directions and depends on the momenta and the polar angles θ of the particles. The impact parameter resolution in $r\phi$ and in z direction can be expressed as

$$\sigma_{r\phi} = a \oplus \frac{b}{p\beta \sin^{3/2}(\theta)} \tag{3.1}$$

$$\text{and} \quad \sigma_z = a \oplus \frac{b}{p\beta \sin^{5/2}(\theta)}, \tag{3.2}$$

where the symbol $\oplus$ denotes the quadratic sum and the term in the denominator is referred to as the pseudo-momentum $\tilde{p}$. The impact parameter resolutions $\sigma_{r\phi}$ and σ_z obtained from distributions of charged particles from cosmic rays are shown in Figure 3.7. The improved performance of the SVD2 detector compared to the SVD1 detector is evident. For $B^0 \to D^+D^-$ decays, the Δz resolution improves by more than 20%.

A detailed description of the silicon vertex detectors operated in the Belle experiment and their performance is given in References [78, 79].

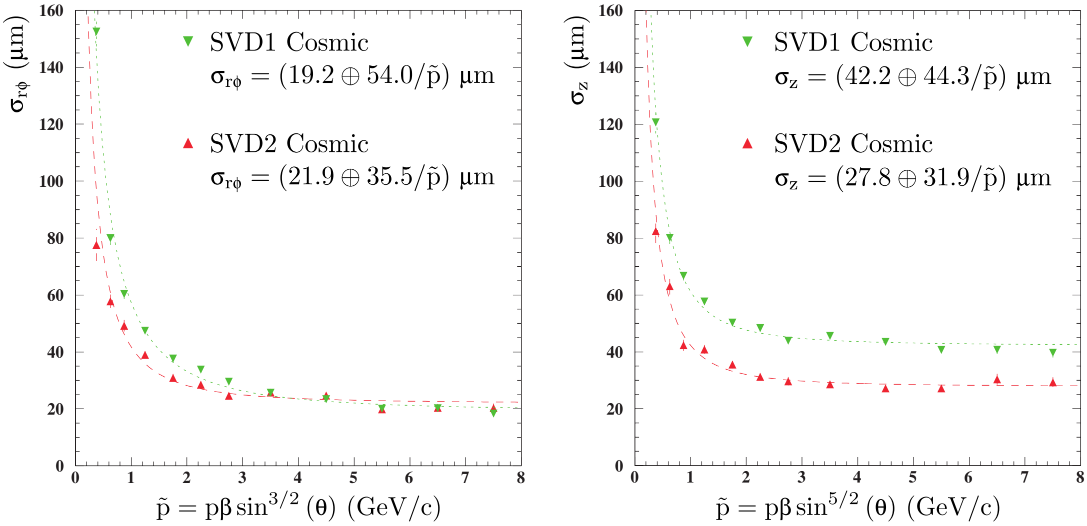

(a) Impact parameter resolution in $r\phi$ (b) Impact parameter resolution in z

Figure 3.7: Impact parameter resolution in $r\phi$ and in z dependent on the pseudo-momentum $\tilde{p}$ for charged tracks from cosmic rays for the SVD1 and SVD2 detectors (taken from Reference [80]).

3.3.3 Extreme Forward Calorimeter

The extreme forward calorimeter (EFC) extends the coverage of the polar angle with respect to the electromagnetic calorimeter. The EFC detects electrons and photons in the extreme forward region of $6.4° < \theta < 11.5°$ and in the extreme backward region of $163.3° < \theta < 171.2°$. It is located at the front faces of the cryostat of the compensation solenoid magnets and functions as a beam mask to reduce the background in the CDC. In addition, the EFC is used as a beam monitor by the KEKB accelerator and for luminosity measurements by the Belle experiment.

Due to its proximity to the beam pipe and to the interaction point, the EFC is exposed to very high levels of radiation. It is constructed from radiation-hard bismuth germanium oxide, $Bi_4Ge_3O_{12}$, crystals (BGO) and the scintillation light is collected by photodiodes. The forward and backward cones of the EFC are composed of 32 segments in the ϕ- and 5 segments in the θ-direction. The BGO crystals point approximately to the interaction point in a tower-like geometry. The arrangement of the BGO crystals in the EFC is shown in Figure 3.8.

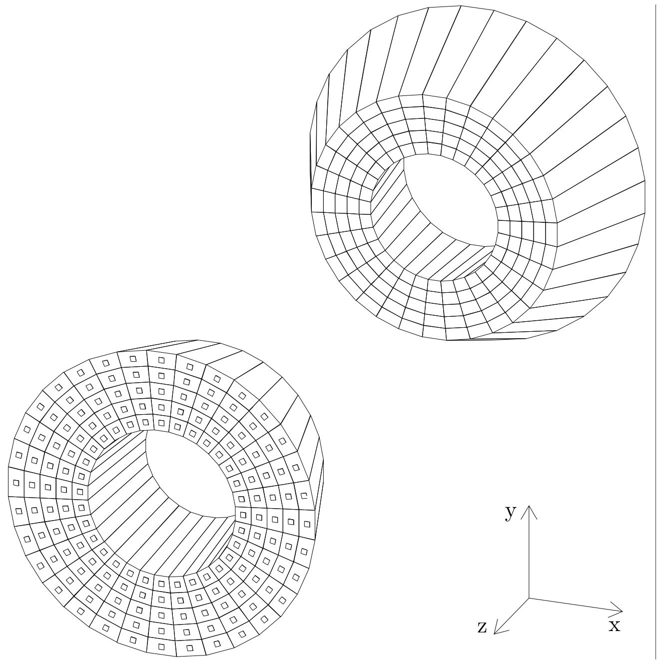

Figure 3.8: Arrangement of BGO crystals in the forward and backward EFC detectors [77].

A detailed description of the EFC operated in the Belle experiment and its performance is given in Reference [77].

3.3.4 Central Drift Chamber

The central drift chamber (CDC) is designed to provide measurements of the trajectories of charged particles. The CDC is located inside a 1.5 T magnetic field provided by a superconducting solenoid and allows to determine the momenta of charged particles from the curvature of the reconstructed tracks. Additionally, the CDC is used for the dE/dx measurements of the specific energy loss of charged particles by ionisation and contributes to particle identification. The tracking information provided by the CDC is also used for decisions of the trigger system.

The CDC is a cylindrical wire drift chamber containing 50 layers of anode wires and 3 cathode strip layers. The overall length of the CDC is 2404 mm and has inner and outer radii of 83 mm and 888 mm. The layout of the CDC is shown in Figure 3.9. To account for the Lorentz boost of the center-of-mass system, the CDC is asymmetric in z direction and covers a polar angle of $17° < \theta < 150°$, corresponding to 92% of the solid angle. In total, the CDC has 8400 drift cells and is organised into 6 axial and 5 small-angle stereo superlayers. Every superlayer is composed of between 3 to 6 radial layers sharing the same number of drift cells in azimuthal direction. The drift cells consist of 8 negatively biased field wires providing an electric field that surrounds a positively biased sense wire. The cell structure and the arrangement of wires is shown in Figure 3.10.

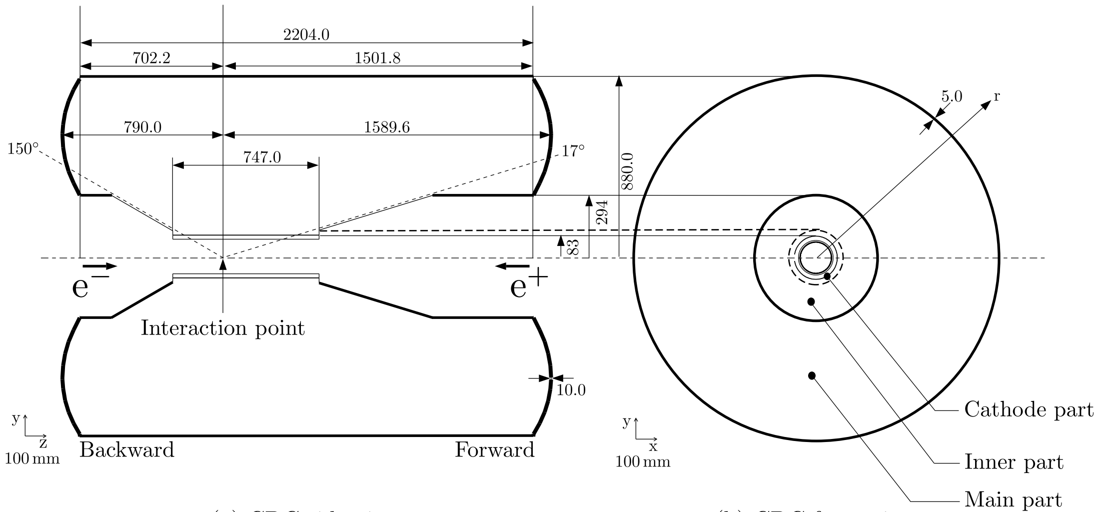

(a) CDC side view (b) CDC front view

Figure 3.9: The geometry of the CDC [77].

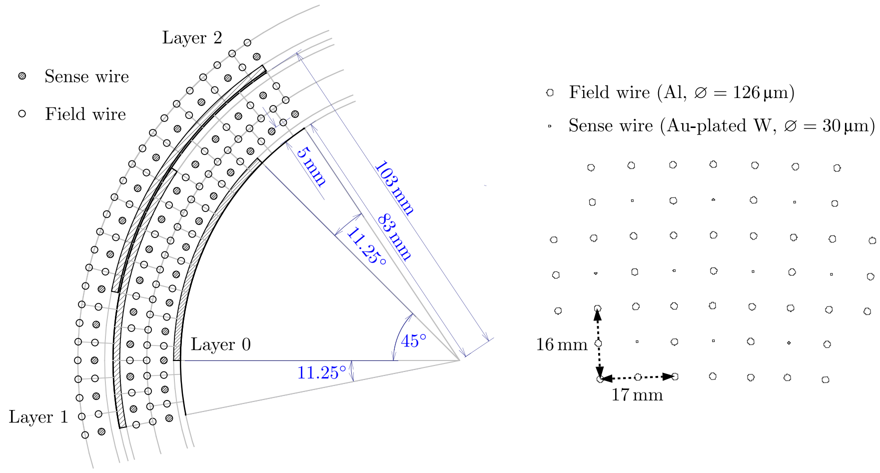

Figure 3.10: Cell structure and arrangement of wires in the CDC [77].

The CDC is filled with a gas mixture of 50% helium and 50% ethane. The low-Z gas mixture minimises the effect multiple Coulomb scattering especially of low momentum particles and reduces the background from synchrotron radiation by a small photo-electric cross-section. In addition, the ethane component allows a good dE/dx resolution.

Charged particles passing through the drift cells ionise the gas along their trajectories. The created electrons and ions drift to the anode and cathode wires. Close to the wires, the electrons undergo an acceleration caused by strong electrical fields. The acceleration results in an avalanche process of secondary ionisations and, as a consequence, in an amplification of the electrical pulses detected by the sense wires. The wires in the axial layers provide information for the measurement of the transverse momenta p_T and the wires in the stereo layers mounted at small angles provide additional information for the measurement of the longitudinal component of the momenta p_L. Details about the applied track finding algorithms and the determination of momenta are given in Reference [81].

The p_T resolution of the CDC is given by:

$$\left.\frac{\sigma_{p_T}}{p_T}\right|_{\mathrm{CDC}} = \left(0.28\, p_T \oplus \frac{0.35}{\beta}\right)\% \tag{3.3}$$

If the measurements of the CDC and the SVD detectors are combined, then the p_T resolution improves to

$$\left.\frac{\sigma_{p_T}}{p_T}\right|_{\mathrm{CDC+SVD}} = \left(0.19\, p_T \oplus \frac{0.30}{\beta}\right)\%. \tag{3.4}$$

The amplitudes of the signal of the hit wires are used to determine the energy loss dE/dx of the charged particles in the CDC. The dE/dx distributions follow the Bethe formula and depend on the velocity of a particle at a given momentum. The velocity at a given momentum changes depends on the mass of the particle and consequently the dE/dx measurements allow to discriminate between different kinds of charged particles. In general, the distributions of dE/dx measurements follow Landau distributions with large tails. In the estimation of the most probable energy loss, the truncated-mean method is applied by removing the 20 % largest values of the dE/dx measurements in order to minimise large fluctuations due to the Landau tails. The distribution of dE/dx measurements by the CDC in dependence of the momenta of particles, as obtained in collision data, is shown in Figure 3.11. The dE/dx measurements are included into the particle identification and is of importance for the $K^\pm/\pi^\pm$ separation in the present analysis.

A detailed description of the CDC operated in the Belle experiment and its performance is given in References [77, 82].

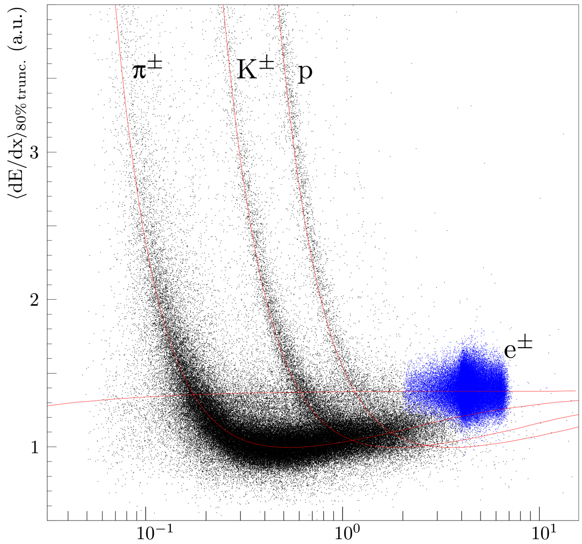

Figure 3.11: Truncated mean of dE/dx measurements showing the momentum-dependent specific energy loss of charged particles in the CDC. The distributions have been obtained by collision data [77].

3.3.5 Aerogel Čerenkov Counter

The aerogel Čerenkov counter (ACC) is a detector dedicated to provide information for the identification of particles, in particular to discriminate $\pi^\pm$ from $K^\pm$ mesons. It is sensitive to the $1\,\mathrm{GeV/c} < p < 4\,\mathrm{GeV/c}$ high momentum range of charged particles and thus is complementary to dE/dx measurements by the CDC and to time-of-flight measurements by the TOF.

Charged particles passing a medium with a velocity larger than the speed of light in the medium radiate Čerenkov radiation. The speed of light in a medium c_{medium} is related to the refractive index n of the medium by

$$c_{\mathrm{medium}} = \frac{c_{\mathrm{vacuum}}}{n}, \tag{3.5}$$

Consequently a charged particle with velocity β, mass m and momentum p radiates Čerenkov radiation, if

$$n > \frac{1}{\beta} = \sqrt{1 + \left(\frac{m}{p}\right)^2}. \tag{3.6}$$

In the ACC, the material of the medium is chosen such, that $\pi^\pm$ mesons with momenta larger than $1\,\mathrm{GeV/c}$ generate Čerenkov radiation, but the heavier $K^\pm$ mesons with the same momenta are below the threshold velocity and do not generate Čerenkov radiation. The ACC functions only as a threshold counter and cannot image the Čerenkov angle, which is directly related to the velocity of the particle and would provide additional information useful for the identification of particles.

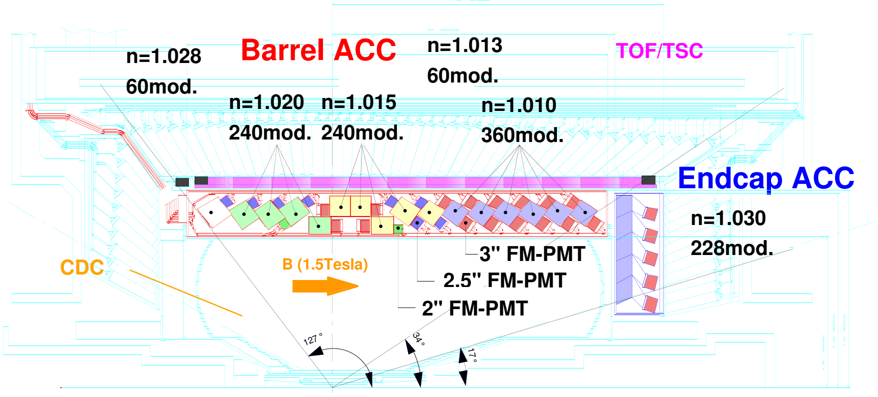

Figure 3.12: The aerogel Čerenkov counter [77].

The ACC is divided into barrel and forward endcap regions and covers a polar angle of $17^\circ < \theta < 127^\circ$. The detector in the barrel region consists of 960 counter modules segmented into 60 cells in the ϕ-direction. The detector in the endcap region consists of 228 counter modules arranged in 5 concentric layers. The counter modules point to the interaction region. The arrangement of the counter modules is shown in Figure 3.12. The counter modules consist of layers of silica aerogels arranged in aluminum boxes of $12 \times 12 \times 12\,\mathrm{cm}^3$ in size. The refractive indices of the silica aerogels are $1.010 \leq n \leq 1.030$ and depend on the polar angle. The Čerenkov light is detected by fine-mesh photomultipliers attached to the aluminum boxes.

Based on measurements by the ACC only, the particle identification for particle momenta up to 4 GeV/c has a kaon identification efficiency of more than 80% with an associated pion misidentification rate of 10% or below.

A detailed description of the ACC operated in the Belle experiment and its performance is given in References [77, 83].

3.3.6 Time-of-Flight Counter

The time-of-flight (TOF) detector system measures the time particles need to travel from the interaction point to a TOF module. Combined with momentum measurements, it contributes to the identification of particles, in particular to discriminate between $\pi^{\pm}$ and $K^{\pm}$ mesons. The TOF is sensitive to charged particles with momenta less than 1.2 GeV/c and is thus complementary to the ACC. In addition, the TOF provides fast timing signals for the trigger system.

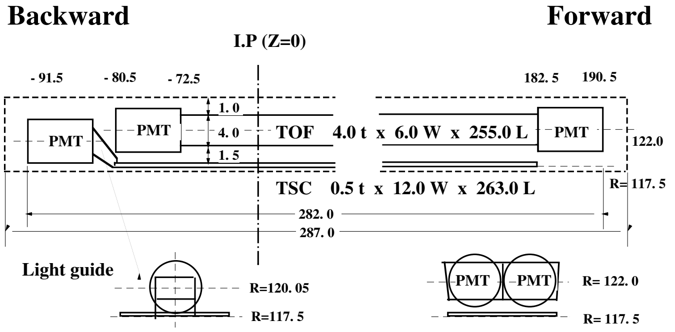

Figure 3.13: Layout of a module of the TOF detector system [77].

The TOF modules consist of plastic scintillation counters attached to photomultiplier tubes, see Figure 3.13. In total, 64 TOF modules are placed in the barrel region of the detector. The radial distance to the interaction point is 1.2 m. The TOF covers a polar angle of $34° < \theta < 120°$ and has a time resolution of approximately 100 ps.

The mass m of a particle is related to the measured time-of-flight T by

$$m = \frac{p}{c}\sqrt{\left(\frac{cT}{L}\right)^2 - 1}\,, \tag{3.7}$$

where p denotes the momentum of the particle measured by the CDC and SVD and L denotes the helical distance traveled by the particle from the interaction point to the TOF module. The mass distribution obtained from TOF measurements in combination with momentum measurements by the CDC for hadronic events and the resulting separation of $\pi^{\pm}$ and $K^{\pm}$ mesons and protons is shown in Figure 3.14.

A detailed description of the TOF operated in the Belle experiment and its performance is given in References [77, 84].

3.3.7 Electromagnetic Calorimeter

The electromagnetic calorimeter (ECL) measures the energy and the position of electromagnetic showers caused by photons and electrons in cascades of bremsstrahlung and pair production processes. It has to provide a high energy resolution over a wide range of energies from

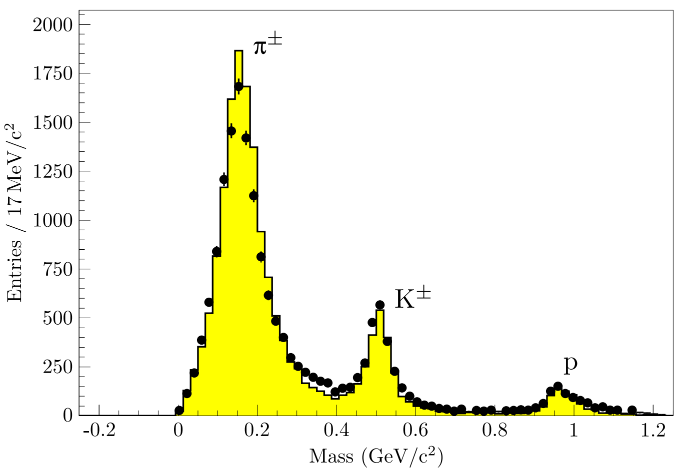

Figure 3.14: Mass distribution obtained by time-of-flight measurements of particles with momenta below 1.2 GeV/c on data (data points with errorbars) and distribution according to Monte Carlo simulations (yellow histogram) [77].

20 MeV/c^2 up to 8 GeV/c^2. The ECL has to detect low-energy photons originating from the end products of cascade decays involving π^0 and η mesons and high-energy photons originating directly from B decays, such as e.g. in $B^0 \rightarrow K^{*0}\gamma$. In addition, luminosity measurements and calibrations are performed by the ECL in Bhabha and in $e^+e^- \rightarrow \gamma\gamma$ processes.

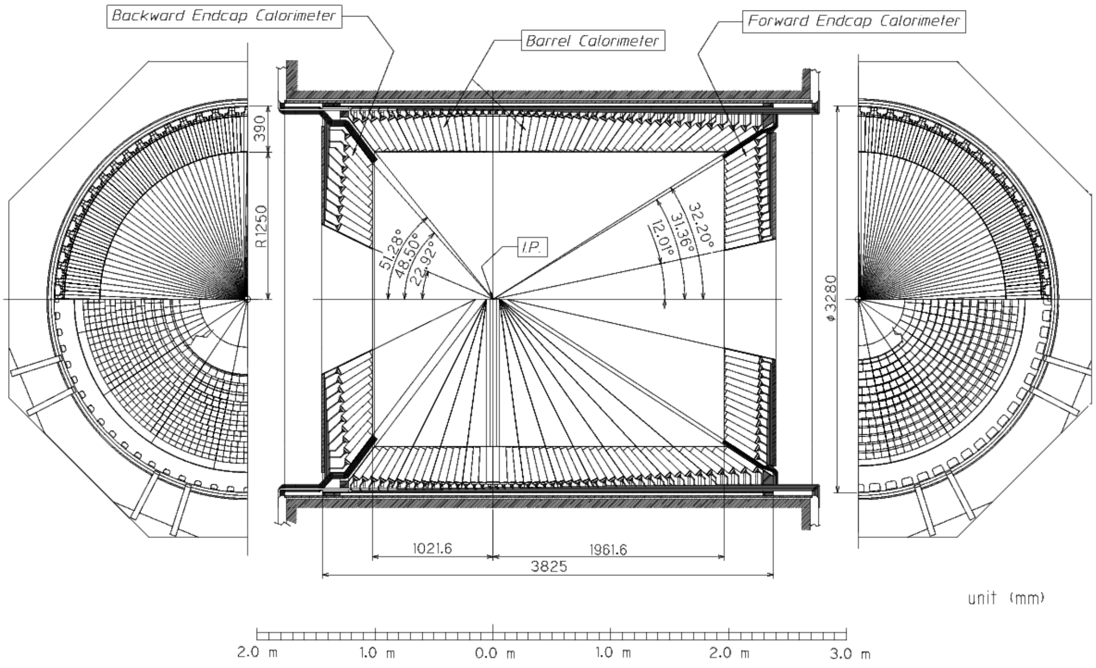

Figure 3.15: Geometry and arrangements of CsI(Tl) crystals in the ECL [77].

The ECL consists of segmented arrays of counters constructed from 8376 scintillating cesium iodide crystals (CsI(Tl)) doped with thallium as wavelength shifter and pairs of silicon PIN photodiodes for readout. In the barrel part of the ECL, 6624 crystals are placed. The forward and backward endcaps contain 1152 and 960 crystals, respectively. The ECL covers a polar angle of $12° < \theta < 155°$. The crystals are arranged with a small tilt of approximately 1.3° to 4.0° in the ϕ- and θ-directions to prevent photons to escape through the gaps between the crystals. The geometry of the ECL and the arrangement of the crystals is shown in Figure 3.15.

The CsI(Tl) crystals in the barrel region have forward and backward faces of $5.5\,\mathrm{cm} \times 5.5\,\mathrm{cm}$ and $6.5\,\mathrm{cm} \times 6.5\,\mathrm{cm}$ and are 30 cm long, corresponding to 16.2 radiation lengths (X_0) for photons and electrons. The crystals in the endcaps have edge lengths of the surfaces with dimensions between 4.5 cm and 8.2 cm. The size of the crystals are chosen by the requirement, that approximately 80% of the total energy deposit of a photon entering through the center of the front face has to be contained within the crystal.

The ECL has an energy resolution of

$$\frac{\sigma_E}{E} = \left(1.34 \oplus \frac{0.066}{E} \oplus \frac{0.81}{E^{1/4}}\right)\%\,, \tag{3.8}$$

where the energy E is measured in units of GeV. The energy resolution is limited by electronic noise, contributing to the first term, and by shower leakage fluctuations, contributing to the second and third term.

An experimental $M_{\gamma\gamma}$ spectrum in the mass region of π^0 and η mesons obtained on hadronic data by the ECL is shown in Figure 5.4. The mass resolution for π^0 and η mesons is approximately $5\,\mathrm{MeV}/c^2$ and $12\,\mathrm{MeV}/c^2$, respectively.

In addition to energy measurements, the ECL contributes to the particle identification of electrons. Charged particles different from electrons, such as $\pi^\pm$ and $K^\pm$ mesons, deposit less energy than electrons in the ECL. These particles can be distinguished from electrons by the differences in shower shapes, e.g. measured by the ratio of shower energies E_9/E_{25} in 3×3 and 5×5 crystal arrays, and by the ratio of energy deposit to momentum E/p, that is close to unity for electrons and small other particles.

A detailed description of the ECL operated in the Belle experiment and its performance is given in References [77, 85].

3.3.8 Superconducting Solenoid Magnet

The superconducting solenoid provides a magnetic field of 1.5 T in a cylindrical volume 3.4 m in diameter and 4.4 m in length. It covers all detector components except the KLM, that is located outside of the solenoid in the iron structure of the Belle detector. The iron structure also serves as return path for the magnetic flux.

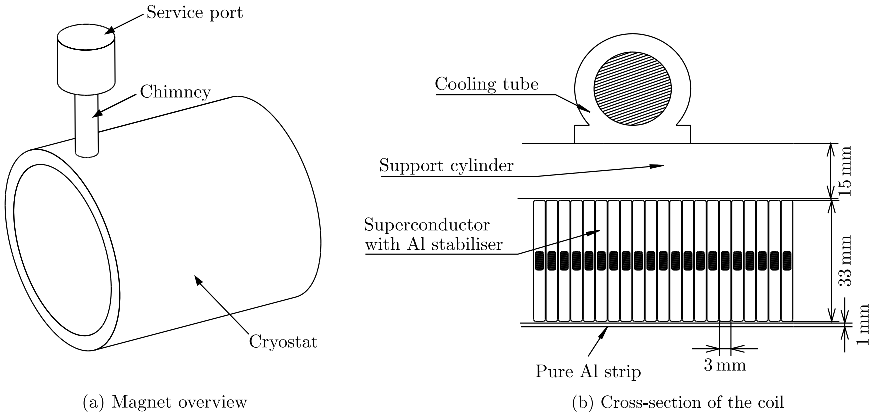

(a) Magnet overview (b) Cross-section of the coil

Figure 3.16: Overview of the superconducting solenoid and cross-section of a coil [77].

The superconducting coil consists of a niobium-titanium-copper (NbTi/Cu) alloy, that is stabilised by aluminum and cooled by liquid helium. The dimension of the conductor is 3 mm × 33 mm. The coil has a nominal current of 4400 A and stores an energy of 35 MJ. An overview over the superconducting solenoid and a cross-section of the coil is shown in Figure 3.16.

A detailed description of the superconducting solenoid is given in Reference [77].

3.3.9 K_L^0 and Muon Detector

The K_L^0 and muon detector (KLM) is the detector component located most outside and is designed to identify long-living neutral kaons and muons. The KLM uses the iron structure of the Belle detector as absorber material and covers a polar angle of $20° < \theta < 155°$. The KLM detector is composed of alternating layers of 4.7 cm thick iron plates and superlayers containing resistive plate counters (RPC) capable to detect charged particles. The barrel (endcap) region contains 14 iron layers and 15 (14) RPC superlayers.

The superlayers are composed of two glass-electrode RPC modules with high bulk resistivity ($\geq 10^{10}\,\Omega$cm) separated by a gas-filled gap. A charged particle passing the gap initiates a streamer in the gas. The streamer in the gas causes a local discharge of the plates, that induces a signal on the external readout strips along the θ- and ϕ-directions. The cross-section of a RPC superlayer in the KLM detector is shown in Figure 3.17.

In addition to the 0.8 interaction lengths provided by the ECL, the iron absorber of the KLM provides 3.9 interaction lengths of material to convert K_L^0 mesons into showers of ionising particles. The KLM measures the location of the showers and thus the flight direction of the K_L^0 mesons. Due to large fluctuations in the size of the showers, the KLM is not capable of providing useful measurements of the K_L^0 energy.

Muons of sufficient energy are able to completely pass the KLM. Muons are identified by detection of particles, that penetrate several layers of the KLM and that are matched to re-

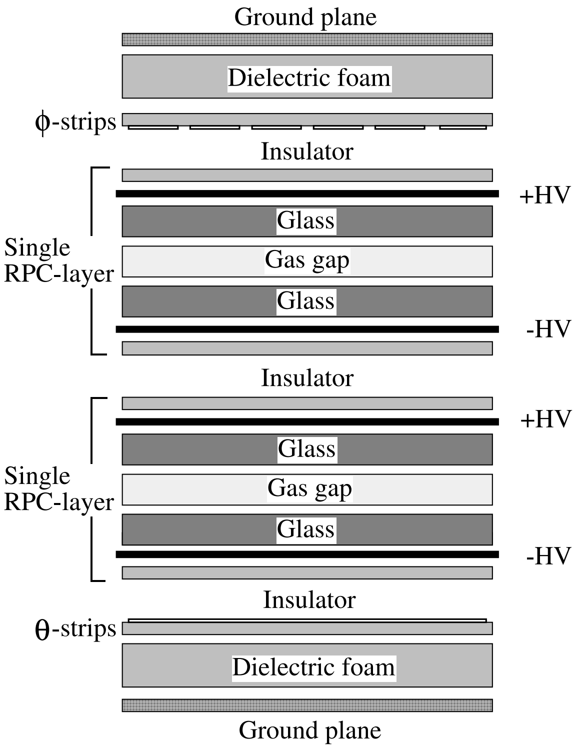

Figure 3.17: Cross-section of a RPC superlayer in the KLM detector [77].

constructed tracks. For particle identification, muons are discriminated from charged hadrons, such as $\pi^{\pm}$ and $K^{\pm}$ mesons. As a consequence of the lack of strong interaction, muons travel in average longer distances and have smaller deflections in the KLM. For particles with momenta of 1.5 GeV/c, the muon identification efficiency is better than 90% with a misidentification rate of less than 5%.

A detailed description of the KLM operated in the Belle experiment and its performance is given in References [77, 86].

3.3.10 Trigger and Data Acquisition System

The acquisition and the storage of data recorded by the Belle detector is controlled by the trigger system. On the basis of fast signals from the subdetectors, the trigger system decides, whether an event is of interest for physics and has to be integrated and recorded by the data acquisition system (DAQ) for analyses at a later stage, or should be discarded. Processes of interest for physics analyses are e.g. hadronic $\Upsilon(4S)$ decays or hadronic continuum events, events containing μ- and τ-pairs, events containing Bhabha scattering or two photon processes. During the normal operation of data taking, events that are discarded and not recorded are beam related background events caused by e.g. synchrotron radiation or interactions of the beam with residual gas in the beam pipe, and background events caused by cosmic rays.

The cross-sections and rates of physical processes at an instantaneous luminosity of $\mathcal{L} = 10^{34}\mathrm{cm}^{-2}\mathrm{s}^{-1}$ are summarised in Table 3.1. The total rate of physics processes is approximately 100 Hz at this luminosity. The rate of the beam background is in the order of 120 Hz and

Physics process	Cross-section (nb)	Rate (Hz)
$\Upsilon(4S) \to B\bar{B}$	1.2	12
$e^+e^- \to q\bar{q}$ ($q \in \{u,d,s,c\}$) continuum	2.8	28
$e^+e^- \to l^+l^-$ ($l \in \{\mu,\tau\}$)	1.6	16
Bhabha ($\theta_{lab} \geq 17°$)	44	$4.4^{(a)}$
$e^+e^- \to \gamma\gamma$ ($\theta_{lab} \geq 17°$)	2.4	$0.24^{(a)}$
2γ processes ($\theta_{lab} \geq 17°$, $p_t \geq 0.1$ GeV/c)	≈ 15	≈ 35
Total	≈ 67	≈ 96

Table 3.1: Cross-sections and rates at an instantaneous luminosity of $\mathcal{L} = 10^{34}\text{cm}^{-2}\text{s}^{-1}$. The superscript $^{(a)}$ indicates the values pre-scaled by a factor 1/100 [77].

depends highly on the accelerator conditions, such as the current and the focusing of the beams, resulting in a total rate of 220 Hz. At peak luminosities of $\mathcal{L} = 2 \times 10^{34}\text{cm}^{-2}\text{s}^{-1}$ of the KEKB accelerator, the event rates for physics and background processes are as high as 200 Hz and 600 Hz, respectively. The trigger system can handle rates up to 1200 Hz and operates on average at a trigger rate of 500 Hz with an occupancy of 5%.

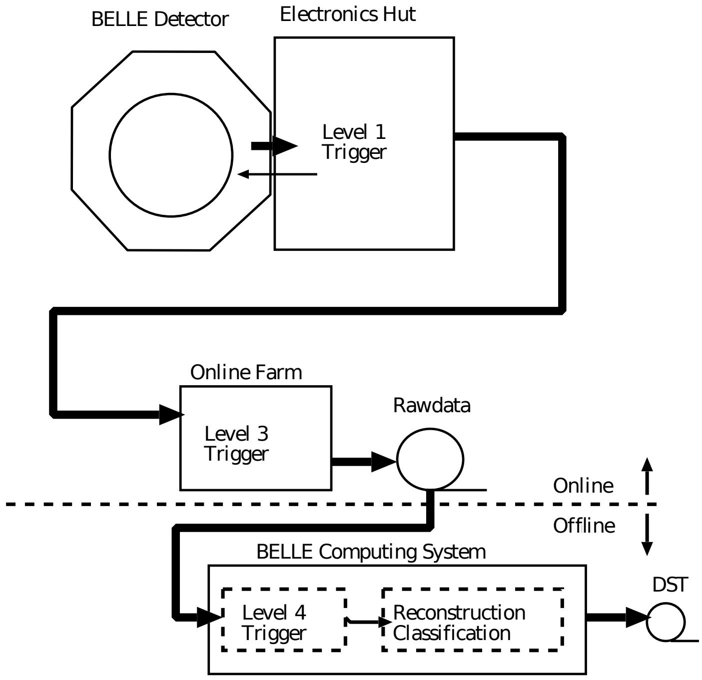

Figure 3.18: The Belle trigger system [77].

An overview of the Belle trigger system is shown in Figure 3.18. The trigger system is subdivided into three different stages: the hardware Level-1 trigger, the online software Level-3 trigger, and the offline software Level-4 trigger.

The Level-1 trigger system is shown in Figure 3.19. It consists of trigger systems of all subdetectors, except the SVD, and a central trigger system, called Global Decision Logic (GDL). The trigger systems of the subdetectors can be divided into two categories: triggers based on detected tracks, and triggers based on energy measurements. For track based triggers, the CDC provides signals of rϕ- and z-hit measurements, the TOF provides timing information and measurements of the topology and multiplicity of hits by charged tracks, and the KLM provides information about muon candidates. For the energy based triggers, the ECL provides complementary triggers sensitive to different kinds of hadronic events based on energy deposit and cluster counting in the crystals. Additionally, the ECL and the EFC trigger Bhabha and two photon events. The GDL processes in parallel trigger signals received by the subdetectors within 1.85 µs after the collision and provides a trigger decision 2.2 µs after the collision. For hadronic events, the GDL has four triggers: the two-track trigger, the three-track trigger, a trigger based on cluster isolation, and a trigger based on the total energy deposit. By combining these triggers, the GDL provides a trigger efficiency for hadronic events of more than 99%.

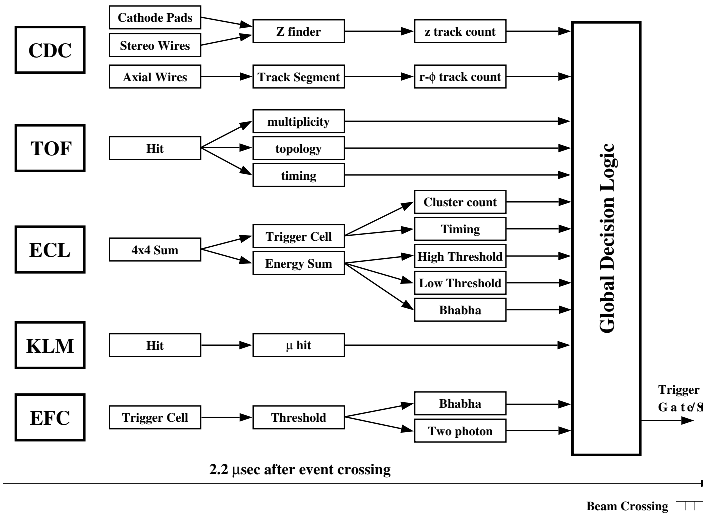

Figure 3.19: The Level-1 trigger system [77].

The DAQ system collects the subdetector information for events specified by the Level-1 trigger. An overview of the DAQ system is shown in Figure 3.20. For signals received by the sequence control (SEQ) from the GDL, the DAQ processes the data of the 7 subdetectors in parallel and integrates them by an event builder into a data stream for the Level-3 trigger. The typical size of hadronic events is approximately 30 kB, corresponding to data transfer rates of 15 MB/s.

The Level-3 trigger is realised by fast track finding algorithms running on an online farm of computers. To reject background events originating e.g. from the beam background, the Level-3 trigger requires events to contain reconstructed tracks with an impact parameter of $|dz| < 5\,\text{cm}$ with respect to the interaction point. This requirement results in a data reduction in the order of a factor 2, while retaining an efficiency for hadronic events of more than 99%.

The Level-4 trigger processes the raw data offline and reduces it by applying a set of minimal selection requirements, such as impact parameters and thresholds of energy deposit. For analyses, it provides fully reconstructed data sets containing, e.g. the momenta of recon-

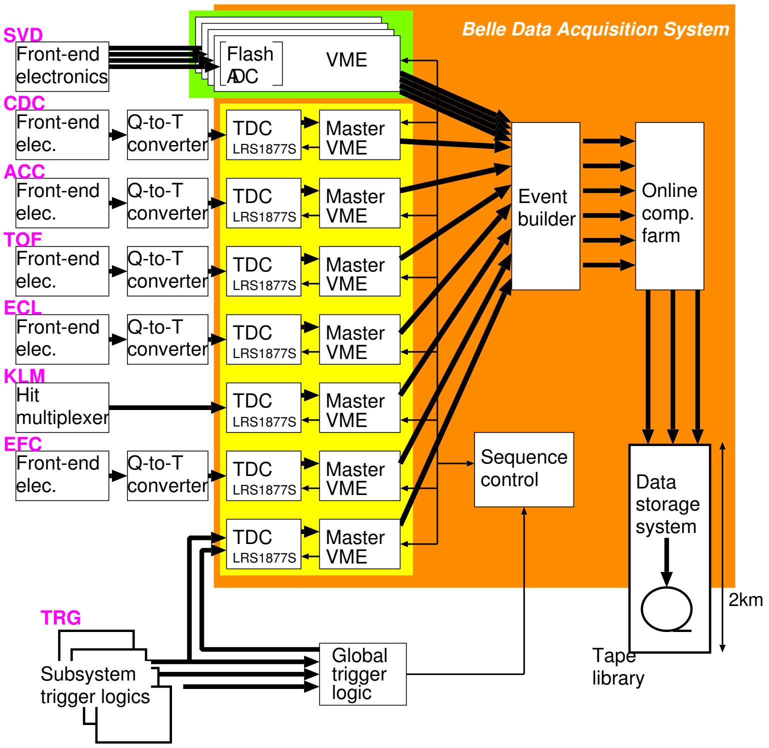

Figure 3.20: The DAQ system [77].

structed charged tracks, photon candidates from reconstructed clusters in the ECL and particle identification information.

A detailed description of the trigger and DAQ systems operated in the Belle experiment is given in References [87, 88, 89].

3.3.11 Illustration of a Reconstructed $B^0 \to D^{*\pm}D^{\mp}$ Event

As an example of the interplay of the individual subsystems of the Belle experiment, a hadronic event recorded by the detector is shown in Figure 3.21. The event contains a reconstructed $B^0 \to D^{*\pm}D^{\mp}$ candidate and is associated with a high signal probability. The signal decay has been reconstructed in the decay chain

$$
\begin{aligned}
&\qquad\quad D^+ \to K^-\pi^+\pi^+ \\
&B^0 \to D^{*-}D^+ \\
&\qquad D^{*-} \to \bar{D}^0\,\pi^-_{\mathrm{soft}} \\
&\qquad\qquad\ \bar{D}^0 \to K^+\pi^-\pi^0 \\
&\qquad\qquad\qquad\qquad \pi^0 \to \gamma\gamma,
\end{aligned}
$$

where the red and blue color denote the assignment tracks in the reconstruction to the detected final-state particles. Furthermore, the figure contains a visualisation of the recorded raw data such as the hits detected in the SVD, the drift times measured by the CDC and the energy deposit measured by the ECL.

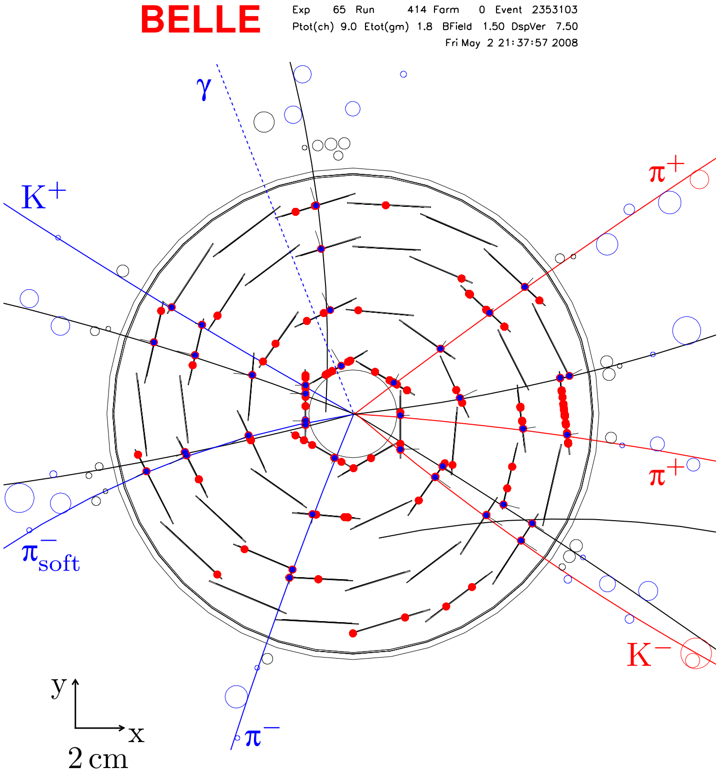

(a) Projection in xy of the SVD subdetector.

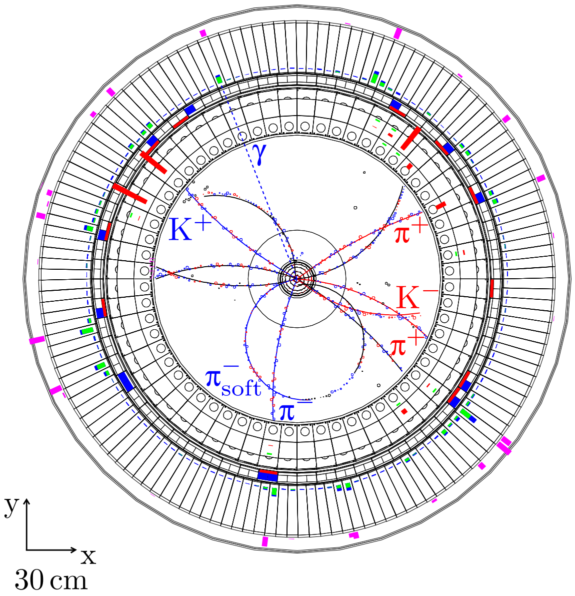

(b) Projection in xy of the ECL, CDC and SVD subdetectors.

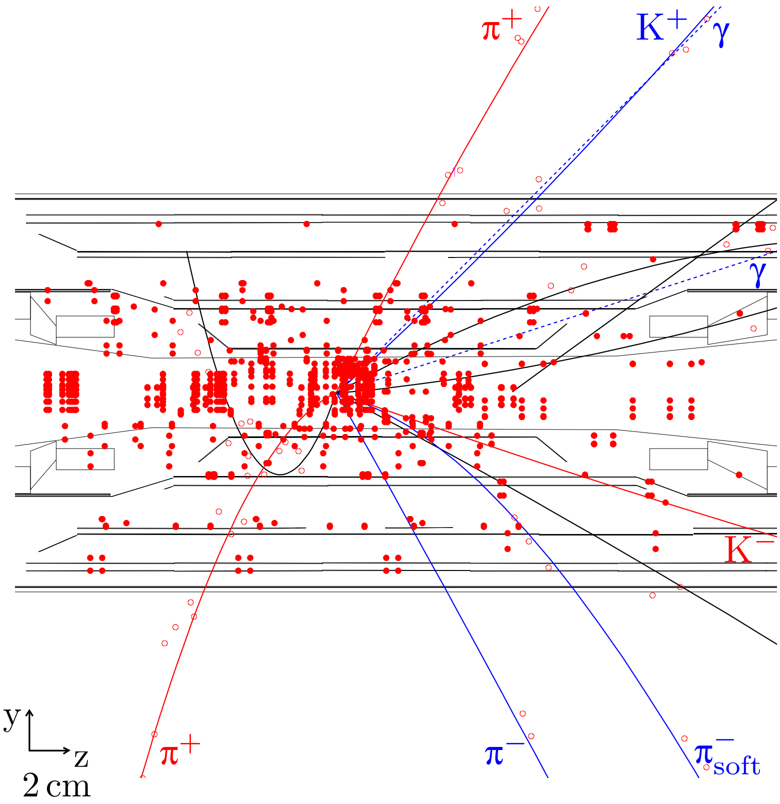

(c) Projection in yz of the SVD subdetector.

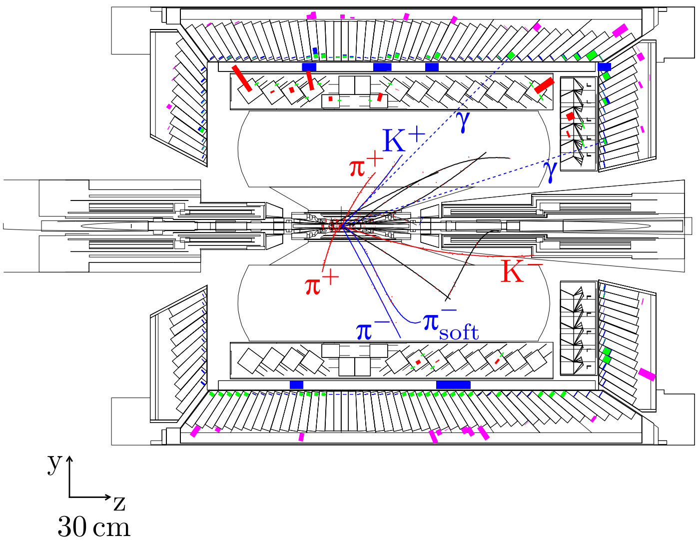

(d) Projection in yz of the ECL, CDC and SVD subdetectors.

Figure 3.21: Illustration of an event containing a $B^0 \to D^{*-}D^+ \to \left[\left(K^+\pi^-(\gamma\gamma)_{\pi^0}\right)_{\bar{D}^0}\ \pi^-_{\mathrm{soft}}\right]_{D^{*-}} (K^-\pi^+\pi^+)_{D^+}$ candidate associated with a high signal probability. The event has been recorded by the Belle detector on 2nd May 2008.

4 Analysis Methods

4.1 Vertex Reconstruction

The reconstruction of decay vertices is of substantial importance in time-dependent measurements. The time-dependent measurements at the B-factory experiments are performed by translating the difference of reconstructed decay vertices with the known Lorentz boost of the asymmetric energy e^+e^--colliders into a proper decay time difference of the two produced B mesons. See the illustration of the principle of time-dependent measurements in Figure 2.8.

In the following, the procedures to determine the vertex of the fully reconstructed meson on the signal-side, referred to as B_{rec}, and the vertex of the accompanying meson on the tagging-side, referred to as B_{tag}, are described.

On the signal-side decay chains such as below occur:

$$
\begin{aligned}
&\qquad\qquad\qquad K_S^0 \rightarrow \pi^+\pi^- \\
&\qquad\quad D^- \rightarrow K_S^0\pi^- \\
B_{rec} \rightarrow & D^{*+}D^- \\
&\quad D^{*+} \rightarrow D^0\pi^+_{soft} \\
&\qquad\qquad D^0 \rightarrow K^-\pi^+\pi^0 \\
&\qquad\qquad\qquad\qquad \pi^0 \rightarrow \gamma\gamma
\end{aligned}
\tag{4.1}
$$

To determine the decay vertex of the B_{rec} meson, the full decay chain is reconstructed from the right-hand side to the left. Starting with the final-state particles associated with measurements by the detector, e.g. charged kaons, charged pions or neutral particles such as photons, virtual particles such as π^0, K_S^0, D^0, D^-, D^{*+} and B_{rec} mesons are formed.

In the combination of virtual particles, information on their decay products has to be merged in a way that the original measurements and their uncertainties are propagated through the decay chain. Furthermore, in the combinations information is added by application of constraints that include knowledge of the underlying physical processes.

In the example of the decay chain given above, several constraints are applied:

1. The reconstruction of the decay vertex of a particle itself involves constraints by requiring that the daughter particles intersect at a common point in space.

2. For neutral particles with imprecise position information such as in reconstruction of π^0 mesons from two photons, constraints on invariant masses are applied in addition to vertex constraints. This improves the energy resolution of the reconstructed particles.

3. Particles such as soft pions from D^{*+} decays are constrained to pass through a previously

and independently determined vertex. This constraint improves the momentum resolution of the soft pion and consequently the resolution of the mass difference $\Delta M_{D^{*+}-D^{0/+}}$.

4. B mesons originate from the interaction region. Therefore the resolution of reconstructed B decay vertices can be improved by constraints that include information on the position of the interaction point.

4.1.1 Description of the Vertex Reconstruction Algorithm

The vertex reconstruction is realised by a kinematic fit in a least-squares approach that includes the constraints as Lagrange multipliers.

Assuming that constraints can be expressed in a set of r vanishing equations of the form $\mathbf{H}(\boldsymbol{\alpha},\mathbf{v}) = 0$, then a χ^2 function for a vertex constraint to an unknown position can be written generally as

$$\chi^2 = (\boldsymbol{\alpha}-\boldsymbol{\alpha}_0)^T \mathbf{V}_{\boldsymbol{\alpha}_0}^{-1}(\boldsymbol{\alpha}-\boldsymbol{\alpha}_0) + (\mathbf{v}-\mathbf{v}_0)^T \mathbf{V}_{\mathbf{v}_0}^{-1}(\mathbf{v}-\mathbf{v}_0) + \lambda^T \mathbf{H}(\boldsymbol{\alpha},\mathbf{v}), \tag{4.2}$$

where $\boldsymbol{\alpha} = (\boldsymbol{\alpha}_1,\boldsymbol{\alpha}_2,...,\boldsymbol{\alpha}_n)$ denotes a vector containing the parameters of n tracks and $\mathbf{v} = (\mathbf{v}_1,\mathbf{v}_2,\mathbf{v}_3)$ a vector of a common space point to which the tracks are required to pass. $\boldsymbol{\alpha}_0$ and $\mathbf{v}_0$ contain the initially unconstrained values and the matrices $\mathbf{V}_{\boldsymbol{\alpha}_0}$ and $\mathbf{V}_{\mathbf{v}_0}$ the corresponding covariances.
Depending on the form of $\mathbf{H}(\boldsymbol{\alpha},\mathbf{v})$, the Lagrange multipliers introduce non-linearities to the χ^2 function. An approach for finding a solution in that case is to linearise $\mathbf{H}(\boldsymbol{\alpha},\mathbf{v})$ and to solve the linearised approximation [90].

$\mathbf{H}(\boldsymbol{\alpha},\mathbf{v})$ can be linearised by expanding around $\boldsymbol{\alpha}_A$ and $\mathbf{v}_A$:

$$0 = \mathbf{H}(\boldsymbol{\alpha}_A,\mathbf{v}_A) + \left.\frac{\partial \mathbf{H}(\boldsymbol{\alpha},\mathbf{v})}{\partial \boldsymbol{\alpha}}\right|_{\substack{\boldsymbol{\alpha}=\boldsymbol{\alpha}_A \\ \mathbf{v}=\mathbf{v}_A}} (\boldsymbol{\alpha}-\boldsymbol{\alpha}_A) + \left.\frac{\partial \mathbf{H}(\boldsymbol{\alpha},\mathbf{v})}{\partial \mathbf{v}}\right|_{\substack{\boldsymbol{\alpha}=\boldsymbol{\alpha}_A \\ \mathbf{v}=\mathbf{v}_A}} (\mathbf{v}-\mathbf{v}_A) \tag{4.3}$$

$$= \mathbf{d} + \mathbf{D}\delta\boldsymbol{\alpha} + \mathbf{E}\delta\mathbf{v} \tag{4.4}$$

The overall χ^2 function then adopts the following form:

$$\chi^2 = (\boldsymbol{\alpha}-\boldsymbol{\alpha}_0)^T \mathbf{V}_{\boldsymbol{\alpha}_0}^{-1}(\boldsymbol{\alpha}-\boldsymbol{\alpha}_0) + (\mathbf{v}-\mathbf{v}_0)^T \mathbf{V}_{\mathbf{v}_0}^{-1}(\mathbf{v}-\mathbf{v}_0) + 2\lambda^T(\mathbf{D}\delta\boldsymbol{\alpha} + \mathbf{E}\delta\mathbf{v} + \mathbf{d}) \tag{4.5}$$

In the example of n charged particles in a solenoid magnetic field, the constraints can be derived from the equations of motion governed by the Lorentz force. In a helical track parameterisation, the position along the trajectory is not constrained and in this case two constraints per track would enter Equation 4.5 and reduce the number of unknowns by 2n.

Equation 4.5 can be solved analytically with respect to a minimum. But due to the linearisation of $\mathbf{H}(\boldsymbol{\alpha},\mathbf{v})$ the minimisation of the χ^2 has to be repeated iteratively by choosing suitable expansion points $\boldsymbol{\alpha}_A$ and $\mathbf{v}_A$ until a convergence is reached.

Detailed description of different constraints used in the vertex reconstruction and the derivation of solutions in terms of minima of χ^2 functions with respect to $\boldsymbol{\alpha}$ and $\mathbf{v}$ are given in Reference [91].

4.1.2 IP Tube Constraint

In the vertex reconstruction of B mesons constraints containing information about the interacting region such as the position and the profile of the interaction point (IP) are applied to improve the resolution.

The position and the profile of the IP is determined by combination of measurements on an event-by-event basis by the Belle detector and by information of the KEKB accelerator. In regular ranges of the order of 10^4 collected events, charged tracks passing the selection requirements for hadronic data are extrapolated to the IP position and monitors of the accelerator measure the beam spread. The uncertainty on the beam conditions by the accelerator is very low in y direction and very large in z direction. The IP profile is obtained by combining the above information in a 3-dimensional fit of a Gaussian. The IP profile is additionally smeared by 21 µm in the xy plane to account for the transverse decay length of B mesons. The typical resolutions are $\sigma_x \approx 100\,\mu\text{m}$, $\sigma_y \approx 5\,\mu\text{m}$ and $\sigma_z \approx 3\,\text{cm}$.

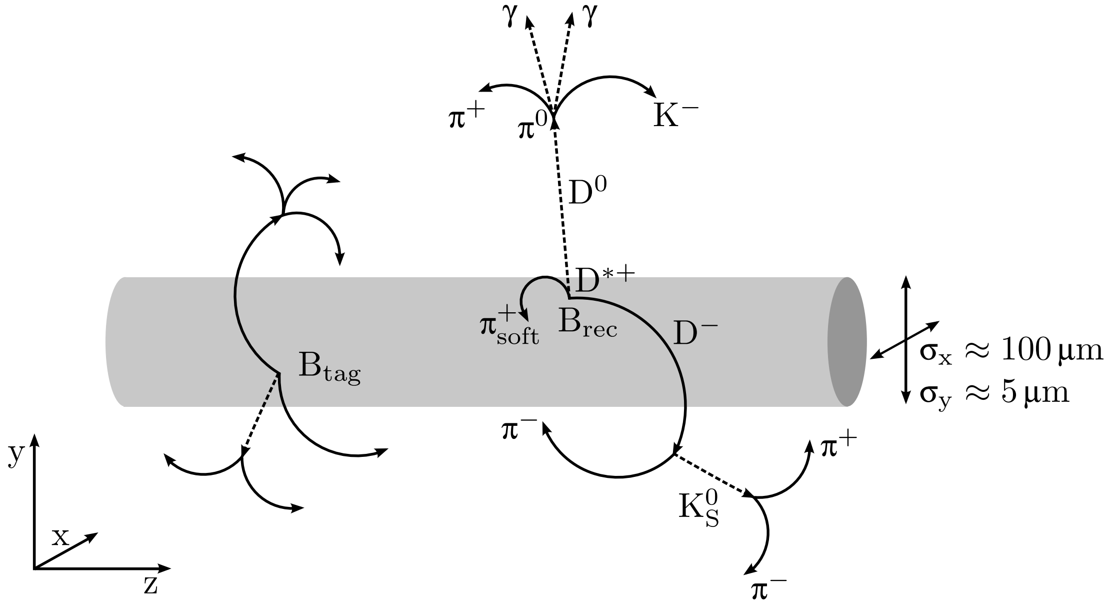

Figure 4.1: Illustration of the IP tube. In the reconstruction of B meson decay vertices a constraint along the beam axis with a Gaussian smearing in the transverse plan is applied to include information about the interaction region and consequently to improve the resolution.

In previous Belle measurements, a 3-dimensional Gaussian corresponding to the interaction point and its finite resolution represented by the IP profile were used as a constraint in the reconstruction of B meson vertices. This procedure caused a bias in the reconstructed Δz distributions. To avoid this bias, the constraint in z direction is loosened in the present analysis. The vertex position is constrained to a line along the beam axis with a Gaussian smearing in the transverse plane as illustrated in Figure 4.1. Due to its shape the constraint is called IP tube.

In addition, the constraint allows to reconstruct B meson decay vertices from single tracks.

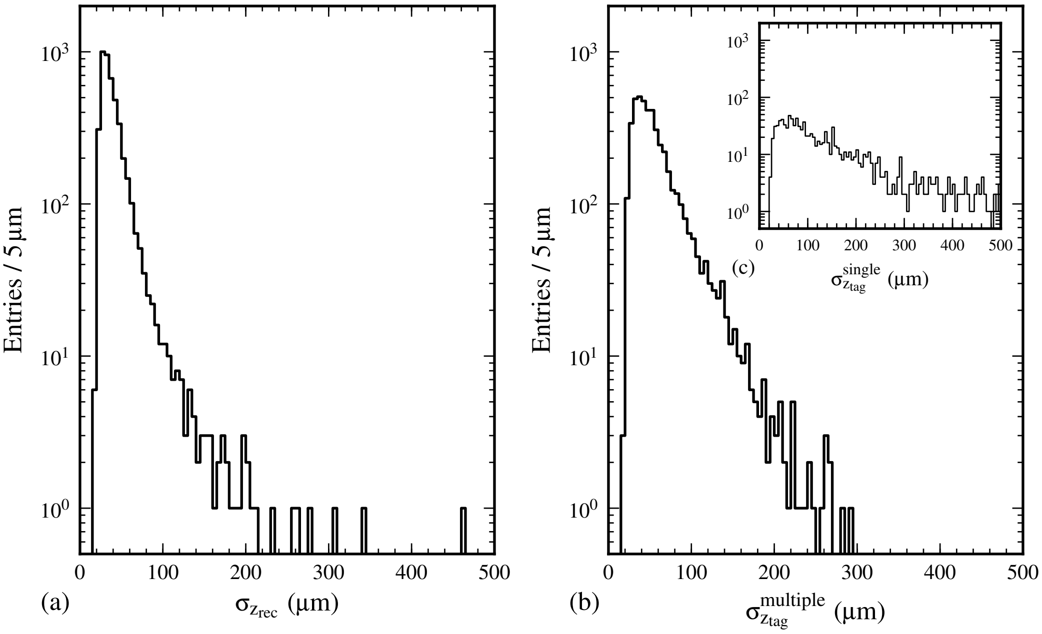

Figure 4.2: Distributions of the uncertainties σ_z of reconstructed decay vertices for (a) $B^0 \to D_s^+ D^-$ decays and (b) B_{tag} mesons on tagging-side obtained on data. The inset plot (c) shows the uncertainties of B_{tag} decay vertices reconstructed from single tracks.

In the present analysis, the inclusion of single track vertices results in a gain in efficiency of about 15%.

4.1.3 B Meson Vertex Reconstruction on Reconstruction- and on Tagging-side

The decay vertex of B_{rec} mesons on reconstruction-side is obtained by a kinematic fit of two D mesons to a common vertex with IP tube constraint applied. The reconstructed D mesons are required to have passed successfully a previous vertex fit as outlined in the example of a decay chain above. In case of $B^0 \to D^{*+} D^-$ decays, the D daughter of the D^{*+} is chosen as one of the two D mesons. Information from D^{*+} and soft pions from D^{*+} decays is neglected, because D^{*+} mesons decay almost instantaneously close to the B_{rec} vertex and the measurements of track parameters of the soft pions are associated with large uncertainties. The Δz resolution on reconstruction-side is approximately 70 µm. Figure 4.2(a) shows the distributions of uncertainties of reconstructed vertices on signal- and tagging-side for $B^0 \to D_s^+ D^-$ decays of the related control sample obtained on data.

The decay vertex of B_{tag} mesons on tagging-side is reconstructed in an inclusive approach by a kinematic fit to a common vertex of all remaining charged tracks which are not assigned to the B_{rec} meson. The selection of remaining tracks may contain tracks which originate from displaced vertices of long-living secondary particles. In an iterative approach, tracks which cause large χ^2 contributions are removed and the tagging-side vertex fit is repeated to reduce the effect of non-primary particles. On tagging-side, the IP tube constraint improves the resolution from approximately 180 µm to 130 µm. The resolution for vertices constructed by single tracks is approximately 270 µm. The distributions of uncertainties of vertices on tagging-side reconstructed from multiple and single tracks are shown in Figure 4.2(b) and (c).

4.1.4 Quality of Vertex Fits

The optimisation of a χ^2 condition does not only provide an estimator for the measured quantities, but the χ^2 value itself can be used to indicate the quality of the fit result. Under the assumption that the model is correct, the χ^2 value can be translated into a probability that the hypothesis would yield the measured quantities.

This information can be used to improve the model description of resolution effects. In Section 4.2 it is described, how the quality of the signal-side and tag-side vertex fits are included into the resolution functions and consequently provide a better modelling of the proper decay time difference distributions.

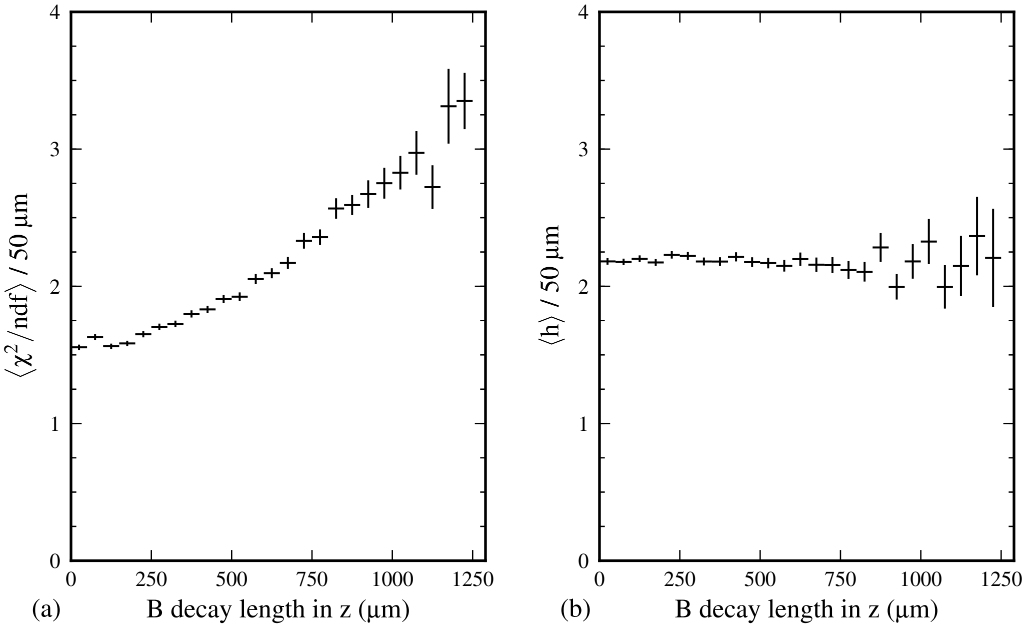

Figure 4.3: Distributions of the vertex fit quality indicators χ^2 and h as a function of the B decay length in z direction for simulated $B^0 \to D^+D^-$ decays.

Figure 4.3(a) shows the χ^2 dependence on the B decay length. The χ^2 exhibits a clear correlation with the decay length, which originates from the IP constraint in the transverse plane. If the χ^2 value would be used directly in the resolution functions, then the correlation would cause that long-living B mesons have on average larger χ^2 values and these events would enter the fit with a lower weight due to their worse resolution, compare Equation 4.9. Consequently in measurements of e.g. B meson lifetimes, the correlation would lead to a systematic bias towards smaller lifetimes than expected.

An uncorrelated quantity can be constructed by utilising the linearity of the χ^2 with respect to its individual contributions. By removing the contribution of the IP tube constraint, the reduced quantity, denoted by h, depends only on the contributions of the tracks:

$$\begin{aligned} \frac{1}{\mathrm{ndf}}\chi^2_{\mathrm{tracks}} &= \frac{1}{\mathrm{ndf}}\left(\chi^2_{\mathrm{vertex\,fit}} - \chi^2_{\mathrm{IP\,tube}}\right) \\ &\approx \frac{1}{2\,n_{\mathrm{trk}}-2}\sum_i \chi^2_{\mathrm{i\text{-}th\,track}} =: h \end{aligned} \tag{4.6}$$

The variable h is only defined for vertices reconstructed from multiple tracks and not for vertices reconstructed from single tracks.

Figure 4.3(b) shows the dependence of h on the B decay length. In contrast to the conventional χ^2 no correlation with the flight length can be found.

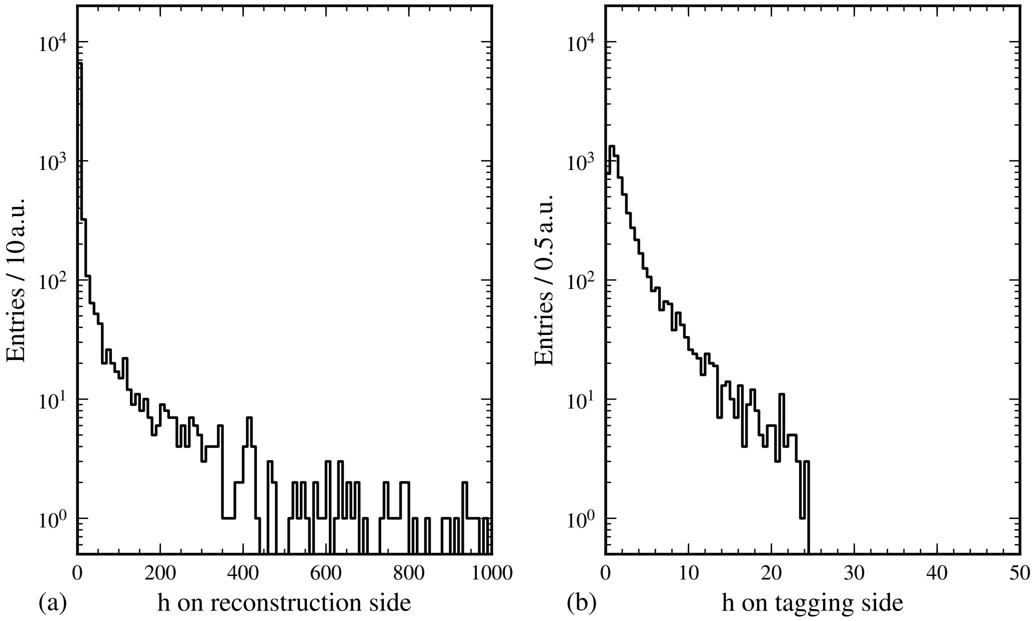

Figure 4.4: Distributions of vertex fit quality indicator h for decay vertices on reconstruction- and on tagging-side for simulated $B^0 \rightarrow D^+D^-$ decays.

The distributions of the vertex fit quality indicator h for vertices on signal- and tagging-side are shown in Figure 4.4. On tagging-side there is a cut at h = 25 visible, because the variable is used to reject tracks of long-living secondary particles.

4.2 Resolution Functions

Due to the low Lorentz boost of the asymmetric energy e^+e^--colliders, the spatial separation of B mesons created at the B factory experiments is of the same order as the resolution of the reconstructed decay length differences. As a consequence the understanding and the model description of experimental resolution effects is essential for time-dependent measurements.

In the following, a detailed summary of the modelling of resolution effects is given. The summary follows partly discussions in References [92, 93], but provides a full description of the improved resolution functions developed at the Belle experiment in the year 2011. It focuses on functions and parameters relevant for the time-dependent measurements performed in the present analysis and gives examples obtained from $B^0 \rightarrow D^+D^-$ decays. The numerical values of all resolution function parameters are summarised in Table 4.1.

The signal probability density function $\mathcal{P}_{sig}$ entering the likelihood function in time-dependent measurements is the convolution of a probability density function P_{sig}, that describes the decay time difference distribution of the physical process, with a resolution function $\mathcal{R}_{sig}$,

$$\mathcal{P}_{sig}(\Delta t) = \int_{-\infty}^{+\infty} P_{sig}(\Delta t')\, \mathcal{R}_{sig}(\Delta t - \Delta t')\, d(\Delta t'). \tag{4.7}$$

The resolution function $\mathcal{R}_{sig}$ is composed of the convolution of four different contributions,

$$\begin{aligned}\mathcal{R}_{sig}(\Delta t) = \iiint_{-\infty}^{+\infty} & \mathcal{R}_{det}^{rec}(\Delta t - \Delta t')\, \mathcal{R}_{det}^{tag}(\Delta t' - \Delta t'') \\ & \mathcal{R}_{np}(\Delta t'' - \Delta t''')\, \mathcal{R}_{k}(\Delta t''')\, d(\Delta t')d(\Delta t'')d(\Delta t''').\end{aligned} \tag{4.8}$$

The functions $\mathcal{R}_{det}^{rec}$ and $\mathcal{R}_{det}^{tag}$ model the detector resolution, which affect the measurements of B meson decay vertices on reconstruction- and on tagging-side. $\mathcal{R}_{np}$ accounts for a smearing occurring in the vertex reconstruction on tagging-side that is caused by the inclusion of tracks that originate from long-living secondary particles, e.g. from K_S^0 mesons or charm decays. The term $\mathcal{R}_k$ takes into account the kinematic approximation that the B mesons are in rest in the center-of-mass system.

4.2.1 Detector Resolution

The finite resolution of the detector in particular of that components involved in the track reconstruction cause a broadening in the measurement of decay vertices on reconstruction-side z_{rec} and on tagging-side z_{tag}.

The $\delta z_{rec} = z_{rec}^{fit} - z_{rec}^{gen}$ residual vertex distribution of simulated $B^0 \rightarrow D^+D^-$ decays and the projection of a fit of the sum of two Gaussian functions with constant width is shown in Figure 4.5(a). The Gaussian functions do not describe the residual distributions properly. As a consequence the detector resolution function $\mathcal{R}_{det}$ is formulated in an approach, in which the resolution is parameterised by usage of event-by-event information.

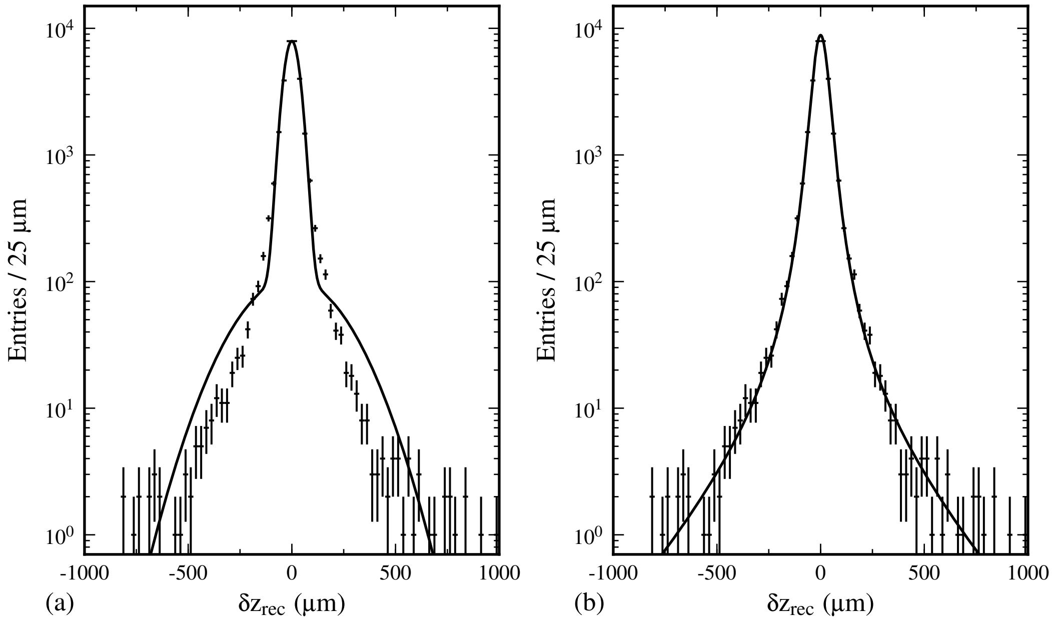

Figure 4.5: Residual distribution for vertices on reconstruction-side and projections of (a) the fit of the sum of two Gaussian functions and (b) the detector resolution function $\mathcal{R}_{\mathrm{det}}^{\mathrm{rec}}$ for simulated $\mathrm{B}^0 \to \mathrm{D}^+\mathrm{D}^-$ decays.

The dependence of the $\left(z^{\mathrm{fit}} - z^{\mathrm{gen}}\right)/\sigma^{z_{\mathrm{fit}}}$ pull distributions on the vertex fit quality indicator h reconstructed from multiple tracks for several decay modes is shown in Figure 4.6(a) and the dependence on tagging-side is shown in Figure 4.6(b). The pull distributions for similar values of the vertex fit quality indicator h can be parameterised by a single Gaussian distribution. In addition, the widths of the pull distributions exhibit a linear dependence on h. Therefore the detector resolution function $\mathcal{R}_{\mathrm{det}}^{\mathrm{q,multiple}}$ for vertices reconstructed from multiple tracks is parameterised as

$$\mathcal{R}_{\mathrm{det}}^{\mathrm{q,multiple}}\left(\delta z_{\mathrm{q}}\right) = \mathcal{G}\left(\delta z_{\mathrm{q}};\, \left(s_{\mathrm{q}}^{0} + s_{\mathrm{q}}^{1} h\right) \sigma_{z_{\mathrm{q}}}\right) \qquad \text{with } \mathrm{q} \in \{\mathrm{rec}, \mathrm{tag}\}. \tag{4.9}$$

The scale factor s_{q}^{0} is in the ideal case equal to one, but can adopt different values due to experimental inaccuracies, e.g. caused by non-Gaussian uncertainty distributions of the helix parameters. The scale factor s_{q}^{1} is given by the slope of the linear dependence of the vertex fit uncertainties $\sigma_{z_{\mathrm{fit}}}$ on h.

In earlier implementations of resolution functions at the Belle experiment, different vertex fit quality indicator quantities were used. In these implementations, the linear relation was dependent on the reconstructed decay mode and thus required different scale factors. In the present implementation, the resolution functions parameterised by the vertex fit quality indicator h are independent of the reconstructed decay mode. This is demonstrated in Figure 4.6(a) by the similar linear dependence of the pull distributions for $\mathrm{B}^0 \to \mathrm{D}^+\mathrm{D}^-$, $\mathrm{B}^0 \to \mathrm{D}^{*+}\mathrm{D}^-$, $\mathrm{B}^0 \to \mathrm{D}^{*+}\mathrm{D}^{*-}$ and $\mathrm{B}^0 \to \pi^+\pi^-$ decays.

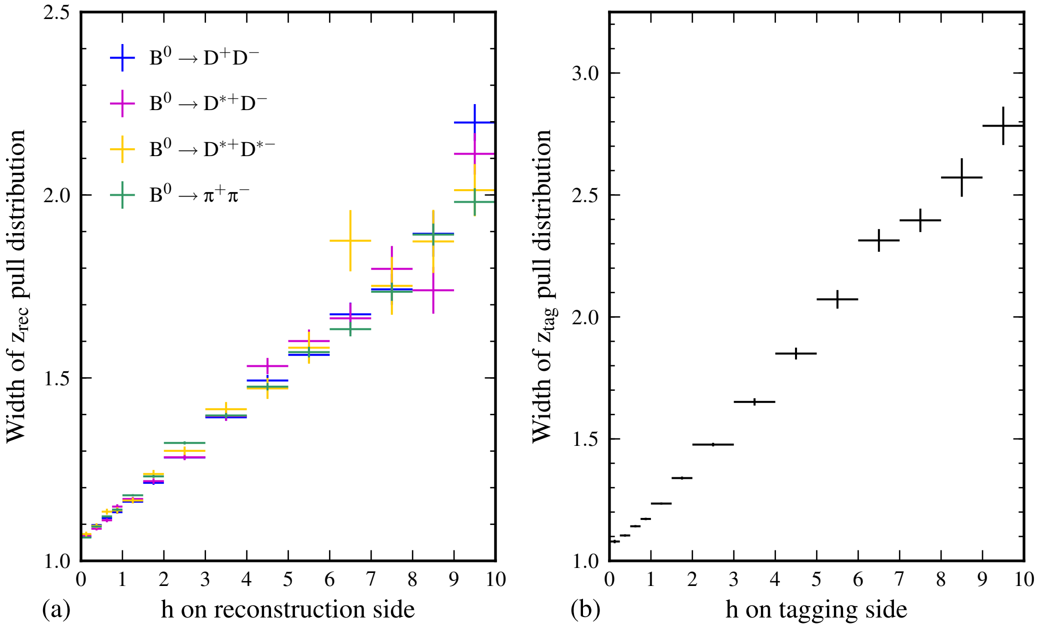

Figure 4.6: Dependence of the $\left(z_{\text{fit}} - z_{\text{gen}}\right)/\sigma_{z_{\text{fit}}}$ pull distributions on the vertex fit quality indicator h for vertices on (a) reconstruction- and on (b) tagging-side. The left plot demonstrates that the resolution model is independent of the particular reconstructed decay mode.

The residual vertex distributions on reconstruction- and on tagging-side and the corresponding projections of the resolution functions $\mathcal{R}_{\text{det}}^{\text{rec,multiple}}$ and $\mathcal{R}_{\text{det}}^{\text{tag,multiple}}$ are shown in Figure 4.5(b) and Figure 4.7(a). In the latter, the distributions are obtained from Monte Carlo simulations, in which long-living secondary particles are required to decays instantaneously to avoid smearing effects caused by the inclusion of non-primary tracks to the tag-side vertex reconstruction. In both examples, the detector resolution function as defined in Equation 4.9 describes accurately the experimental distributions. The detector resolution on the reconstruction-side is approximately 70 µm. The detector resolution on the tagging-side for vertices reconstructed from multiple tracks without the effect of smearing due to non-primary tracks is approximately 100 µm.

For decay vertices reconstructed from single tracks, the vertex fit quality indicator h is not defined. In the present analysis, single track vertices are used only on the tagging-side. The resolution function $\mathcal{R}_{\text{det}}^{\text{tag,single}}$ is parameterised by the sum of Gaussian functions with a width that has a linear dependence on the vertex fit uncertainty $\sigma_{z_{\text{tag}}}$,

$$\begin{aligned}\mathcal{R}_{\text{det}}^{\text{tag,single}}\left(\delta z_{\text{tag}}\right) = \left(1 - f_{\text{tag}}^{\text{tail}}\right) \mathcal{G}\left(\delta z_{\text{tag}};\, s_{\text{tag}}^{\text{main}}\, \sigma_{z_{\text{tag}}}\right) \\ + f_{\text{tag}}^{\text{tail}}\, \mathcal{G}\left(\delta z_{\text{tag}};\, s_{\text{tag}}^{\text{tail}}\, \sigma_{z_{\text{tag}}}\right).\end{aligned} \tag{4.10}$$

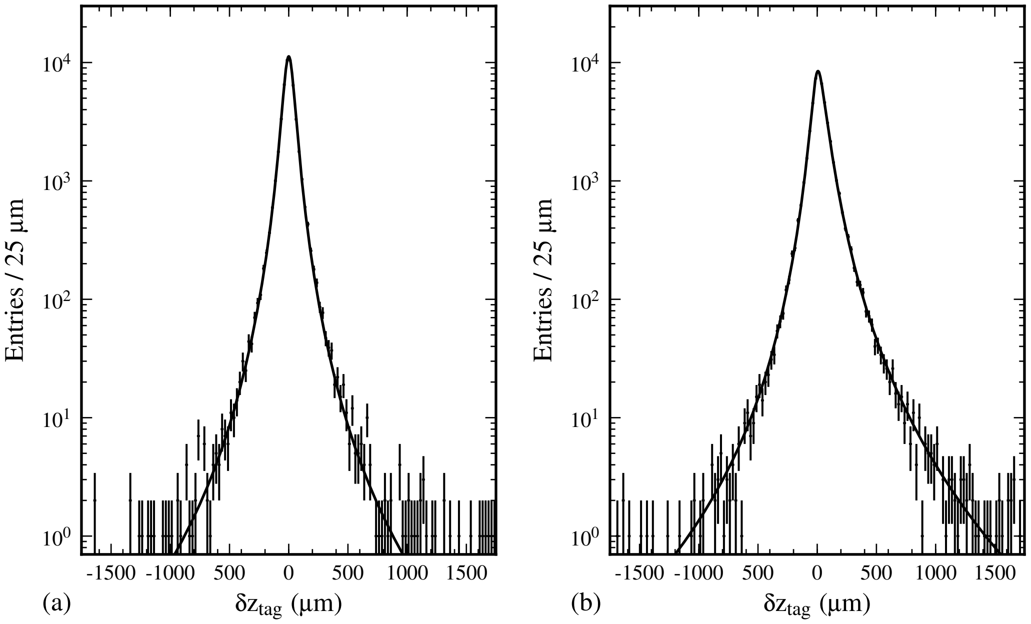

Figure 4.7: Residual distributions and projections of the detector resolution function (a) $\mathcal{R}_{\mathrm{det}}^{\mathrm{tag}}$ and (b) the convolution $\mathcal{R}_{\mathrm{det}}^{\mathrm{tag}} \otimes \mathcal{R}_{\mathrm{np}}$ for simulated $B^0 \to D^+D^-$ decays. The left figure has been generated by special Monte Carlo simulations in which secondary particles are required to decay instantaneously. In comparison with the right figure, the effect of non-primary tracks on the tag-side vertex reconstruction becomes apparent in the larger and asymmetric tails.

4.2.2 Smearing due to Non-Primary Tracks

The inclusion of charged tracks that originate from decays of long-living particles, such as K_S^0 mesons or particles with charm-quark content, causes a smearing in the reconstruction of the vertex of the B_{tag} meson on the tagging-side. This effect is studied by Monte Carlo simulations, in which all secondary particles are required to decay instantaneously. The residual distributions obtained from such simulations is shown in Figure 4.7(a). In contrast, the distributions from simulations containing long-living non-primary tracks show larger and asymmetric tails as shown in Figure 4.7(b). The smearing reduces the resolution for vertices reconstructed on the tagging-side from approximately 100 µm to 130 µm.

The resolution function $\mathcal{R}_{\mathrm{np}}$, that accounts for the smearing effect due to the inclusion of non-primary tracks, is composed of a prompt component modelled by a Dirac δ-function and a non-prompt component,

$$\begin{aligned}\mathcal{R}_{\mathrm{np}}\left(\delta z_{\mathrm{tag}}\right) &= f_\delta\, \delta^{\mathrm{Dirac}}\left(\delta z_{\mathrm{tag}}\right) \\ &\quad + (1-f_\delta)\left[f_p\, E_p\left(z_{\mathrm{tag}};\, c\,(\beta\gamma)_{\Upsilon(4S)}\, \tau_{\mathrm{np}}^{p}\right) + \left(1-f_p\right) E_n\left(z_{\mathrm{tag}};\, c\,(\beta\gamma)_{\Upsilon(4S)}\, \tau_{\mathrm{np}}^{n}\right)\right].\end{aligned} \tag{4.11}$$

The fraction f_δ of the prompt and the fraction f_p of the non-prompt components are fixed to constant values. Their values depend on the presence of a high momentum lepton detected in the flavor tagging procedure. The non-prompt component allows for lifetime effects and is modelled asymmetrically by the exponential functions E_p and E_n:

$$E_p(x;\tau) = \begin{cases} \frac{1}{\tau} e^{-\frac{x}{\tau}} & \text{if } x > 0 \\ 0 & \text{if } x \leq 0 \end{cases} \tag{4.12}$$

$$E_n(x;\tau) = \begin{cases} 0 & \text{if } x > 0 \\ \frac{1}{\tau} e^{+\frac{x}{\tau}} & \text{if } x \leq 0 \end{cases} \tag{4.13}$$

For decay vertices reconstructed from multiple tracks, the effective lifetimes are given by combinations of event-by-event vertex information such as h and $\sigma_{z_{tag}}$ and a global scaling factor s_{np}^{global}:

$$\tau_{np}^{p} = s_{np}^{global}\left[\tau_p^0 + \tau_p^1 \frac{\sigma_{z_{tag}}}{c(\beta\gamma)_{\Upsilon(4S)}} + \tau_p^2 h_{tag} + \tau_p^3 \frac{\sigma_{z_{tag}}}{c(\beta\gamma)_{\Upsilon(4S)}} h_{tag}\right] \tag{4.14}$$

$$\tau_{np}^{n} = s_{np}^{global}\left[\tau_n^0 + \tau_n^1 \frac{\sigma_{z_{tag}}}{c(\beta\gamma)_{\Upsilon(4S)}} + \tau_n^2 h_{tag} + \tau_n^3 \frac{\sigma_{z_{tag}}}{c(\beta\gamma)_{\Upsilon(4S)}} h_{tag}\right] \tag{4.15}$$

For vertices reconstructed from single tracks the model is simplified by assuming constant effective lifetimes τ_{np}^{p} and τ_{np}^{n}.

In Figure 4.7(b) the projection of the convolution $\mathcal{R}_{det}^{tag} \otimes \mathcal{R}_{np}$ on the residual vertex distributions is shown for simulated $B^0 \to D^+D^-$ decays.

4.2.3 Kinematic Approximation

The calculation of the proper decay time difference from reconstructed decay length differences and the Lorentz boost of the $\Upsilon(4S)$, given by $\Delta t = \frac{z_{rec}-z_{tag}}{c(\beta\gamma)_{\Upsilon(4S)}}$, neglects the small but non-zero momentum of the two B mesons in the center-of-mass frame. A resolution function $\mathcal{R}_k$ which accounts for this effect can be derived from the two body kinematics of $\Upsilon(4S)$ decays.

The difference of Δt from the true proper decay time difference $\Delta t_{true} = t_{rec} - t_{tag}$ is given by

$$\begin{aligned} x &= \Delta t - \Delta t_{true} \\ &= \frac{z_{rec} - z_{tag}}{c(\beta\gamma)_{\Upsilon(4S)}} - \left(t_{rec} - t_{tag}\right) \\ &= \frac{c(\beta\gamma)_{B_{rec}} t_{rec} - c(\beta\gamma)_{B_{tag}} t_{tag}}{c(\beta\gamma)_{\Upsilon(4S)}} - \left(t_{rec} - t_{tag}\right) \\ &= \left[\frac{(\beta\gamma)_{B_{rec}}}{(\beta\gamma)_{\Upsilon(4S)}}\right] t_{rec} + \left[\frac{(\beta\gamma)_{B_{tag}}}{(\beta\gamma)_{\Upsilon(4S)}}\right] t_{tag}. \end{aligned} \tag{4.16}$$

The Lorentz boost factors $(\beta\gamma)_{B_{rec}}$ and $(\beta\gamma)_{B_{tag}}$ of the mesons on the reconstruction-side B_{rec}

and on the tagging-side $\mathrm{B_{tag}}$ are related to the Lorentz boost factor $(\beta\gamma)_{\Upsilon(4S)}$ of the $\Upsilon(4S)$ by

$$\begin{aligned}
(\beta\gamma)_{\mathrm{B_{rec}}} &= \frac{(\beta\gamma)_{\Upsilon(4S)}\,E^{\mathrm{cms}}_{\mathrm{B_{rec}}} + (\gamma)_{\Upsilon(4S)}\,p^{\mathrm{cms}}_{\mathrm{B_{rec}}}\cos\theta^{\mathrm{cms}}_{\mathrm{B_{rec}}}}{m_B} \\
&= (\beta\gamma)_{\Upsilon(4S)}\left(\frac{E^{\mathrm{cms}}_{\mathrm{B_{rec}}}}{m_B} + \frac{p^{\mathrm{cms}}_{\mathrm{B_{rec}}}\cos\theta^{\mathrm{cms}}_{\mathrm{B_{rec}}}}{(\beta)_{\Upsilon(4S)}\,m_B}\right) \\
&=: (\beta\gamma)_{\Upsilon(4S)}\,(a_k + c_k) \qquad (4.17)\\
\text{and}\quad (\beta\gamma)_{\mathrm{B_{tag}}} &= (\beta\gamma)_{\Upsilon(4S)}\left(\frac{E^{\mathrm{cms}}_{\mathrm{B_{rec}}}}{m_B} - \frac{p^{\mathrm{cms}}_{\mathrm{B_{rec}}}\cos\theta^{\mathrm{cms}}_{\mathrm{B_{rec}}}}{(\beta)_{\Upsilon(4S)}\,m_B}\right) \\
&=: (\beta\gamma)_{\Upsilon(4S)}\,(a_k - c_k)\,, \qquad (4.18)
\end{aligned}$$

where $E^{\mathrm{cms}}_{\mathrm{B_{rec}}} \approx 5.292\,\mathrm{GeV}$, $p^{\mathrm{cms}}_{\mathrm{B_{rec}}} \approx 0.340\,\mathrm{GeV/c}$ and $\cos\theta^{\mathrm{cms}}_{\mathrm{B_{rec}}}$ denote the energy, the momentum and the cosine of the angle with respect to the beam axis of the reconstructed meson $\mathrm{B_{rec}}$ in the center-of-mass frame.

By applying the relations in Equations 4.17 and 4.18 to Equation 4.16, the difference $x = \Delta t - \Delta t_{\mathrm{true}}$ can be expressed as

$$x = (a_k + c_k - 1)\,t_{\mathrm{rec}} - (a_k - c_k - 1)\,t_{\mathrm{tag}}. \qquad (4.19)$$

If a probability density function $f\left(t_{\mathrm{rec}}, t_{\mathrm{tag}}\right)$ for obtaining t_{rec} and t_{tag} simultaneously can be generally written as

$$f\left(t_{\mathrm{rec}}, t_{\mathrm{tag}}\right) = \frac{1}{\tau_B^2}\,e^{-\frac{t_+}{\tau_B}}\,g(t_-)\,, \qquad (4.20)$$

where $t_+ = t_{\mathrm{rec}} + t_{\mathrm{tag}}$ is the sum of proper decay times, $t_- = t_{\mathrm{rec}} - t_{\mathrm{tag}}$ is the difference of proper decay times, and $g(t_-)$ denotes any function depending on the proper decay time difference, then the probability density $F(x, \Delta t_{\mathrm{true}})$ for obtaining both x and Δt_{true} simultaneously is given by

$$\begin{aligned}
F(x, \Delta t_{\mathrm{true}}) &= \int_0^{+\infty}\!\!\int_0^{+\infty} f\left(t_{\mathrm{rec}}, t_{\mathrm{tag}}\right)\,\delta^{\mathrm{Dirac}}\left(\Delta t_{\mathrm{true}} - \left(t_{\mathrm{rec}} - t_{\mathrm{tag}}\right)\right) \\
&\qquad \delta^{\mathrm{Dirac}}\left(x - \left[(a_k + c_k - 1)\,t_{\mathrm{rec}} - (a_k - c_k - 1)\,t_{\mathrm{tag}}\right]\right)\,dt_{\mathrm{rec}}\,dt_{\mathrm{tag}} \\
&= \int_{-\infty}^{+\infty}\!\!\int_{|t_-|}^{+\infty} \frac{1}{2}\,\frac{1}{\tau_B^2}\,e^{-\frac{t_+}{\tau_B}}\,g(t_-)\,\delta^{\mathrm{Dirac}}(\Delta t_{\mathrm{true}} - t_-)\,\delta^{\mathrm{Dirac}}\left(x - \left[(a_k - 1)\,t_- + c_k\,t_+\right]\right)\,dt_+\,dt_-.
\end{aligned}$$

The probability density $F(\Delta t_{\mathrm{true}})$ for obtaining Δt_{true} is

$$\begin{aligned}
F(\Delta t_{\mathrm{true}}) &= \int_0^{+\infty}\!\!\int_0^{+\infty} f\left(t_{\mathrm{rec}}, t_{\mathrm{tag}}\right)\,\delta^{\mathrm{Dirac}}\left(\Delta t_{\mathrm{true}} - \left(t_{\mathrm{rec}} - t_{\mathrm{tag}}\right)\right)\,dt_{\mathrm{rec}}\,dt_{\mathrm{tag}} \\
&= \int_{-\infty}^{+\infty}\!\!\int_{|t_-|}^{+\infty} \frac{1}{2}\,\frac{1}{\tau_B^2}\,e^{-\frac{t_+}{\tau_B}}\,g(t_-)\,\delta^{\mathrm{Dirac}}(\Delta t_{\mathrm{true}} - t_-)\,dt_+\,dt_-.
\end{aligned}$$

The resolution function $\mathcal{R}_k(x)$ accounting for the kinematic approximation is defined by the conditional probability for obtaining x at given Δt_{true}.

Using $\mathcal{R}_k(x) = F(x, \Delta t_{true}) / F(\Delta t_{true})$, $\mathcal{R}_k(x)$ can be expressed as

$$\mathcal{R}_k(x) = \begin{cases} E_p\left(x - \left[(a_k - 1)\Delta t_{true}\right] + c_k|\Delta t_{true}|;\, \tau_B|c_k|\right) & \text{if } \cos\theta^{cms}_{B_{rec}} > 0 \\ \delta^{Dirac}\left(x - (a_k - 1)\Delta t_{true}\right) & \text{if } \cos\theta^{cms}_{B_{rec}} = 0 \\ E_n\left(x - \left[(a_k - 1)\Delta t_{true}\right] + c_k|\Delta t_{true}|;\, \tau_B|c_k|\right) & \text{if } \cos\theta^{cms}_{B_{rec}} < 0. \end{cases} \tag{4.21}$$

The distribution of $x = \Delta t - \Delta t_{true}$ and the projection of the resolution function $\mathcal{R}_k(x)$ for simulated $B^0 \to D^+D^-$ decays is shown in Figure 4.8. The resolution due to the kinematic approximation is about 35 μm.

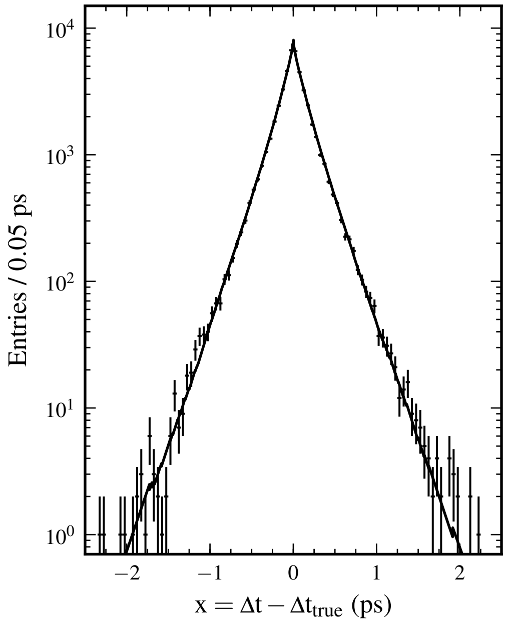

Figure 4.8: Distribution of $x = \Delta t - \Delta t_{true}$ and projection of the resolution function $\mathcal{R}_k$ for simulated $B^0 \to D^+D^-$ decays.

The convolution of a true probability density function $P(\Delta t_{true})$ with the resolution function $\mathcal{R}_k(x = \Delta t - \Delta t_{true})$ results in the expected theoretical Δt distribution $P(\Delta t)$. For example in a lifetime measurement, the exponential probability density function is then

$$P(\Delta t, \tau_B) = \begin{cases} \frac{1}{2a_k\tau_B} e^{-\frac{|\Delta t|}{(a_k+c_k)\tau_B}} & \text{if } \Delta t \geq 0 \\ \frac{1}{2a_k\tau_B} e^{-\frac{|\Delta t|}{(a_k-c_k)\tau_B}} & \text{if } \Delta t < 0. \end{cases} \tag{4.22}$$

The resolution function $\mathcal{R}_k$ in Equation 4.21 can be applied to any probability density function that can be written in the form in Equation 4.20. This includes the probability density functions describing the distributions of physical processes in lifetime, $B^0\bar{B}^0$ oscillation frequency or CP violation measurements. Because $\mathcal{R}_{\mathrm{k}}$ can be calculated analytically once one B is fully reconstructed, it does not require additional resolution function parameters.

	Monte Carlo Simulation		Data	
Parameter	SVD1	SVD2	SVD1	SVD2
$s_{\rm rec}^{0}$	+0.96	+0.93	$+0.70^{+0.19}_{-0.11}$	$+0.81^{+0.27}_{-0.15}$
$s_{\rm rec}^{1}$	+0.20	+0.21	$+0.21^{+0.04}_{-0.05}$	$+0.23^{+0.07}_{-0.05}$
$s_{\rm tag}^{0}$	+0.73	+0.82	$+0.48^{+0.28}_{-0.08}$	$+0.64^{+0.39}_{-0.07}$
$s_{\rm tag}^{1}$	+0.17	+0.14	$+0.24^{+0.04}_{-0.06}$	$+0.23^{+0.03}_{-0.05}$
$s_{\rm np}^{\rm global}$	+1.00	+1.00	$+1.06^{+0.12}_{-0.17}$	$+1.01^{+0.08}_{-0.16}$
$s_{\rm tag}^{\rm main}$	+1.11	+1.05	$+0.98^{+0.28}_{-0.04}$	$+1.01^{+0.44}_{-0.04}$
$s_{\rm tag}^{\rm tail}$	+1.00	+4.32	$+1.00^{+0.00}_{+0.00}$	$+3.66^{+3.61}_{-0.39}$
$f_{\rm tag}^{\rm tail}$	+0.00	+0.07	$+0.00^{+0.00}_{+0.00}$	$+0.11^{+0.02}_{-0.04}$
$f_{\delta}^{0,\,\rm single}$	+0.78	+0.77	$+0.78^{+0.01}_{-0.01}$	$+0.77^{+0.01}_{-0.01}$
$f_{\delta}^{1,\,\rm single}$	+1.00	+1.00	$+1.00^{+0.00}_{+0.00}$	$+1.00^{+0.00}_{+0.00}$
$f_{\rm p}^{0,\,\rm single}$	+0.82	+0.80	$+0.82^{+0.02}_{-0.02}$	$+0.80^{+0.02}_{-0.02}$
$f_{\rm p}^{1,\,\rm single}$	+0.85	+0.83	$+0.85^{+0.02}_{-0.02}$	$+0.83^{+0.04}_{-0.04}$
$\tau_{\rm p}^{0,\,\rm single}$ (ps)	+1.85	+1.63	$+1.85^{+0.09}_{-0.08}$	$+1.63^{+0.05}_{-0.05}$
$\tau_{\rm n}^{0,\,\rm single}$ (ps)	+2.04	+0.92	$+2.04^{+0.28}_{-0.24}$	$+0.92^{+0.08}_{-0.08}$
$f_{\delta}^{0,\,\rm multiple(0)}$	+0.47	+0.56	$+0.47^{+0.04}_{-0.04}$	$+0.56^{+0.01}_{-0.01}$
$f_{\delta}^{0,\,\rm multiple(1)}$	+0.64	+0.75	$+0.64^{+0.04}_{-0.04}$	$+0.75^{+0.01}_{-0.01}$
$f_{\delta}^{1,\,\rm multiple(0)}$	+0.27	+0.16	$+0.27^{+0.07}_{-0.07}$	$+0.16^{+0.03}_{-0.03}$
$f_{\delta}^{1,\,\rm multiple(1)}$	+0.31	+0.19	$+0.31^{+0.07}_{-0.07}$	$+0.19^{+0.03}_{-0.03}$
$f_{\delta}^{2,\,\rm multiple(0)}$	−0.22	−0.20	$-0.22^{+0.02}_{-0.02}$	$-0.20^{+0.00}_{-0.00}$
$f_{\delta}^{2,\,\rm multiple(1)}$	−0.18	−0.19	$-0.18^{+0.02}_{-0.01}$	$-0.19^{+0.00}_{-0.00}$
$f_{\delta}^{3,\,\rm multiple(0)}$	+0.22	+0.23	$+0.22^{+0.03}_{-0.03}$	$+0.23^{+0.01}_{-0.01}$
$f_{\delta}^{3,\,\rm multiple(1)}$	+0.20	+0.23	$+0.20^{+0.03}_{-0.03}$	$+0.23^{+0.01}_{-0.01}$
$f_{\rm n}^{\rm multiple}$	+0.12	+0.12	$+0.12^{+0.01}_{-0.01}$	$+0.12^{+0.00}_{-0.00}$
$f_{\rm p}^{\rm multiple}$	+0.14	+0.12	$+0.14^{+0.01}_{-0.01}$	$+0.12^{+0.00}_{-0.00}$
$\tau_{\rm p}^{0,\,\rm multiple}$ (ps)	−0.01	+0.04	$-0.01^{+0.02}_{-0.02}$	$+0.04^{+0.01}_{-0.01}$
$\tau_{\rm p}^{1,\,\rm multiple}$ (ps)	+0.72	+0.77	$+0.72^{+0.04}_{-0.04}$	$+0.77^{+0.02}_{-0.02}$
$\tau_{\rm p}^{2,\,\rm multiple(0)}$ (ps)	−0.03	−0.03	$-0.03^{+0.01}_{-0.01}$	$-0.03^{+0.00}_{-0.00}$
$\tau_{\rm p}^{2,\,\rm multiple(1)}$ (ps)	−0.03	−0.02	$-0.03^{+0.00}_{-0.00}$	$-0.02^{+0.00}_{-0.00}$
$\tau_{\rm p}^{3,\,\rm multiple(0)}$ (ps)	+0.25	+0.32	$+0.25^{+0.01}_{-0.01}$	$+0.32^{+0.01}_{-0.01}$
$\tau_{\rm p}^{3,\,\rm multiple(1)}$ (ps)	+0.24	+0.28	$+0.24^{+0.01}_{-0.01}$	$+0.28^{+0.01}_{-0.01}$
$\tau_{\rm p}^{0,\,\rm multiple}$ (ps)	+0.05	+0.08	$+0.05^{+0.03}_{-0.03}$	$+0.08^{+0.01}_{-0.01}$
$\tau_{\rm p}^{1,\,\rm multiple}$ (ps)	+0.52	+0.53	$+0.52^{+0.06}_{-0.06}$	$+0.53^{+0.03}_{-0.03}$
$\tau_{\rm p}^{2,\,\rm multiple(0)}$ (ps)	−0.08	−0.03	$-0.08^{+0.01}_{-0.01}$	$-0.03^{+0.00}_{-0.00}$
$\tau_{\rm p}^{2,\,\rm multiple(1)}$ (ps)	−0.04	−0.02	$-0.04^{+0.01}_{-0.01}$	$-0.02^{+0.00}_{-0.00}$
$\tau_{\rm p}^{3,\,\rm multiple(0)}$ (ps)	+0.43	+0.39	$+0.43^{+0.03}_{-0.03}$	$+0.39^{+0.02}_{-0.02}$
$\tau_{\rm p}^{3,\,\rm multiple(1)}$ (ps)	+0.34	+0.33	$+0.34^{+0.03}_{-0.03}$	$+0.33^{+0.01}_{-0.01}$
$\sigma_{\rm ol}$ (ps)	+33.2	+30.6	$+43.7^{+15.0}_{-13.4}$	$+33.5^{+1.6}_{-9.2}$
$f_{\rm ol}^{\rm single}$	+0.04	+0.02	$+0.04^{+0.03}_{-0.01}$	$+0.03^{+0.00}_{-0.00}$
$f_{\rm ol}^{\rm multiple}$ ($\times 10^{2}$)	+0.02	+0.01	$+0.01^{+0.01}_{-0.01}$	$+0.02^{+0.01}_{-0.01}$

Table 4.1: The resolution function parameters applied in the time-dependent measurements of the present analysis. The resolution function parameters are determined from hadronic decays of neutral B mesons, e.g. from $B^0 \to D^-\pi^+$, $D^{*-}\pi^+$ and $D^{*-}\rho^+$ decays [94, 95].

4.3 Flavor Tagging

To perform time-dependent CP violation measurements, it is required to identify the flavor of the accompanying B meson on the tagging-side, B_{tag}. The identification is performed by inferring the flavor content of B_{tag} from its decay products. All final-state particles not assigned to the fully reconstructed B meson on the signal-side, B_{rec}, enter a procedure, referred to as flavor tagging, in which algorithms estimate the flavor content on the basis of known possible decays.

In general, the identification of the flavor cannot be perfect for several reasons: due to the experimental conditions such as inefficiencies in the particle detection and identification, due to the possibility of non-flavor specific decays and due to the limitations in the algorithms itself. For these reasons the decisions for a flavor of the B_{tag} mesons by the algorithms allow quantitative conclusions only in the statistical limit. More precisely, the flavor tagging algorithms make only decisions for a fraction of B mesons. This is quantified by the tagging efficiency ε. Additionally, only a fraction of the tagged B mesons are tagged correctly. The fraction of events identified incorrectly is measured by the mistag fraction ω.

In Section 2.5, the probability density function defined in Equation 2.104 for B_{rec} mesons decaying to a CP eigenstate is derived from the coherent time evolution of two neutral B mesons produced in $\Upsilon(4S)$ decays. The probability density function, denoted in the following by P^{theory}, depends on the flavor content of the accompanying B meson on the tagging-side and is given by

$$P^{theory}(\Delta t, q) = \frac{1}{4\tau_{B^0}} e^{-|\Delta t|/\tau_{B^0}} \left[1 + q\Big(\mathcal{S}\sin(\Delta m \Delta t) - \mathcal{C}\cos(\Delta m \Delta t)\Big)\right], \tag{4.23}$$

where $q = +1$ (-1) represents the b-flavor charge of the accompanying B meson tagged as a $B_{tag} = B^0$ $(\bar{B}^0)$. The probability density function P^{theory} describes the proper decay time distributions for B_{rec} mesons, when the tagging decision is correct.

By allowing for incorrect flavor assignments and introducing the mistag fractions ω_{B^0} and $\omega_{\bar{B}^0}$ for B^0 and $\bar{B}^0$ mesons, the probability density function P^{exp} describing the experimental proper decay time distributions in dependence of the b-flavor charge q^{meas} obtained by imperfect flavor tagging can be expressed as

$$P^{exp}(\Delta t, q^{meas} = +1) = (1 - \omega_{B^0})P^{theory}(\Delta t, q^{true} = +1) + \omega_{\bar{B}^0}\, P^{theory}(\Delta t, q^{true} = -1), \tag{4.24}$$

$$P^{exp}(\Delta t, q^{meas} = -1) = \omega_{B^0}\, P^{theory}(\Delta t, q^{true} = +1) + (1 - \omega_{\bar{B}^0})P^{theory}(\Delta t, q^{true} = -1). \tag{4.25}$$

By defining $\omega := \frac{1}{2}(\omega_{B^0} + \omega_{\bar{B}^0})$ and $\Delta\omega := \frac{1}{2}(\omega_{B^0} - \omega_{\bar{B}^0})$, omitting the superscript labels, and rearrangement of the terms, the probability density function describing the experimental proper decay time distributions in the CP violation measurements defined as

$$\begin{aligned} P(\Delta t, q, \omega, \Delta\omega) = \frac{1}{4\tau_{B^0}} e^{-|\Delta t|/\tau_{B^0}} \Big[& 1 - q\Delta\omega \\ & + q(1 - 2\omega) \times \big(\mathcal{S}\sin(\Delta m \Delta t) - \mathcal{C}\cos(\Delta m \Delta t)\big)\Big]. \end{aligned} \tag{4.26}$$

In Equation 4.26, the amplitudes of the CP violation parameters are modified by a coefficient of $(1-2\omega)$ which is less than one. As a consequence, the amplitudes of the observed CP violation parameters are diluted by this factor. Additionally, if taking into account the tagging efficiency ε, the number of signal events needed to achieve a certain statistical significance in a time-dependent CP violation measurement is proportional to the inverse of $\varepsilon_{\mathrm{eff}} := \varepsilon(1-2\omega)^2$. The quantity $\varepsilon_{\mathrm{eff}}$ can be used to quantify the performance of the flavor tagging procedure and is called the effective tagging efficiency.

To allow for precise CP violating asymmetry measurements, the flavor tagging procedure at the Belle experiment is optimised to achieve a high effective tagging efficiency $\varepsilon_{\mathrm{eff}}$ and low uncertainties on the mistag fractions ω and $\Delta\omega$. In the determination of the flavor of the tagging B meson from its decay products, the following categories are considered:

1. In $\bar{b} \to X l^+ \nu$ decays, the charge of the high-momentum lepton tags the b-flavor.
2. Sequential $\bar{b} \to \bar{c} \to \bar{s}$ transitions are favored due to the involved CKM elements V_{cb} and V_{cs}. Most of these cascades involve $B^0 \to X K^+$ decays, where the charge of the kaon tags the b-flavor.
3. In $\bar{b} \to \bar{c} \to \bar{s} l^- \bar{\nu}$ transitions, the charge of the intermediate-momentum lepton tags the b-flavor.
4. In $B^0 \to X D^{(*)} \pi^+$ decays, the charge of the high-momentum pion tags the b-flavor.
5. In $B^0 \to X D^{*-}$ and subsequent $D^{*-} \to \bar{D}^0 \pi^-_{\mathrm{soft}}$ decays, the charge of the soft pion tags the b-flavor.
6. In $\bar{b} \to \bar{c} \to \bar{s}$ transitions, $\bar{\Lambda}$ baryons are created and tag the b-flavor.

The Belle flavor tagging algorithms assign the signed product $q \cdot r$ as a tagging decision in a likelihood approach on an event-by-event basis. The value of $q = +1$ (-1) corresponds to a B^0 $(\bar{B}^0)$ tag and the tagging quality variable r ranges from $r = 0$ (no flavor information) to $r = 1$ (unambiguous flavor information).

The flavor tagging procedure is realised in a two stage process by a likelihood approach. The first stage operates on particle level. The final state particles are assigned to the categories of lepton, kaon, pion or Λ candidates. In each category, discriminants such as charge, particle identification information and kinematic and event shape quantities are used to identify the flavor. The second stage operates on the event level. The categories from the first stage are combined and correlations of possible multiple track-level tags are taken into account to assign the signed product of $q \cdot r$.

The $q \cdot r$ distributions for self-tagging $B^0 \to D_s^+ D^-$ and $B^0 \to D_s^+ D^{*-}$ decays obtained from data and from Monte Carlo simulations are shown in Figure 4.9. For both, B^0 and $\bar{B}^0$ mesons, the distributions obtained from data and from Monte Carlo simulations agree. The distributions for $B^0(\bar{B}^0)$ mesons peak at $+1(-1)$. The peak at $+1(-1)$ is caused mainly by high-momentum lepton tags in semileptonic decays, which allow to tag the B flavor nearly unambiguously. The peak-like structure close to $+0.7(-0.7)$ originates mainly from kaon tags. The involved decays occur often, but the flavor information from the kaons is not as high as from the leptons and the

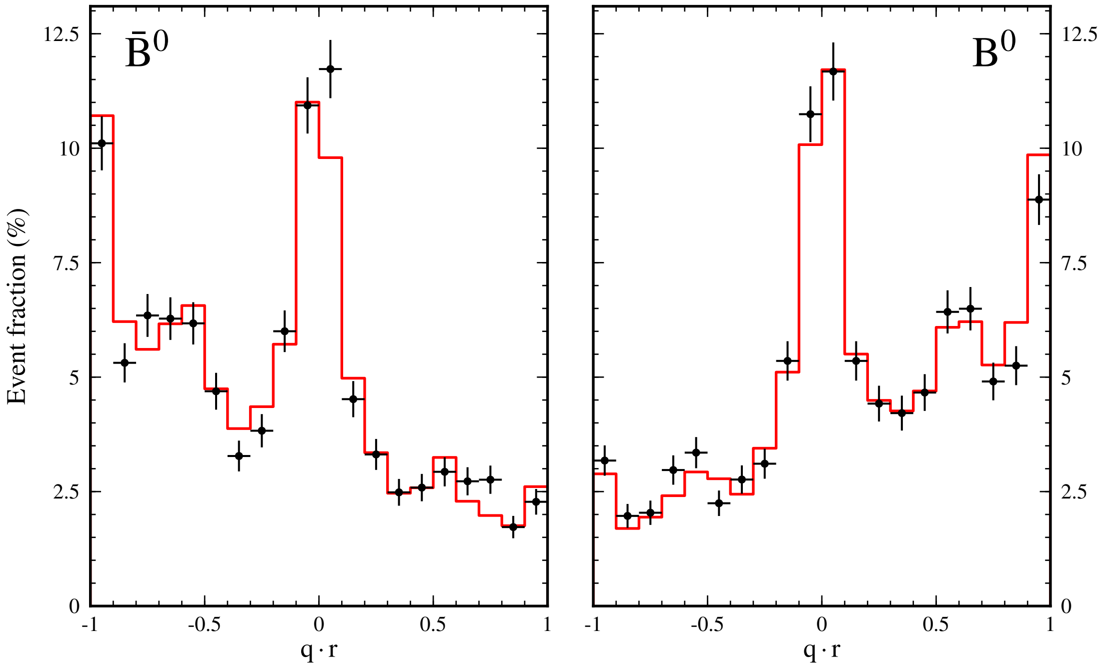

Figure 4.9: The $q \cdot r$ distributions for $\bar{B}^0$ (left) and B^0 (right) mesons. The points with error bars are obtained from self-tagging $B^0 \to D_s^+ D^-$ and $B^0 \to D_s^+ D^{*-}$ decays on data. The red histograms are obtained from Monte Carlo simulations.

tagging decision has a larger uncertainty. A significant contribution to the peak close to zero is caused by pions, which are the most frequent particles, but carry little flavor information.

For perfect calibration of the flavor tagging algorithms, the tagging quality variable r and the mistag fraction ω are related by $r = 1 - 2\omega$. For the calibration of the mistag fractions and for the application of the flavor tagging algorithms in the measurements, the tagging quality variable is subdivided into seven r intervals. The mistag fractions ω and the mistag fraction differences $\Delta\omega$ are determined by flavor-specific semileptonic $B^0 \to D^{*-} l^+ \nu_l$ decays. The results from the calibration of the flavor tagging algorithms performed within the context of Belle's recent $\sin(2\beta)$ measurement in $b \to c\bar{c}s$ transitions [94, 95] are summarised in Table 4.2.

The effective tagging efficiency for data from the first period of the Belle experiment, referred to as SVD1, is $\varepsilon_{\text{eff}}^{\text{SVD1}} = (28.4 \pm 1.0\,(\text{stat.} + \text{syst.}))\,\%$, and for the second period, referred to as SVD2, it is $\varepsilon_{\text{eff}}^{\text{SVD2}} = (30.1 \pm 0.4\,(\text{stat.} + \text{syst.}))\,\%$. For the final Belle data set, the effective tagging efficiency of the flavor tagging algorithms is $\varepsilon_{\text{eff}} = (29.9 \pm 0.4\,(\text{stat.} + \text{syst.}))\,\%$.

Sensitive tests for the validity and performance of the flavor tagger are mixing frequency measurements of self-tagging decays. In Section 7.2.3, such measurements are performed as a cross-check using the $B^0 \to D_s^+ D^-$ and $B^0 \to D_s^+ D^{*-}$ control samples.

A detailed description of the flavor tagging algorithms applied in time-dependent measurements at the Belle experiment is given in Reference [96].

	SVD1		SVD2	
r-bin	ω	$\Delta\omega$	ω	$\Delta\omega$
$0 \leq r \leq 0.1$	0.5	0	0.5	0
$0.1 < r \leq 0.25$	$0.419^{+0.007}_{-0.006}$	$+0.057^{+0.009}_{-0.009}$	$0.419^{+0.004}_{-0.004}$	$-0.009^{+0.004}_{-0.004}$
$0.25 < r \leq 0.5$	$0.330^{+0.007}_{-0.006}$	$+0.013^{+0.009}_{-0.009}$	$0.319^{+0.003}_{-0.003}$	$+0.010^{+0.004}_{-0.004}$
$0.5 < r \leq 0.625$	$0.234^{+0.007}_{-0.008}$	$-0.015^{+0.010}_{-0.010}$	$0.223^{+0.004}_{-0.003}$	$-0.011^{+0.004}_{-0.004}$
$0.625 < r \leq 0.75$	$0.171^{+0.007}_{-0.006}$	$-0.001^{+0.009}_{-0.009}$	$0.163^{+0.003}_{-0.004}$	$-0.019^{+0.004}_{-0.005}$
$0.625 < r \leq 0.75$	$0.100^{+0.007}_{-0.009}$	$+0.009^{+0.009}_{-0.009}$	$0.104^{+0.003}_{-0.004}$	$+0.002^{+0.004}_{-0.004}$
$0.875 < r \leq 1$	$0.023^{+0.004}_{-0.005}$	$+0.005^{+0.006}_{-0.006}$	$0.025^{+0.002}_{-0.003}$	$-0.004^{+0.002}_{-0.002}$

Table 4.2: Mistag fractions ω and the mistag fraction differences $\Delta\omega$ in intervals of the flavor tagging quality variable r. The values of ω and $\Delta\omega$ have been determined from control samples in the calibration of the flavor tagging algorithms performed within the context of Belle's recent $\sin(2\beta)$ measurement in $b \to c\bar{c}s$ transitions [94, 95].

4.4 Fit Models and Extraction of Signal in Time-Integrated Measurements

In $B^0 \to D^+D^-$ and in $B^0 \to D^{*\pm}D^{\mp}$ decays, the signal yields are extracted by two-dimensional extended maximum likelihood fits to the distributions of the beam-energy-constrained mass M_{bc} and of the energy difference ΔE. These are kinematic observables that utilise the unique feature of e^+e^--colliders that the initial energy of the events is known to high precision from the experimental conditions of the accelerator. The beam-energy-constrained mass M_{bc} is defined by

$$M_{bc} = \sqrt{(E^*_{beam}/c^2)^2 - (p^*_B/c)^2}, \tag{4.27}$$

and the energy difference ΔE is defined by

$$\Delta E = E^*_B - E^*_{beam}, \tag{4.28}$$

where E^*_{beam} is the energy of the accelerator beam in the center-of-mass frame. The quantities p^*_B and E^*_B denote the momenta and energy of reconstructed B^0 candidates in the center-of-mass frame.

In the following, the signal and background parameterisations of the M_{bc} and ΔE distributions are summarised and the fit procedure for the extraction of signal yields from data distributions is described.

Probability Density Function for Signal in M_{bc}

For correctly reconstructed B^0 decays, the M_{bc} distributions peak at the invariant mass of B mesons of 5.279 GeV/c^2. For $B^0 \to D^+D^-$ and $B^0 \to D^{*\pm}D^{\mp}$ decays, the signal distributions in M_{bc} are parameterised by a single Gaussian function.

Probability Density Function for Background in M_{bc}

For the background originating from continuum events and from combinatorial B decays, the M_{bc} distributions are related to the phase space of the decays. The background distributions are parameterised by an empirically determined threshold function introduced by the ARGUS Collaboration [97]. The so-called ARGUS function is defined as

$$\mathcal{P}^{ARGUS}\left(M_{bc};\alpha,E^*_{beam}\right) = M_{bc}\sqrt{1-\left(\frac{M_{bc}}{E^*_{beam}}\right)^2}\, e^{-\alpha\left(1-\left(M_{bc}/E^*_{beam}\right)^2\right)}, \tag{4.29}$$

where the parameter α defines the shape of the distribution and $E^*_{beam} = 5.289$ GeV/c^2 defines the threshold, which corresponds to half of the center-of-mass energy.

Probability Density Function for Signal in ΔE

For correctly reconstructed B^0 decays, the ΔE distributions peak at zero. For $B^0 \to D^+D^-$, the signal distributions in ΔE are parameterised by the sum of two Gaussian functions with common mean. For $B^0 \to D^{*\pm}D^{\mp}$, the ΔE distributions are asymmetric and have tails towards lower values. The asymmetry is induced by decay modes that involve π^0 mesons in the reconstruction. For this reason in $B^0 \to D^{*\pm}D^{\mp}$, the ΔE distributions are parameterised by the sum of a Gaussian function and an empirically determined function introduced by the Crystal Ball Collaboration [98]. The so-called Crystal Ball function is related to the calorimeter resolution and accounts for tails caused by radiative decays. It is defined as

$$\mathcal{P}^{\mathrm{CB}}(\Delta E; E_0, \sigma, \alpha, n) = \begin{cases} e^{-\frac{(\Delta E - E_0)}{2\sigma^2}} & \text{if } \Delta E > E_0 - \alpha\sigma \\ \left(\frac{n}{\alpha}\right)^n e^{-\frac{\alpha^2}{2}} \left(\frac{E_0 - \Delta E}{\sigma} + \frac{n}{\alpha} - \alpha\right)^{-n} & \text{if } \Delta E \leq E_0 - \alpha\sigma, \end{cases} \tag{4.30}$$

where E_0 and σ denote the mean and the width of the distribution. The Crystall Ball function is basically a Gaussian function that undergoes a transition to the distribution of a power law in dependence on the parameters α and n.

Probability Density Function for Background in ΔE

For the background originating from continuum events and from combinatorial B decays, the ΔE distributions increase for decreasing ΔE values. The background distributions are parameterised by a linear function.

Extended Likelihood Function

The extended likelihood function is constructed from the probability density functions for the signal and background components and poisson factors to estimate the signal and background yields [99],

$$\mathcal{L} = \frac{e^{-(N_{\mathrm{sig}}+N_{\mathrm{bkg}})}}{N!} \prod_{i=1}^{N} \left\{ N_{\mathrm{sig}} \mathcal{P}_{\mathrm{sig}}(M_{\mathrm{bc}}, \Delta E) + N_{\mathrm{bkg}} \mathcal{P}_{\mathrm{bkg}}(M_{\mathrm{bc}}, \Delta E) \right\}. \tag{4.31}$$

The two-dimensional probability density functions $\mathcal{P}_{\mathrm{sig}}(M_{\mathrm{bc}}, \Delta E)$ and $\mathcal{P}_{\mathrm{bkg}}(M_{\mathrm{bc}}, \Delta E)$ are composed of the products of the corresponding one-dimensional M_{bc} and ΔE functions.

In the two-dimensional fits to the M_{bc} and ΔE distributions, the shape parameters of the signal components in $B^0 \to D^+D^-$ ($B^0 \to D^{*\pm}D^{\mp}$) are fixed to values obtained from $B^0 \to D_s^+D^-$ ($B^0 \to D^{*+}D^{*-}$) data distributions, where the relative widths and fractions of the signal components in ΔE are fixed to values obtained from Monte Carlo simulations. The agreement in the signal parameterisation between the $B^0 \to D_s^+D^-$ ($B^0 \to D^{*+}D^{*-}$) control samples and $B^0 \to D^+D^-$ ($B^0 \to D^{*\pm}D^{\mp}$) decays has been verified by Monte Carlo simulations. The fit procedures are validated by ensemble tests and measurements on inclusive Monte Carlo simulation samples and data distributions in Chapter 6.

4.5 Likelihood Function of Proper Decay Time Difference Distributions

The time-dependent analyses are performed by maximising a likelihood function with respect to the quantities to be measured, for example lifetimes, oscillation frequencies or CP violating asymmetries. The likelihood function is constructed from the probability density functions of signal, background and outlier components, describing the experimental proper decay time difference distributions of N measurements,

$$\mathcal{L} = \prod_{i=1}^{N} \left\{ \left(1 - f_{ol}\right) \left[\left(1 - f^{i}_{sig}\right) \mathcal{P}^{i}_{bkg}(\Delta t) + f^{i}_{sig} \mathcal{P}^{i}_{sig}(\Delta t) \right] + f_{ol} \mathcal{P}^{i}_{ol}(\Delta t) \right\}. \tag{4.32}$$

The probability density function for signal $\mathcal{P}_{sig}$ is a convolution of a probability density function P_{sig} motivated by the underlying physical processes with a resolution function $\mathcal{R}_{sig}$ to account for the finite vertex resolution. Because of the importance of resolution effects in time-dependent measurements at the Belle experiment, the resolution functions contributing to $\mathcal{R}_{sig}$ are described in detail in Section 4.2. In the present analysis, P_{sig} describes lifetime distributions of untagged B meson decays, neutral B meson oscillation distributions of flavor specific decays, or distributions of decays that allow to extract CP violating parameters. The signal probability density functions relevant for the present analysis are introduced in Section 4.5.1.

The probability density function for background decays $\mathcal{P}_{bkg}$ is similar to that of signal decays parameterised as the convolution of a probability density function P_{bkg} motivated by the underlying physics with a resolution function $\mathcal{R}_{bkg}$, see Section 4.5.3.

A contribution of events with large Δt is considered as outliers and its parameterisation by the function $\mathcal{P}_{ol}$ is described in Section 4.5.4.

The evaluation of the signal probability f_{sig} on an event-by-event basis is explained in Section 4.5.5.

4.5.1 Probability Density Function of Signal

The probability density functions for signal P_{sig} are given by the underlying physics of the particular microscopic process. In the present analysis, the processes cover the parameterisation of exponential decays for the description of lifetime difference distributions of untagged decays, the parameterisation of neutral B meson oscillations allowing for the measurements of B^0-$\bar{B}^0$ mixing-frequencies in self-tagging decays and the parameterisation of decays that allow to extract CP violating asymmetries.

In the following, the different types of signal probability density functions P_{sig} used in the time-dependent measurements of the present analysis are defined.

Probability Density Function for Lifetime Measurements

The probability density function describing the proper decay time differences between two B^0 or B^+ mesons from $\Upsilon(4S)$ decays follows an exponential decay with lifetimes τ_{B^0} or τ_{B^+},

$$P_{sig}(\Delta t; \tau_{B^{0/+}}) = \frac{1}{2\tau_{B^{0/+}}} e^{-|\Delta t|/\tau_{B^{0/+}}}. \tag{4.33}$$

Probability Density Function for Lifetime and Mixing-Frequency Measurements

The B^0-$\bar{B}^0$ oscillation measurements utilise the coherent time evolution of neutral B mesons from $\Upsilon(4S)$ decays described in Section 2.5. If the B_{rec} meson is reconstructed in a flavor specific decay such as $B^0 \to D_s^+ D^-$ or $B^0 \to D_s^+ D^{*-}$, where the D_s^+ (D_s^-) tags the flavor of B_{rec} at the time of its decay as a B^0 ($\bar{B}^0$), and the flavor of the accompanying B_{tag} meson is determined by its decay products, then it is possible to determine the B^0-$\bar{B}^0$ mixing frequency Δm from the measurements of the proper decay time difference of both neutral mesons.

The probabilities to observe an initially pure meson B^0 at time $t > 0$ without mixing as a B^0 or with mixing as a $\bar{B}^0$ are defined in Equations 2.74 and 2.75. Adapting the mixing probabilities to the above described case of two neutral mesons from $\Upsilon(4S)$ decays, results in the following probabilities to find B_{rec} and B_{tag} mesons with same flavor (SF) content or with opposite flavor (OF) content as a function of Δt:

$$P^{SF}(\Delta t; \tau_{B^0}, \Delta m) = \frac{1}{4\tau_{B^0}} e^{-|\Delta t|/\tau_{B^0}} \left[1 - \cos(\Delta m \Delta t)\right] \tag{4.34}$$

$$P^{OF}(\Delta t; \tau_{B^0}, \Delta m) = \frac{1}{4\tau_{B^0}} e^{-|\Delta t|/\tau_{B^0}} \left[1 + \cos(\Delta m \Delta t)\right] \tag{4.35}$$

Equations 4.34 and 4.35 describe the proper decay time difference distributions of events, in which the assignment of same or opposite flavor content is correct. To take into account the experimentally imperfect flavor tagging decisions and to allow for wrong flavor assignments, the distributions need to be modified. Events with same sign (SS) or opposite sign (OS) of the flavor tagging decision and of the charge of the D_s^+ meson are described by

$$P^{SS}(\Delta t; \tau_{B^0}, \Delta m) = (1 - \omega_{SS}) P^{SF} + \omega_{OS} P^{OF} \tag{4.36}$$

$$P^{OS}(\Delta t; \tau_{B^0}, \Delta m) = (1 - \omega_{OS}) P^{OF} + \omega_{SS} P^{SF}, \tag{4.37}$$

where ω_{OS} and ω_{SS} denote the fractions of wrong flavor tagging decisions in SS and OS events. Expressing ω_{OS} and ω_{SS} by ω and $\Delta\omega$ and the rearrangement of Equations 4.36 and 4.37 result in the probability density functions $P_{sig}^{SS/OS}$ entering the likelihood function in the measurements of lifetimes and mixing-frequencies:

$$P_{sig}^{SS}(\Delta t; \tau_{B^0}, \Delta m) = \frac{1}{4\tau_{B^0}} e^{-|\Delta t|/\tau_{B^0}} \left[1 - \left(1 - 2\omega\right) \cos(\Delta m \Delta t)\right] \tag{4.38}$$

$$P_{sig}^{OS}(\Delta t; \tau_{B^0}, \Delta m) = \frac{1}{4\tau_{B^0}} e^{-|\Delta t|/\tau_{B^0}} \left[1 + \left(1 - 2\omega\right) \cos(\Delta m \Delta t)\right] \tag{4.39}$$

Probability Density Function for CP Violation Measurements in $B^0 \to D^+D^-$ Decays

The probability density function describing the proper decay time difference distribution of events, where one B meson decays to a CP eigenstate, such as in $B^0 \to D^+D^-$, and the accompanying B meson on the tagging-side is tagged with $q = +1$ (-1) as a B^0 ($\bar{B}^0$), is dependent on the mixing-induced CP violation $\mathcal{S}_{D^+D^-}$ and the direct CP violation $\mathcal{C}_{D^+D^-}$. In Section 2.5, the probability density function is derived from the coherent time evolution of entangled B^0-$\bar{B}^0$ pairs created from $\Upsilon(4S)$ decays. The effect of incorrect flavor assignments on the probability density function for CP violating asymmetry measurements is demonstrated in Section 4.3. The probability density function, accounting for incorrect flavor assignments by the wrong tag fractions ω and wrong tag fraction differences Δω, is

$$
\begin{aligned}
\mathrm{P_{sig}}\left(\Delta t;\mathcal{S}_{D^+D^-},\mathcal{C}_{D^+D^-}\right) = \frac{1}{4\tau_{B^0}}\, e^{-|\Delta t|/\tau_{B^0}} \Big[1 - q\Delta\omega + q\left(1-2\omega\right) \\
\times \Big(\mathcal{S}_{D^+D^-}\sin\left(\Delta m\Delta t\right) - \mathcal{C}_{D^+D^-}\cos\left(\Delta m\Delta t\right)\Big)\Big]. \quad (4.40)
\end{aligned}
$$

Probability Density Function for CP Violation Measurements in $B^0 \rightarrow D^{*\pm}D^{\mp}$ Decays

The decays of $B^0 \rightarrow D^{*+}D^-$ and $B^0 \rightarrow D^{*-}D^+$ are individually no CP eigenstates. The time-dependent decay rate accounts for four flavor-charge configurations and is given in Equation 2.117. After the inclusion of the effects of incorrect flavor assignments, the corresponding signal probability density function can be written as

$$
\begin{aligned}
P_{sig}^{D^{*\pm}D^{\mp}}&\left(\Delta t;\mathcal{A}_{D^*D},\mathcal{S}_{D^*D},\mathcal{C}_{D^*D},\Delta\mathcal{S}_{D^*D},\Delta\mathcal{C}_{D^*D}\right) = \\
&\left(1\pm\mathcal{A}_{D^*D}\right)\frac{1}{8\tau_{B^0}}\, e^{-|\Delta t|/\tau_{B^0}} \\
&\times\Big\{ 1 - q\Delta\omega + q(1-2\omega)\Big[\Big(\mathcal{S}_{D^*D} \pm \Delta\mathcal{S}_{D^*D}\Big)\sin(\Delta m\Delta t) \\
&- \Big(\mathcal{C}_{D^*D} \pm \Delta\mathcal{C}_{D^*D}\Big)\cos(\Delta m\Delta t)\Big]\Big\}. \quad (4.41)
\end{aligned}
$$

As described in Section 2.7.2, the time- and flavor-integrated asymmetry $\mathcal{A}_{D^*D}$ measures direct CP violation. The parameters $\mathcal{S}_{D^*D}$ and $\mathcal{C}_{D^*D}$ are related to mixing-induced and flavor-dependent direct CP violation. The parameters $\Delta\mathcal{S}_{D^*D}$ and $\Delta\mathcal{C}_{D^*D}$ are related to relative strong phases and rate asymmetries in the decays.

In Section 2.7.2, an equivalent parameterisation is introduced. The corresponding signal probability density function is given by

$$
\begin{aligned}
P_{sig}^{D^{*\pm}D^{\mp}}&\left(\Delta t;\mathcal{A}_{D^*D},\mathcal{S}_{D^{*+}D^-},\mathcal{C}_{D^{*+}D^-},\mathcal{S}_{D^{*-}D^+},\mathcal{C}_{D^{*-}D^+}\right) = \\
&\left(1\pm\mathcal{A}_{D^*D}\right)\frac{1}{8\tau_{B^0}}\, e^{-|\Delta t|/\tau_{B^0}}\Big\{1 - q\Delta\omega + q(1-2\omega) \\
&\times\Big[\mathcal{S}_{D^{*\pm}D^{\mp}}\sin(\Delta m\Delta t) - \mathcal{C}_{D^{*\pm}D^{\mp}}\cos(\Delta m\Delta t)\Big]\Big\}. \quad (4.42)
\end{aligned}
$$

In this parameterisation, the sets of parameters $\mathcal{S}_{D^{*+}D^-}$, $\mathcal{C}_{D^{*+}D^-}$ and $\mathcal{S}_{D^{*-}D^+}$, $\mathcal{C}_{D^{*-}D^+}$ are assigned to both possible decays, $B^0 \rightarrow D^{*+}D^-$ and $B^0 \rightarrow D^{*-}D^+$, respectively.

4.5.2 Probability Density Function of Peaking Background

In the reconstruction of $B^0 \rightarrow D^+D^-$ and $B^0 \rightarrow D^{*\pm}D^{\mp}$ decays, background can contribute that peaks in the M_{bc} and ΔE signal region and therefore cannot be discriminated from signal decays. In the branching fraction measurements, the amount of peaking background is estimated using two-dimensional fits to the M_{bc} and ΔE distributions in the D mass sidebands, see Section 6.5. The amount of peaking background is small. Therefore in the time-dependent analyses, the peaking background is neglected in the measurements of CP violation. The possible effect of peaking background is estimated using Monte Carlo simulations at a later stage. In this study, the proper decay time difference distributions of the possible peaking background are generated according to the probability density functions defined in the following.

In general two types of peaking background sources can occur: decays that are caused by a single amplitude, and decays that involve the interference of several amplitudes, which can be CP violating.

Decays that are caused by a single amplitude are modelled by the probability density function of the exponential decay,

$$P_{\text{peak.bkg.}}(\Delta t; \tau_{B^0}) = \frac{1}{2\tau_{B^0}} e^{-|\Delta t|/\tau_{B^0}} . \tag{4.43}$$

The probability density function describing the peaking background originating from decays that involve several amplitudes are introduced by means of $B^0 \to D^{(*)-} K^0_S \pi^+$ decays, which can be considered as the main possible source of peaking background in this analysis. These decays can peak in the M_{bc} and ΔE signal region when reconstructing $B^0 \to D^{(*)-}(K^0_S\pi^+)_{D^+}$ decays. The final state of $D^{(*)-}K^0_S\pi^+$ can be accessed by both, B^0 and $\bar{B}^0$, via $\bar{b} \to \bar{c}$ and $b \to u$ transitions. To treat the resulting asymmetry on the proper decay time difference distributions correctly, the probability density function describing these decays is derived from the theory of time-dependent decay rates of non-CP final states f and $\bar{f}$ with amplitudes $A(B^0 \to f)$, $A(B^0 \to \bar{f})$, $\bar{A}(B^0 \to f)$ and $\bar{A}(B^0 \to \bar{f})$.

The probability density distributions corresponding to the time-dependent decay rates are:

$$P_{\text{peak.bkg.}}\left(\Delta t, q = +1, D^{(*)-}K^0_S\pi^+; C, S_-\right) = N e^{-\Gamma|\Delta t|}\left[1 + C\cos(\Delta m\Delta t) - S_-\sin(\Delta m\Delta t)\right] \tag{4.44}$$

$$P_{\text{peak.bkg.}}\left(\Delta t, q = +1, D^{(*)+}K^0_S\pi^-; C, S_+\right) = N e^{-\Gamma|\Delta t|}\left[1 - C\cos(\Delta m\Delta t) - S_+\sin(\Delta m\Delta t)\right] \tag{4.45}$$

$$P_{\text{peak.bkg.}}\left(\Delta t, q = -1, D^{(*)-}K^0_S\pi^+; C, S_-\right) = N e^{-\Gamma|\Delta t|}\left[1 - C\cos(\Delta m\Delta t) + S_-\sin(\Delta m\Delta t)\right] \tag{4.46}$$

$$P_{\text{peak.bkg.}}\left(\Delta t, q = -1, D^{(*)+}K^0_S\pi^-; C, S_+\right) = N e^{-\Gamma|\Delta t|}\left[1 + C\cos(\Delta m\Delta t) + S_+\sin(\Delta m\Delta t)\right] \tag{4.47}$$

The factor C is related to the ratio R of suppressed to favored amplitudes, and the parameters S_+ and S_- are additionally related to the relative weak phases β and γ and the relative strong phase δ according to the following definitions:

$$R = \frac{\bar{A}(\bar{B}^0 \to D^{(*)-}K^0_S\pi^+)}{A(B^0 \to D^{(*)-}K^0_S\pi^+)} \tag{4.48}$$

$$C = \frac{1-R^2}{1+R^2} \tag{4.49}$$

$$S_\pm = \frac{2R}{1+R^2}\sin(2\beta + \gamma \pm \delta) \tag{4.50}$$

Equations 4.44 to 4.47 are normalised according to

$$\int_{-\infty}^{+\infty} \mathrm{d}(\Delta t) \sum_{q=+1,-1} \Big(P_{\mathrm{peak.bkg.}}\big(\Delta t, q, D^+ K_S^0 \pi^-; C\big) + P_{\mathrm{peak.bkg.}}\big(\Delta t, q, D^- K_S^0 \pi^+; C\big) \Big) = 1, \qquad (4.51)$$

and are used after including the effect of imperfect flavor assignments to describe the proper decay time difference distribution of the asymmetric and possibly CP violating peaking background.

4.5.3 Probability Density Function and Resolution Function of Background

In the fits performed for the time-dependent measurements, the background probability density function $\mathcal{P}_{\mathrm{bkg}}$ is parameterised by the convolution of a probability density function P_{bkg} that models the Δt distribution of the underlying physical processes and a resolution function $\mathcal{R}_{\mathrm{bkg}}$ that takes into account the experimental smearing,

$$\mathcal{P}_{\mathrm{bkg}}(\Delta t) = \int_{-\infty}^{+\infty} P_{\mathrm{bkg}}(\Delta t')\, \mathcal{R}_{\mathrm{bkg}}(\Delta t - \Delta t')\, \mathrm{d}(\Delta t'). \qquad (4.52)$$

The probability density function P_{bkg} is composed of a Dirac δ-function describing prompt decays and an exponential function describing non-prompt decays with an effective lifetime τ_{bkg},

$$P_{\mathrm{bkg}}(\Delta t) = f_\delta\, \delta\big(\Delta t - \mu_\delta\big) + \big(1 - f_\delta\big)\, e^{\frac{-|\Delta t - \mu_{\tau_{\mathrm{bkg}}}|}{\tau_{\mathrm{bkg}}}}. \qquad (4.53)$$

The resolution function for background is parameterised by the sum of two Gaussian functions with a width that depends linearly on the uncertainty $\sigma_{\mathrm{vtx}} = \sqrt{\sigma^2_{z_{\mathrm{rec}}} + \sigma^2_{z_{\mathrm{tag}}}}$ of the reconstructed decay vertices on reconstruction-side z_{rec} and on tagging-side z_{tag},

$$\begin{aligned} \mathcal{R}_{\mathrm{bkg}}(\Delta t) = & \big(1 - f^{\mathrm{tail}}_{\mathrm{bkg}}\big) \frac{1}{\sqrt{2\pi}\, s^{\mathrm{main}}_{\mathrm{bkg}}\, \sigma_{\mathrm{vtx}}}\, e^{\left(-\frac{\Delta t^2}{2\left(s^{\mathrm{main}}_{\mathrm{bkg}}\, \sigma_{\mathrm{vtx}}\right)^2}\right)} \\ & + \big(1 - f^{\mathrm{tail}}_{\mathrm{bkg}}\big) \frac{1}{\sqrt{2\pi}\, s^{\mathrm{tail}}_{\mathrm{bkg}}\, s^{\mathrm{main}}_{\mathrm{bkg}}\, \sigma_{\mathrm{vtx}}}\, e^{\left(-\frac{\Delta t^2}{2\left(s^{\mathrm{tail}}_{\mathrm{bkg}}\, s^{\mathrm{main}}_{\mathrm{bkg}}\, \sigma_{\mathrm{vtx}}\right)^2}\right)}. \end{aligned} \qquad (4.54)$$

The background parameters f_δ, μ_δ, $\mu_{\tau_{\mathrm{bkg}}}$, τ_{bkg}, $f^{\mathrm{tail}}_{\mathrm{bkg}}$, $s^{\mathrm{tail}}_{\mathrm{bkg}}$ and $s^{\mathrm{main}}_{\mathrm{bkg}}$ are estimated from $M_{\mathrm{bc}} < 5.26\ \mathrm{GeV}/c^2$ sideband samples that contain no signal. The background parameters are fixed in subsequent fits of the signal region, see Section 7.3.1. The assumption that the background in the sideband region agrees with the background in the signal region is verified using large samples of Monte Carlo simulations of inclusive B decays and continuum events.

4.5.4 Probability Density Function of Outlier Components

In the experimental proper decay time difference distributions a broad component, referred to as outliers and allowing for large Δt values, occurs. The outliers can arise from multiple scattering effects. The outlier component emerges for signal and background components in the same way and has a width of about 35 ps. Due to the broad width, the underlying Δt distributions and resolution functions can be neglected. The probability density function $\mathcal{P}_{ol}$ describing the outlier component is parameterised by a single Gaussian function,

$$\mathcal{P}_{ol}(\Delta t) = \mathcal{G}(\Delta t; \sigma_{ol}). \tag{4.55}$$

The fraction of outliers f_{ol} is, being approximately 2×10^{-4}, relatively small. The fraction f_{ol} and the width σ_{ol} differ for vertices reconstructed from single or multiple tracks and are estimated from control samples. The numerical values relevant for the present analysis are given in Table 4.1.

4.5.5 Signal Probability

The probability f_{sig} for an event to be a signal decay is evaluated on an event-by-event basis as a function of the M_{bc} and ΔE observables. The calculation applies the fit models introduced in Section 4.4 by replacing the poisson factor in Equation 4.31 by the signal fraction F_{sig}. The signal probability f_{sig} in the time-dependent measurements is related to the signal fraction F_{sig} in the M_{bc} and ΔE parameterisation by

$$f_{sig} = \frac{F_{sig}\mathcal{P}_{sig}(M_{bc}, \Delta E)}{F_{sig}\mathcal{P}_{sig}(M_{bc}, \Delta E) + (1 - F_{sig})\,\mathcal{P}_{bkg}(M_{bc}, \Delta E)}. \tag{4.56}$$

As in the time-integrated studies, e.g. in the measurements of the branching fractions in Chapter 6, the signal shapes in $B^0 \to D^{(*)\pm}D^{\mp}$ are fixed to that of the $B^0 \to D^{(*)\pm}D_s^{\mp}$ control samples. The signal fraction F_{sig} in the M_{bc} and ΔE distributions and consequently the signal fraction f_{sig} in time-dependent measurements depend on the quality of the flavor tag. Figure 4.10 shows the distribution of signal and background events dependent on the flavor tag quality indicator $r = 1 - 2\omega$. For events in low r-intervals, the flavor tagging decision is associated with large uncertainties and the signal-to-background ratio is low. In contrast for events in high r-intervals, the flavor tagging decision is associated with lower uncertainties and has a higher signal-to-background ratio. To increase the statistical sensitivity in time-dependent measurements, the dependence of the signal-to-background ratio on the flavor tagging decision is utilised by estimating the signal fraction F_{sig} in intervals of the flavor tag quality indicator r. Due to the relatively low statistics in $B^0 \to D^+D^-$ and $B^0 \to D^{*\pm}D^{\mp}$, the original seven r-intervals of the flavor tagging algorithms are merged to the three r-intervals shown in Figure 4.10.

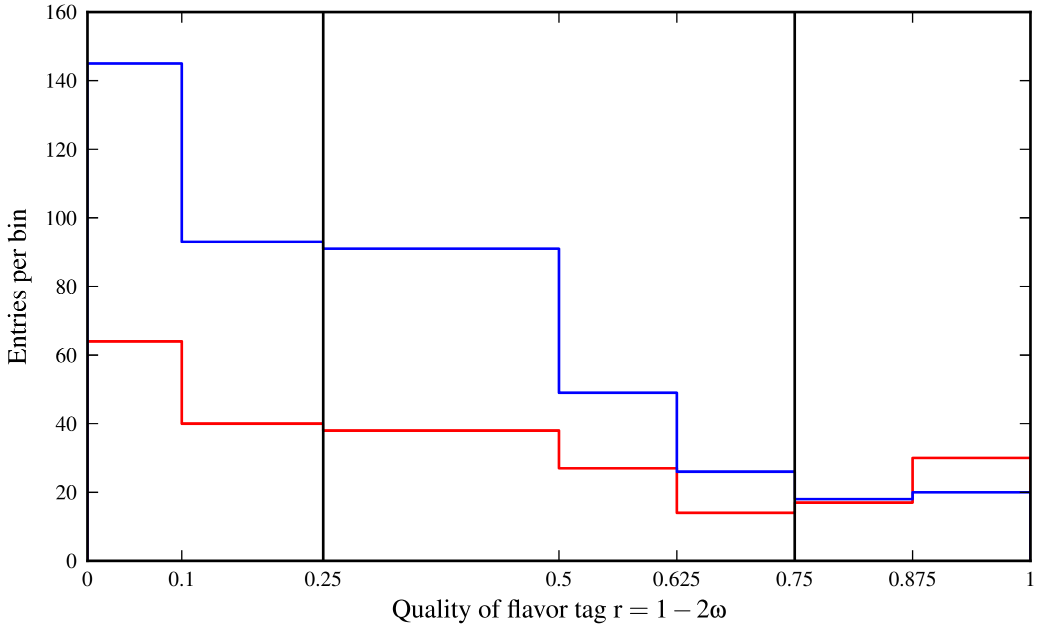

Figure 4.10: Distribution of signal (red) and background (blue) events in intervals of the flavor tag quality indicator $r = 1 - 2\omega$ for reconstructed $B^0 \to D^+D^-$ decays in the M_{bc} and ΔE signal region. The black vertical lines mark the boundary of the three intervals that are used in the r-interval dependent evaluation of the signal purity in the time-dependent measurements. Please note the non-equidistant binning of the histogram.

4.6 Continuum Suppression

The B mesons studied in the present analysis are created by decays of the $\Upsilon(4S)$ resonance produced by the KEKB e^+e^--collider. The process of $e^+e^- \to \Upsilon(4S)$ has a cross section of approximately 1 nb and has to be compared to the competing process of $e^+e^- \to q\bar{q}$ ($q \in \{u,d,s,c\}$), which has a cross section of approximately 3 nb. The pairs of up-, down-, strange- or charm-quarks created in the e^+e^--annihilation fragment into light hadrons and can give rise to a large source of background, also referred to as continuum background.

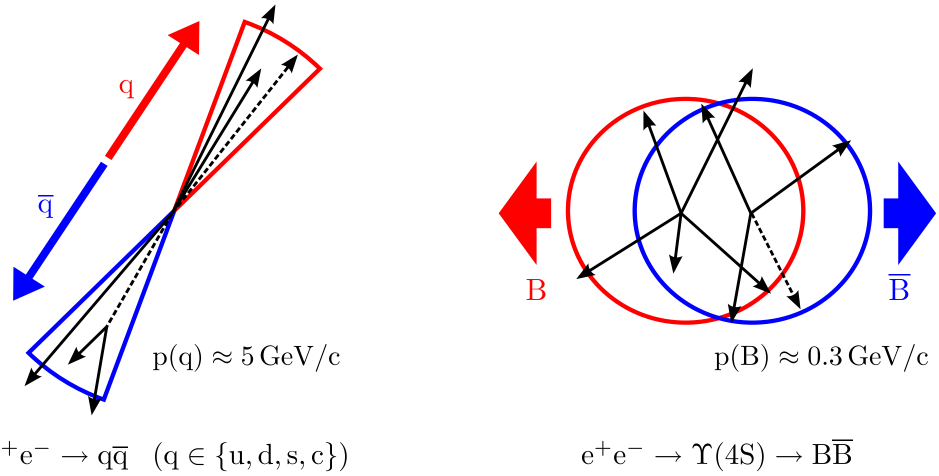

Figure 4.11: Illustration of the shapes of continuum (left) and $B\bar{B}$ (right) events. Light quark pairs produced in the e^+e^--annihilation are produced back-to-back and give rise to a jet-like structure of continuum events, while $B\bar{B}$ events have spherical shape.

The shapes of continuum and $B\bar{B}$ events are illustrated in Figure 4.11. In continuum events, the initial pairs of light quarks are created back-to-back in the center-of-mass frame and have a high momentum that carries almost half of the accelerator energy. The hadrons produced in the fragmentation acquire only small transverse momenta equivalent to $k_T \approx 0.3\,\mathrm{GeV/c}$. As a consequence, the particles are spatially confined into a jet-like structure. In $B\bar{B}$ events, the produced B mesons are almost at rest in the center-of-mass frame. Since the pseudo-scalar B mesons have spin 0, the momenta of their daughter particles have no directional preference and are distributed isotropically. Therefore, $B\bar{B}$ events have spherical shape.

In the $B^0 \to D^+D^-$ analysis, unlike in the $B^0 \to D^{*\pm}D^{\mp}$ analysis, two-third of the background originates from $e^+e^- \to q\bar{q}$ ($q \in \{u,d,s,c\}$) continuum events. To suppress this background, a continuum suppression on the basis of artificial neural networks has been developed. The neural networks combine information about the event topology and allow to discriminate between continuum and $B\bar{B}$ events. The variables used to characterise the event shapes and the chosen conceptual arrangement of neural networks are described in the following.

B Meson Flight Direction with Respect to the Beam

The $\Upsilon(4S) \to B\bar{B}$ decay is a transition of a vector meson to two pseudo-scalar mesons. In the center-of-mass frame, the polar angle θ_B of reconstructed B meson candidates with respect to the beam axis follows a $1-\cos^2\theta_B$ distribution for $B\bar{B}$ events. For continuum events, the corresponding distribution is uniform. The $\cos\theta_B$ distributions for continuum and $B\bar{B}$ events are shown in Figure 4.12.

Thrust

The concept of thrust has been developed to quantify jets at high energy experiments at the PEP and PETRA accelerators in the 1980s. The thrust axis **T** is defined by the direction which maximises the sum of the longitudinal momenta of particles. The thrust T is related to the thrust axis by

$$T = \max_{\mathbf{T}} = \frac{\sum_i |\mathbf{p}_i \cdot \mathbf{T}|}{\sum_i |\mathbf{p}_i|}, \qquad (4.57)$$

where $\mathbf{p}_i$ denotes the momentum of the i-th final-state particle in an event [100]. For event shapes that have a strong directional preference, such as caused by the back-to-back production of light quark pairs in continuum events, the thrust tends to acquire maximal values of $T \to 1$. Contrary, the thrust tends to acquire minimal values of $T \to 0.5$ in isotropic events.

One discriminating variable between continuum and $B\bar{B}$ events is $|\cos\theta_{Thrust}|$, where θ_{Thrust} is the angle between the thrust axis of the reconstructed B candidate and the thrust axis of all remaining particles in an event that are not assigned in the reconstruction of the B candidate. Because the B mesons are almost at rest in the center-of mass frame and the decay products have no directional preference, their thrust axes are distributed randomly and the distribution of $|\cos\theta_{Thrust}|$ is uniform for $B\bar{B}$ events. In continuum events, the momenta of particles are confined into jet-like structures. The reconstructed B candidates are likely to be located in one of the jets, and the thrust axes of the B candidates are collinear to the thrust axes with respect to the remaining particles in an event. As a consequence, $|\cos\theta_{Thrust}|$ tends to peak towards 1 in continuum events.

CLEO Cones

The CLEO cones have been introduced by the CLEO Collaboration in measurements of charmless B decays that are typically associated with large continuum backgrounds [101]. The CLEO cones are a refinement of the concept of thrust and have higher separation power than $\cos\theta_{Thrust}$. The variables measure the scalar momentum flow into concentric cones in angular intervals of 10° around the thrust axis of reconstructed B candidates. The distributions of the nine CLEO cone variables used in the present analysis for continuum and $B\bar{B}$ events are shown in Figure 4.12.

Fox-Wolfram Moments

The k-th Fox-Wolfram moment H_k and the k-th normalised Fox-Wolfram moment R_k are defined as

$$H_k = \sum_{i,j} \frac{|\mathbf{p}_i||\mathbf{p}_j| P_k(\cos\theta_{ij})}{E^2_{vis}} \quad \text{and} \quad R_k = \frac{H_k}{H_0}, \qquad (4.58)$$

where P_k denotes the k-th Legendre polynomial, θ_{ij} is the opening angle between the momentum **p** of the i-th and the j-th particle and E_{vis} is the sum of the measured energy in an event [102, 103]. In the limit of negligible invariant masses of the particles, the energy-momentum conservation requires $\mathrm{H_k} = 1$. The Fox-Wolfram moments $\mathrm{R_k}$ provide separation power between continuum and $\mathrm{B\bar{B}}$ events. In continuum events with 2 jet-like structures, the k-th normalised moment $\mathrm{R_k}$ has values close to one (zero) for k being an even (odd) number, while other topologies such as spherical $\mathrm{B\bar{B}}$ events adopt different values.

Modified Fox-Wolfram Moments

The modified Fox-Wolfram moments, also referred to as Super-Fox-Wolfram Moments, have been introduced by the Belle Collaboration for charm-less B decay measurements and are a refinement of the above introduced Fox-Wolfram moments [104].

In the modified Fox-Wolfram moments, the summation over the momenta of the i-th and the j-th particle in Equation 4.58 is not taken over all final-state particles in an event. Instead, the indices are chosen to run over the final-state particles of the reconstructed B candidate, denoted by the superscript "s", or to run over the remaining final-state particles in the event, denoted by the superscript "o". The combinations give rise to the moments $\mathrm{R_k^{so}}$, $\mathrm{R_k^{oo}}$ and $\mathrm{R_k^{ss}}$.

The modified Fox-Wolfram moments $\mathrm{R_k^{so}}$ and $\mathrm{R_k^{oo}}$ are used to discriminate between continuum and $\mathrm{B\bar{B}}$ events. The moments $\mathrm{R_k^{ss}}$ are excluded due to correlations with the $\mathrm{M_{bc}}$ and $\Delta\mathrm{E}$ observables that are used in the measurements to extract the signal yields. Also the moments $\mathrm{R_1^{so}}$ and $\mathrm{R_3^{so}}$ are excluded due to correlations with $\mathrm{M_{bc}}$ and $\Delta\mathrm{E}$. An additional improvement in the discrimination power is achieved by performing the calculation of $\mathrm{R_k^{so}}$ in categories that represent the quality of the reconstructed events based on the missing mass in the event.

The distributions of the modified Fox-Wolfram moments used in the present analysis for continuum and $\mathrm{B\bar{B}}$ events are shown in Figure 4.12.

Neural Network Continuum Suppression

A standard approach in measurements at the B-factory experiments is to combine one set of event shape variables such as the CLEO cones or the modified Fox-Wolfram moments into one discriminating variable. The combination is in most cases realised by a Fisher discriminant that takes into account possible linear correlations among the variables [105]. The resulting discriminating variable can then be combined with other uncorrelated variables, such as $\cos\theta_\mathrm{B}$, to form a likelihood-ratio between signal and continuum background components.

In the present analysis, the event shape variables of the CLEO cones and the modified Fox-Wolfram moments are combined in a multivariate classification approach by artificial neural networks. Neural networks allow to handle potentially non-linear complex correlations among the input variables, and thus allow to better exploit the available information with regard to the achievable separation power. The neural networks used in the present analysis are realised by the NeuroBayes package that provides additionally powerful algorithms to preprocess the input data [106, 107].

The training of the neural networks is performed by usage of distributions obtained from reconstructed Monte Carlo simulation data. For continuum events, large samples of inclusive Monte Carlo simulations of $\mathrm{e^+e^-} \to \mathrm{q\bar{q}}$ ($\mathrm{q} \in \{\mathrm{u,d,s,c}\}$) decays and for $\mathrm{B\bar{B}}$ events Monte Carlo simulations of $\mathrm{B^0} \to \mathrm{D^+D^-}$ signal decays are used.

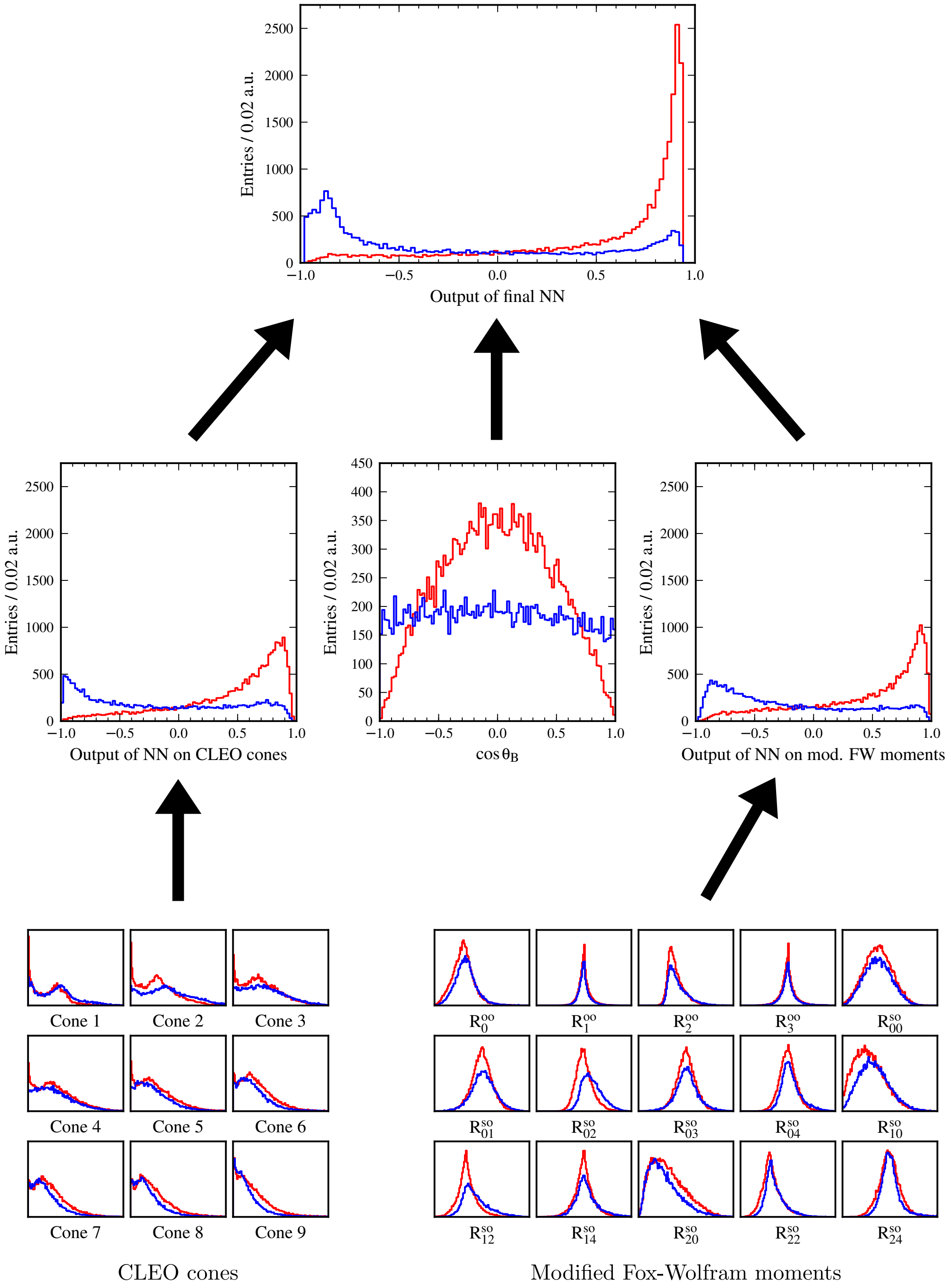

Figure 4.12: Illustration of the hierarchical arrangement of neural networks (NN) developed as a continuum suppression for the $B^0 \rightarrow D^+D^-$ analysis. The neural networks combine event shape information and allow to discriminate between $e^+e^- \rightarrow q\bar{q}$ ($q \in \{u, d, s, c\}$) continuum (blue) and $B\bar{B}$ (red) events.

The present analysis uses three different neural networks:

- The first network combines the event shape information provided by the CLEO cones.
- The second network combines the event shape information provided by the modified Fox-Wolfram moments.
- The third network uses as input the output of the first two networks and combines them with the $\cos\theta_B$ variable that contains information about the B flight direction with respect to the beam. This network is referred to as the final neural network.

The distributions of the input variables and the distributions of the output of the neural networks for continuum and $B\bar{B}$ events and an illustration of the hierarchical organisation of the networks are shown in Figure 4.12.

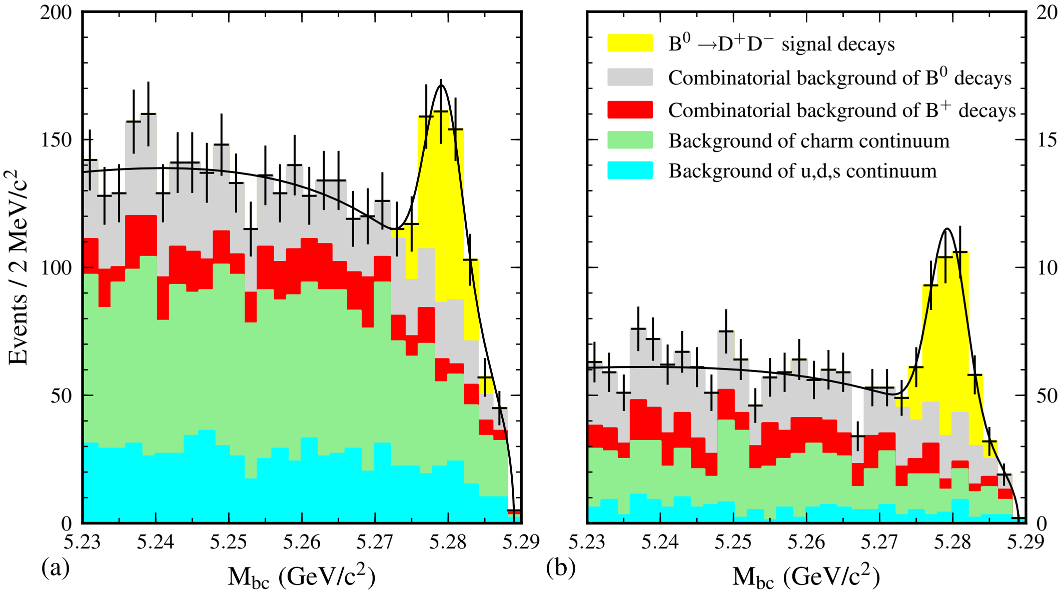

Figure 4.13: M_{bc} distributions of reconstructed $B^0 \to D^+D^-$ decays obtained from inclusive Monte Carlo simulation samples (a) before and (b) after applying selection requirements on the neural network continuum suppression. A $|\Delta E| < 30\,\mathrm{MeV}$ requirement is applied in plotting the M_{bc} distributions.

The chosen hierarchical arrangement of the neural networks has proven to be of superior separation power compared to both: to only one network that operates only on the CLEO cones or on the modified Fox-Wolfram moments, and to a large neural network that uses all variables, CLEO cones, modified Fox-Wolfram moments and $\cos\theta_B$, simultaneously.

The standard Belle continuum suppression approach is based on a Fisher discriminant on the modified Fox-Wolfram moments in combination with $\cos\theta_B$ in a likelihood-ratio approach. In a direct comparison to the standard approach, the developed continuum suppression based on the neural networks described above has a 16% higher signal reconstruction efficiency for $B^0 \to D^+D^-$ decays, when compared at a working point with similar background level. The effect of the continuum suppression is illustrated in Figure 4.13. The figure shows a comparison of the M_{bc} distributions for reconstructed $B^0 \rightarrow D^+D^-$ decays without and with applied selection requirements on the final neural network. The selection requirements applied on the final neural network are described in Section 5.3.11.

5 Reconstruction and Selection

The reconstruction of B^0 mesons and the application of appropriate selection criteria to the reconstructed samples provide the basis for the measurements performed at a later stage. The selection criteria are optimised mostly using Monte Carlo simulations. To account for possible differences between Monte Carlo simulations and data in the definition of the selection criteria, a detailed comparison of the relevant distributions is performed. In the following, the reconstruction of all decay modes, the comparison between distributions in Monte Carlo simulations and in data and the applied selection requirements are described.

5.1 Reconstructed Decay Modes

The exclusive reconstruction of particles follows a bottom-up approach. Starting from charged particles, such as π^+ and K^+ mesons, measured by the tracking system and photons measured by clusters of deposited energy in the electromagnetic calorimeter intermediate particles, such as π^0, K_S^0, D^0, D^+, D_s^+ and D^{*+} mesons, are combined to reconstruct B^0 mesons. An example of a possible decay chain is given in Equation 4.1. The reconstruction strategy is to include as many decay chains as possible to enhance the signal in the decay modes of interest and thus to improve the statistical sensitivity of the subsequent time-integrated and time-dependent measurements.

As turned out during the present analysis, not every possible reconstructed decay mode can be included. For example the inclusion of the $D^+ \to K^+K^-\pi^+$ decay mode to the reconstruction of $B^0 \to D^{(*)-}D^+$ decays introduces a non-negligible contamination of the signal by $B^0 \to D^{(*)-}K^+\bar{K}^*(892)^0$ decays. This contamination is indistinguishable from signal and is referred to as peaking background.

In addition, to the $B^0 \to D^+D^-$ and $B^0 \to D^{*\pm}D^{\mp}$ modes reconstructed for the subsequent measurements of their branching fractions and time-dependent CP violation, $B^0 \to D_s^+D^-$ and $B^0 \to D_s^+D^{*-}$ decays are reconstructed as control samples. These decays are dominated by a single Cabibbo-favored amplitude. This allows to cross-check the $B^0 \to D^+D^-$ and $B^0 \to D^{*\pm}D^{\mp}$ measurements on kinematically very similar control samples with high statistics.

In the following, the reconstructed decay modes used in the present analysis are summarised. Charge conjugated modes are always implied unless otherwise stated.

π^0 Mesons

π^0 mesons are reconstructed by combining photons measured by the electromagnetic calorimeter in the decay mode:

$$\pi^0 \to \gamma\gamma \tag{5.1}$$

K^0_S Mesons

K^0_S mesons are reconstructed by combining oppositely charged tracks in the decay mode:

$$K^0_S \to \pi^+\pi^- \tag{5.2}$$

D^0 and D^+ Mesons

D^0 and D^+ mesons are reconstructed in the following decay modes:

$$\begin{aligned} D^0 &\to K^-\pi^+ \\ &\to K^-\pi^+\pi^-\pi^+ \\ &\to K^-\pi^+\pi^0 \\ &\to K^0_S\pi^+\pi^- \end{aligned} \tag{5.3}$$

$$\begin{aligned} D^+ &\to K^-\pi^+\pi^+ \\ &\to K^0_S\pi^+ \end{aligned} \tag{5.4}$$

Other D^0 and D^+ decay modes have been considered, but are not reconstructed due to the following reasons:

- The inclusion of $D^+ \to K^+K^-\pi^+$ to the reconstruction of $B^0 \to D^{(*)-}D^+$ introduces a peaking background originating from $B^0 \to D^{(*)-}K^+\bar{K}^*(892)^0$ decays.
- The inclusion of $D^+ \to K^0_S\pi^+\pi^0$ to the reconstruction of $B^0 \to D^{(*)-}D^+$ does not improve the statistical sensitivity of the measurements due to high background levels and low reconstruction efficiencies in spite of large branching fractions.
- The decay modes $D^+ \to K^0_S K^+$ and $D^0 \to K^+K^-$ are not included due to their very low branching fractions.

D^{*+} Mesons

D^{*+} mesons are reconstructed by combining D^0 and D^+ mesons with low momentum charged and neutral pions, referred to as soft pions, in the following decay modes:

$$\begin{aligned} D^{*+} \to D^0\pi^+_{\text{soft}} &\to (K^-\pi^+)_{D^0}\,\pi^+_{\text{soft}} \\ &\to (K^-\pi^+\pi^-\pi^+)_{D^0}\,\pi^+_{\text{soft}} \\ &\to \left(K^-\pi^+\pi^0\right)_{D^0}\pi^+_{\text{soft}} \\ &\to \left(K^0_S\pi^+\pi^-\right)_{D^0}\pi^+_{\text{soft}} \end{aligned} \tag{5.5}$$

$$\begin{aligned} D^{*+} \to D^+\pi^0_{\text{soft}} &\to (K^-\pi^+\pi^+)_{D^+}\,\pi^0_{\text{soft}} \\ &\to \left(K^0_S\pi^+\right)_{D^+}\pi^0_{\text{soft}} \end{aligned} \tag{5.6}$$

$\mathrm{D_s^+}$ Mesons

$\mathrm{D_s^+}$ mesons are reconstructed in the following decay modes:

$$\begin{aligned}\mathrm{D_s^+} &\to \mathrm{K^+K^-\pi^+}\\ &\to \mathrm{K_S^0K^+}\end{aligned} \tag{5.7}$$

$\mathrm{B^0}$ Mesons

$\mathrm{B^0}$ mesons are reconstructed by combining $\mathrm{D^+}$ and $\mathrm{D_s^+}$ mesons with $\mathrm{D^-}$ and $\mathrm{D^{*-}}$ mesons.

- $\mathrm{B^0 \to D^+D^-}$ decays are reconstructed in the following decay modes:

$$\begin{aligned}\mathrm{B^0 \to D^+D^-} &\to \mathrm{(K^-\pi^+\pi^+)_{D^+}\,(K^+\pi^-\pi^-)_{D^-}}\\ &\to \mathrm{(K^-\pi^+\pi^+)_{D^+}\left(K_S^0\pi^-\right)_{D^-}}\end{aligned} \tag{5.8}$$

  The decay mode $\mathrm{B^0 \to D^+D^- \to \left(K_S^0\pi^+\right)_{D^+}\left(K_S^0\pi^-\right)_{D^-}}$ is not reconstructed due to its low branching fraction.

- $\mathrm{B^0 \to D_s^+D^-}$ decays are reconstructed as a control sample for $\mathrm{B^0 \to D^+D^-}$ decays in the following decay modes:

$$\begin{aligned}\mathrm{B^0 \to D_s^+D^-} &\to \mathrm{(K^+K^-\pi^+)_{D_s^+}\,(K^+\pi^-\pi^-)_{D^-}}\\ &\to \mathrm{(K^+K^-\pi^+)_{D_s^+}\left(K_S^0\pi^-\right)_{D^-}}\\ &\to \mathrm{\left(K_S^0K^+\right)_{D_s^+}(K^+\pi^-\pi^-)_{D^-}}\end{aligned} \tag{5.9}$$

- $\mathrm{B^0 \to D^{*+}D^-}$ decays are reconstructed in the following decay modes:

$$\begin{aligned}\mathrm{B^0 \to D^{*+}D^-} &\to \mathrm{\left[(K^-\pi^+)_{D^0}\,\pi^+_{soft}\right]_{D^{*+}}(K^+\pi^-\pi^-)_{D^-}}\\ &\to \mathrm{\left[(K^-\pi^+\pi^-\pi^+)_{D^0}\,\pi^+_{soft}\right]_{D^{*+}}(K^+\pi^-\pi^-)_{D^-}}\\ &\to \mathrm{\left[\left(K^-\pi^+\pi^0\right)_{D^0}\,\pi^+_{soft}\right]_{D^{*+}}(K^+\pi^-\pi^-)_{D^-}}\\ &\to \mathrm{\left[\left(K_S^0\pi^+\pi^-\right)_{D^0}\,\pi^+_{soft}\right]_{D^{*+}}(K^+\pi^-\pi^-)_{D^-}}\\ \\ &\to \mathrm{\left[(K^-\pi^+)_{D^0}\,\pi^+_{soft}\right]_{D^{*+}}\left(K_S^0\pi^-\right)_{D^-}}\\ &\to \mathrm{\left[(K^-\pi^+\pi^-\pi^+)_{D^0}\,\pi^+_{soft}\right]_{D^{*+}}\left(K_S^0\pi^-\right)_{D^-}}\\ &\to \mathrm{\left[\left(K^-\pi^+\pi^0\right)_{D^0}\,\pi^+_{soft}\right]_{D^{*+}}\left(K_S^0\pi^-\right)_{D^-}}\\ &\to \mathrm{\left[\left(K_S^0\pi^+\pi^-\right)_{D^0}\,\pi^+_{soft}\right]_{D^{*+}}\left(K_S^0\pi^-\right)_{D^-}}\\ \\ &\to \mathrm{\left[(K^-\pi^+\pi^+)_{D^+}\,\pi^0_{soft}\right]_{D^{*+}}(K^+\pi^-\pi^-)_{D^-}}\\ &\to \mathrm{\left[\left(K_S^0\pi^+\right)_{D^+}\,\pi^0_{soft}\right]_{D^{*+}}(K^+\pi^-\pi^-)_{D^-}}\end{aligned} \tag{5.10}$$

- $B^0 \to D_s^+ D^{*-}$ decays are reconstructed as a control sample for $B^0 \to D^{*+} D^-$ decays in the following decay modes:

$$\begin{aligned}
B^0 \to D_s^+ D^{*-} &\to (K^+K^-\pi^+)_{D_s^+}\left[(K^+\pi^-)_{\bar{D}^0}\,\pi^-_{\text{soft}}\right]_{D^{*-}}\\
&\to (K^+K^-\pi^+)_{D_s^+}\left[(K^+\pi^-\pi^+\pi^-)_{\bar{D}^0}\,\pi^-_{\text{soft}}\right]_{D^{*-}}\\
&\to (K^+K^-\pi^+)_{D_s^+}\left[\left(K^+\pi^-\pi^0\right)_{\bar{D}^0}\,\pi^-_{\text{soft}}\right]_{D^{*-}}\\
&\to (K^+K^-\pi^+)_{D_s^+}\left[\left(K^0_S\pi^-\pi^+\right)_{\bar{D}^0}\,\pi^-_{\text{soft}}\right]_{D^{*-}}\\
\\
&\to \left(K^0_S K^+\right)_{D_s^+}\left[(K^+\pi^-)_{\bar{D}^0}\,\pi^-_{\text{soft}}\right]_{D^{*-}}\\
&\to \left(K^0_S K^+\right)_{D_s^+}\left[(K^+\pi^-\pi^+\pi^-)_{\bar{D}^0}\,\pi^-_{\text{soft}}\right]_{D^{*-}}\\
&\to \left(K^0_S K^+\right)_{D_s^+}\left[\left(K^+\pi^-\pi^0\right)_{\bar{D}^0}\,\pi^-_{\text{soft}}\right]_{D^{*-}}\\
&\to \left(K^0_S K^+\right)_{D_s^+}\left[\left(K^0_S\pi^-\pi^+\right)_{\bar{D}^0}\,\pi^-_{\text{soft}}\right]_{D^{*-}}\\
\\
&\to (K^+K^-\pi^+)_{D_s^+}\left[(K^+\pi^-\pi^-)_{D^-}\,\pi^0_{\text{soft}}\right]_{D^{*-}}\\
&\to (K^+K^-\pi^+)_{D_s^+}\left[\left(K^0_S\pi^-\right)_{D^-}\,\pi^0_{\text{soft}}\right]_{D^{*-}}
\end{aligned} \tag{5.11}$$

In total, neutral B mesons are reconstructed exclusively in 25 decay modes.

5.2 Study of Differences between Monte Carlo Simulations and Data

The definition and optimisation of selection requirements include the results of the study of differences between Monte Carlo simulations and data. The study covers a comparison of the mass and mass-difference distributions of each reconstructed D^0, D^+ and D^{*+} decay mode. In addition, the performance of the neural networks to suppress $e^+e^- \to q\bar{q}$ ($q \in \{u,d,s,c\}$) continuum events in Monte Carlo simulations and in data is studied using the control sample of $B^0 \to D_s^+ D^-$ decays.

5.2.1 D^0 and D^+ Mass Distributions

Differences between Monte Carlo simulations and data with respect to the D^0 and D^+ mass distributions can affect the branching fraction measurements, if the selection criteria are chosen too strict and thus the estimated reconstruction efficiencies determined by Monte Carlo simulations do not agree with those on data. The deviations of the D^0 and D^+ mass distributions in Monte Carlo simulations from the distributions in data are quantified using $e^+e^- \to c\bar{c}$ samples. For the study, $e^+e^- \to c\bar{c}$ samples are chosen instead of B decays, because the purity of decay modes associated with high background levels such as $D^0 \to K^-\pi^+\pi^0$ decays is enhanced.

$e^+e^- \to c\bar{c}$ events are selected by requiring the momentum of reconstructed D^0 and D^+ meson candidates to be $p^* > 2.3$ GeV/c in the center-of-mass frame. As a fit model the sum of a Gaussian function and a Crystal Ball function are applied. The results of the core widths $\sigma_{0,\mathrm{data}}$ in data and $\sigma_{0,\mathrm{MC}}$ in Monte Carlo simulations obtained from the fits are summarised in Table 5.1. In all reconstructed decay modes, the distributions in data are approximately 1.2-times broader than the distributions in Monte Carlo simulations. Examples of mass distributions in Monte Carlo simulations and in data for reconstructed $D^0 \to K^-\pi^+\pi^0$ and $D^+ \to K_S^0\pi^+$ decay modes and the corresponding projections of the fits are shown in Figures 5.1(a)-(d).

Decay mode	$\sigma_{0,\mathrm{data}}$ (MeV/c^2)	$\sigma_{0,\mathrm{MC}}$ (MeV/c^2)	$\sigma_{0,\mathrm{data}}/\sigma_{0,\mathrm{MC}}$
$D^0 \to K^-\pi^+$	5.51 ± 0.01	4.63 ± 0.01	1.188 ± 0.002
$D^0 \to K^-\pi^+\pi^-\pi^+$	4.28 ± 0.01	3.58 ± 0.01	1.196 ± 0.005
$D^0 \to K^-\pi^+\pi^0$	17.56 ± 0.12	15.02 ± 0.10	1.169 ± 0.011
$D^0 \to K_S^0\pi^+\pi^-$	5.24 ± 0.03	4.30 ± 0.02	1.219 ± 0.009
$D^+ \to K^-\pi^+\pi^+$	4.63 ± 0.01	3.89 ± 0.03	1.19 ± 0.01
$D^+ \to K_S^0\pi^+$	5.98 ± 0.05	5.02 ± 0.13	1.19 ± 0.02

Table 5.1: Fit results for the core widths $\sigma_{0,\mathrm{data}}$ in data and $\sigma_{0,\mathrm{MC}}$ in Monte Carlo simulations and their ratios for the reconstructed D^0 and D^+ decay modes. The results are obtained by fits to distributions from reconstructed $e^+e^- \to c\bar{c}$ samples ($p^* > 2.3$ GeV/c).

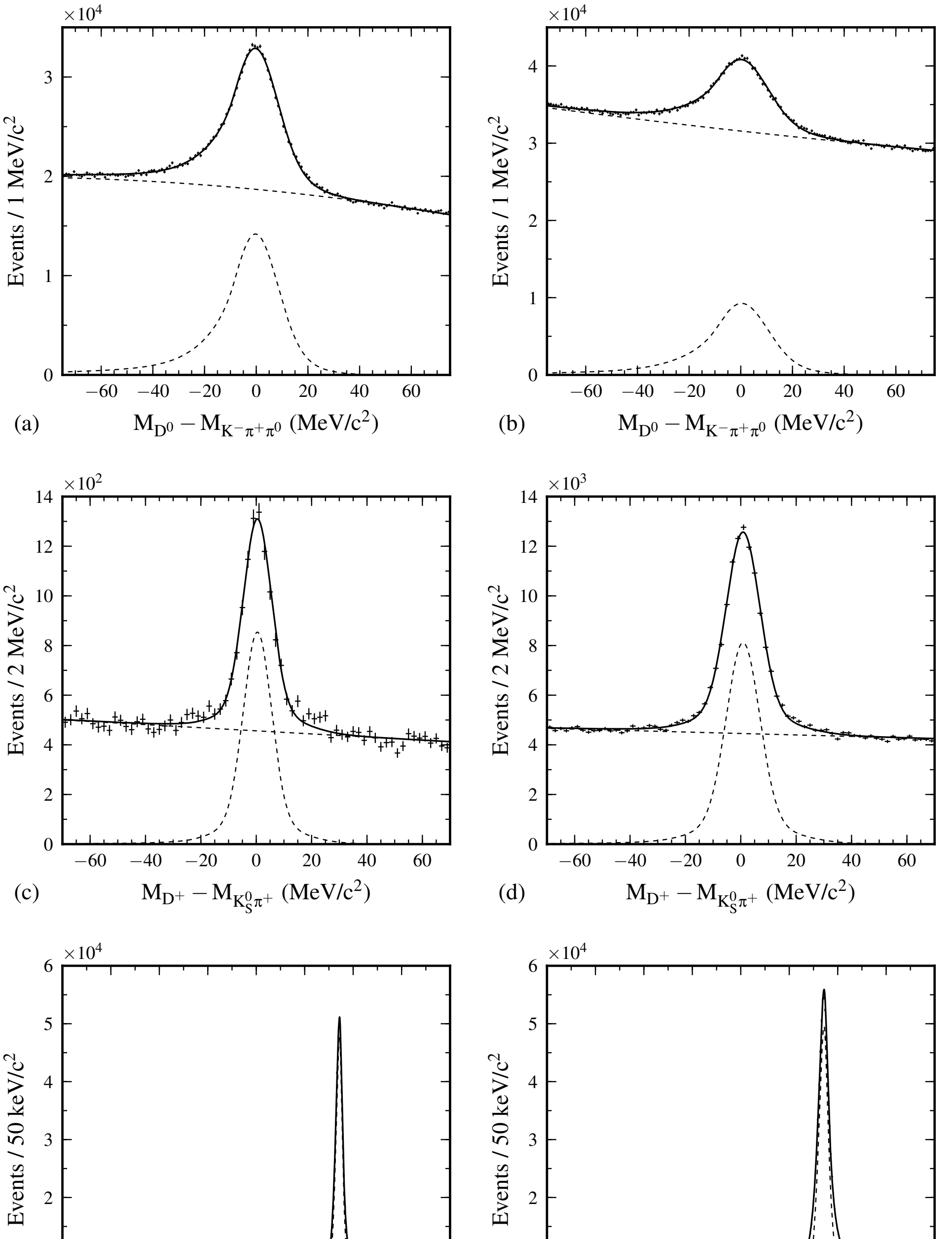

Figure 5.1: Examples of (a)-(b) D^0 mass, (c)-(d) D^+ mass and (e)-(f) D^{*+}-D^0 mass-difference distributions in MC simulations (left) and in data (right). The decays are reconstructed from $e^+e^- \to c\bar{c}$ samples ($p^* > 2.3$ GeV/c). The solid (dashed) lines show projections of all (signal and background) components in the fits.

5.2.2 D^{*+}-$D^{0/+}$ Mass-Difference Distributions

Differences between Monte Carlo simulations and data in the D^{*+}-$D^{0/+}$ mass-difference distributions are studied in a similar way as in the comparison of D^0 and D^+ mass distributions using $e^+e^- \to c\bar{c}$ samples. As a fit model a bifurcated Student's t-distribution is used. The results are summarised in Table 5.2. In all reconstructed D^{*+} decay modes, the distributions in data are broader than the corresponding distributions in Monte Carlo simulations. The distributions of D^{*+} decay modes reconstructed by combining D^0 mesons with charged soft pions are approximately 1.5-times broader in data than in the Monte Carlo simulations. The differences between Monte Carlo simulations and data in D^{*+} decay modes reconstructed by combining D^+ mesons with neutral soft pions are smaller. In these decay modes, the distributions in data are approximately 1.1-times broader than the distributions in Monte Carlo simulations. As an example for the comparison of the mass-difference distributions, the distributions for reconstructed $D^{*+} \to (K^-\pi^+\pi^-\pi^+)_{D^0}\pi^+_{soft}$ decays and the corresponding projections of the fits are shown in Figures 5.1(e)-(f).

Decay mode	$\sigma_{0,data}$ (keV/c^2)	$\sigma_{0,MC}$ (keV/c^2)	$\sigma_{0,data}/\sigma_{0,MC}$
$D^{*+} \to (K^-\pi^+)_{D^0}\pi^+_{soft}$	249.5 ± 0.4	166.0 ± 0.3	1.503 ± 0.004
$D^{*+} \to (K^-\pi^+\pi^-\pi^+)_{D^0}\pi^+_{soft}$	250.0 ± 0.6	166.4 ± 0.4	1.503 ± 0.005
$D^{*+} \to \left(K^-\pi^+\pi^0\right)_{D^0}\pi^+_{soft}$	398.5 ± 7.1	299.8 ± 0.9	1.329 ± 0.024
$D^{*+} \to \left(K^0_S\pi^+\pi^-\right)_{D^0}\pi^+_{soft}$	256.9 ± 1.0	175.5 ± 0.8	1.464 ± 0.009
$D^{*+} \to (K^-\pi^+\pi^+)_{D^+}\pi^0_{soft}$	798.1 ± 7.9	716.6 ± 6.2	1.114 ± 0.015
$D^{*+} \to \left(K^0_S\pi^+\right)_{D^+}\pi^0_{soft}$	781.5 ± 19.5	726.5 ± 16.9	1.076 ± 0.037

Table 5.2: Fit results for the widths $\sigma_{0,data}$ in data and $\sigma_{0,MC}$ in Monte Carlo simulations and their ratios for D^{*+}-$D^{0/+}$ mass-difference distributions. The results are obtained by fits to distributions from reconstructed $e^+e^- \to c\bar{c}$ samples ($p^* > 2.3$ GeV/c).

5.2.3 Continuum Network

In the reconstruction of $B^0 \to D^+D^-$ decays, the major source of background arises from continuum events. In Section 4.6, the developed hierarchical set of neural networks to discriminate between $e^+e^- \to q\bar{q}$ ($q \in \{u,d,s,c\}$) continuum and $B\bar{B}$ events is described. The neural networks are trained with input from distributions of variables that characterise the event shapes. The distributions are obtained from Monte Carlo simulations. To check, whether the neural networks perform the same on data distributions as on simulated distributions, a comparison of the neural networks using $B^0 \to D_s^+D^-$ decays is performed. $B^0 \to D_s^+D^-$ decays provide a kinematically similar control sample to $B^0 \to D^+D^-$ decays.

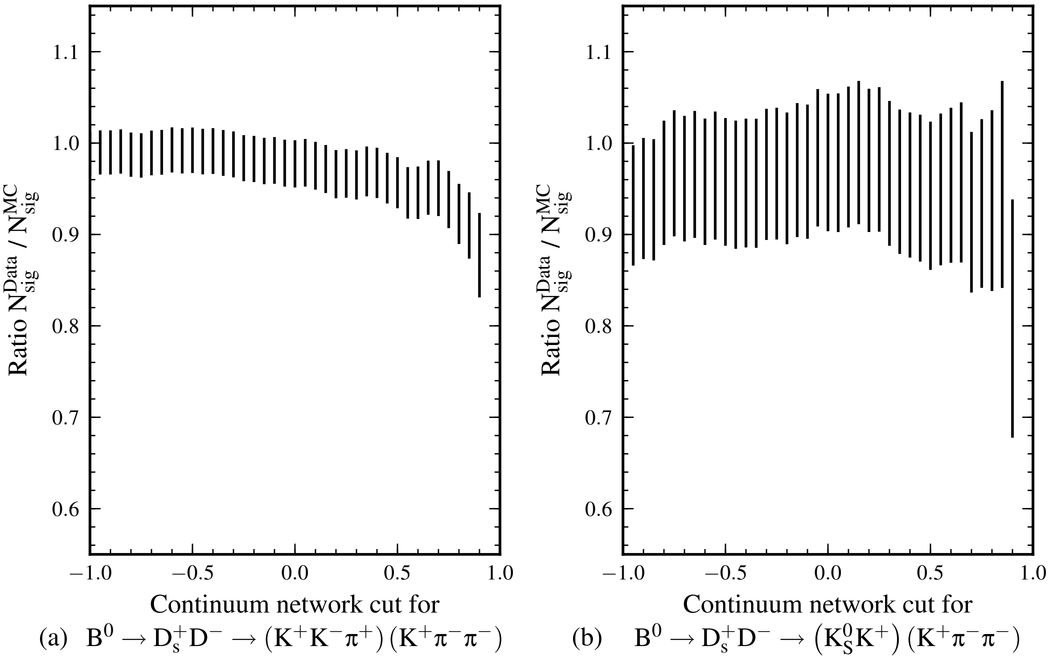

Figure 5.2: Ratio of signal yields in data and in Monte Carlo simulations dependent on the selection requirement on the final continuum network for (a) $B^0 \to D_s^+D^- \to (K^+K^-\pi^+)(K^+\pi^-\pi^-)$ and (b) $B^0 \to D_s^+D^- \to (K^+K^-\pi^+)\left(K_S^0\pi^-\right)$ decays.

For both reconstructed $B^0 \to D^+D^-$ decay modes, the signal yields in Monte Carlo simulations and in data of the corresponding $B^0 \to D_s^+D^-$ control samples are extracted by unbinned extended two-dimensional maximum likelihood fits of the M_{bc} and ΔE distributions. The signal yields are extracted for different selection requirements on the final neural network of the continuum suppression. Figure 5.2 shows the ratio of signal yields in data and in Monte Carlo simulations for both decay modes dependent on the selection requirement. The ratios without selection requirements for both decay modes are close to one as expected, because the signal decays in Monte Carlo simulations have been generated according to the branching fractions in data. The ratios remain constant over a wide range of possible cut values. The selection requirements on the neural network applied at a later stage of the measurements are at negative cut values, see Figure 5.10. Therefore, the neural networks are considered to perform comparable for data distributions as for distributions from Monte Carlo simulations.

5.3 Selection Requirements

Selection criteria are applied at all stages of the reconstruction from charged tracks over intermediate particles such as π^0, K^0_S, D^0, D^+, D^{*+} and D^+_s mesons to B^0 mesons in order to increase the signal purity of the measurements. In the following, all selection requirements applied in the analysis are described.

5.3.1 Track Impact Parameters

A standard requirement on the impact parameter of charged tracks is applied to remove tracks that do not originate from the interaction point. The reconstructed tracks of charged particles forming π^+ and K^+ meson candidates are required to have a transverse (longitudinal) distance of closest approach to the interaction point of less than 2 (4) cm. This requirement is not applied to π^+_{soft} mesons from D^{*+} decays because of the low resolution of low momentum particles.

5.3.2 Particle Identification

The selection requirements on the particle identification are determined in a global optimisation procedure. The optimisation is realised by a multidimensional scan that performs parallel cut variations of particle identification variables such as the pion-ID, kaon-ID and electron-ID. The pion-ID and kaon-ID allow to separate between π^+ and K^+ mesons by combining measurements of energy deposition in the CDC and measurements of the ACC and TOF in a likelihood-ratio approach. The electron-ID allows to identify charged tracks as electrons by additionally taking into account the measurements of shower shapes and energy deposit in the ECL. Charged tracks identified as electrons are rejected.

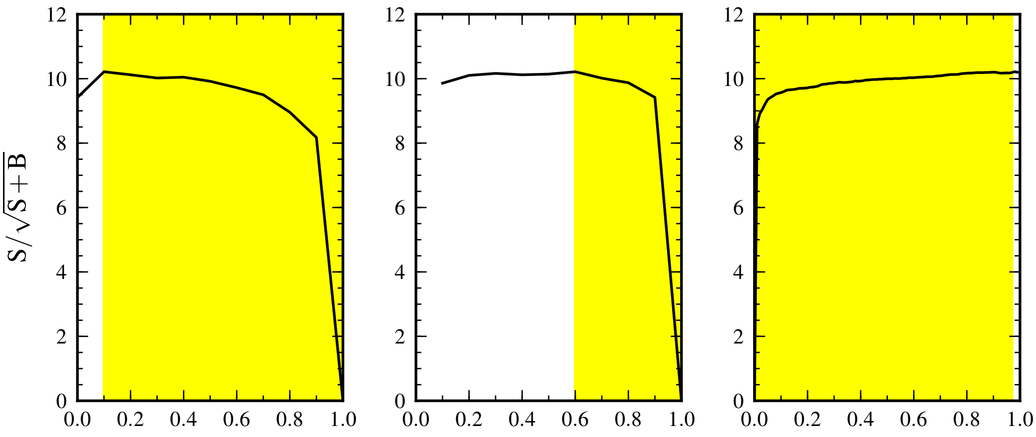

(a) Pion-ID selection (b) Kaon-ID selection (c) Electron-ID selection

Figure 5.3: Result of the multidimensional optimisation of selection requirements for particle identification realised by parallel cut variations. Each figure is a projection on one of the variables while keeping all other selection requirements at the identified optimal point. The yellow bands highlight the selected regions.

The optimisation is performed for the $B^0 \to D^+D^- \to (K^-\pi^+\pi^+)(K^+\pi^-\pi^-)$ decay mode. This decay mode provides the main contribution to the $B^0 \to D^+D^-$ analysis. To determine the best working point for the selection requirements on the particle identification variables and to allow the optimisation procedure to find a global maximum, additionally other selection variables, such as D^+ masses and continuum suppression requirements, are included in the optimisation.

Because the $B^0 \to D^+D^-$ samples have relatively low statistics, the samples are enriched in signal and background events to avoid statistical fluctuations. The optimisation is performed with respect to a figure of merit in terms of the significance $S/\sqrt{S+B}$. To account for the enrichment of signal and background events, appropriate scaling factors are applied in the calculation. The dependence of the significance on the selection requirements for single particle identification quantities is shown in Figure 5.3(a)-(c). In each figure, all other selection requirements are fixed to the identified optimal point. The yellow bands highlight the selected regions. The selection requirements corresponding to the identified optimal working point are applied to the particle identification of charged tracks.

The chosen selection requirements have a kaon (pion) identification efficiency of 91% (99%) with an associated pion (kaon) misidentification rate of 2% (18%). No selection requirements on particle identification variables are applied to π^+_{soft} mesons from D^{*+} decays.

5.3.3 π^0 Mesons

The photons forming π^0 candidates are required to have a minimal energy of 30 MeV. The invariant mass of photon pairs is required to be within 15 MeV/c^2 of the nominal π^0 mass. This mass window corresponds to a width of 3.3σ of the π^0 mass distribution on data. An experimental $M_{\gamma\gamma}$ spectrum obtained on data is shown in Figure 5.4.

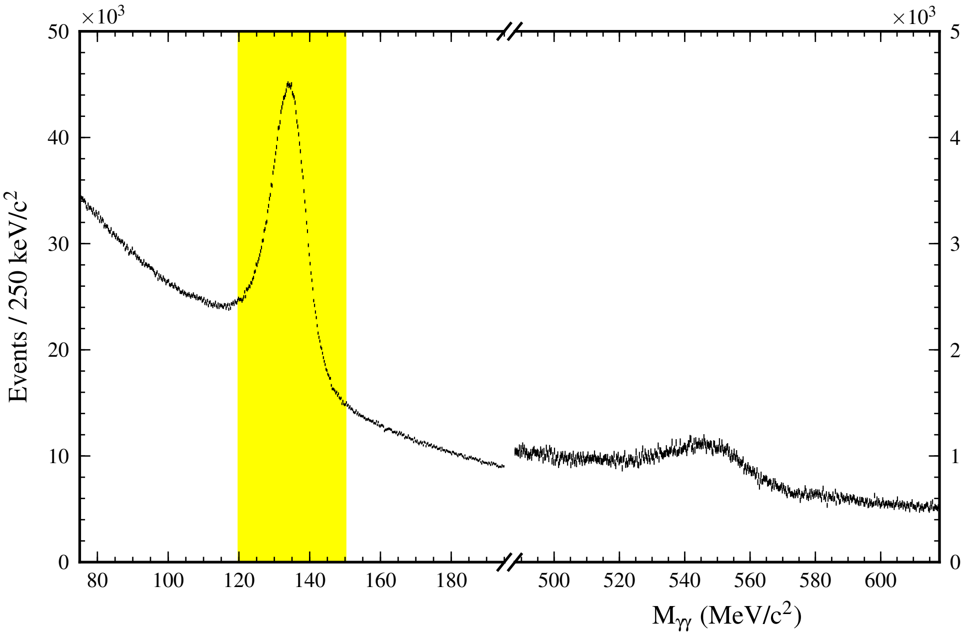

Figure 5.4: Invariant mass spectrum of two photons for the mass regions of π^0 (left) and η (right) mesons. The mass region used to select π^0 mesons is highlighted by a yellow band.

5.3.4 K_S^0 Mesons

The selection requirements on K_S^0 meson candidates reconstructed from two oppositely charged pions consider the possible displacement of the decay vertex from the interaction point.

The following four variables characterise the displacement:

dr: Minimum value of the impact parameters of the two pions with respect to the interaction point.

z_dist: Distance between the pion tracks in z-direction at their interception point in the xy-plane.

dϕ: Azimuthal angle between the momentum and the decay vertex vector of a K_S^0 candidate.

fl: Flight length of the K_S^0 candidate in the xy-plane.

The applied selection requirements are chosen dependent on the momentum of the K_S^0 candidate and are summarised in Table 5.3. In addition, the invariant mass of the K_S^0 candidate is

Momentum (GeV/c)	dr (cm)	z_dist (cm)	dϕ (rad)	fl (cm)
< 0.5	> 0.05	< 0.8	< 0.3	-
$0.5 - 1.5$	> 0.03	< 1.8	< 0.1	> 0.08
> 1.5	> 0.02	< 2.4	< 0.3	> 0.22

Table 5.3: Momentum-dependent selection requirements on K^0_S candidates [108].

required to be within 15 MeV/c^2 of the nominal K^0_S mass. This mass window corresponds to a width of 5.8σ of the K^0_S mass distribution on data.

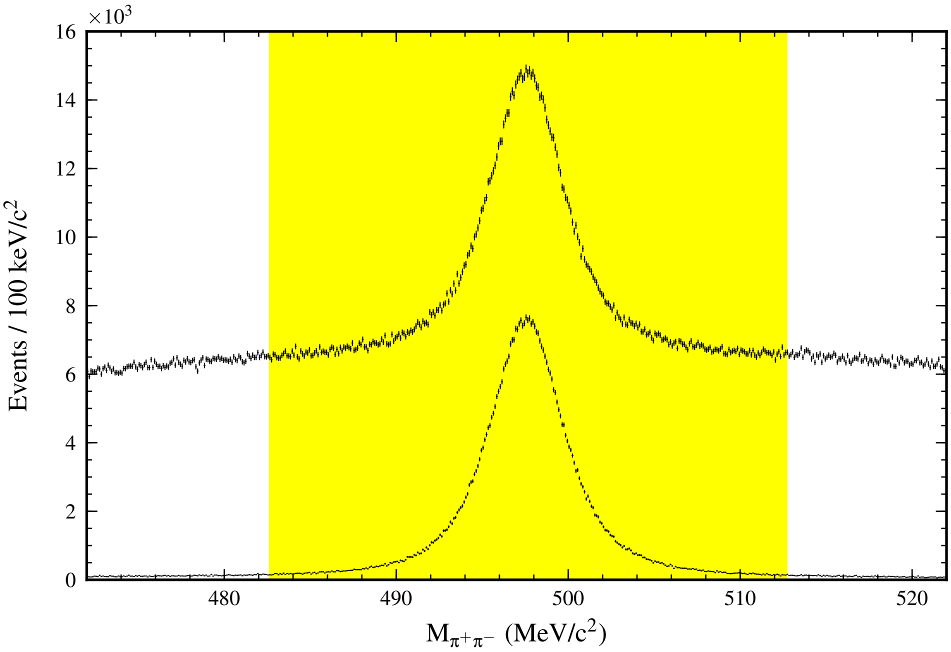

Figure 5.5: Invariant mass spectrum of two oppositely charged pions before and after applying the momentum-dependent selection requirements on K^0_S candidates. The yellow band highlights the selected mass region.

The effect of the K^0_S selection is shown for $M_{\pi^+\pi^-}$ data distributions in Figure 5.5. After applying the above requirements, the correct K^0_S candidate is selected with an efficiency of 82% and a purity of 93%.

5.3.5 D^0 and D^+ Mesons

D^0 and D^+ mesons are selected by requirements on the reconstructed invariant masses of the candidates. The requirements on D^0 and D^+ masses are chosen to select mass regions corresponding to a width of approximately 3σ or more in the data distributions. The study of difference between Monte Carlo simulations and data described in Section 5.2.1 is taken into account in the definition of the selection requirements. The applied selection requirements and the corresponding widths in the data distributions are:

$$\begin{aligned}
\left|M_{D^0} - M_{K^-\pi^+}\right| &< 15\ \mathrm{MeV}/c^2 \quad (3.3\sigma) \\
\left|M_{D^0} - M_{K^-\pi^+\pi^-\pi^+}\right| &< 15\ \mathrm{MeV}/c^2 \quad (3.7\sigma) \\
\left|M_{D^0} - M_{K^-\pi^+\pi^0}\right| &< 32\ \mathrm{MeV}/c^2 \quad (3.0\sigma) \\
\left|M_{D^0} - M_{K^0_S\pi^+\pi^-}\right| &< 15\ \mathrm{MeV}/c^2 \quad (3.3\sigma)
\end{aligned} \tag{5.12}$$

$$\begin{aligned}
\left|M_{D^+} - M_{K^-\pi^+\pi^+}\right| &< 12\ \mathrm{MeV}/c^2 \quad (3.4\sigma) \\
\left|M_{D^+} - M_{K^0_S\pi^+}\right| &< 12\ \mathrm{MeV}/c^2 \quad (2.9\sigma)
\end{aligned} \tag{5.13}$$

The data distributions of invariant masses of the reconstructed D^0 and D^+ modes obtained in $e^+e^- \to c\bar{c}$ samples and the applied selection requirements are shown in Figure 5.6.

5.3.6 D^{*+} Mesons

The difference in masses between reconstructed D^{*+} and D^0 and between D^{*+} and D^+ mesons are used to select D^{*+} mesons. The requirements on D^{*+}-D^0 and D^{*+}-D^+ mass-difference distributions are chosen to select mass-difference regions corresponding to a width of approximately 3σ or more in the data distributions. The study of differences between Monte Carlo simulations and data described in Section 5.2.2 is taken into account in the definition of the following selection requirements:

$$\begin{aligned}
\left|\Delta M_{PDG} - M_{\left[(K^-\pi^+)_{D^0}\pi^+_{soft}\right]_{D^{*+}}} - M_{(K^-\pi^+)_{D^0}}\right| &< 1.5\ \mathrm{MeV}/c^2 \quad (3.7\sigma) \\
\left|\Delta M_{PDG} - M_{\left[(K^-\pi^+\pi^-\pi^+)_{D^0}\pi^+_{soft}\right]_{D^{*+}}} - M_{(K^-\pi^+\pi^-\pi^+)_{D^0}}\right| &< 2.0\ \mathrm{MeV}/c^2 \quad (4.6\sigma) \\
\left|\Delta M_{PDG} - M_{\left[(K^-\pi^+\pi^0)_{D^0}\pi^+_{soft}\right]_{D^{*+}}} - M_{(K^-\pi^+\pi^0)_{D^0}}\right| &< 2.0\ \mathrm{MeV}/c^2 \quad (3.2\sigma) \\
\left|\Delta M_{PDG} - M_{\left[(K^0_S\pi^+\pi^-)_{D^0}\pi^+_{soft}\right]_{D^{*+}}} - M_{(K^0_S\pi^+\pi^-)_{D^0}}\right| &< 1.5\ \mathrm{MeV}/c^2 \quad (3.6\sigma)
\end{aligned} \tag{5.14}$$

$$\begin{aligned}
\left|\Delta M_{PDG} - M_{\left[(K^-\pi^+\pi^+)_{D^+}\pi^0_{soft}\right]_{D^{*+}}} - M_{(K^-\pi^+\pi^+)_{D^+}}\right| &< 2.5\ \mathrm{MeV}/c^2 \quad (3.1\sigma) \\
\left|\Delta M_{PDG} - M_{\left[(K^0_S\pi^+)_{D^+}\pi^0_{soft}\right]_{D^{*+}}} - M_{(K^0_S\pi^+)_{D^+}}\right| &< 2.5\ \mathrm{MeV}/c^2 \quad (3.2\sigma)
\end{aligned} \tag{5.15}$$

The data distributions of D^{*+}-D^0 and D^{*+}-D^+ mass-differences of the reconstructed D^{*+} decay modes obtained in $e^+e^- \to c\bar{c}$ samples and the applied selection requirements are shown in Figure 5.7.

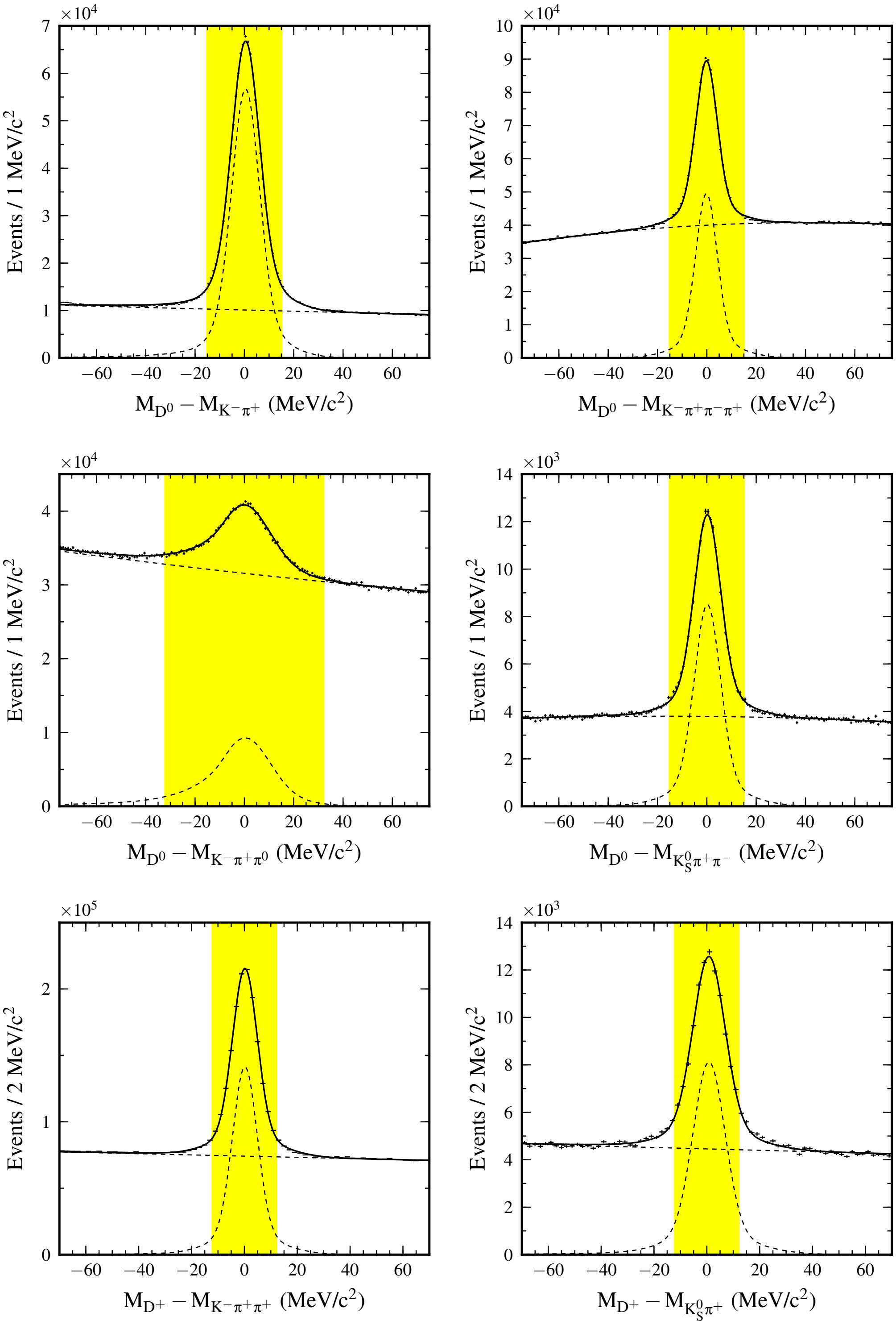

Figure 5.6: Invariant mass distributions of D^0 and D^+ candidates in all reconstructed decay modes. The distributions are obtained on $e^+e^- \to c\bar{c}$ data samples ($p^* > 2.3$ GeV/c). The solid (dashed) lines show projections of all (signal and background) components in the fits. The yellow bands highlight the selected mass regions.

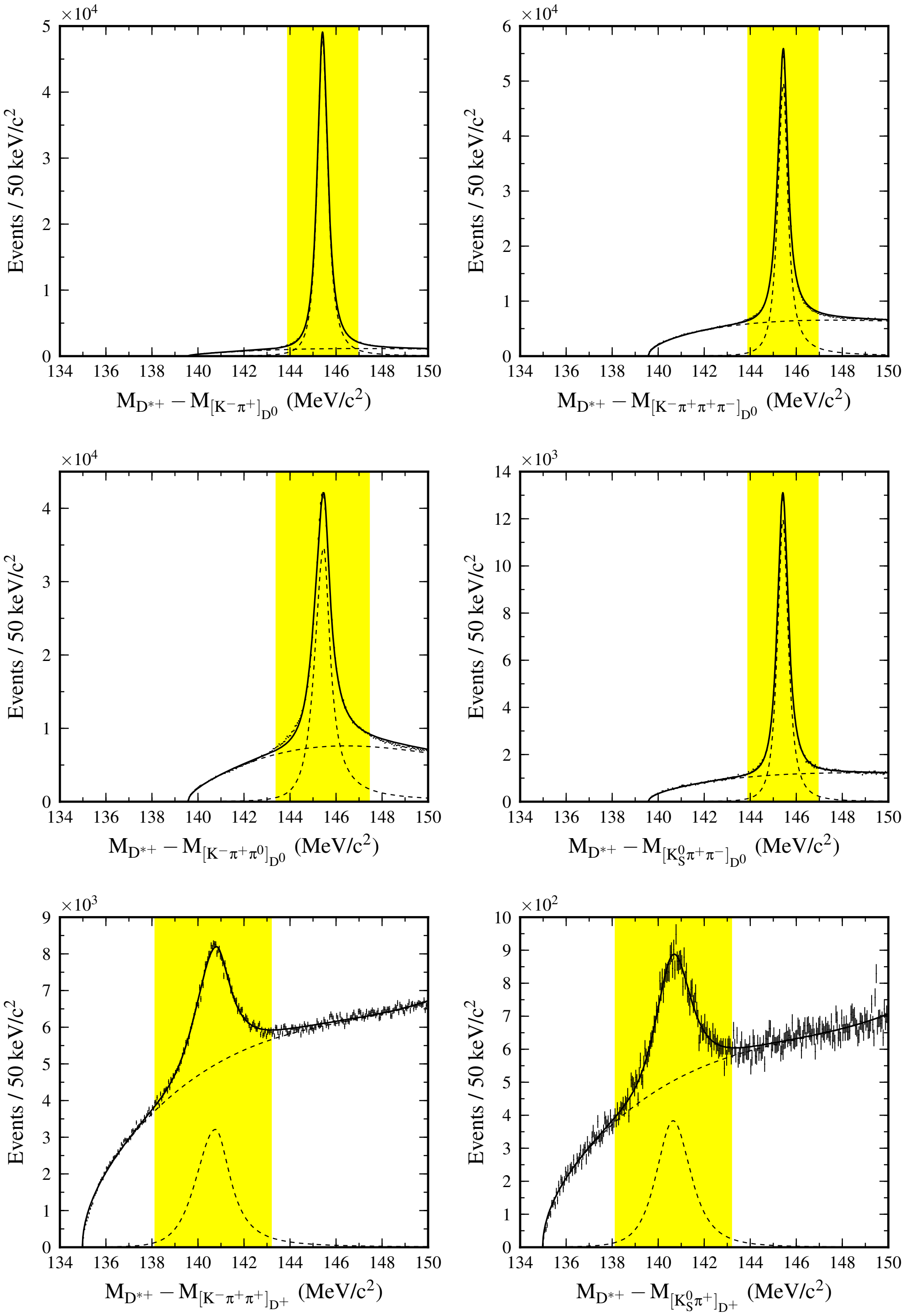

Figure 5.7: Invariant D^{*+}-D^0 and D^{*+}-D^+ mass-difference distributions of all reconstructed D^{*+} decay modes. The distributions are obtained on $e^+e^- \rightarrow c\bar{c}$ data samples ($p^* > 2.3$ GeV/c). The solid (dashed) lines show projections of all (signal and background) components in the fits. The yellow bands highlight the selected regions.

5.3.7 D_s^+ Mesons

The same selection requirements on the invariant mass of reconstructed D_s^+ meson candidates are chosen as on the corresponding D^+ decay modes. Additionally, the $\phi(1020)$ and $\bar{K}^*(892)^0$ bands are selected in the $D_s^+ \to K^+K^-\pi^+$ decay mode by the following requirements:

$$\begin{aligned} \left|M_{\phi(1020)} - M_{K^+K^-}\right| &< 20\ \mathrm{MeV/c^2} \\ \left|M_{\bar{K}^*(892)^0} - M_{K^-\pi^+}\right| &< 100\ \mathrm{MeV/c^2} \end{aligned} \tag{5.16}$$

The resonant substructure of $D_s^+ \to K^+K^-\pi^+$ decays and the selected $\phi(1020)$ and $\bar{K}^*(892)^0$ bands obtained in $e^+e^- \to c\bar{c}$ data samples are shown in Figure 5.8.

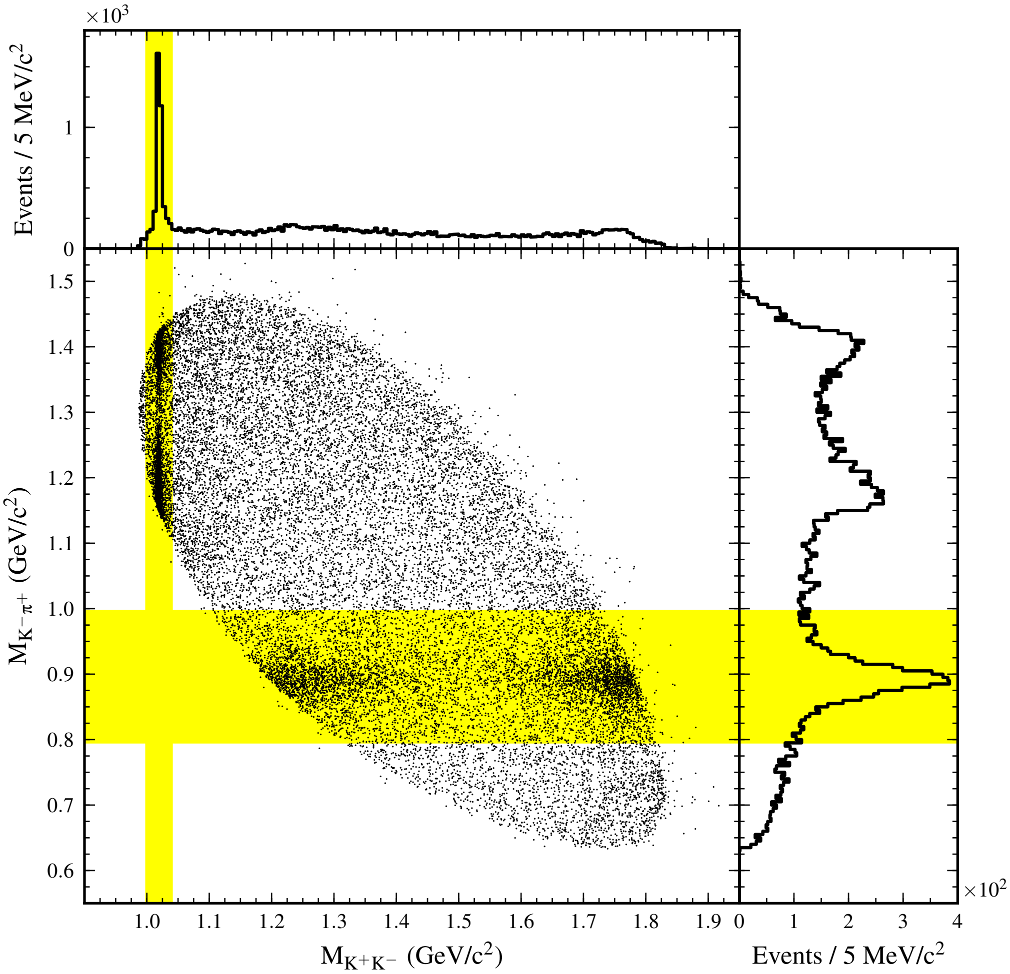

Figure 5.8: Invariant $M_{K^+K^-}$ and $M_{K^-\pi^+}$ distributions of reconstructed $D_s^+ \to K^+K^-\pi^+$ decays obtained in $e^+e^- \to c\bar{c}$ data samples ($p^* > 2.3$ GeV/c). The yellow regions highlight the $\phi(1020)$ and $\bar{K}^*(892)^0$ bands selected in the resonant substructure.

5.3.8 B^0 Mesons

B^0 mesons are selected by the beam-energy-constrained mass M_{bc} and the energy difference ΔE defined in Equations 4.27 and 4.28. The distributions of M_{bc} and ΔE observables from inclusive Monte Carlo simulations for reconstructed $B^0 \to D^+D^-$ decays are shown in Figure 5.9.

The following regions are selected:

$$5.2\ \mathrm{GeV}/c^2 < M_{bc} < 5.3\ \mathrm{GeV}/c^2$$
$$-50\ \mathrm{MeV} < \Delta E < 100\ \mathrm{MeV}$$

The lower boundary for ΔE is chosen to exclude reflections from misidentified $B^0 \to D_s^+D^{(*)-}$ decays that populate the M_{bc} signal region at $\Delta E \approx -75$ MeV in the reconstruction of $B^0 \to D^+D^{(*)-}$ decays.

The M_{bc} and ΔE observables allow to define a signal region. In the present analysis, the signal region is defined by:

$$\begin{aligned} 5.273\ \mathrm{GeV}/c^2 < M_{bc} <&\ 5.289\ \mathrm{GeV}/c^2 \\ \left|\Delta E\right| <&\ 30\ \mathrm{MeV} \end{aligned} \qquad (5.17)$$

5.3.9 Selection of Best B^0 Candidates

After applying the above selection requirements, 12% of the signal events in reconstructed $B^0 \to D^+D^-$ decays and 16% of the signal events in reconstructed $B^0 \to D^{*\pm}D^{\mp}$ decays contain more than one B^0 candidate. In the case of multiple reconstructed B^0 candidates in an event, a candidate, referred to as best B^0 candidate, is chosen dependent on a χ^2 condition. The χ^2 condition is constructed to minimise the quadratic sum of deviations of reconstructed masses of $D^{0/+}$ daughters and mass-differences of D^{*+} daughters from nominal values measured in units of the width of corresponding signal peaks.

The χ^2 condition applied in $B^0 \to D^+D^-$ is given by

$$\chi^2 = \left(\frac{M_{D^+} - M_{D^+,PDG}}{\sigma_{D^+}}\right)^2 + \left(\frac{M_{D^-} - M_{D^-,PDG}}{\sigma_{D^-}}\right)^2, \qquad (5.18)$$

and the χ^2 condition applied in $B^0 \to D^{*\pm}D^{\mp}$ is given by

$$\chi^2 = \left(\frac{M_{D^-} - M_{D^-,PDG}}{\sigma_{M_{D^-}}}\right)^2 + \left(\frac{M_{D^{0/+}} - M_{D^{0/+},PDG}}{\sigma_{M_{D^{0/+}}}}\right)^2 + \left(\frac{\Delta M_{D^{*+}-D^{0/+}} - \Delta M_{D^{*+}-D^{0/+},PDG}}{\sigma_{\Delta M_{D^{*+}-D^{0/+}}}}\right)^2. \qquad (5.19)$$

The widths of the signal peaks σ_{D^+}, σ_{D^0} and $\sigma_{\Delta M_{D^{*+}-D^{0/+}}}$ are determined using simulated signal decays for each reconstructed D^+, D^0 and D^{*+} decay mode and are summarised in Tables 5.4 and 5.5.

The performance of the applied method is evaluated for every reconstructed B^0 decay mode.

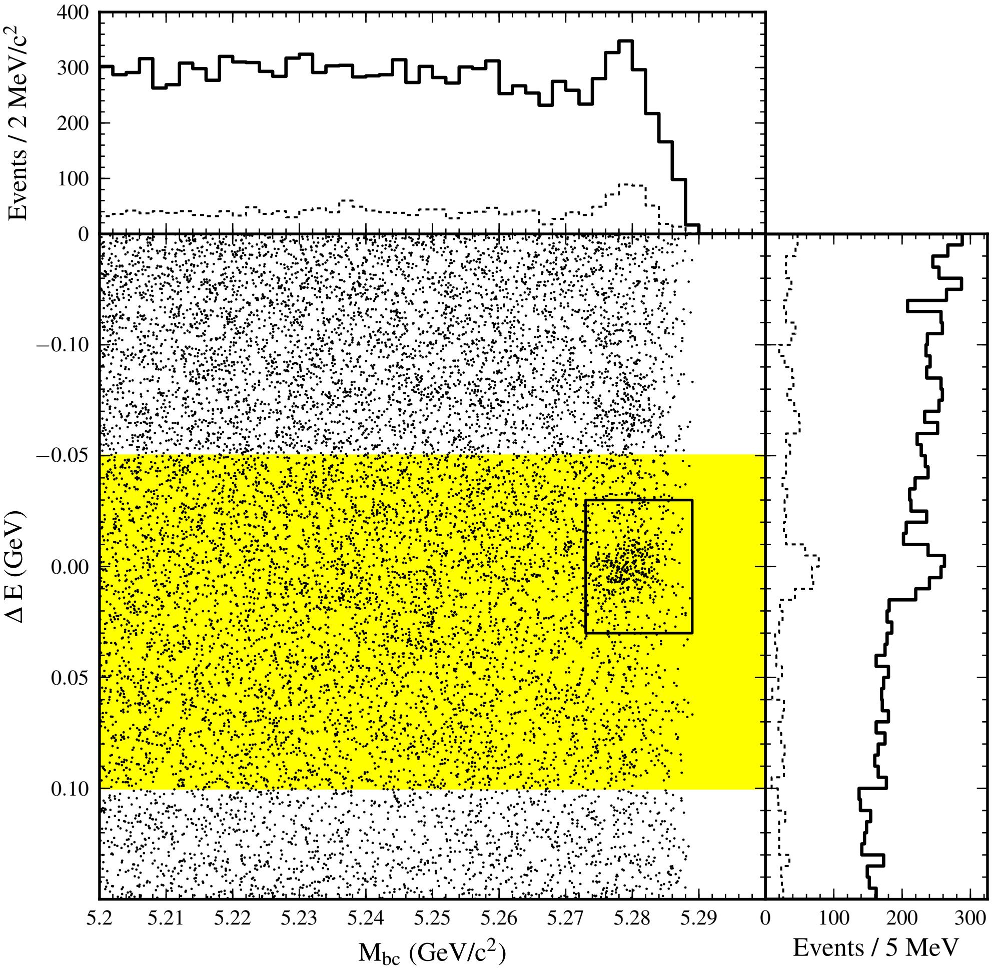

Figure 5.9: Distributions of M_{bc} and ΔE observables from Monte Carlo simulations containing $B^0 \rightarrow D^+D^-$ signal decays and background. The rectangle drawn by the solid black line represents the defined signal region and the yellow band represent the selected M_{bc} and ΔE regions. In the histograms, the dotted lines show projections of one observable within the signal region of the other observable, while the solid lines show all events.

In total, the method selects in case of multiple B^0 candidates in an event the correct signal candidate with a probability of 96% in $B^0 \rightarrow D^+D^-$ and of 92% in $B^0 \rightarrow D^{*\pm}D^{\mp}$.

Decay mode	$\mu_{M_{\mathrm{rec}}-M_{\mathrm{PDG}}}$ (MeV/c^2)	σ_0 (MeV/c^2)	f(σ_0)	n	α	σ_1 (MeV/c^2)
$D^+ \to K^-\pi^+\pi^+$	-0.334 ± 0.002	3.48 ± 0.04	0.75 ± 0.01	2.0	1.88 ± 0.06	9.56 ± 0.30
$D^+ \to K^0_S\pi^+$	0.117 ± 0.004	4.12 ± 0.04	0.75 ± 0.01	2.0	1.67 ± 0.04	10.90 ± 0.34
$D^0 \to K^-\pi^+$	0.168 ± 0.0234	3.87 ± 0.04	0.73 ± 0.01	2.0	1.42 ± 0.03	9.18 ± 0.28
$D^0 \to K^-\pi^+\pi^-\pi^+$	-0.572 ± 0.0237	9.33 ± 0.29	0.26 ± 0.01	2.0	5.00 ± 4.99	3.39 ± 0.04
$D^0 \to K^-\pi^+\pi^0$	-0.068 ± 0.0171	16.06 ± 2.12	0.23 ± 0.06	2.0	0.99 ± 0.08	9.03 ± 0.46
$D^0 \to K^0_S\pi^+\pi^-$	-0.298 ± 0.0029	3.78 ± 0.05	0.74 ± 0.01	2.0	2.00 ± 0.07	10.09 ± 0.35

Table 5.4: Result of fits to mass distributions of simulated decays in all reconstructed D^+ and D^0 modes. The signal is parameterised by the sum of a Gaussian function (σ_0) and a Crystal Ball function (n, α, σ_1). When comparing σ_0 and σ_1, the more narrow width is used for the best B^0 candidate selection.

Decay mode	$\mu_{\Delta M}$ (MeV/c^2)	$\sigma_{\Delta M}$ (keV/c^2)	$\delta_{\sigma_{\Delta M}}$	$n^l_{\Delta M}$	$n^r_{\Delta M}$
$D^{*+} \to (K^-\pi^+)_{D^0}\,\pi^+_{\mathrm{soft}}$	145.370 ± 0.003	273.7 ± 1.3	0.137 ± 0.008	1.37 ± 0.03	1.93 ± 0.04
$D^{*+} \to (K^-\pi^+\pi^-\pi^+)_{D^0}\,\pi^+_{\mathrm{soft}}$	145.390 ± 0.005	291.3 ± 2.6	0.111 ± 0.013	0.76 ± 0.05	2.01 ± 0.08
$D^{*+} \to \left(K^-\pi^+\pi^0\right)_{D^0}\,\pi^+_{\mathrm{soft}}$	145.440 ± 0.000	472.8 ± 0.0	0.073 ± 0.001	0.55 ± 0.00	2.31 ± 0.00
$D^{*+} \to \left(K^0_S\pi^+\pi^-\right)_{D^0}\,\pi^+_{\mathrm{soft}}$	145.370 ± 0.006	283.7 ± 2.5	0.148 ± 0.015	1.45 ± 0.07	2.09 ± 0.10
$D^{*+} \to (K^-\pi^+\pi^+)_{D^+}\,\pi^0_{\mathrm{soft}}$	140.710 ± 0.035	714.2 ± 5.9	0.069 ± 0.036	1.22 ± 0.14	5.10 ± 0.60
$D^{*+} \to \left(K^0_S\pi^+\right)_{D^+}\,\pi^0_{\mathrm{soft}}$	140.710 ± 0.013	718.5 ± 5.6	0.017 ± 0.014	2.26 ± 0.19	3.70 ± 0.16

Table 5.5: Result of fits to D^{*+}-$D^{0/+}$ mass-difference distributions in simulated decays in all reconstructed D^{*+} modes. The signal is parameterised by a bifurcated Student's t-distribution. The width $\sigma_{\Delta M}$ is used for the best B^0 candidate selection.

5.3.10 Kinematic Vertex Fits and SVD Hit Requirements

Due to their importance for the time-dependent measurements, the algorithms and methods for reconstructing decay vertices by kinematic fits are described in detail in Section 4.1. In the following, the procedure of the reconstruction of decay vertices and the selection requirements on vertex fit quantities and on the minimal number of SVD hits applied in time-dependent measurements are summarised.

The decay vertices of reconstructed particles are determined in the following way:

π^0 mesons: In a kinematic fit, the photon daughters are required to originate from IP tube and the reconstructed mass is constrained to the nominal mass of π^0 mesons.

K_S^0 mesons: The charged pion daughters are required to originate from a common vertex. No constraints are applied to the reconstruction of K_S^0 decay vertices.

D^0, D^+ and D_s^+ mesons: The daughter particles are required to originate from a common vertex. No constraints are applied to the reconstruction of D^0, D^+ and D_s^+ decay vertices.

D^{*+} mesons: The decay vertices of D^{*+} mesons are determined by a kinematic fit of the D daughters with the constraint to originate from IP tube. The momentum resolution of soft pions from D^{*+} decays and consequently the resolution of D^{*+}-$D^{0/+}$ mass-difference distributions are improved by a kinematic fit in which the soft pions are constrained to originate from the D^{*+} decay vertex.

B^0 mesons: The decay vertex of B^0 mesons on reconstruction-side is reconstructed by a kinematic fit of the D daughters to a common vertex. The D daughters are constrained to originate from IP tube.

In the time-dependent measurements, selection requirements on the reconstructed decay vertices are applied. The requirements comprise the Δt range, the vertex fit quality indicator h and the uncertainty σ_z of reconstructed decay vertices of B mesons on reconstruction- and on tagging-side. The selection requirements on h and σ_z are chosen in such a way that signal and background distributions of these variables are in agreement to minimise the Punzi effect [109]. This effect can lead to wrong signal and background fractions in the likelihood function and consequently to biases in the time-dependent measurements when the distributions of the quantities used on an event-by-event basis differ for signal and background components.

In addition, a requirement on the minimal number of SVD hits of charged tracks used in the reconstruction of D daughters is applied. The standard requirement in time-dependent measurements at the Belle experiment is that any charged track has to be associated with ≥ 1 SVD hit in $r\phi$ and ≥ 2 SVD hits in z direction. Due to the high multiplicity of charged tracks in the present analysis, this requirement would decrease the signal efficiency by approximately 20%. Following previous studies of the Δz resolution in B decays to double-charm modes [110, 111], this requirement is relaxed.

The following selection requirements are applied:

Δt range:	$\lvert\Delta t\rvert < 70$ ps	
Reconstruction-side:	$0 < h < 50$ and $0 < \sigma_z < 200$ µm	
Tagging-side:	$0 < h < 50$ and $0 < \sigma_z < 200$ µm	for multi-track vertices
	no cut on h and $0 < \sigma_z < 500$ µm	for single-track vertices
SVD hit requirements:	at least one D meson has to be reconstructed by at least 2 tracks associated with ≥ 1 SVD hit in $r\phi$ and ≥ 2 SVD hits in z	

The above requirements reduce the reconstruction efficiency in $B^0 \to D^+D^-$ by 12% and in $B^0 \to D^{*\pm}D^{\mp}$ by 14%. Therefore the selection requirements are applied only in the time-dependent and not in the time-integrated measurements, such as the measurements of branching fractions.

5.3.11 Continuum Suppression

In $B^0 \to D^+D^-$, unlike in $B^0 \to D^{*\pm}D^{\mp}$, the major source of background arises from $e^+e^- \to q\bar{q}$ ($q \in \{u, d, s, c\}$) continuum events. Inside the D mass, M_{bc} and ΔE signal region and without a requirement on the continuum suppression, the background of reconstructed $B^0 \to D^+D^-$ decays is composed of 25% background from neutral B decays, of 10% background from charged B decays, of 47% continuum background from charm-quarks and of 18% continuum background from up-, down- or strange-quarks. The continuum background in $B^0 \to D^+D^-$ is suppressed by a hierarchical arrangement of neural networks, implemented by the NeuroBayes package [107], that combines information about the event topology. The developed continuum suppression is described in detail in Section 4.6.

	Requirement on neural network		Background	Signal
Decay mode	$0 \leq r \leq 0.75$	$0.75 < r \leq 1$	rejected	kept
$B^0 \to D^+D^- \to (K^-\pi^+\pi^+)(K^+\pi^-\pi^-)$	−0.2	−0.8	69%	91%
$B^0 \to D^+D^- \to (K^-\pi^+\pi^+)\left(K^0_S\pi^-\right)$	−0.8	−0.8	42%	98%

Table 5.6: Requirements on the neural network selection to suppress $e^+e^- \to q\bar{q}$ ($q \in \{u, d, s, c\}$) continuum events in the $B^0 \to D^+D^-$ analysis, see Section 5.3.11. To utilise the increased signal purity for events associated with good tags, the requirements are relaxed in high intervals of $r = 1 - 2\omega$.

The selection requirements on the final neural network are chosen dependent on the decision of the flavor tagging algorithms. Events associated with tags of high quality have on average a higher signal purity than events with tags of low quality, see Figure 4.10 and Section 4.5.5. To utilise this effect, the requirement on the neural network selection is chosen less strict for high r-intervals.

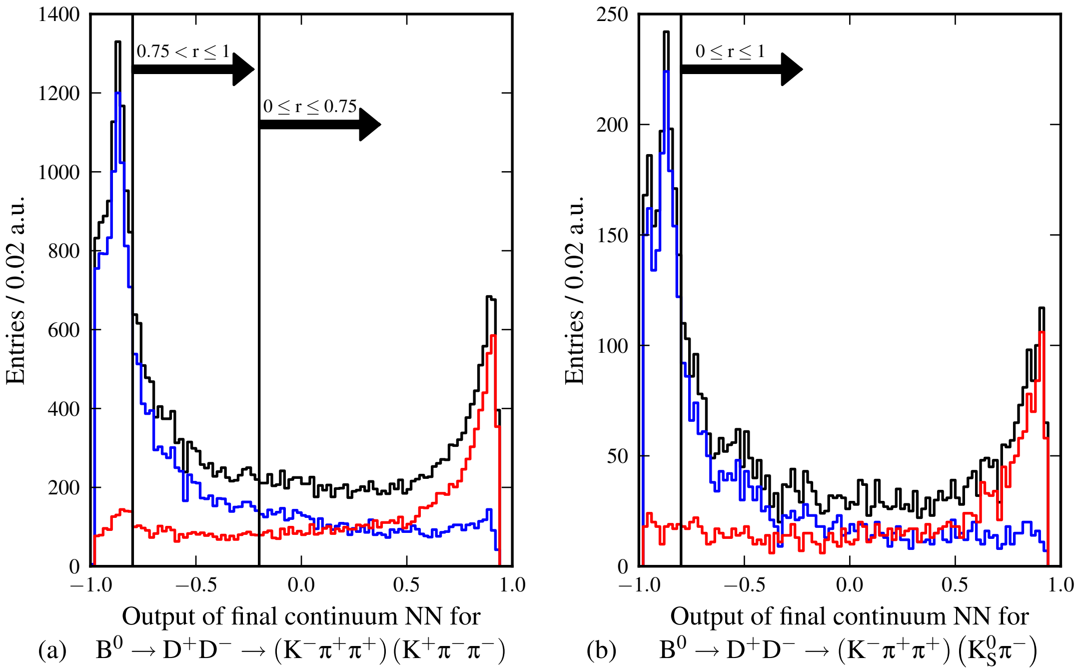

Figure 5.10: Distributions of the final neural network to suppress $e^+e^- \to q\bar{q}$ ($q \in \{u, d, s, c\}$ continuum events for (a) $B^0 \to D^+D^- \to (K^-\pi^+\pi^+)(K^+\pi^-\pi^-)$ and (b) $B^0 \to D^+D^- \to (K^-\pi^+\pi^+)\left(K^0_S\pi^-\right)$ decays. The blue (red) lines show continuum ($B\bar{B}$) components. The arrows indicate the applied selection requirements, which in (a) are chosen dependent on the quality of the flavor tag to utilise the higher signal purity for events associated with high quality flavor tags.

The distributions of the output of the final neural network and the applied selection requirements for all reconstructed $B^0 \to D^+D^-$ decay modes are shown in Figure 5.10. The applied selection requirements are summarised in Table 5.6. In total, the requirements on the neural network selection reject 64% of the background while retaining 92% of the signal.

6 Branching Fraction Measurements

The branching fractions of $B^0 \to D^+D^-$ and $B^0 \to D^{*\pm}D^{\mp}$ decays are determined in time-integrated measurements prior to the time-dependent analysis and the extraction of the CP violation parameters. The branching fraction measurements are performed as blind analyses. The reconstruction and selection procedure, the method to extract the signal, and the determination of reconstruction efficiencies are developed and refined using Monte Carlo simulations, data distributions in sidebands and control samples on data.

Before unblinding of the $B^0 \to D^+D^-$ and $B^0 \to D^{*\pm}D^{\mp}$ data distributions, the branching fraction measurements are performed on large inclusive Monte Carlo simulation samples, that contain signal and background to represent the data set in a realistic way. The branching fraction measurements are further validated by performing the same measurements for the control samples of $B^0 \to D_s^+D^-$ and $B^0 \to D_s^+D^{*-}$ decays. In addition, ensemble tests based on pseudo-experiments of $B^0 \to D^+D^-$ and $B^0 \to D^{*\pm}D^{\mp}$ decays are performed. In the following, the procedure of the branching fraction measurements and is described in detail.

6.1 Estimation of Reconstruction Efficiencies

The reconstruction efficiencies are determined by Monte Carlo simulations of signal decays and are corrected afterwards to account for possible differences on data. The simulations of signal decays are generated by the EvtGen package [112] and the detector response is simulated by the GEANT3 package [113]. For every decay mode, large samples of Monte Carlo simulations, in the order of 5×10^5 signal decays, are generated according to the luminosities and experimental conditions of the different periods of data taking of the Belle experiment.

The reconstruction efficiency $\varepsilon_{\mathrm{rec}}$ is defined as the ratio of reconstructed to generated signal decays,

$$\varepsilon_{\mathrm{rec}} = \frac{N_{\mathrm{rec}}}{N_{\mathrm{gen}}}. \tag{6.1}$$

The number of generated signal decays N_{gen} is determined by counting the signal decays in the simulated samples using Monte Carlo information on the generator level. The number of reconstructed signal decays N_{rec} is determined by unbinned extended two-dimensional maximum likelihood fits to the M_{bc} and ΔE distributions in the same way as in the signal extraction of the branching fraction measurements at a later stage.

Figure 6.1 shows the reconstruction efficiencies of the $B^0 \to D^+D^-$ and $B^0 \to D^{*\pm}D^{\mp}$ decay modes used in the branching fraction measurements over the different periods of data taking, referred to as experiments. Three different periods can be identified: The first period covers the years 2000 to 2003 (experiments 7 to 27). During this time, a 3-layer silicium vertex detector was operated in the Belle experiment. For data from this period, the reconstruction efficiencies

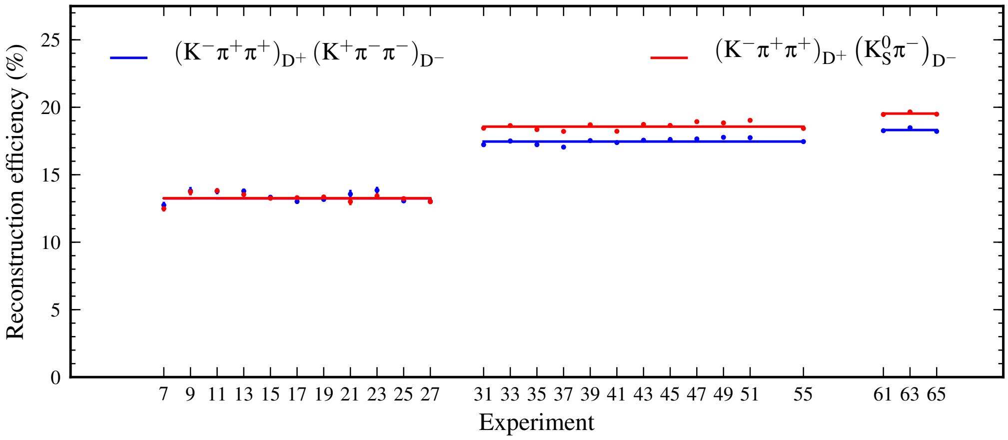

(a) $B^0 \to D^+D^-$

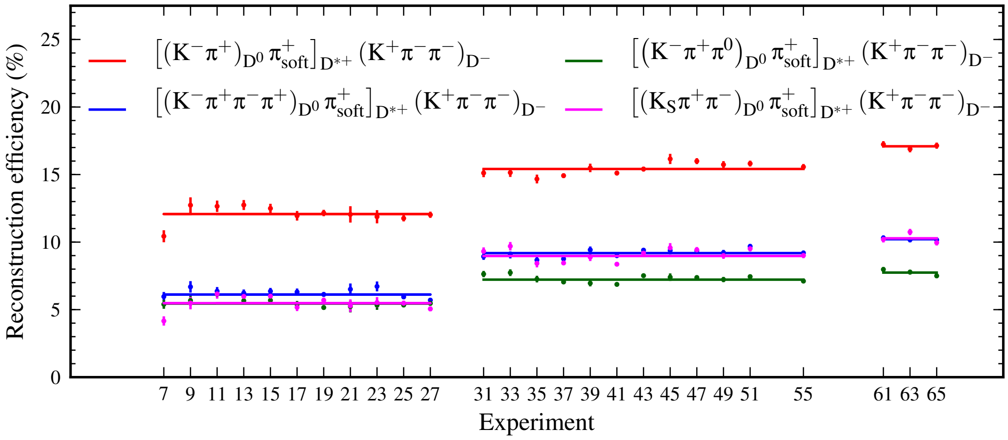

(b) $B^0 \to D^{*+}D^- \to \left[(\text{all } D^0 \text{ modes})\,\pi^+_{\text{soft}}\right]_{D^{*+}}\,(K^+\pi^-\pi^-)_{D^-}$

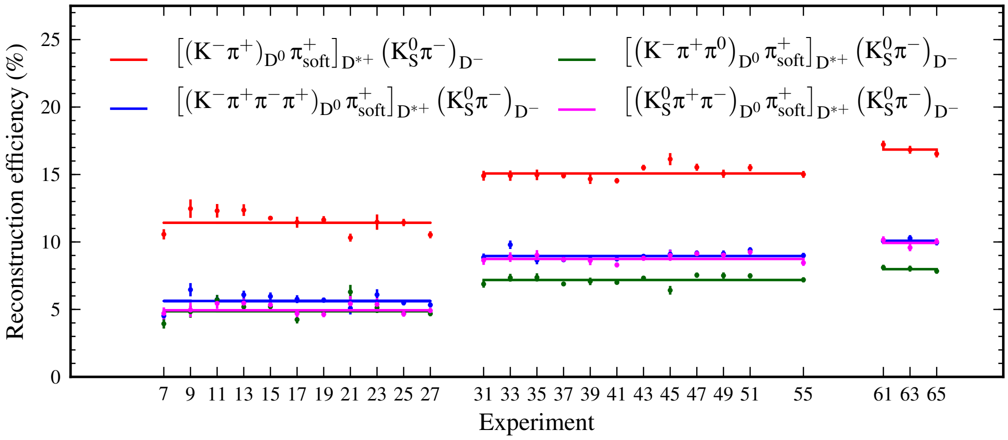

(c) $B^0 \to D^{*+}D^- \to \left[(\text{all } D^0 \text{ modes})\,\pi^+_{\text{soft}}\right]_{D^{*+}}\,(K^0_S\pi^-)_{D^-}$

Figure 6.1: Reconstruction efficiencies (data points with error bars) of individual $B^0 \to D^+D^-$ and $B^0 \to D^{*\pm}D^{\mp}$ decay modes for the three periods of data taking of the Belle experiment. The efficiencies are determined by Monte Carlo simulations of signal decays. The horizontal lines represent the average weighted by luminosities of the different periods.

are lowest. The second period covers the years 2003 to 2006 (experiments 31 to 55). For this period, the silicium vertex detector was replaced by a detector with 4 layers and a larger angular acceptance. The data of this period were reprocessed several times using improved track finding algorithms and have a higher reconstruction efficiency compared to the first period. The third period covers the years 2006 to 2010 (experiments 61 to 65). For this period, the KEKB accelerator was upgraded by crab cavities and improved track finding algorithms were applied directly after data taking. The reconstruction efficiencies are highest for data from this period.

The determined efficiencies of reconstructed $B^0 \to D^+D^-$ and $B^0 \to D^{*\pm}D^{\mp}$ decay modes and of the corresponding $B^0 \to D_s^+D^-$ and $B^0 \to D_s^+D^{*-}$ control samples are summarised in Table 6.1. In addition, the products of efficiencies and branching fractions, $\varepsilon_{\mathrm{rec}}\mathcal{B}$, of reconstructed D^{*+}, D^0, D^+, D_s^+ and K_S^0 decay modes are given. The statistical uncertainty on the reconstruction efficiencies is negligible due to the size of the Monte Carlo simulation samples. In total, the reconstruction efficiencies are low due to the high multiplicity of charged tracks in the final states and are in the order of 5% to 15%. For $B^0 \to D^+D^-$ decays, the reconstruction efficiency is higher than for $B^0 \to D^{*\pm}D^{\mp}$ decays, because of lower reconstruction efficiencies for soft pions from D^{*+} decays. The product of reconstruction efficiencies and branching fractions is approximately 17×10^{-4} for both decays. The reconstruction efficiencies of the $B^0 \to D_s^+D^-$ and $B^0 \to D_s^+D^{*-}$ control samples are lower than for $B^0 \to D^+D^-$ and $B^0 \to D^{*\pm}D^{\mp}$, because of tighter particle identification requirements and lower reconstruction efficiencies for charged kaons.

Possible differences in the reconstruction and in the selection between Monte Carlo simulations and data are taken into account by corrections. Correction factors are determined based on information from measurements of $D^{*+} \to (K^-\pi^+)_{D^0}\pi^+_{\mathrm{soft}}$ decays in inclusive D^{*+} samples [114]. The correction factors are determined by comparing the efficiencies of each charged kaon and pion from each reconstructed $B^0 \to D^+D^-$ and $B^0 \to D^{*\pm}D^{\mp}$ decay mode with the kaons and pions from the inclusive D^{*+} samples. The comparison takes into account the kinematics of the particles depending on the transverse momentum p_T and the polar angle θ in the laboratory frame. In total, the efficiencies determined by Monte Carlo simulations need to be corrected by a reduction of approximately 5%. The determined efficiency correction factors are summarised in Table 6.1.

			ε_{rec} correction	PID systematics (%)	
$B^0 \to D^+D^-$ decay mode	ε_{rec} (%)	$\varepsilon_{rec}\mathcal{B}$ ($\times 10^{-4}$)	factor	$K^\pm$	$\pi^\pm$
$(K^-\pi^+\pi^+)_{D^+}\,(K^+\pi^-\pi^-)_{D^-}$	16.76	14.0	0.950	1.98	3.77
$(K^-\pi^+\pi^+)_{D^+}\left(K^0_S\pi^-\right)_{D^-}$	17.66	3.1	0.955	0.99	2.75
		$\sum_i \varepsilon_{rec,i}\mathcal{B}_i = 17.1$			

			ε_{rec} correction	PID systematics (%)	
$B^0 \to D^{*\pm}D^\mp$ decay mode	ε_{rec} (%)	$\varepsilon_{rec}\mathcal{B}$ ($\times 10^{-4}$)	factor	$K^\pm$	$\pi^\pm$
$\left[(K^-\pi^+)_{D^0}\,\pi^+_{soft}\right]_{D^{*+}}(K^+\pi^-\pi^-)_{D^-}$	15.01	3.59	0.959	1.88	2.72
$\left[(K^-\pi^+\pi^-\pi^+)_{D^0}\,\pi^+_{soft}\right]_{D^{*+}}(K^+\pi^-\pi^-)_{D^-}$	8.79	4.38	0.967	2.06	5.05
$\left[\left(K^-\pi^+\pi^0\right)_{D^0}\,\pi^+_{soft}\right]_{D^{*+}}(K^+\pi^-\pi^-)_{D^-}$	7.17	6.16	0.971	1.95	2.90
$\left[\left(K^0_S\pi^+\pi^-\right)_{D^0}\,\pi^+_{soft}\right]_{D^{*+}}(K^+\pi^-\pi^-)_{D^-}$	8.49	1.02	0.953	0.99	3.90
$\left[(K^-\pi^+)_{D^0}\,\pi^+_{soft}\right]_{D^{*+}}\left(K^0_S\pi^-\right)_{D^-}$	14.62	0.39	0.962	0.88	1.70
$\left[(K^-\pi^+\pi^-\pi^+)_{D^0}\,\pi^+_{soft}\right]_{D^{*+}}\left(K^0_S\pi^-\right)_{D^-}$	8.50	0.47	0.971	1.06	4.04
$\left[\left(K^-\pi^+\pi^0\right)_{D^0}\,\pi^+_{soft}\right]_{D^{*+}}\left(K^0_S\pi^-\right)_{D^-}$	7.01	0.67	0.974	0.95	1.86
$\left[\left(K^0_S\pi^+\pi^-\right)_{D^0}\,\pi^+_{soft}\right]_{D^{*+}}\left(K^0_S\pi^-\right)_{D^-}$	8.23	0.11	0.957	-	2.87
		$\sum_i \varepsilon_{rec,i}\mathcal{B}_i = 16.8$			

$B^0 \to D_s^+D^-$ decay mode	ε_{rec} (%)	$\varepsilon_{rec}\mathcal{B}$ ($\times 10^{-4}$)
$(K^+K^-\pi^+)_{D_s^+}\,(K^+\pi^-\pi^-)_{D^-}$	12.38	6.2
$(K^+K^-\pi^+)_{D_s^+}\left(K^0_S\pi^-\right)_{D^-}$	12.18	0.7
$\left(K^0_SK^+\right)_{D_s^+}(K^+\pi^-\pi^-)_{D^-}$	14.14	1.0
		$\sum_i \varepsilon_{rec,i}\mathcal{B}_i = 7.9$

$B^0 \to D_s^+D^{*-}$ decay mode	ε_{rec} (%)	$\varepsilon_{rec}\mathcal{B}$ ($\times 10^{-4}$)
$(K^+K^-\pi^+)_{D_s^+}\left[(K^+\pi^-)_{\bar{D}^0}\,\pi^-_{soft}\right]_{D^{*-}}$	9.77	1.41
$(K^+K^-\pi^+)_{D_s^+}\left[(K^+\pi^-\pi^+\pi^-)_{\bar{D}^0}\,\pi^-_{soft}\right]_{D^{*-}}$	5.62	1.69
$(K^+K^-\pi^+)_{D_s^+}\left[\left(K^+\pi^-\pi^0\right)_{\bar{D}^0}\,\pi^-_{soft}\right]_{D^{*-}}$	4.68	2.42
$(K^+K^-\pi^+)_{D_s^+}\left[\left(K^0_S\pi^-\pi^+\right)_{\bar{D}^0}\,\pi^-_{soft}\right]_{D^{*-}}$	5.50	0.40
$\left(K^0_SK^+\right)_{D_s^+}\left[(K^+\pi^-)_{\bar{D}^0}\,\pi^-_{soft}\right]_{D^{*-}}$	11.37	0.31
$\left(K^0_SK^+\right)_{D_s^+}\left[(K^+\pi^-\pi^+\pi^-)_{\bar{D}^0}\,\pi^-_{soft}\right]_{D^{*-}}$	6.48	0.36
$\left(K^0_SK^+\right)_{D_s^+}\left[\left(K^+\pi^-\pi^0\right)_{\bar{D}^0}\,\pi^-_{soft}\right]_{D^{*-}}$	5.41	0.52
$\left(K^0_SK^+\right)_{D_s^+}\left[\left(K^0_S\pi^-\pi^+\right)_{\bar{D}^0}\,\pi^-_{soft}\right]_{D^{*-}}$	6.35	0.09
		$\sum_i \varepsilon_{rec,i}\mathcal{B}_i = 7.2$

Table 6.1: Reconstruction efficiencies determined by Monte Carlo simulations, efficiency correction factors for data and systematic uncertainties of the particle identification (PID) selection.

6.2 Branching Fraction Measurements on Inclusive Monte Carlo Simulation Samples

The Belle experiment provides Monte Carlo simulation samples of inclusive generic B decays and continuum events, referred to as generic Monte Carlo simulations, which allow to perform the measurements several times on simulated samples prior to unblinding of the data distributions. The simulated samples contain signal and background and are of equivalent size to the real data set. This section describes the generic Monte Carlo simulation samples and the $\mathrm{B^0 \to D^+D^-}$ and $\mathrm{B^0 \to D^{*\pm}D^{\mp}}$ branching fraction measurements including the study of peaking background sources. The measurements using the data set are performed in the same way at a later stage.

Decay mode	Branching fraction	CPV parameter $\mathcal{S}$	CPV parameter $\mathcal{C}$
$\mathrm{B^0 \to D^+D^-}$	$(2.11 \pm 0.31) \times 10^{-4}$	0.68	0
$\mathrm{B^0 \to D^{*\pm}D^{\mp}}$	$(6.1 \pm 1.5) \times 10^{-4}$	0.68	0
$\mathrm{B^0 \to D_s^+D^-}$	$(7.2 \pm 0.8) \times 10^{-3}$	0	0
$\mathrm{B^0 \to D_s^+D^{*-}}$	$(8.0 \pm 1.1) \times 10^{-3}$	0	0
$\mathrm{D^0 \to K^-\pi^+}$	$(3.87 \pm 0.05) \times 10^{-2}$	-	-
$\mathrm{D^0 \to K^-\pi^+\pi^-\pi^+}$	$(8.07 \pm 0.21) \times 10^{-2}$	-	-
$\mathrm{D^0 \to K^-\pi^+\pi^0}$	$(13.9 \pm 0.5) \times 10^{-2}$	-	-
$\mathrm{D^0 \to K_S^0\pi^+\pi^-}$	$(2.81 \pm 0.15) \times 10^{-2}$	-	-
$\mathrm{D^+ \to K^-\pi^+\pi^+}$	$(9.13 \pm 0.19) \times 10^{-2}$	-	-
$\mathrm{D^+ \to K_S^0\pi^+}$	$(1.47 \pm 0.07) \times 10^{-2}$	-	-
$\mathrm{D^{*+} \to D^0\pi^+_{soft}}$	$(67.7 \pm 0.5) \times 10^{-2}$	-	-
$\mathrm{D^{*+} \to D^+\pi^0_{soft}}$	$(30.7 \pm 0.5) \times 10^{-2}$	-	-
$\mathrm{D_s^+ \to K^+K^-\pi^+}$	$(5.50 \pm 0.27) \times 10^{-2}$	-	-
$\mathrm{D_s^+ \to K_S^0K^+}$	$(1.49 \pm 0.08) \times 10^{-2}$	-	-
$\mathrm{K_S^0 \to \pi^+\pi^-}$	$(69.2 \pm 0.05) \times 10^{-2}$	-	-

Table 6.2: Branching fractions according to current world averages [115] of the decay modes reconstructed in the present analysis and CP violation parameters according the current world averages from measurements in $\mathrm{b \to c\bar{c}s}$ transitions [58]. The summarised values are used in the branching fraction measurements and in the generation of signal replacement for the measurements on inclusive Monte Carlo simulation samples.

The decays in the generic Monte Carlo simulation samples are generated by Evtgen [112] and Pythia [116], and the detector response is simulated by GEANT3 [113]. The simulated decays are generated according to known branching fractions and cross sections and are scaled according to the luminosities of the Belle experiment.

In order to improve the simulations and to represent the data as realistically as possible, the signal decays of the reconstructed decay modes, which are already present in the inclusive Monte Carlo simulation samples provided by the Belle Collaboration, are replaced in the present analysis by signal decays generated according to current world averages of branching fractions and CP violating parameters. Additionally, in the signal decays the resonant substructures of three-body D^0, D^+ and D_s^+ decays are simulated according to appropriate Dalitz models. The numerical values of the parameters used as input in the generation of the signal replacement are summarised in Table 6.2.

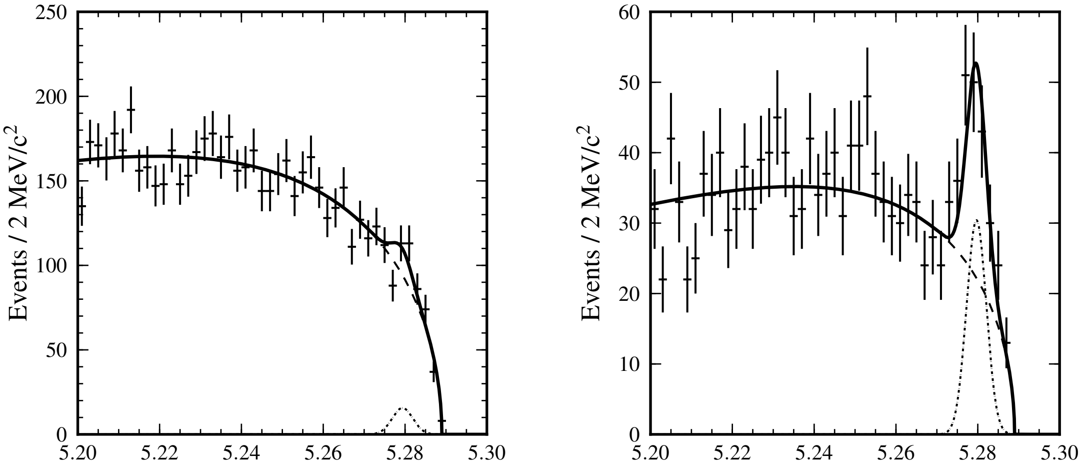

(a) $B^0 \to D^+ \left(K^+\pi^-\pi^-\right)_{D^-}$ in $M_{K^+\pi^-\pi^-}$ sideband (b) $B^0 \to D^+ \left(K_S^0\pi^-\right)_{D^-}$ in $M_{K_S^0\pi^-}$ sideband

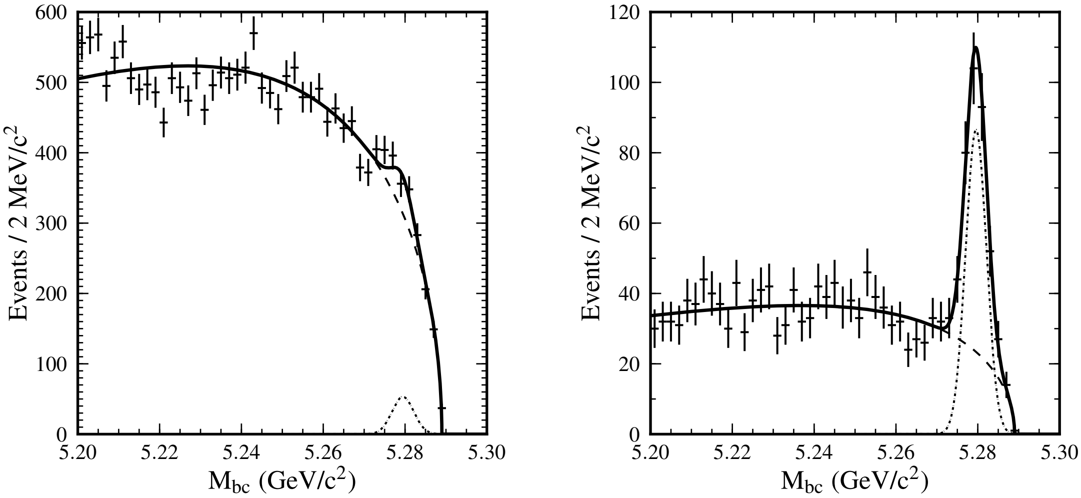

(c) $B^0 \to D^{*+} \left(K^+\pi^-\pi^-\right)_{D^-}$ in $M_{K^+\pi^-\pi^-}$ sideband (d) $B^0 \to D^{*+} \left(K_S^0\pi^-\right)_{D^-}$ in $M_{K_S^0\pi^-}$ sideband

Figure 6.2: M_{bc} distributions from inclusive Monte Carlo simulation samples in D^- mass sidebands for $B^0 \to D^+D^-$ and $B^0 \to D^{*+}D^-$ decay modes reconstructed from $D^- \to K^+\pi^-\pi^-$ and $D^- \to K_S^0\pi^-$ decays. Superimposed are projections of the fits. The dotted (dashed) lines show projections of the signal (background) components of the fits. A requirement of $|\Delta E| < 30$ MeV ($M_{bc} > 5.27$ GeV/c^2) is applied when plotting the M_{bc} (ΔE) distributions.

Peaking Background Study

Decays such as $\bar{B}^0 \to D^{(*)+}K^{*-}$, $\bar{B}^0 \to D^{(*)+}\bar{K}^0\pi^-$ and $\bar{B}^0 \to D^{(*)+}\pi^-\pi^-\pi^+$ have the same final states as the reconstructed $B^0 \to D^+D^-$ and $B^0 \to D^{*\pm}D^{\mp}$ decay modes and can possibly populate the M_{bc} and ΔE signal region. These decays are indistinguishable from signal decays and are referred to as peaking background. The contribution of possible peaking background is detected and quantified in fits to the M_{bc} and ΔE distributions in the D mass sidebands.

For D^- mesons, the mass sidebands are defined by

$$\begin{aligned} & -95\ \mathrm{MeV}/c^2 < M_{D^-}^{rec} - M_{D^-}^{PDG} < -25\ \mathrm{MeV}/c^2, \\ \text{and} \quad & 25\ \mathrm{MeV}/c^2 < M_{D^-}^{rec} - M_{D^-}^{PDG} < 75\ \mathrm{MeV}/c^2. \end{aligned} \tag{6.2}$$

The widths of the sidebands correspond to 5-times the width of the signal region. Using Monte Carlo simulations of peaking background decays, it was checked, that the number of events in the sidebands scaled down by a factor of 5 agree with the number of peaking background events inside of the signal region.

Figure 6.2 shows M_{bc} distributions from inclusive Monte Carlo simulation samples in the D^- mass sidebands. For $B^0 \to D^+D^-$ and $B^0 \to D^{*+}D^-$ decay modes reconstructed from $D^- \to K^+\pi^-\pi^-$ decays, the fits to the sidebands return yields consistent with zero and the modes are considered to be free of peaking background, compare Figure 6.2(a) and (c). These decay modes provide the main contribution to the present analysis. For modes reconstructed from $D^- \to K_S^0\pi^-$ decays, large contributions of peaking background are found and are estimated to be approximately 80 events in $B^0 \to D^+D^-$ and approximately 300 events in $B^0 \to D^{*+}D^-$, compare Figure 6.2(b) and (d) and Table 6.3.

The peaking background contribution appearing in the $B^0 \to D^{(*)+}\left(K_S^0\pi^-\right)_{D^-}$ reconstruction of the inclusive Monte Carlo simulation samples is multiple times larger than on data. The reason for this overestimation is a wrong tuning in the simulation of the quark fragmentation following $b \to c\bar{u}s$ decays.

Determination of the Branching Fractions

The yields in the signal peaks are extracted by unbinned extended two-dimensional maximum likelihood fits to the M_{bc} and ΔE distributions. The peaking background contributions are estimated from the D mass sidebands as described above. The contributions are then scaled down to the signal region and subtracted from the yields in the peaks to obtain the final signal yields. The results for the $B^0 \to D^+D^-$ and $B^0 \to D^{*\pm}D^{\mp}$ yields for separate inclusive Monte Carlo simulation samples are summarised in Table 6.3.

The $B^0 \to D^+D^-$ and $B^0 \to D^{*\pm}D^{\mp}$ branching fractions are calculated from the signal yields N_{signal}, from the reconstruction efficiencies ε_{rec}, from the branching fractions $\mathcal{B}'$ of the D^{*+}, D^0, D^+, D_s^+ and K_S^0 decay modes involved in the reconstruction and from the number $N_{B\bar{B}}$ of $B\bar{B}$ pairs in the data set,

$$\mathcal{B}\left(B^0 \to D^{(*)\pm}D^{\mp}\right) = \frac{N_{signal}}{\varepsilon_{rec}\mathcal{B}' N_{B\bar{B}}}. \tag{6.3}$$

In $B^0 \to D^+D^-$, the branching fraction measurement is performed for both reconstructed decay modes separately. The separate branching fractions provide an additional cross-check for possible peaking background in one of the modes. The branching fractions are then averaged according to weights given by the uncertainties of the individual measurements by a least-squares technique. Both reconstructed decay modes are statistically independent and correlations in the average can be neglected.

The weighted average $\hat{\mathcal{B}}$ and the corresponding uncertainty $\hat{\sigma}$ are estimated by the center values $\mathcal{B}_\mathrm{i}$ and uncertainties σ_i of the two individual $\mathrm{B}^0 \rightarrow \mathrm{D}^+\mathrm{D}^-$ branching fraction measurements [99],

$$\hat{\mathcal{B}} = \frac{\sum_{\mathrm{i}=1}^{2} \frac{\mathcal{B}_\mathrm{i}}{\sigma_\mathrm{i}^2}}{\sum_{\mathrm{j}=1}^{2} \frac{1}{\sigma_\mathrm{j}^2}} \quad \text{and} \quad \hat{\sigma}_\lambda = \frac{1}{\sqrt{\sum_{\mathrm{i}=1}^{2} \frac{1}{\sigma_\mathrm{i}^2}}}. \tag{6.4}$$

Due to the large number of exclusively reconstructed $\mathrm{B}^0 \rightarrow \mathrm{D}^{*\pm}\mathrm{D}^{\mp}$ decay modes, the branching fraction of $\mathrm{B}^0 \rightarrow \mathrm{D}^{*\pm}\mathrm{D}^{\mp}$ decays is determined from the total yield and the product of reconstruction efficiencies and branching fractions of all reconstructed decay modes.

The results of the $\mathrm{B}^0 \rightarrow \mathrm{D}^+\mathrm{D}^-$ and $\mathrm{B}^0 \rightarrow \mathrm{D}^{*\pm}\mathrm{D}^{\mp}$ branching fraction measurements on the inclusive Monte Carlo simulation samples are summarised in Table 6.3. For both reconstructed $\mathrm{B}^0 \rightarrow \mathrm{D}^+\mathrm{D}^-$ decay modes individually and for their averages, the measured branching fractions reproduce the generator input value of $\mathcal{B}\left(\mathrm{B}^0 \rightarrow \mathrm{D}^+\mathrm{D}^-\right) = 2.11 \times 10^{-4}$. The measured branching fractions for $\mathrm{B}^0 \rightarrow \mathrm{D}^{*\pm}\mathrm{D}^{\mp}$ reproduce the generator input value of $\mathcal{B}\left(\mathrm{B}^0 \rightarrow \mathrm{D}^{*\pm}\mathrm{D}^{\mp}\right) = 6.1 \times 10^{-4}$.

The agreement of the inclusive Monte Carlo measurements with the input values used in the generation of the samples indicates, that the procedure for the estimation and subtraction of possible peaking background and the procedure for the determination of the branching fractions perform correctly.

$B^0 \to D^+D^-$ decay mode	N_{peak}	$N_{sideband}$	N_{signal}	$\mathcal{B}\left(B^0 \to D^+D^-\right)\left(\times 10^{-4}\right)$	
$(K^-\pi^+\pi^+)(K^+\pi^-\pi^-)$	232.1 ± 19.5	–	232.1 ± 19.5	2.03 ± 0.17	Sample 1
$(K^-\pi^+\pi^+)\left(K^0_S\pi^-\right)$	48.8 ± 9.2	83.9 ± 12.2	32.0 ± 9.5	2.50 ± 0.54	
			Weighted average:	2.07 ± 0.16	
$(K^-\pi^+\pi^+)(K^+\pi^-\pi^-)$	213.8 ± 18.7	–	213.8 ± 18.7	1.87 ± 0.16	Sample 2
$(K^-\pi^+\pi^+)\left(K^0_S\pi^-\right)$	51.8 ± 9.5	60.6 ± 11.6	39.7 ± 9.8	3.10 ± 0.55	
			Weighted average:	1.97 ± 0.15	
$(K^-\pi^+\pi^+)(K^+\pi^-\pi^-)$	239.7 ± 19.5	–	239.7 ± 19.5	2.10 ± 0.17	Sample 3
$(K^-\pi^+\pi^+)\left(K^0_S\pi^-\right)$	48.7 ± 9.3	92.4 ± 13.2	30.2 ± 9.7	2.36 ± 0.55	
			Weighted average:	2.12 ± 0.16	
$(K^-\pi^+\pi^+)(K^+\pi^-\pi^-)$	259.8 ± 20.0	–	259.8 ± 20.0	2.27 ± 0.18	Sample 4
$(K^-\pi^+\pi^+)\left(K^0_S\pi^-\right)$	37.4 ± 8.4	80.7 ± 12.5	21.3 ± 8.8	1.67 ± 0.50	
			Weighted average:	2.19 ± 0.17	
$B^0 \to D^{*\pm}D^{\mp}$ decays	N_{peak}	$N_{sideband}$	N_{signal}	$\mathcal{B}\left(B^0 \to D^{*\pm}D^{\mp}\right)\left(\times 10^{-4}\right)$	
Sample 1	833.4 ± 39.0	298.4 ± 21.5	773.7 ± 39.2	5.97 ± 0.30	
Sample 2	860.0 ± 39.2	315.1 ± 22.4	797.0 ± 39.5	6.15 ± 0.31	
Sample 3	876.4 ± 39.6	296.2 ± 21.6	817.2 ± 39.8	6.30 ± 0.31	

Table 6.3: Yields and results of the branching fraction measurements performed on inclusive Monte Carlo simulation samples. In the Monte Carlo simulations, the signal decays are generated according to $\mathcal{B}\left(B^0 \to D^+D^-\right) = 2.11 \times 10^{-4}$ and $\mathcal{B}\left(B^0 \to D^{*\pm}D^{\mp}\right) = 6.1 \times 10^{-4}$. Each generic Monte Carlo simulation sample mimics the real data set in size and composition.

6.3 Ensemble Tests

Ensemble tests are performed to validate the fit procedure, which is used to extract the signal yields for the branching fraction measurements of $B^0 \to D^+D^-$ and $B^0 \to D^{*\pm}D^{\mp}$ decays. In the ensemble tests, a Monte Carlo technique is used to create pseudo-experiments of M_{bc} and ΔE distributions according to a generator model, referred to as toy Monte Carlo, and the fits of the measurements are performed to the distributions of the pseudo-experiments. Because the creation of pseudo-experiments is computationally not intensive compared to the complete simulation of the underlying physical decay processes and the simulation of the detector response, it is possible to repeat the measurement many times and to study the results of the measurements in the large sample limit. This allows to test the applied fit models, to identify possible biases in the measurements and to study the fit uncertainties. Furthermore, if the generated pseudo-experiments represent the data distributions as realistically as possible, then the ensemble tests give an estimate of the expected statistical sensitivity of the measurements.

In the present analysis, a hybrid Monte Carlo technique is applied to create the pseudo-experiments. The approach uses different kinds of models for the generation of signal and background events. Background events are generated according to a background probability density function with parameters obtained from fits to generic Monte Carlo simulation samples. The signal generator model is directly derived from the distributions of reconstructed signal decays, that are simulated by EvtGen [112] and GEANT3 [113] to mimic the M_{bc} and ΔE distributions of signal events as realistically as possible.

For the ensemble tests of $B^0 \to D^+D^-$ and $B^0 \to D^{*\pm}D^{\mp}$ decays, 1000 pseudo-experiments are generated for each decay. The expected number of signal events is calculated from the luminosity of the data set, the current world averages of branching fractions in Table 6.2 and the determined reconstruction efficiencies in Table 6.1. The expected number of background events is taken from measurements on inclusive Monte Carlo simulation samples. In the generation of pseudo-experiments, the number of signal and background events are fluctuated according to a Poisson distribution.

	Center value		Pull		
Decay	μ	σ	μ	σ	$\langle\sigma_{fit}\rangle$
$B^0 \to D^+D^-$	279.3 ± 0.7	21.2 ± 0.5	$+0.058 \pm 0.032$	1.002 ± 0.023	21.2
$B^0 \to D^{*\pm}D^{\mp}$	787.2 ± 1.2	36.5 ± 0.8	$+0.121 \pm 0.032$	1.014 ± 0.023	35.9

Table 6.4: Results of the ensemble tests performed for the validation of the $B^0 \to D^+D^-$ and $B^0 \to D^{*\pm}D^{\mp}$ branching fraction measurements. The mean μ and width σ of the center value and pull distributions with respect to the yield of signal events are obtained by fits of Gaussian functions to the distributions shown in Figure 6.3.

The distributions of center values, pulls and fit uncertainties of the ensemble tests and the projections of the fits to the distributions are shown in Figure 6.3 and the results are summarised in Table 6.4. For both, $B^0 \to D^+D^-$ and $B^0 \to D^{*\pm}D^{\mp}$, the fits of the ensemble tests reproduce the generated number of signal events. In $B^0 \to D^{*\pm}D^{\mp}$, unlike in $B^0 \to D^+D^-$, the mean of the pull distribution, defined by the deviation of the signal yield obtained in the fit from

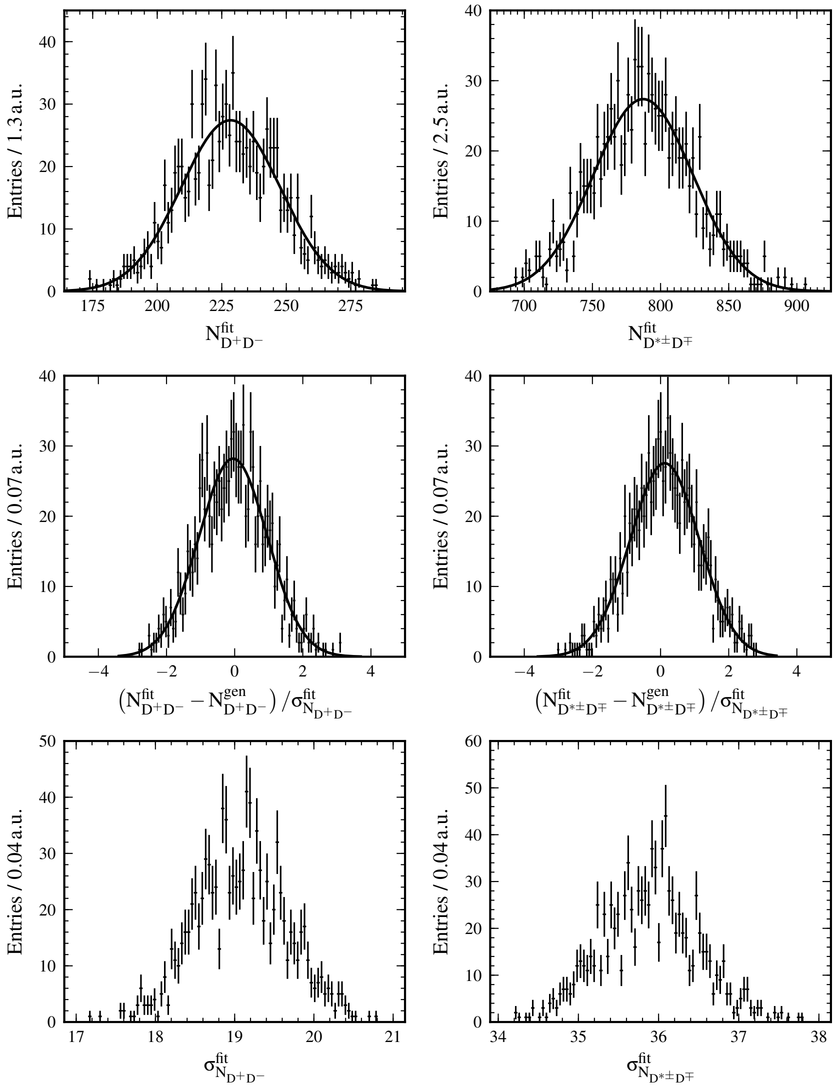

Figure 6.3: Center value (top), pull (middle) and fit uncertainty distributions (bottom) from the ensemble tests performed for the validation of the $B^0 \to D^+D^-$ (left) and $B^0 \to D^{*\pm}D^{\mp}$ (right) branching fraction measurements.

the number of generated signal events, measured in units of the fit error, deviates significantly from 0 indicating a small bias. The bias corresponds to 12% of the statistical uncertainty or, if expressed absolutely, to approximately four signal events and is considered to be negligible at the precision of the measurement. For both decays, the widths of the pull distributions are consistent with one indicating that the obtained fit uncertainties are reliable.

In $B^0 \to D^+D^-$, the inclusion of the $B^0 \to D^+D^- \to (K^-\pi^+\pi^+)\left(K^0_S\pi^-\right)$ decay mode improves the statistical uncertainty of the branching fraction measurement by 10%. The expected relative statistical uncertainty of the $B^0 \to D^+D^-$ branching fraction is 7.6%. The expected relative statistical uncertainty of the $B^0 \to D^{*\pm}D^{\mp}$ branching fraction is 4.6%.

6.4 Branching Fraction Measurements of $B^0 \to D_s^+ D^{(*)-}$ Decays

Prior to the branching fraction measurements of $B^0 \to D^+D^-$ and $B^0 \to D^{*\pm}D^{\mp}$ decays, the branching fractions of the corresponding $B^0 \to D_s^+D^-$ and $B^0 \to D_s^+D^{*-}$ control samples are measured. The procedure of the measurements follows the procedure applied in the measurements on inclusive Monte Carlo simulation samples in Section 6.2.

In addition to the D^- mass sidebands, possible peaking background is estimated in the D_s^+ mass sidebands. For D_s^+ mesons the sidebands are defined by

$$\begin{aligned} &-50\ \mathrm{MeV}/c^2 < M_{D_s^+}^{\mathrm{rec}} - M_{D_s^+}^{\mathrm{PDG}} < -25\ \mathrm{MeV}/c^2 \\ \text{and}\quad &25\ \mathrm{MeV}/c^2 < M_{D_s^+}^{\mathrm{rec}} - M_{D_s^+}^{\mathrm{PDG}} < 100\ \mathrm{MeV}/c^2, \end{aligned} \tag{6.5}$$

corresponding to a width of 4.2-times the signal region. Significant contributions of peaking background, likely to originate from $B^0 \to D^{(*)-}K^+\bar{K}^*$ and $B^0 \to D_s^+\bar{K}^0\pi^-$ decays, are found. After scaling down the mass sidebands to the signal region, the contributions are subtracted from the yields in the signal peak.

$B^0 \to D_s^+D^-$ decay mode	N_{peak}	N_{sideband}	N_{signal}	$\mathcal{B}\left(B^0 \to D^+D^-\right)\left(\times 10^{-3}\right)$
$(K^+K^-\pi^+)_{D_s^+}(K^+\pi^-\pi^-)_{D^-}$	3248.6 ± 58.8	128.3 ± 14.0	3218.1 ± 58.9	6.50 ± 0.12
$(K^+K^-\pi^+)_{D_s^+}\left(K_S^0\pi^-\right)_{D^-}$	403.7 ± 20.4	16.7 ± 4.8	394.9 ± 20.5	7.45 ± 0.39
$\left(K_S^0K^+\right)_{D_s^+}(K^+\pi^-\pi^-)_{D^-}$	725.2 ± 27.6	26.4 ± 7.7	720.0 ± 27.6	6.81 ± 0.27
			Weighted average:	6.62 ± 0.11

$B^0 \to D_s^+D^{*-}$ decay mode	N_{peak}	N_{sideband}	N_{signal}	$\mathcal{B}\left(B^0 \to D_s^+D^{*-}\right)\left(\times 10^{-3}\right)$
$(K^+K^-\pi^+)_{D_s^+}\left[\left(\text{all }\bar{D}^0\text{modes}\right)\pi^-_{\mathrm{soft}}\right]_{D^{*-}}$	3720.1 ± 64.7	581.2 ± 29.6	3581.7 ± 65.1	7.85 ± 0.14
$\left(K_S^0K^+\right)_{D_s^+}\left[\left(\text{all }\bar{D}^0\text{modes}\right)\pi^-_{\mathrm{soft}}\right]_{D^{*-}}$	778.7 ± 29.4	–	778.7 ± 29.4	7.91 ± 0.30
Above combined	4504.4 ± 70.8	581.2 ± 29.6	4366.0 ± 71.2	7.87 ± 0.13

Table 6.5: Yields and results of the branching fraction measurements of $B^0 \to D_s^+D^-$ and $B^0 \to D_s^+D^{*-}$ decays.

The M_{bc} and ΔE distributions of $B^0 \to D_s^+D^-$ and $B^0 \to D_s^+D^{*-}$ decays are shown in Figure 6.4. The results of the fits to the signal region and to the sidebands are summarised in Table 6.5. Each of the control samples provides approximately 4300 signal decays at very high purity. In $B^0 \to D_s^+D^-$, the branching fraction is estimated for each reconstructed mode and then combined by the weighted average given in Equation 6.4. In $B^0 \to D_s^+D^{*-}$, the branching fraction is estimated for all reconstructed modes in combination. Additionally, the results for both reconstructed D_s^+ modes are given separately as a cross-check.

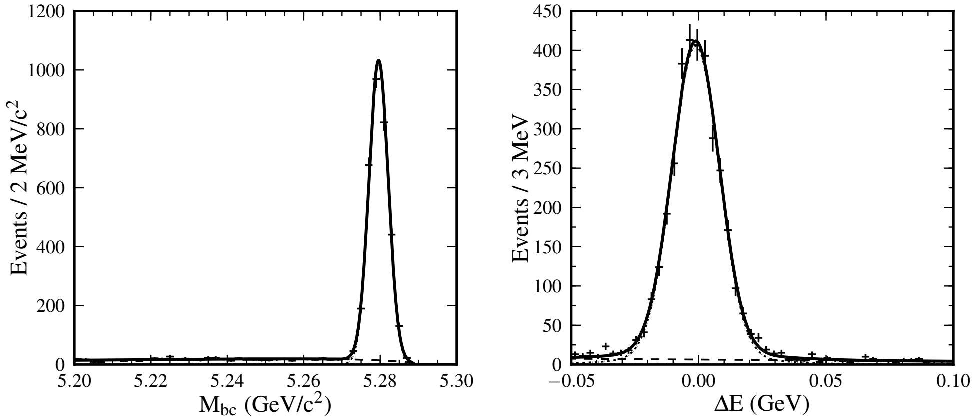

(a) $B^0 \to D_s^+ D^- \to (K^+K^-\pi^+)_{D_s^+} (K^+\pi^-\pi^-)_{D^-}$

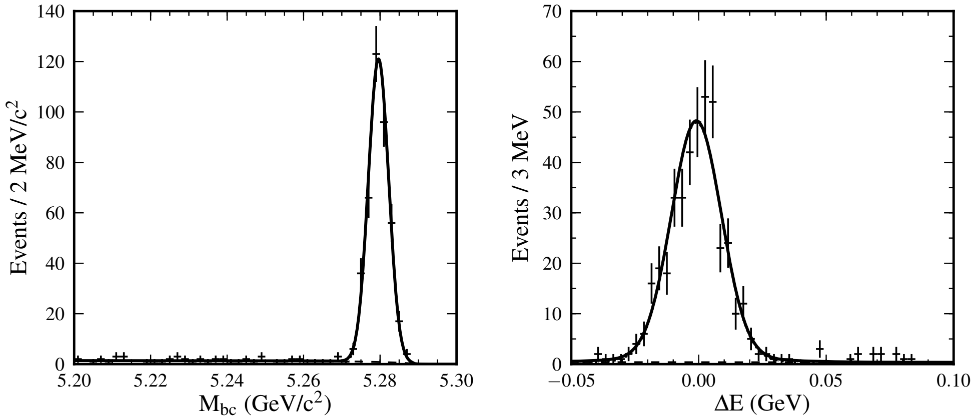

(b) $B^0 \to D_s^+ D^- \to (K^+K^-\pi^+)_{D_s^+} \left(K_S^0\pi^-\right)_{D^-}$

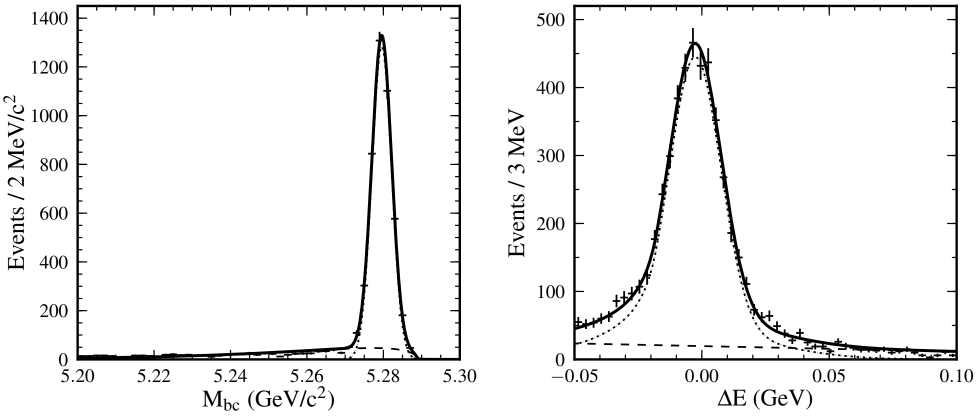

(c) $B^0 \to D_s^+ D^{*-}$

Figure 6.4: M_{bc} and ΔE data distributions of (a) $B^0 \to D_s^+ D^- \to (K^+K^-\pi^+)(K^+\pi^-\pi^-)$, (b) $B^0 \to D_s^+ D^- \to (K^+K^-\pi^+)\left(K_S^0\pi^-\right)$ and (c) $B^0 \to D_s^+ D^{*-}$ decays. The dotted (dashed) lines show projections of the signal (background) components of the fits. A requirement of $|\Delta E| < 30$ MeV ($M_{bc} > 5.27$ GeV/c^2) is applied when plotting the M_{bc} (ΔE) distributions.

The measured branching fractions are:

$$\mathcal{B}\left(\mathrm{B}^0 \to \mathrm{D}_\mathrm{s}^+\mathrm{D}^-\right) = (6.62 \pm 0.11\ (\mathrm{stat.})) \times 10^{-3} \tag{6.6}$$

$$\text{and}\quad \mathcal{B}\left(\mathrm{B}^0 \to \mathrm{D}_\mathrm{s}^+\mathrm{D}^{*-}\right) = (7.87 \pm 0.13\ (\mathrm{stat.})) \times 10^{-3}. \tag{6.7}$$

The results are in agreement with the current world averages of [115]:

$$\mathcal{B}^{\mathrm{PDG}}\left(\mathrm{B}^0 \to \mathrm{D}_\mathrm{s}^+\mathrm{D}^-\right) = (7.2 \pm 0.8) \times 10^{-3},$$

$$\text{and}\quad \mathcal{B}^{\mathrm{PDG}}\left(\mathrm{B}^0 \to \mathrm{D}_\mathrm{s}^+\mathrm{D}^{*-}\right) = (8.0 \pm 1.1) \times 10^{-3}.$$

The agreement of the $\mathrm{B}^0 \to \mathrm{D}_\mathrm{s}^+\mathrm{D}^-$ and $\mathrm{B}^0 \to \mathrm{D}_\mathrm{s}^+\mathrm{D}^{*-}$ branching fraction measurements with the nominal values confirms that the procedures of the branching fraction measurement including the estimation and subtraction of possible peaking background contributions perform correctly on data distributions.

6.5 Branching Fraction Measurements of $B^0 \to D^+D^-$ and $B^0 \to D^{*\pm}D^{\mp}$ Decays

The $B^0 \to D^+D^-$ and $B^0 \to D^{*\pm}D^{\mp}$ branching fraction measurements are performed on the data distributions according to the procedure developed and validated by the measurements on inclusive Monte Carlo simulation samples in Section 6.2 and by the $B^0 \to D_s^+D^-$ and $B^0 \to D_s^+D^{*-}$ measurements in Section 6.4.

In the $B^0 \to D^{*\pm}D^{\mp}$ branching fraction measurement, only decay modes involving low momentum π^+_{soft} mesons from D^{*+} decays are included to avoid systematic effects caused by possible differences between Monte Carlo simulations and data in the reconstruction efficiencies of low momentum π^0_{soft} mesons. Because the $B^0 \to D^{*\pm}D^{\mp}$ branching fraction measurement is expected to be limited by systematic and not by statistical uncertainties, the restriction has no negative influence on the precision of the result.

$B^0 \to D^+D^-$ decay mode	N_{peak}	$N_{sideband}$	N_{signal}	$\mathcal{B}\left(B^0 \to D^+D^-\right)\left(\times 10^{-4}\right)$
$(K^-\pi^+\pi^+)_{D^+}(K^+\pi^-\pi^-)_{D^-}$	221.4 ± 18.6	–	221.4 ± 18.6	2.16 ± 0.18
$(K^-\pi^+\pi^+)_{D^+}\left(K^0_S\pi^-\right)_{D^-}$	48.7 ± 8.8	3.7 ± 7.4	48.0 ± 8.9	1.96 ± 0.36
			Weighted average:	2.12 ± 0.16

$B^0 \to D^{*\pm}D^{\mp}$ decay mode	N_{peak}	$N_{sideband}$	N_{signal}	$\mathcal{B}\left(B^0 \to D^{*\pm}D^{\mp}\right)\left(\times 10^{-4}\right)$
$\left[\left(\text{all } D^0 \text{ modes}\right)\pi^+_{soft}\right]_{D^{*+}}(K^+\pi^-\pi^-)_{D^-}$	711.5 ± 34.5	–	711.5 ± 34.5	-
$\left[\left(\text{all } D^0 \text{ modes}\right)\pi^+_{soft}\right]_{D^{*+}}\left(K^0_S\pi^-\right)_{D^-}$	61.9 ± 9.8	23.5 ± 10.5	57.2 ± 10.0	-
$\left[(\text{all } D^+ \text{ modes})\pi^0_{soft}\right]_{D^{*+}}(K^+\pi^-\pi^-)_{D^-}$	125.0 ± 16.5	–	125.0 ± 16.5	-
$\left[\left(\text{all } D^0 \text{ modes}\right)\pi^+_{soft}\right]_{D^{*+}}(\text{all } D^- \text{modes})_{D^-}$	773.9 ± 35.9	23.5 ± 10.5	769.2 ± 36.0	6.14 ± 0.29
$\left[\left(\text{all } D^0 \text{ modes}\right)\pi^+_{soft}\right]_{D^{*+}}(\text{all } D^- \text{modes})_{D^-}$ + $\left[(\text{all } D^+ \text{ modes})\pi^0_{soft}\right]_{D^{*+}}(K^+\pi^-\pi^-)_{D^-}$	891.5 ± 39.2	23.5 ± 10.5	886.8 ± 39.3	-

Table 6.6: Yields and results of the branching fraction measurements of $B^0 \to D^+D^-$ and $B^0 \to D^{*\pm}D^{\mp}$ decays.

Possible contributions of peaking background caused by decays with common final states as the reconstructed $B^0 \to D^+D^-$ and $B^0 \to D^{*\pm}D^{\mp}$ decay modes, such as $\bar{B}^0 \to D^{(*)+}K^{*-}$, $\bar{B}^0 \to D^{(*)+}\bar{K}^0\pi^-$ and $\bar{B}^0 \to D^{(*)+}\pi^-\pi^-\pi^+$ decays, are estimated by unbinned extended two-dimensional maximum likelihood fits to the M_{bc} and ΔE distributions in the D^- mass sidebands defined in Equation 6.2. The M_{bc} distributions in the D^- mass sidebands and projections of the fits are shown in Figure 6.5. After scaling the yields from the sidebands down to the signal region, a contribution of 0.7 ± 1.5 peaking background events for $B^0 \to D^+D^-$ and a contribution of 4.7 ± 2.1 peaking background for $B^0 \to D^{*\pm}D^{\mp}$ is found in the $D^- \to K^0_S\pi^-$ mass sidebands. The $D^- \to K^+\pi^-\pi^-$ mass sidebands are free of peaking background. The estimated peaking background contributions are subtracted from the yields in the peak to obtain the signal yields. The amount of peaking background is significantly less than in the measurements on the inclusive Monte Carlo simulation samples and does not need to be treated explicitly in the subsequent time-dependent measurements.

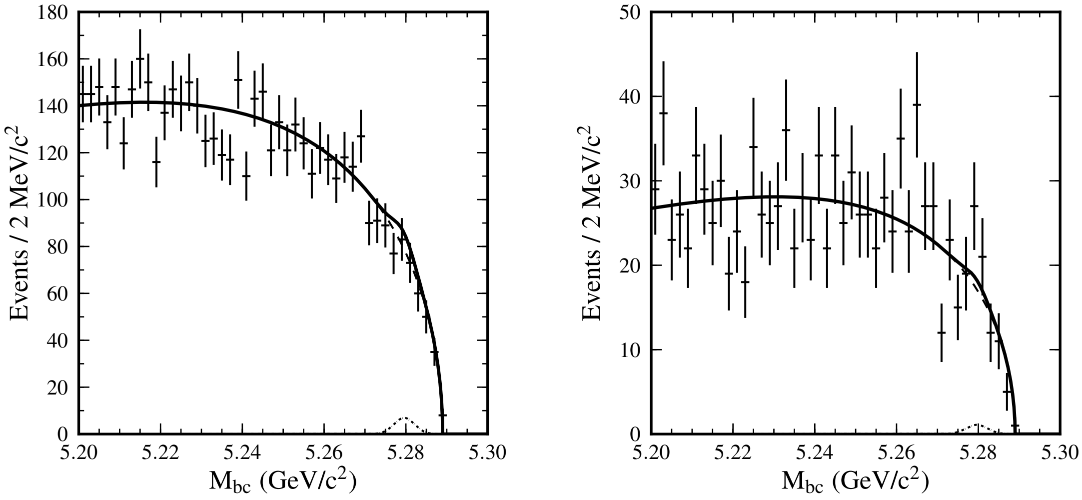

(a) $B^0 \to D^+ (K^+\pi^-\pi^-)_{D^-}$ in $M_{K^+\pi^-\pi^-}$ sideband (b) $B^0 \to D^+ \left(K^0_S\pi^-\right)_{D^-}$ in $M_{K^0_S\pi^-}$ sideband

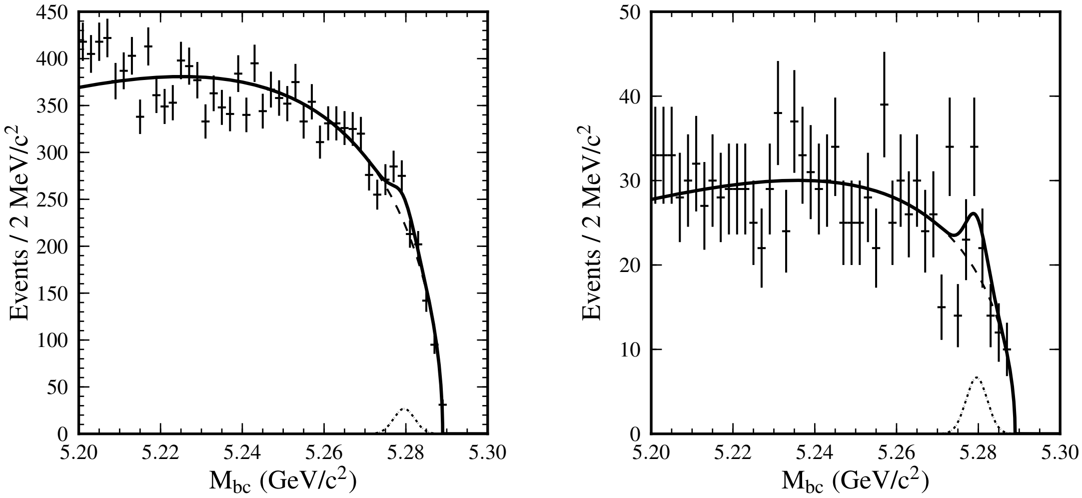

(c) $B^0 \to D^{*+} (K^+\pi^-\pi^-)_{D^-}$ in $M_{K^+\pi^-\pi^-}$ sideband (d) $B^0 \to D^{*+} \left(K^0_S\pi^-\right)_{D^-}$ in $M_{K^0_S\pi^-}$ sideband

Figure 6.5: M_{bc} data distributions in the D^- mass sidebands of $B^0 \to D^+D^-$ and $B^0 \to D^{*+}D^-$ decays reconstructed in $D^- \to K^+\pi^-\pi^-$ and $D^- \to K^0_S\pi^-$ decays modes. The dotted (dashed) lines show projections of the signal (background) components of the fits. A requirement of $|\Delta E| < 30$ MeV ($M_{bc} > 5.27$ GeV/c^2) is applied when plotting the M_{bc} (ΔE) distributions.

Figure 6.6 shows the M_{bc} and ΔE data distributions of $B^0 \to D^+D^-$ and $B^0 \to D^{*\pm}D^{\mp}$ decays and projections of the fits. The results of the fits and the determined branching fractions are summarised in Table 6.6.

The branching fractions are calculated from the signal yields, the reconstruction efficiencies, the branching fractions of the D^{*+}, D^0, D^+, D_s^+ and K^0_S decay modes involved in the reconstruction, and the number of $B\bar{B}$ pairs in the data set as defined in Equation 6.3. The reconstruction efficiencies determined by Monte Carlo simulations are corrected by applying the correspon-

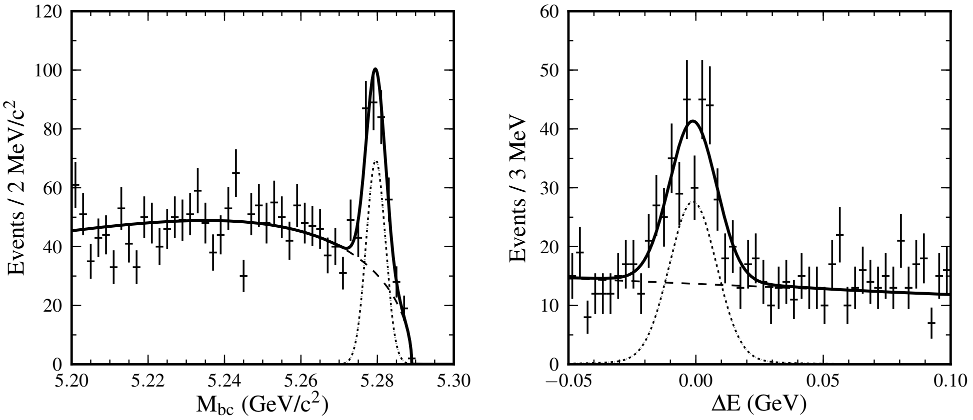

(a) $B^0 \to D^+D^- \to \left(K^-\pi^+\pi^+\right)_{D^+}\left(K^+\pi^-\pi^-\right)_{D^-}$

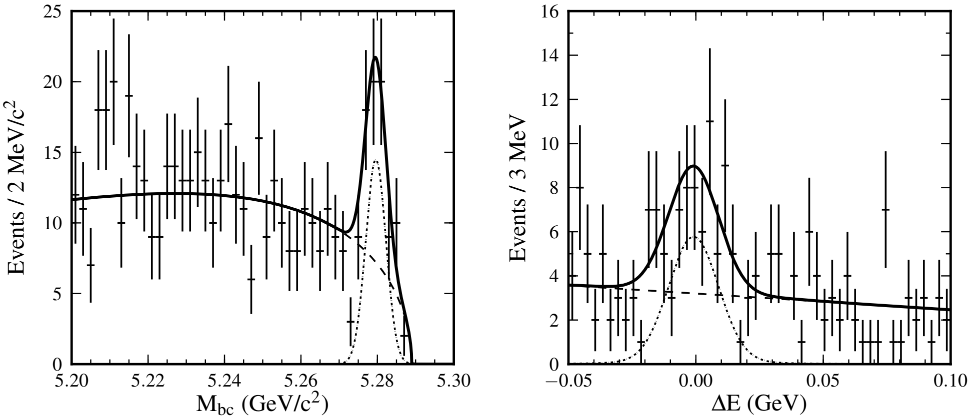

(b) $B^0 \to D^+D^- \to \left(K^-\pi^+\pi^+\right)_{D^+}\left(K^0_S\pi^-\right)_{D^-}$

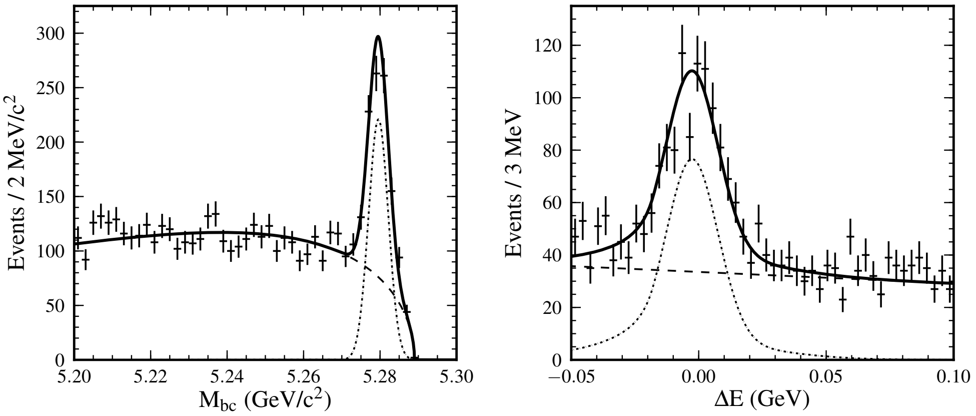

(c) $B^0 \to D^{*\pm}D^{\mp}$

Figure 6.6: M_{bc} and ΔE data distributions of (a) $B^0 \to D^+D^- \to (K^-\pi^+\pi^+)(K^+\pi^-\pi^-)$, (b) $B^0 \to D^+D^- \to (K^-\pi^+\pi^+)\left(K^0_S\pi^-\right)$ and (c) $B^0 \to D^{*\pm}D^{\mp}$ decays. The dotted (dashed) lines show projections of the signal (background) components of the fit. A requirement of $|\Delta E| < 30$ MeV ($M_{bc} > 5.27$ GeV/c^2) is applied when plotting the M_{bc} (ΔE) distributions.

ding correction factors given in Table 6.1 to account for efficiency differences between Monte Carlo simulations and data.

In $B^0 \to D^+D^-$, the branching fraction is determined for both reconstructed decay modes separately, and both results are consistent. The combined $B^0 \to D^+D^-$ branching fraction is calculated by the weighted average defined in Equation 6.4.

In $B^0 \to D^{*\pm}D^{\mp}$, the branching fraction is determined by the signal yield in all modes excluding those involving low momentum π^0_{soft} from D^{*+} decays.

The results of the $B^0 \to D^+D^-$ and $B^0 \to D^{*\pm}D^{\mp}$ branching fraction measurements are

$$\mathcal{B}\left(B^0 \to D^+D^-\right) = (2.12 \pm 0.16\ (\text{stat.}) \pm 0.18\ (\text{syst.})) \times 10^{-4}, \tag{6.8}$$

$$\text{and} \quad \mathcal{B}\left(B^0 \to D^{*\pm}D^{\mp}\right) = (6.14 \pm 0.29\ (\text{stat.}) \pm 0.50\ (\text{syst.})) \times 10^{-4}. \tag{6.9}$$

The contributions of the above given systematic uncertainties and their evaluation are described in the following Section 6.6.

6.6 Systematic Uncertainties

The sources of systematic uncertainties in the branching fractions of $B^0 \to D^+D^-$ and $B^0 \to D^{*\pm}D^{\mp}$ decays and their evaluation are described below.

Track reconstruction efficiency

As the systematic uncertainty related to the track reconstruction efficiency, an uncertainty of 0.35% is assigned to each charged track. This value has been determined in an internal study by the Belle Collaboration of the track finding efficiencies using partially reconstructed D^{*+} decays following the method described in Reference [117].

For low momentum π^+_{soft} mesons from D^{*+} decays, a systematic uncertainty of 1.83% has been assigned per track. This value has been determined in an internal study by the Belle Collaboration of systematic uncertainties of low momentum π^+ and π^0 mesons [118].

K^0_S reconstruction efficiency

As the systematic uncertainty related to the reconstruction efficiency of K^0_S mesons, an uncertainty of 4.5% is assigned. This value has been determined in an internal study by the Belle Collaboration of systematics uncertainties of K^0_S mesons [119].

π^0 reconstruction efficiency

As the systematic uncertainty related to the reconstruction efficiency of π^0 mesons, an uncertainty of 4% is assigned. This value has been determined in an internal study by the Belle Collaboration of systematics uncertainties of π^0 mesons [120].

K/π selection efficiency

The systematic uncertainty related to possible efficiency differences in the particle identification between Monte Carlo simulations and data with respect to the applied K/π selection is determined using information from measurements of $D^{*+} \to (K^-\pi^+)_{D^0}\pi^+_{soft}$ decays in inclusive D^{*+} samples [114]. The difference in the selection efficiency between Monte Carlo simulations and data is estimated by comparing each final state particle in each reconstructed decay mode to the particles of the inclusive D^{*+} samples. In the comparison, the kinematics of the particles dependent on the transverse momentum p_T and the polar angle θ in the laboratory frame are taken into account. The results of the comparison for $K^\pm$ and $\pi^\pm$ mesons in all reconstructed $B^0 \to D^+D^-$ and $B^0 \to D^{*\pm}D^{\mp}$ decay modes are summarised in Table 6.1.

Event reconstruction efficiency

The systematic uncertainty due to the statistics of the Monte Carlo simulations used to determine the reconstruction efficiencies is negligible because of the size of the samples.

The selection requirements on mass and mass-difference distributions of D^0, D^+, D^{*+} decay modes are chosen to avoid differences between Monte Carlo simulations and data. In one of the decay modes, $D^+ \to K^0_S\pi^+$, a possible deviation of the mass distribution from Monte Carlo simulations and from data can affect the determined event reconstruction efficiencies. The possible effect on the branching fractions is quantified by comparison of the mass distributions to 1.0% in $B^0 \to D^+D^-$ and to 0.1% in $B^0 \to D^{*\pm}D^{\mp}$ and is assigned as systematic uncertainty.

Continuum suppression

In $B^0 \to D^+D^-$, neural networks are used to suppress $e^+e^- \to q\bar{q}$ ($q \in \{u,d,s,c\}$) continuum events. Possible differences in the performance of the neural networks between Monte Carlo simulations and data are studied using the $B^0 \to D_s^+D^-$ control sample in Section 5.2.3. The largest deviations in the signal yield ratios of data and Monte Carlo simulations in the interval [-1,0.25], as shown in Figures 5.2(a) and (b), are assigned as systematic uncertainty related to the selection requirements on the neural network continuum suppression. The upper boundary of the interval is significantly larger than the selection requirements applied on the neural networks, see Figure 5.10. Averaged over both reconstructed $B^0 \to D^+D^-$ decay modes, the systematic uncertainty is estimated to be 4.1%.

Fit models

The systematic uncertainty related to the fit models applied to extract the signal yields in the $B^0 \to D^+D^-$ and $B^0 \to D^{*\pm}D^{\mp}$ branching fraction measurements is determined by varying separately every fixed parameter in the fits by $\pm 1\sigma$ and repeating the fit. For each parameter, the largest deviation with and without variation is assigned as a systematic uncertainty. The total systematic uncertainties related to the fit models are obtained by the quadratic sum of the contributions of all parameters.

D^0, D^+, D^{*+} branching fractions

The systematic uncertainty due to uncertainties on the branching fractions of D^0, D^+, D^{*+} decay modes involved in the reconstruction is determined by propagation of the uncertainties of current world averages given in Table 6.2 for each reconstructed $B^0 \to D^+D^-$ and $B^0 \to D^{*\pm}D^{\mp}$ decay mode.

Number of $B\bar{B}$ events

The uncertainty of the number of $(772 \pm 11) \times 10^6$ $B\bar{B}$ events in the data set is propagated to the branching fractions. A systematic uncertainty of 1.4% is obtained.

The contributions of the individual sources of systematics uncertainties to the measured $B^0 \to D^+D^-$ and $B^0 \to D^{*\pm}D^{\mp}$ branching fractions are summarised in Table 6.7. The contributions that are evaluated for individual $B^0 \to D^+D^-$ and $B^0 \to D^{*\pm}D^{\mp}$ decay modes are averaged according to the efficiencies and branching fractions of the corresponding modes. The total systematic uncertainties on the branching fractions are calculated by the quadratic sum of the individual contributions. A relative systematic uncertainty on the measured branching fractions of 8.6% in $B^0 \to D^+D^-$ and of 8.1% in $B^0 \to D^{*\pm}D^{\mp}$ is obtained.

Source	$B^0 \to D^+D^-$	$B^0 \to D^{*\pm}D^{\mp}$
Track reconstruction efficiency	2.0	4.1
K_S^0 reconstruction efficiency	0.7	0.7
π^0 reconstruction efficiency	-	1.6
K/π selection efficiency	5.5	5.3
Event reconstruction efficiency	1.0	0.1
Continuum suppression	4.1	-
Fit models	1.1	0.6
D^0, D^+, D^{*+} branching fractions	4.3	3.9
Number of $B\bar{B}$ events	1.4	1.4
Total	8.6	8.1

Table 6.7: Systematic uncertainties of the $B^0 \to D^+D^-$ and $B^0 \to D^{*\pm}D^{\mp}$ branching fraction measurements (in %).

7 Time-Dependent Measurements

The time-dependent measurements of CP violation in $B^0 \to D^+D^-$ and $B^0 \to D^{*\pm}D^{\mp}$ decays are performed as blind analyses after the time-integrated measurements. The fit procedures to extract the CP violation parameters described in Section 4.5 are validated by a wide variety of cross-checks by usage of Monte Carlo simulations and by time-dependent measurements of the $B^0 \to D_s^+D^-$ and $B^0 \to D_s^+D^{*-}$ control samples. Only after the validation of the fit procedures, the $B^0 \to D^+D^-$ and $B^0 \to D^{*\pm}D^{\mp}$ data distributions are unblinded and the time-dependent measurements are performed.

7.1 Validation of the Time-Dependent CP Violation Measurements

In the following the validation of the time-dependent CP violation measurements prior to the unblinding of the data distributions are described. The validation comprises the measurements of lifetimes of simulated signal decays, linearity tests, the measurements on large Monte Carlo simulation samples of inclusive decays and ensemble tests.

7.1.1 Measurements of Lifetimes of Simulated Signal Decays

The measurements of lifetimes of untagged samples of B decays allow to validate the fit procedure applied in the time-dependent analyses. In particular, the fits of lifetimes of large samples of simulated signal decays allow to identify possible biases. Biases in the lifetime measurements can indicate wrong decay vertex reconstruction procedures or an inaccurate treatment of resolution effects.

For this study, large Monte Carlo simulation samples of $B^0 \to D^+D^-$, $B^0 \to D^{*\pm}D^{\mp}$, $B^0 \to D_s^+D^-$ and $B^+ \to \bar{D}^0D^+$ decays are generated. For $B^0 \to D^+D^-$, the sample comprises 100000 signal decays and for $B^0 \to D^{*\pm}D^{\mp}$ 25000 signal decays in each reconstructed decay mode. The sample sizes are significant larger than the expected yields of 250 signal decays in $B^0 \to D^+D^-$ and of 900 signal decays in $B^0 \to D^{*\pm}D^{\mp}$. The decays are generated by EvtGen [112] according to lifetimes of $\tau_{B^0} = 1.5344\,\mathrm{ps}$ and $\tau_{B^+} = 1.6545\,\mathrm{ps}$. The detector response is simulated by GEANT3 [113].

All selection requirements described in Section 5.3, for example on the particle identification, on the minimal number of SVD hits or on the continuum suppression in $B^0 \to D^+D^-$, are applied to the reconstructed signal decays. Additionally, the reconstructed signal decays are required to be correctly reconstructed.

The B meson lifetimes are estimated by unbinned maximum likelihood fits to the untagged proper decay time difference distributions by using the signal probability density function in Equation 4.33 and the outlier parameterisation in Equation 4.55. Because the samples contain only correctly reconstructed signal decays, the fits do not include the background parameterisation.

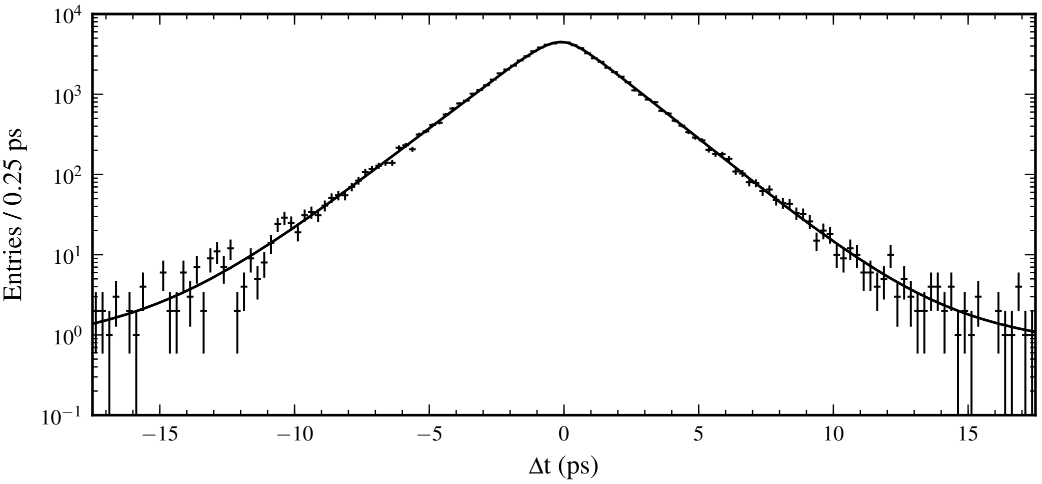

(a) $B^0 \to D^+D^- \to (K^-\pi^+\pi^+)\,(K^+\pi^-\pi^-)$

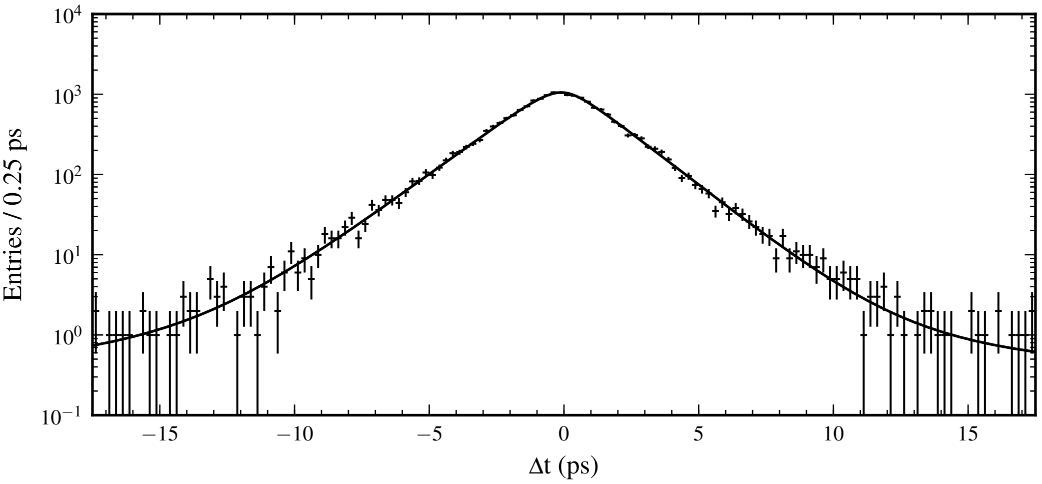

(b) $B^0 \to D^{*+}D^- \to [(K^-\pi^+\pi^-\pi^+)_{D^0}]_{D^{*+}}\,(K^+\pi^-\pi^-)_{D^-}$

Figure 7.1: Proper decay time difference distributions and projections of the limetime fits for simulated (a) $B^0 \to D^+D^- \to (K^-\pi^+\pi^+)(K^+\pi^-\pi^-)$ and (b) $B^0 \to D^{*+}D^- \to \left[(K^-\pi^+\pi^-\pi^+)_{D^0}\,\pi^+_{\text{soft}}\right]_{D^{*+}}(K^+\pi^-\pi^-)_{D^-}$ decays. The results of the fits are given in Table 7.1.

Examples for proper decay time difference distributions and projections of the lifetime fits for each of the reconstructed $B^0 \to D^+D^-$ and $B^0 \to D^{*\pm}D^{\mp}$ decay modes are shown in Figure 7.1. The results of the lifetime fits for all reconstructed decay modes are summarised in Table 7.1. The lifetimes obtained in the fits are all consistent and show no significant deviation from the lifetimes used as input to the generation of the simulated signal decays.

The successful lifetime measurements provide an important confirmation for the validity of the parameterisation of the resolution effects and indicate that the time-dependent measurements perform correctly on untagged Monte Carlo simulation samples.

Decay mode	τ_{fit} (ps)	$\left(\tau_{\mathrm{fit}}-\tau_{\mathrm{gen}}\right)/\sigma_{\mathrm{fit}}$
$B^+ \to \bar{D}^0 D^+ \to (K^+\pi^-)(K^-\pi^+\pi^+)$	1.645 ± 0.006	-1.7
$B^0 \to D^+ D^- \to (K^-\pi^+\pi^+)(K^+\pi^-\pi^-)$	1.530 ± 0.006	-0.8
$B^0 \to D^+ D^- \to (K^-\pi^+\pi^+)\left(K^0_S\pi^-\right)$	1.535 ± 0.006	0
$B^0 \to D_s^+ D^- \to (K^+K^-\pi^+)\left(K^0_S\pi^-\right)$	1.533 ± 0.006	-0.3
$B^0 \to D_s^+ D^- \to (K^+K^-\pi^+)\left(K^0_S\pi^-\right)$	1.546 ± 0.006	$+2.0$
$B^0 \to D^{*\pm} D^{\mp}$ decay mode	τ_{fit} (ps)	$\left(\tau_{\mathrm{fit}}-\tau_{\mathrm{gen}}\right)/\sigma_{\mathrm{fit}}$
$\left[(K^-\pi^+)_{D^0}\,\pi^+_{\mathrm{soft}}\right]_{D^{*+}}(K^+\pi^-\pi^-)_{D^-}$	1.528 ± 0.012	-0.5
$\left[(K^-\pi^+\pi^-\pi^+)_{D^0}\,\pi^+_{\mathrm{soft}}\right]_{D^{*+}}(K^+\pi^-\pi^-)_{D^-}$	1.521 ± 0.012	-1.1
$\left[\left(K^-\pi^+\pi^0\right)_{D^0}\,\pi^+_{\mathrm{soft}}\right]_{D^{*+}}(K^+\pi^-\pi^-)_{D^-}$	1.533 ± 0.013	-0.1
$\left[\left(K^0_S\pi^+\pi^-\right)_{D^0}\,\pi^+_{\mathrm{soft}}\right]_{D^{*+}}(K^+\pi^-\pi^-)_{D^-}$	1.517 ± 0.012	-1.4
$\left[(K^-\pi^+)_{D^0}\,\pi^+_{\mathrm{soft}}\right]_{D^{*+}}\left(K^0_S\pi^-\right)_{D^-}$	1.515 ± 0.012	-1.6
$\left[(K^-\pi^+\pi^-\pi^+)_{D^0}\,\pi^+_{\mathrm{soft}}\right]_{D^{*+}}\left(K^0_S\pi^-\right)_{D^-}$	1.520 ± 0.012	-1.2
$\left[\left(K^-\pi^+\pi^0\right)_{D^0}\,\pi^+_{\mathrm{soft}}\right]_{D^{*+}}\left(K^0_S\pi^-\right)_{D^-}$	1.536 ± 0.015	$+0.1$
$\left[\left(K^0_S\pi^+\pi^-\right)_{D^0}\,\pi^+_{\mathrm{soft}}\right]_{D^{*+}}\left(K^0_S\pi^-\right)_{D^-}$	1.505 ± 0.014	-2.1
$\left[(K^-\pi^+\pi^+)_{D^+}\,\pi^0_{\mathrm{soft}}\right]_{D^{*+}}(K^+\pi^-\pi^-)_{D^-}$	1.524 ± 0.012	-0.8
$\left[\left(K^0_S\pi^+\right)_{D^+}\,\pi^0_{\mathrm{soft}}\right]_{D^{*+}}(K^+\pi^-\pi^-)_{D^-}$	1.524 ± 0.012	-0.9

Table 7.1: Results of the B^+ and B^0 lifetime measurements of correctly reconstructed signal decays. The signal decays are generated according to lifetimes of $\tau_{B^+} = 1.6545\,\mathrm{ps}$ and $\tau_{B^0} = 1.5344\,\mathrm{ps}$.

7.1.2 Linearity Tests

The response of the time-dependent fit procedure to different generator input values of the CP violation parameters $\mathcal{S}$ and $\mathcal{C}$ is verified by linearity tests. The linearity tests are performed for simulated $B^0 \to D^+D^-$ and $B^0 \to D^{*\pm}D^{\mp}$ decays. For $B^0 \to D^{*\pm}D^{\mp}$ decays, only the charge-configuration $B^0 \to D^{*+}D^-$ is considered. The fit procedure considering both charge-configurations $B^0 \to D^{*+}D^-$ and $B^0 \to D^{*-}D^+$ and all five CP violation parameters are validated by ensemble tests in Section 7.1.5.

		Coefficients of linear function	
Linearity test	Distribution	c_0	c_1
$B^0 \to D^+D^-$ linearity test in $\mathcal{S}$	$\mathcal{S}_{\text{fit}} - \mathcal{S}_{\text{gen}}$ vs. $\mathcal{S}_{\text{gen}}$	-0.002 ± 0.006	$+0.004 \pm 0.010$
	$\mathcal{C}_{\text{fit}}$ vs. $\mathcal{S}_{\text{gen}}$	$+0.001 \pm 0.005$	$+0.003 \pm 0.007$
$B^0 \to D^+D^-$ linearity test in $\mathcal{C}$	$\mathcal{C}_{\text{fit}} - \mathcal{C}_{\text{gen}}$ vs. $\mathcal{C}_{\text{gen}}$	$+0.004 \pm 0.005$	-0.008 ± 0.007
	$\mathcal{S}_{\text{fit}}$ vs. $\mathcal{C}_{\text{gen}}$	-0.000 ± 0.008	$+0.009 \pm 0.012$
$B^0 \to D^{*+}D^-$ linearity test in $\mathcal{S}$	$\mathcal{S}_{\text{fit}} - \mathcal{S}_{\text{gen}}$ vs. $\mathcal{S}_{\text{gen}}$	-0.006 ± 0.003	$+0.007 \pm 0.005$
	$\mathcal{C}_{\text{fit}}$ vs. $\mathcal{S}_{\text{gen}}$	$+0.001 \pm 0.002$	$+0.002 \pm 0.004$
$B^0 \to D^{*+}D^-$ linearity test in $\mathcal{C}$	$\mathcal{C}_{\text{fit}} - \mathcal{C}_{\text{gen}}$ vs. $\mathcal{C}_{\text{gen}}$	-0.003 ± 0.002	$+0.002 \pm 0.003$
	$\mathcal{S}_{\text{fit}}$ vs. $\mathcal{C}_{\text{gen}}$	$+0.002 \pm 0.003$	$+0.001 \pm 0.005$

Table 7.2: Results of the fits of a linear function $f(x) = c_0 + c_1 \cdot x$ to the distributions obtained in the linearity tests for the CP violation parameters $\mathcal{S}$ and $\mathcal{C}$. The distributions of the $B^0 \to D^{*+}D^-$ linearity tests are shown in Figure 7.2.

For the linearity tests, different sets of simulated signal decays are generated. In each set, one CP violation parameter is varied within the physical boundary defined by the interval $[-1, 1]$, while the other CP violation parameter is fixed to zero.

The generation of the simulated signal decays for the linearity test in $\mathcal{S}$ and $\mathcal{C}$ is performed by different approaches. For the linearity tests in $\mathcal{S}$, the signal decays are generated by EvtGen [112] and the full detector response is simulated by GEANT3 [113]. For the linearity test in $\mathcal{C}$, the signal decays are created by pseudo-experiments in a hybrid Monte Carlo technique to reduce the computational effort in the generation of the simulations. The hybrid Monte Carlo technique follows the approach, that is applied in a similar way in the ensemble tests performed for the validation of the branching fraction measurements in Section 6.3. In the hybrid Monte Carlo technique, the proper decay time difference distributions are generated according to the signal probability density function of the fit model, while all other parameters, for example the flavor tagging quantities and the decay vertex uncertainties, are generated according to distributions obtained from EvtGen/GEANT3 simulations. The hybrid Monte Carlo technique is applied to simulate signal events in the pseudo-experiments as realistic as possible.

The CP violation parameters $\mathcal{S}$ and $\mathcal{C}$ of different sets of simulated $B^0 \to D^+D^-$ and $B^0 \to D^{*+}D^-$ decays are estimated by unbinned maximum likelihood fits to the flavor-tagged proper decay time difference distributions. The likelihood function is composed of the signal probabi-

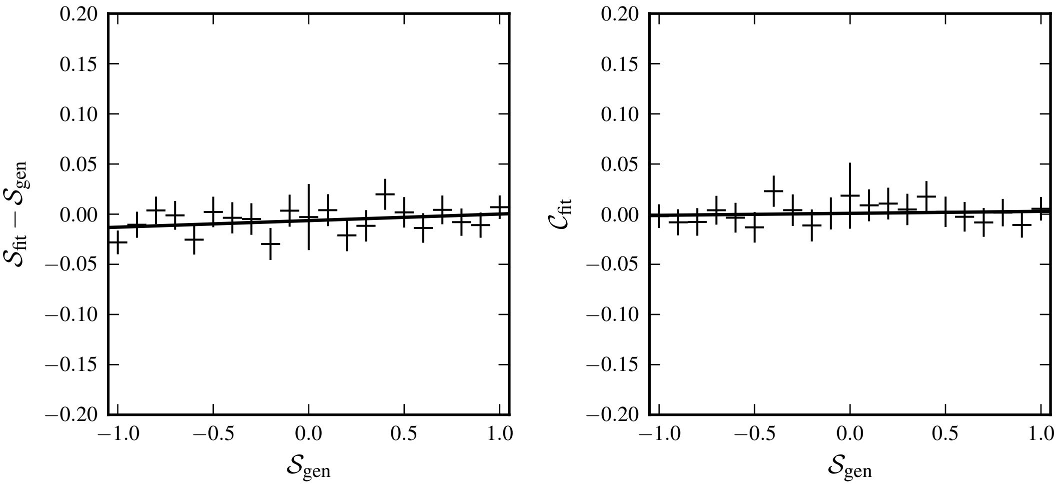

(a) $\mathcal{S}$ linearity test: $\mathcal{S} \in [-1,1]$ and $\mathcal{C} = 0$

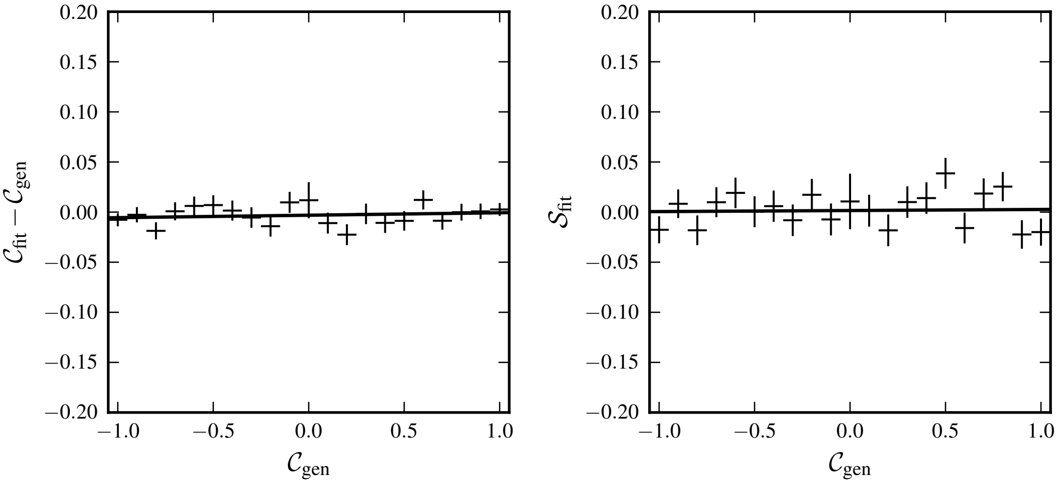

(b) $\mathcal{C}$ linearity test: $\mathcal{C} \in [-1,1]$ and $\mathcal{S} = 0$

Figure 7.2: Linearity tests for the CP violation parameters (a) $\mathcal{S}$ and (b) $\mathcal{C}$ performed for $B^0 \rightarrow D^{*+}D^-$ decays. The data points with error bars represent the values obtained in the measurement dependent on the generator input value. The solid lines show the projections of the fits of a linear function to the data points. The fit results of the linear function are summarised in Table 7.2.

lity density function for the measurement of CP violation parameters defined in Equation 4.40, and an outlier term.

In all sets of simulated $B^0 \rightarrow D^+D^-$ and $B^0 \rightarrow D^{*+}D^-$ decays, the CP violation parameters determined by fits are consistent with the values used as input to the generation of the simulations. A linear function is fitted to the residual distributions of fit and generator values in dependence of the generator values. The distributions of the linearity tests in $\mathcal{S}$ and in $\mathcal{C}$ for $B^0 \rightarrow D^{*+}D^-$ decays and corresponding fit projections of the linear function are shown in Figure 7.2. The fit results for the coefficients of the linear function for all linearity tests are given in Table 7.2. The coefficients are consistent with a constant function.

The tests confirm the linearity of the response of the time-dependent fit procedure within the boundary of the physical parameter space of the CP violation parameters.

7.1.3 Measurements of CP Violation on Inclusive Monte Carlo Simulation Samples

The time-dependent measurements of the CP violation in $B^0 \rightarrow D^+D^-$ and $B^0 \rightarrow D^{*\pm}D^{\mp}$ decays are performed several times on Monte Carlo simulation samples of inclusive generic B decays and continuum events, referred to as generic Monte Carlo simulations. The generic Monte Carlo simulation samples contain signal and background of equivalent composition and size as the data sample and allow to test the complete CP fit procedure.

	CPV parameter		Number events			
$B^0 \rightarrow D^+D^-$ decay mode	$\mathcal{S}_{D^+D^-}$	$\mathcal{C}_{D^+D^-}$	Signal	Bkg.	Total	
$(K^-\pi^+\pi^+)_{D^+}\,(K^+\pi^-\pi^-)_{D^-}$	-0.64 ± 0.21	-0.19 ± 0.18	215	132	346	Sample 1
$(K^-\pi^+\pi^+)_{D^+}\left(K^0_S\pi^-\right)_{D^-}$	-2.20 ± 1.24	$+0.27 \pm 0.59$	25	45	70	
$(K^-\pi^+\pi^+)_{D^+}\,(K^+\pi^-\pi^-)_{D^-} + (K^-\pi^+\pi^+)_{D^+}\left(K^0_S\pi^-\right)_{D^-}$	-0.68 ± 0.20	-0.17 ± 0.18	239	177	415	
$(K^-\pi^+\pi^+)_{D^+}\,(K^+\pi^-\pi^-)_{D^-}$	-0.66 ± 0.28	$+0.11 \pm 0.17$	196	106	301	Sample 2
$(K^-\pi^+\pi^+)_{D^+}\left(K^0_S\pi^-\right)_{D^-}$	-0.54 ± 0.70	$+0.19 \pm 0.56$	33	50	83	
$(K^-\pi^+\pi^+)_{D^+}\,(K^+\pi^-\pi^-)_{D^-} + (K^-\pi^+\pi^+)_{D^+}\left(K^0_S\pi^-\right)_{D^-}$	-0.65 ± 0.26	$+0.11 \pm 0.16$	229	156	384	
$(K^-\pi^+\pi^+)_{D^+}\,(K^+\pi^-\pi^-)_{D^-}$	-0.66 ± 0.19	-0.13 ± 0.16	215	117	331	Sample 3
$(K^-\pi^+\pi^+)_{D^+}\left(K^0_S\pi^-\right)_{D^-}$	-1.73 ± 0.70	$+0.74 \pm 0.43$	24	47	71	
$(K^-\pi^+\pi^+)_{D^+}\,(K^+\pi^-\pi^-)_{D^-} + (K^-\pi^+\pi^+)_{D^+}\left(K^0_S\pi^-\right)_{D^-}$	-0.71 ± 0.18	-0.07 ± 0.15	243	160	402	
$(K^-\pi^+\pi^+)_{D^+}\,(K^+\pi^-\pi^-)_{D^-}$	-0.61 ± 0.24	-0.10 ± 0.17	216	124	339	Sample 4
$(K^-\pi^+\pi^+)_{D^+}\left(K^0_S\pi^-\right)_{D^-}$	$+0.06 \pm 0.78$	-0.35 ± 0.53	20	47	68	
$(K^-\pi^+\pi^+)_{D^+}\,(K^+\pi^-\pi^-)_{D^-} + (K^-\pi^+\pi^+)_{D^+}\left(K^0_S\pi^-\right)_{D^-}$	-0.55 ± 0.24	-0.12 ± 0.16	236	171	407	

Table 7.3: Results of the CP violation measurements performed on inclusive Monte Carlo simulation samples for individual $B^0 \rightarrow D^+D^-$ decay modes and their combinations. In the Monte Carlo simulations, the signal decays are generated according to $\mathcal{S}_{D^+D^-} = -0.68$ and $\mathcal{C}_{D^+D^-} = 0$. The given yields are determined by integration of the particular components of the fit functions.

To represent the expected data distributions as realistically as possible, the $B^0 \rightarrow D^+D^-$ and $B^0 \rightarrow D^{*\pm}D^{\mp}$ signal decays in the generic Monte Carlo simulation samples provided by the Belle Collaboration are replaced by signal decays that are generated according to current world averages of branching fractions and CP violation parameters from recent precision measurements in $b \rightarrow c\bar{c}s$ transitions [121, 95]. The generic Monte Carlo simulation samples and the signal replacement are described in Section 6.2. The numerical values used for the generation of the signal replacement are summarised in Table 6.2.

The parameters of the probability density function and the resolution function of the background components described in Section 4.5.2 are determined by fits to the $M_{bc} < 5.26\ \text{GeV}/c^2$ sidebands. The parameters obtained in the sidebands are fixed in subsequent CP fits of the signal region. The agreement of the background shape in the sidebands with the background shape in the signal region is verified by χ^2-tests of the corresponding distributions. Additionally, the background composition in the sidebands is found to be consistent with the background composition inside the signal region based on Monte Carlo information.

In the measurements of $B^0 \to D^+D^-$ decays, the CP violation parameters $\mathcal{S}_{D^+D^-}$ and $\mathcal{C}_{D^+D^-}$ are extracted by the signal probability density function in Equation 4.40. Both reconstructed $B^0 \to D^+D^-$ decay modes are fitted separately and in combination. The results of the measurements are summarised in Table 7.3. The inclusion of the $B^0 \to D^+D^- \to (K^-\pi^+\pi^+)\left(K^0_S\pi^-\right)$ decay mode in addition to the $B^0 \to D^+D^- \to (K^-\pi^+\pi^+)(K^+\pi^-\pi^-)$ decay mode improves the statistical uncertainty on the CP violation parameters by up to 7%. The CP violation parameters determined in the fits are consistent with the values of $\mathcal{S}_{D^+D^-} = -0.68$ and $\mathcal{C}_{D^+D^-} = 0$ used as input to the generation of the simulated signal decays.

$B^0 \to D^{*\pm}D^{\mp}$ decays	$\mathcal{A}_{D^{*\pm}D^{\mp}}$	$\mathcal{S}_{D^{*+}D^-}$	$\mathcal{C}_{D^{*+}D^-}$	$\mathcal{S}_{D^{*-}D^+}$	$\mathcal{C}_{D^{*-}D^+}$
Sample 1	-0.02 ± 0.05	-0.86 ± 0.15	-0.26 ± 0.16	-0.46 ± 0.21	$+0.07 \pm 0.16$
Sample 2	0.03 ± 0.05	-0.76 ± 0.17	-0.05 ± 0.14	-0.28 ± 0.23	-0.06 ± 0.14
Sample 3	0.04 ± 0.05	-0.73 ± 0.16	-0.08 ± 0.14	-0.74 ± 0.16	$+0.26 \pm 0.13$

Table 7.4: Results of the CP violation measurements performed on generic Monte Carlo simulation samples for $B^0 \to D^{*\pm}D^{\mp}$ decays. In the measurements, the parameterisation in Equation 4.42 is applied. In the Monte Carlo simulations, the signal decays are generated according to $\mathcal{A}_{D^{*\pm}D^{\mp}} = 0$, $\mathcal{S}_{D^{*+}D^-} = \mathcal{S}_{D^{*-}D^+} = -0.68$ and $\mathcal{C}_{D^{*+}D^-} = \mathcal{C}_{D^{*-}D^+} = 0$.

In the measurements of $B^0 \to D^{*\pm}D^{\mp}$ decays, the CP violation parameters $\mathcal{A}_{D^{*\pm}D^{\mp}} = 0$, $\mathcal{S}_{D^{*+}D^-}$, $\mathcal{C}_{D^{*+}D^-}$, $\mathcal{S}_{D^{*-}D^+}$ and $\mathcal{C}_{D^{*-}D^+}$ are extracted by the signal probability density function in Equation 4.42. The fits are performed to all ten reconstructed $B^0 \to D^{*\pm}D^{\mp}$ decay modes combined including the modes involving low momentum π^0_{soft} mesons from D^{*+} decays. The results are summarised in Table 7.4. All measurements are consistent with the generator input values of $\mathcal{A}_{D^{*\pm}D^{\mp}} = 0$, $\mathcal{S}_{D^{*+}D^-} = \mathcal{S}_{D^{*-}D^+} = -0.68$ and $\mathcal{C}_{D^{*+}D^-} = \mathcal{C}_{D^{*-}D^+} = 0$.

The agreement of the results obtained in the inclusive Monte Carlo simulations with the generator input values indicate that the time-dependent measurements perform correctly in the presence of background.

7.1.4 Ensemble Test for the Entire Physical Parameter Space

For the validation of the time-dependent measurements, advanced ensemble tests for $\mathrm{B}^0 \to \mathrm{D}^+\mathrm{D}^-$ decays are performed. In the ensemble tests, the response of the fit procedure to CP violation parameters within the entire physical parameter space, defined by $\sqrt{\mathcal{S}^2+\mathcal{C}^2} \leq 1$, is studied.

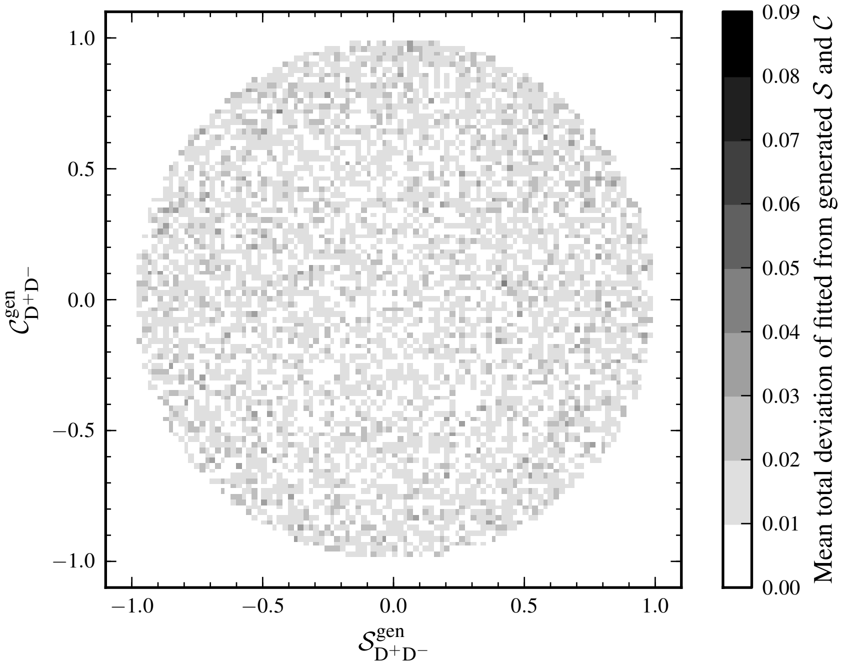

Figure 7.3: Averaged total deviations of the measurements of the CP violation parameters $\mathcal{S}$ and $\mathcal{C}$ from the values used in the generation of the pseudo-experiments. The physical parameter space of the CP violation parameters is defined by $\sqrt{\mathcal{S}^2+\mathcal{C}^2} \leq 1$ and is sampled by a two-dimensional grid with a spacing of 2×10^{-2} in $\mathcal{S}$ and in $\mathcal{C}$ direction. On each grid point, 500 pseudo-experiments are generated and the measurements are performed.

The physical parameter space is sampled by a two-dimensional grid with a spacing of 2×10^{-2} with respect to the parameters $\mathcal{S}$ and $\mathcal{C}$. On each grid point, 500 pseudo-experiments are generated according to the data distributions from the time-integrated measurements of $\mathrm{B}^0 \to \mathrm{D}^+\mathrm{D}^-$ decays. The model for generation of the pseudo-experiments represents the real data distributions with respect to the M_{bc} and $\Delta\mathrm{E}$ parameterisation, the signal and background yields, the distributions of vertex fit uncertainties and quality indicators, the distributions related to the flavor tagging and the background parameterisation. The CP violation parameters are extracted from the pseudo-experiments by the same fit procedure that is applied to the data distributions at a later stage.

The deviations of the CP violation parameters $\mathcal{S}$ and $\mathcal{C}$ obtained in the measurements performed on the pseudo-experiments from the values used for the generation provide a measure for possible systematic deviations in the CP violation parameter space for the fit procedure.

The averaged total deviations of the measured CP violation parameters in dependence of the generator values are shown in Figure 7.3. The total deviation is defined as the geometric distance of the individual deviations of $\mathcal{S}$ and $\mathcal{C}$ within the parameter space. The deviations fluctuate at a level that is small compared to the statistical uncertainty in the CP violation measurement. The fluctuations show no structures, that could indicate regions of possible systematic biases.

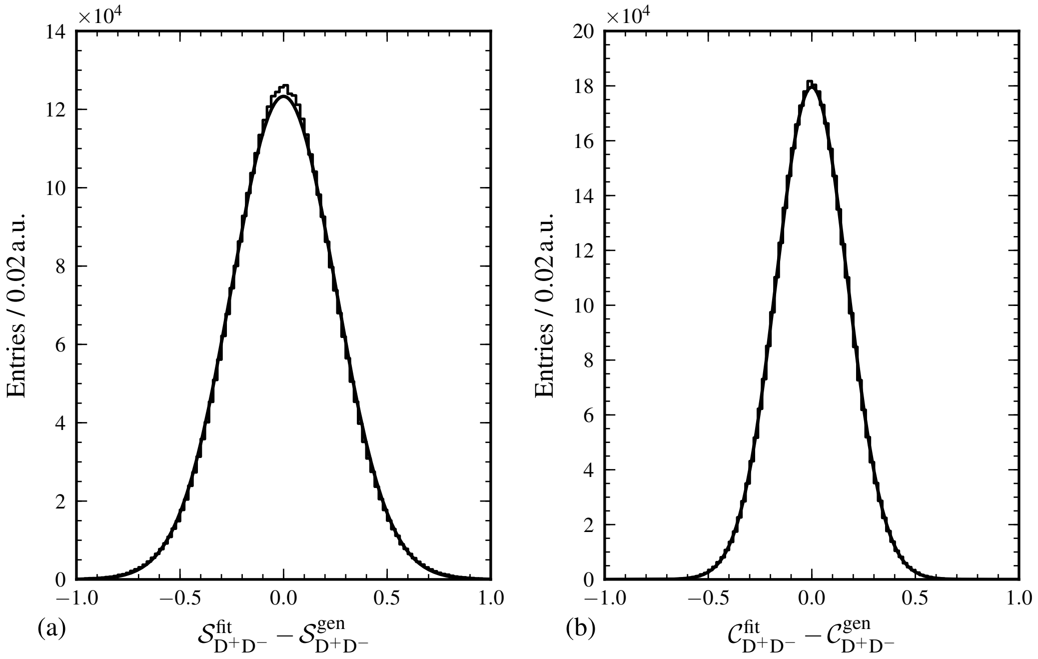

Figure 7.4: Residual distributions of (a) $\mathcal{S}_{\rm fit} - \mathcal{S}_{\rm gen}$ and of (b) $\mathcal{C}_{\rm fit} - \mathcal{C}_{\rm gen}$ obtained in the tests performed within the entire physical parameter space of $\mathcal{S}$ and $\mathcal{C}$ for $\rm B^0 \to D^+D^-$ decays. The solid curves show projections of the fit of a Gaussian distribution to the residual distributions. The results of the fits are summarised in Table 7.5.

If in $\rm B^0 \to D^+D^-$ decays the contribution of penguin amplitudes is negligible, then the same CP violation is expected as in $\rm b \to c\bar{c}s$ transitions. Precision measurements of $\rm b \to c\bar{c}s$ transitions suggest $\mathcal{S} = -0.68$ and $\mathcal{C} = 0$ [121, 95]. For the pseudo-experiments generated according to CP violation parameters close to these values, the measurements in the ensemble tests return values outside of the physical boundary in approximately 15% of all cases.

	$\mathcal{S}^{\rm fit}_{\rm D^+D^-} - \mathcal{S}^{\rm gen}_{\rm D^+D^-}$	$\mathcal{C}^{\rm fit}_{\rm D^+D^-} - \mathcal{C}^{\rm gen}_{\rm D^+D^-}$
Mean	-0.0002 ± 0.0001	-0.0002 ± 0.0001
Width	0.2510 ± 0.0001	0.1724 ± 0.0001

Table 7.5: Result of the fits of a Gaussian function to the residual distributions in Figure 7.4.

The residual distributions of $\mathcal{S}$ and $\mathcal{C}$ for the measurements of all pseudo-experiments in the ensemble tests are shown in Figure 7.4. The residual distributions are fitted by Gaussian functions. The results of the fits are summarised in Table 7.5. The mean value of the residual distributions are consistent with zero indicating no bias. The width of the residual distributions provide an estimate of the expected statistical uncertainties on the CP violation parameters in the measurements. According to the ensemble tests, for $\mathcal{S}$ an uncertainty of 0.25 and for $\mathcal{C}$ an uncertainty of 0.17 is expected.

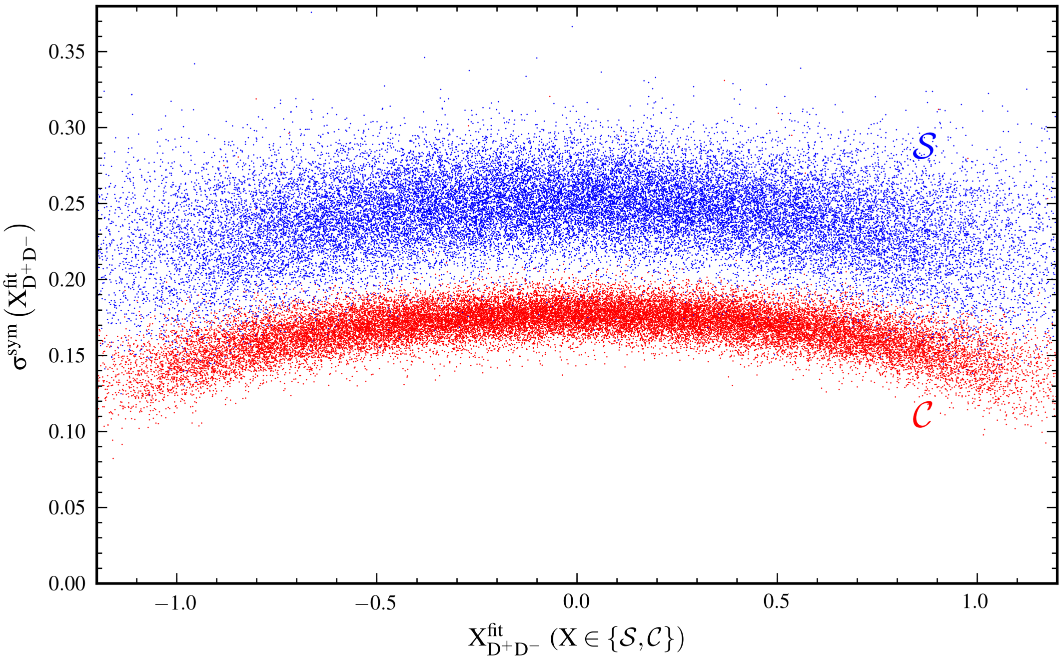

Figure 7.5: Dependence of the symmetric statistical uncertainty on the center values of the CP violation measurements of $\mathcal{S}$ (blue) and $\mathcal{C}$ (red). The distributions are determined by ensemble tests within the entire physical parameter space, defined by $\sqrt{\mathcal{S}^2+\mathcal{C}^2} \leq 1$.

In addition, the ensemble tests within the entire physical parameter space allow further studies of the uncertainty distributions. The distributions of the symmetric statistical uncertainties $\sigma^{\mathrm{sym}}(\mathcal{S})$ and $\sigma^{\mathrm{sym}}(\mathcal{C})$ in dependence of the measured center values of $\mathcal{S}$ and $\mathcal{C}$ are shown in Figure 7.5. The uncertainty of $\mathcal{S}$ is on average larger than the uncertainty of $\mathcal{C}$. The probability density function describing the proper decay time difference distribution of signal events in Equation 4.40 is symmetric with respect to the cosine term parameterising the direct CP violation $\mathcal{C}$ and has its maximum for vanishing $\mathcal{S}$ at $\Delta t = 0$. The mixing-induced CP violation $\mathcal{S}$ is parameterised by an antisymmetric sine term. As a consequence, the maxima of the proper decay time difference distributions for B^0 and $\bar{B}^0$ flavor tags are shifted away from $\Delta t = 0$ for increasing $\mathcal{S}$. Due to the exponential decay, most of the statistics in the time-dependent measurements is at low Δt values. Therefore, the likelihood function in dependence on the CP violation parameters is steeper for $\mathcal{C}$ than for $\mathcal{S}$, and the values of $\sigma^{\mathrm{sym}}(\mathcal{C})$ are on average lower than the values of $\sigma^{\mathrm{sym}}(\mathcal{S})$.

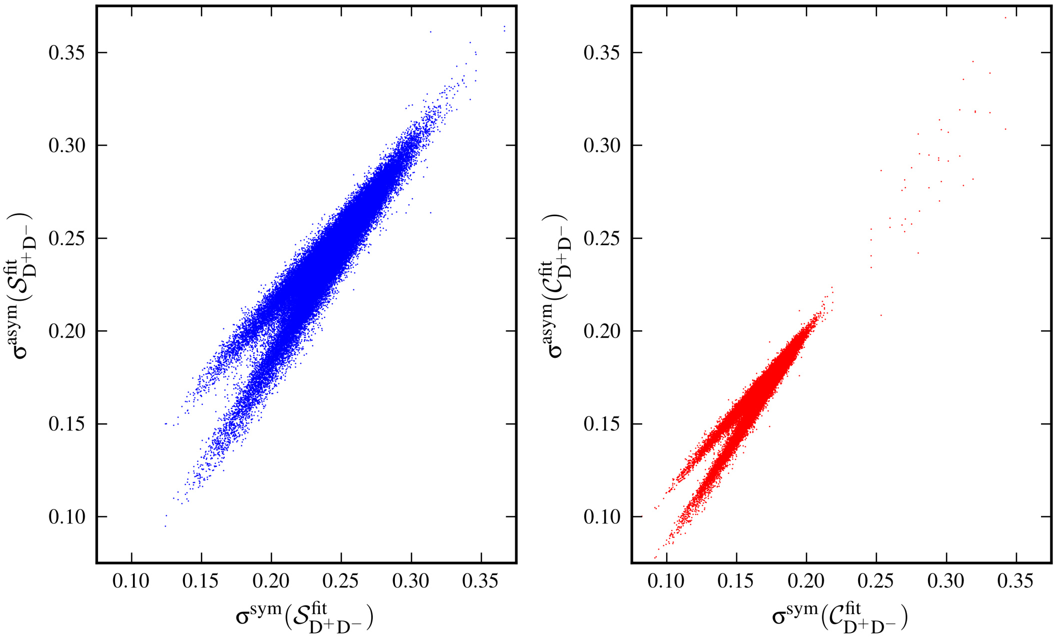

Figure 7.6: Dependence of the asymmetric statistical uncertainties on the symmetric uncertainties in the CP violation measurements of $\mathcal{S}$ (left) and $\mathcal{C}$ (red). The distributions are determined by ensemble tests within the entire physical parameter space, defined by $\sqrt{\mathcal{S}^2+\mathcal{C}^2} \leq 1$.

Furthermore, the symmetric statistical uncertainties $\sigma^{\mathrm{sym}}(\mathcal{S})$ and $\sigma^{\mathrm{sym}}(\mathcal{C})$ depend on the measured center values of $\mathcal{S}$ and $\mathcal{C}$. The statistical uncertainties are highest for low center values, and decrease with increasing center values. In proximity to the physical boundary of the CP violation parameters, the statistical uncertainties have the lowest values. This effect can again be explained by the increasing slope of the likelihood function when approaching the physical boundary.

The likelihood function can have different profiles for the left-hand and right-hand side of the fit parameters, which results in asymmetric uncertainties. The dependence of the asymmetric uncertainties $\sigma^{\mathrm{asym}}(\mathcal{S})$ and $\sigma^{\mathrm{asym}}(\mathcal{C})$ on the particular symmetric uncertainties are shown in Figure 7.6. For large values, the asymmetric and symmetric uncertainties are identical. When the uncertainties decrease, the asymmetric and symmetric uncertainty distributions start to deviate until a clear bifurcation is visible. For even lower values of the uncertainties, corresponding to large center values of the CP violation parameters, the uncertainty facing away from the physical region is significantly smaller than the uncertainty pointing towards the physical region.

7.1.5 Ensemble Test for Specific CP Violation Parameters

Ensemble tests for $B^0 \to D^+D^-$ and $B^0 \to D^{*\pm}D^{\mp}$ decays are performed for different sets of CP violation parameters to validate the CP fit procedure and to obtain estimates for the expected statistical uncertainties. The Monte Carlo pseudo-experiments are generated according to the full likelihood function described in Section 4.32. For $B^0 \to D^+D^-$ decays, the signal decays are generated according to the probability density function in Equation 4.40. For $B^0 \to D^{*\pm}D^{\mp}$ decays, the signal parameterisation in Equation 4.42 is applied which uses the time- and flavor-integrated CP violating asymmetry $\mathcal{A}_{D^*D}$, the parameters $\mathcal{S}_{D^{*+}D^-}$ and $\mathcal{C}_{D^{*+}D^-}$ for the charge-configuration of $B^0 \to D^{*+}D^-$ and the parameters $\mathcal{S}_{D^{*-}D^+}$ and $\mathcal{C}_{D^{*-}D^+}$ for the charge-configuration of $B^0 \to D^{*-}D^+$.

The inputs to the generation of pseudo-experiments are the signal and background yields, the distributions of vertex fit uncertainties and quality indicators, the distributions of flavor tagging quantities, and the background parameterisations obtained in the time-integrated measurements of $B^0 \to D^+D^-$ and $B^0 \to D^{*\pm}D^{\mp}$ decays on data.

For $B^0 \to D^+D^-$ decays, 1000 pseudo-experiments according to three different sets of $\mathcal{S}_{D^+D^-}$ and $\mathcal{C}_{D^+D^-}$ are generated and ensemble tests are performed. The input values of the three different sets are

$$\begin{aligned}
1:\ & \mathcal{S}_{D^+D^-} = -0.7, && \mathcal{C}_{D^+D^-} = 0; \\
2:\ & \mathcal{S}_{D^+D^-} = -0.3, && \mathcal{C}_{D^+D^-} = -0.5; \\
3:\ & \mathcal{S}_{D^+D^-} = 0, && \mathcal{C}_{D^+D^-} = -0.7.
\end{aligned} \tag{7.1}$$

For the first set, that is close to the theoretically expected CP violation in $B^0 \to D^+D^-$ decays under the assumption of negligible penguin contributions, the residual, pull and fit uncertainty distributions are shown in Figure 7.7. For all ensemble tests, the mean and width of the pull distributions indicate, that the fit uncertainties are reliable, and no significant bias is found. The ensemble tests in $B^0 \to D^+D^-$ are performed for both decay modes separately and combined. The inclusion of the $B^0 \to D^+D^- \to (K^-\pi^+\pi^+)\left(K^0_S\pi^-\right)$ decay mode in addition to the $B^0 \to D^+D^- \to (K^-\pi^+\pi^+)(K^+\pi^-\pi^-)$ decay mode to the time-dependent measurement improves the statistical uncertainty of the CP violation measurements by approximately 10%. In total, the expected statistical uncertainties are $\sigma_{\mathcal{S}_{D^+D^-}} = 0.24$ and $\sigma_{\mathcal{C}_{D^+D^-}} = 0.18$.

For $B^0 \to D^{*\pm}D^{\mp}$ decays, 1000 pseudo-experiments according to six different sets of CP violation parameters are generated and ensemble tests are performed. The input values of the six different sets are

$$\begin{aligned}
1:\ & \mathcal{A}_{D^{*\pm}D^{\mp}} = 0, && \mathcal{S}_{D^{*+}D^-} = -0.7, && \mathcal{C}_{D^{*+}D^-} = 0, && \mathcal{S}_{D^{*-}D^+} = -0.7, && \mathcal{C}_{D^{*-}D^+} = 0; \\
2:\ & \mathcal{A}_{D^{*\pm}D^{\mp}} = 0.2, && \mathcal{S}_{D^{*+}D^-} = -0.7, && \mathcal{C}_{D^{*+}D^-} = 0, && \mathcal{S}_{D^{*-}D^+} = -0.7, && \mathcal{C}_{D^{*-}D^+} = 0; \\
3:\ & \mathcal{A}_{D^{*\pm}D^{\mp}} = 0, && \mathcal{S}_{D^{*+}D^-} = -0.9, && \mathcal{C}_{D^{*+}D^-} = 0, && \mathcal{S}_{D^{*-}D^+} = -0.5, && \mathcal{C}_{D^{*-}D^+} = 0; \\
4:\ & \mathcal{A}_{D^{*\pm}D^{\mp}} = 0.4, && \mathcal{S}_{D^{*+}D^-} = -0.9, && \mathcal{C}_{D^{*+}D^-} = 0, && \mathcal{S}_{D^{*-}D^+} = -0.5, && \mathcal{C}_{D^{*-}D^+} = 0; \\
5:\ & \mathcal{A}_{D^{*\pm}D^{\mp}} = 0, && \mathcal{S}_{D^{*+}D^-} = -0.3, && \mathcal{C}_{D^{*+}D^-} = -0.5, && \mathcal{S}_{D^{*-}D^+} = -0.3, && \mathcal{C}_{D^{*-}D^+} = -0; \\
6:\ & \mathcal{A}_{D^{*\pm}D^{\mp}} = 0, && \mathcal{S}_{D^{*+}D^-} = 0, && \mathcal{C}_{D^{*+}D^-} = -0.7, && \mathcal{S}_{D^{*-}D^+} = 0, && \mathcal{C}_{D^{*-}D^+} = -0.7.
\end{aligned} \tag{7.2}$$

For the first set, that is close to the theoretical expectation, the residual, pull and fit uncertainty distributions are shown in Figure 7.8. For all ensemble tests, the mean and width of the pull distributions indicate, that the the fit uncertainties are reliable, and no significant bias is found. The expected statistical uncertainties are $\sigma_{\mathcal{A}_{\mathrm{D^*D}}} = 0.05$, $\sigma_{\mathcal{S}_{\mathrm{D^{*+}D^-}}} = \sigma_{\mathcal{S}_{\mathrm{D^{*-}D^+}}} = 0.21$ and $\sigma_{\mathcal{C}_{\mathrm{D^{*+}D^-}}} = \sigma_{\mathcal{C}_{\mathrm{D^{*-}D^+}}} = 0.15$.

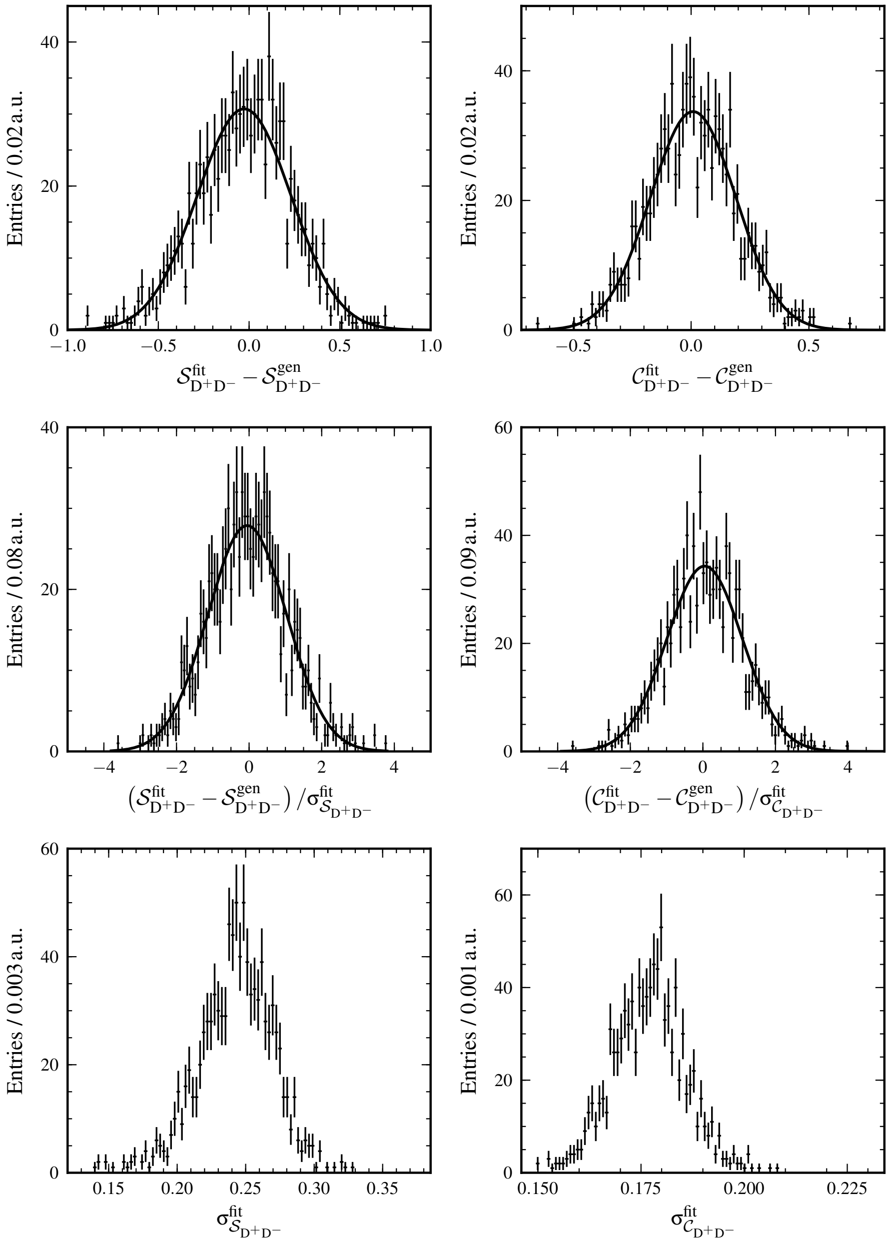

Figure 7.7: Residual (top), pull (middle) and fit uncertainty distributions (bottom) obtained by 1000 pseudo-experiments of $\mathrm{B^0} \to \mathrm{D^+D^-}$ decays generated according to the data distributions and the CP violation parameters $\mathcal{S}_{\mathrm{D^+D^-}} = -0.7$ and $\mathcal{C}_{\mathrm{D^+D^-}} = 0$. The input parameters are close to the expected values.

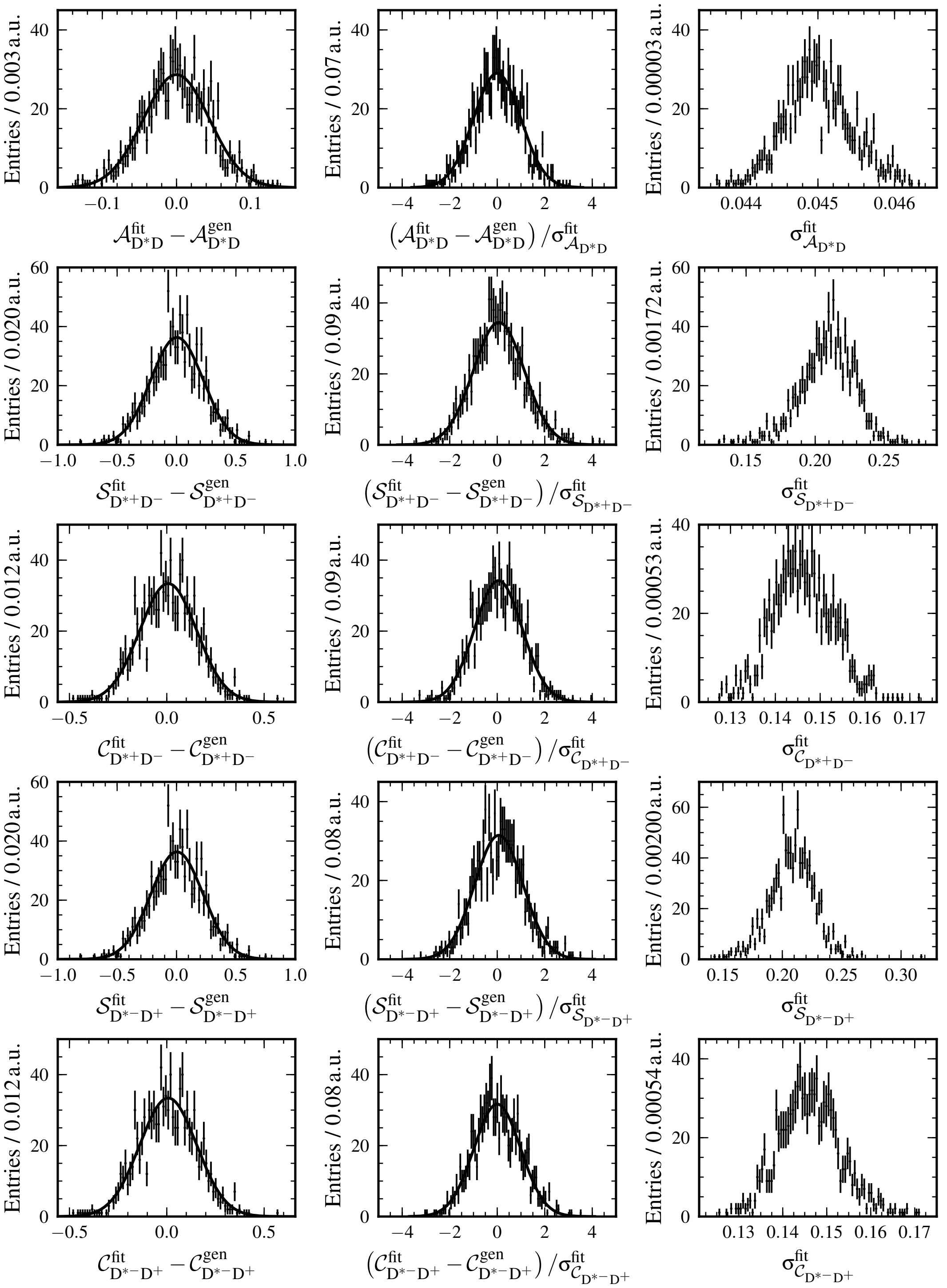

Figure 7.8: Residual (left), pull (middle) and fit uncertainty distributions (right) obtained by 1000 pseudo-experiments of $B^0 \to D^{*\pm}D^{\mp}$ decays generated according to the data distributions and the CP violation parameters $\mathcal{A}_{D^{*\pm}D^{\mp}} = 0$, $\mathcal{S}_{D^{*+}D^-} = \mathcal{S}_{D^{*-}D^+} = -0.7$ and $\mathcal{C}_{D^{*+}D^-} = \mathcal{C}_{D^{*-}D^+} = 0$. The input parameters are close to the expected values.

7.2 Time-Dependent Measurements of $B^0 \rightarrow D_s^+ D^{(*)-}$ Decays

The procedures for the time-dependent measurements in $B^0 \rightarrow D^+D^-$ and $B^0 \rightarrow D^{*\pm}D^{\mp}$ decays are validated by performing the same measurements in $B^0 \rightarrow D_s^+D^-$ and $B^0 \rightarrow D_s^+D^{*-}$ decays. In addition to the measurements of lifetimes and CP violation, the B^0-$\bar{B}^0$ mixing frequency is measured.

7.2.1 Determination of Background Parameters

The background parameterisation for the time-dependent measurements of $B^0 \rightarrow D_s^+D^-$ and $B^0 \rightarrow D_s^+D^{*-}$ decays is determined by fits to the data distributions in the $M_{bc} < 5.26$ GeV/c^2 sidebands. The fits are performed by applying the background probability density function and the resolution function described in Section 4.5.3.

Parameter	$B^0 \rightarrow D_s^+D^-$	$B^0 \rightarrow D_s^+D^{*-}$
f_δ	0.12 ± 0.13	0.13 ± 0.08
μ_δ (ps)	-0.22 ± 0.15	0.10 ± 0.04
τ_{bkg} (ps)	1.05 ± 0.15	1.16 ± 0.11
μ_τ (ps)	-0.02 ± 0.10	-0.09 ± 0.09
s_{bkg}^{main}	0.89 ± 0.29	1.21 ± 0.11
s_{bkg}^{tail}	7.32 ± 3.37	5.99 ± 1.25
f_{bkg}^{tail}	0.09 ± 0.07	0.05 ± 0.02

Table 7.6: Background parameterisation determined by fits to $B^0 \rightarrow D_s^+D^-$ and $B^0 \rightarrow D_s^+D^{*-}$ data distributions in the $M_{bc} < 5.26$ GeV/c^2 sidebands.

The results for the background parameters are summarised in Table 7.6. In total, the background level in $B^0 \rightarrow D_s^+D^-$ and $B^0 \rightarrow D_s^+D^{*-}$ is very low. The determined background parameters are in agreement with the parameters obtained in measurements of inclusive Monte Carlo simulation samples.

7.2.2 Measurements of Lifetime

The neutral B meson lifetime is determined from the untagged $B^0 \to D_s^+ D^-$ and $B^0 \to D_s^+ D^{*-}$ data samples by using the signal probability density function in Equation 4.33. The proper decay time difference distributions and projections of the lifetime fits are shown in Figure 7.9.

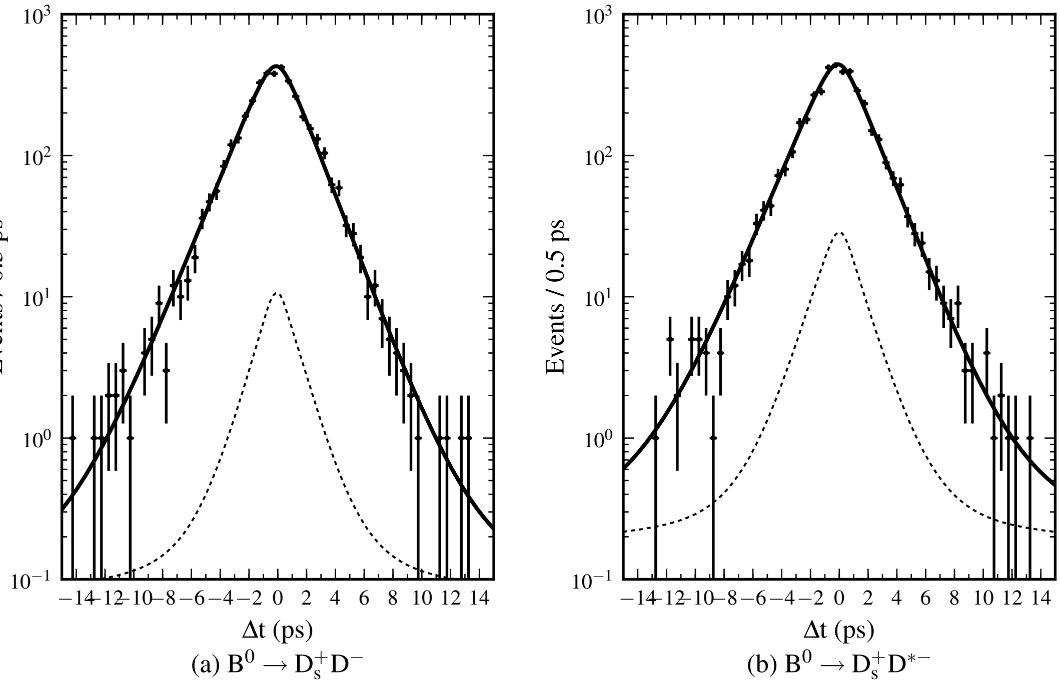

(a) $B^0 \to D_s^+ D^-$

(b) $B^0 \to D_s^+ D^{*-}$

Figure 7.9: Proper decay time difference distributions of untagged (a) $B^0 \to D_s^+ D^-$ and (b) $B^0 \to D_s^+ D^{*-}$ decays and projections of lifetime fits. The dashed lines show projections of the background components in the fits.

The following lifetimes are obtained:

$$\begin{aligned}\tau_{B^0 \to D_s^+ D^-} &= \left(1.510 \pm 0.029\ (\text{stat.})\right)\ \text{ps}\\ \tau_{B^0 \to D_s^+ D^{*-}} &= \left(1.476 \pm 0.030\ (\text{stat.})\right)\ \text{ps} \qquad (7.3)\end{aligned}$$

The lifetime determined in $B^0 \to D_s^+ D^-$ deviates by less than 0.1σ and the lifetime determined in $B^0 \to D_s^+ D^{*-}$ deviates by 1.4σ from the current world average of $\tau_{B^0}^{PDG} = \left(1.519 \pm 0.007\right)$ ps [115].

7.2.3 Measurements of Lifetime and Mixing Frequency

In addition to the lifetime, the B^0-$\bar{B}^0$ mixing frequency can be measured from the time evolution of $B^0 \to D_s^+ D^-$ and $B^0 \to D_s^+ D^{*-}$ decays, when the decay flavor of the B mesons on the reconstruction- and on the tagging-side are determined. The decays of $B^0 \to D_s^+ D^-$ and $B^0 \to D_s^+ D^{*-}$ are self-tagging. The decay flavor of a neutral B meson is tagged as a $B^0(\bar{B}^0)$ by the charge of the $D_s^+(D_s^-)$.

The lifetime and the B^0-$\bar{B}^0$ mixing frequency are extracted from the flavor tagged $B^0 \to D_s^+ D^-$ and $B^0 \to D_s^+ D^{*-}$ decays by the probability density function in Equation 4.39. The measurement is performed for $B^0 \to D_s^+ D^-$ and $B^0 \to D_s^+ D^{*-}$ decays separately and combined in a simultaneous fit. The proper decay time distribution and the fit projections of the simultaneous lifetime and mixing frequency measurements in $B^0 \to D_s^+ D^-$ and $B^0 \to D_s^+ D^{*-}$ decays is shown in Figure 7.10. The corresponding mixing asymmetry resolves approximately one oscillation period. The fit results are summarised in Table 7.7. The determined lifetimes and mixing frequencies are in agreement with the current world averages of $\tau_{B^0}^{PDG} = \left(1.519 \pm 0.007\right)$ ps and $\Delta m^{PDG} = \left(0.507 \pm 0.004\right)\,ps^{-1}$ [115].

Decay mode	$\tau_{B^0}^{fit}$ (ps)	$\left(\tau_{B^0}^{fit} - \tau_{B^0}^{PDG}\right)/\sigma_{\tau_{B^0}^{fit}}$	Δm^{fit} (ps^{-1})	$\left(\Delta m^{fit} - \Delta m^{PDG}\right)/\sigma_{\Delta m^{fit}}$
$B^0 \to D_s^+ D^-$	1.517 ± 0.029	-0.1σ	0.522 ± 0.018	$+0.8\sigma$
$B^0 \to D_s^+ D^{*-}$	1.480 ± 0.030	-1.3σ	0.502 ± 0.019	-0.3σ
$B^0 \to D_s^+ D^-$ $+ B^0 \to D_s^+ D^{*-}$	1.499 ± 0.021	-1.0σ	0.512 ± 0.013	$+0.4\sigma$

Table 7.7: Results of the lifetime and mixing frequency measurements in $B^0 \to D_s^+ D^-$ and $B^0 \to D_s^+ D^{*-}$ decays.

The mixing asymmetry depends on the quality of the flavor tag as expressed by the quality indicator $r = 1 - 2\omega$. The mixing asymmetry in intervals of r for the combined measurement of $B^0 \to D_s^+ D^-$ and $B^0 \to D_s^+ D^{*-}$ decays is shown in Figure 7.11. The amplitude of the mixing asymmetry increases with the quality of the tags. This is an effect of the decreasing dilution for tagging decisions associated with low uncertainties. The performance of the flavor tagging algorithms can be expressed by the effective tagging efficiency ε_{eff}, defined by $\varepsilon_{eff} = \sum_i f_i (1 - \omega_i)^2$. The effective tagging efficiency depends on the event fraction f_i and the dilution $(1 - \omega_i)$ in the i-th r-interval.

The effective tagging efficiency is estimated to $(28.8 \pm 0.9\ (stat.))\,\%$ in the measurements of $B^0 \to D_s^+ D^-$ and $B^0 \to D_s^+ D^{*-}$ decays. This value agrees with the effective tagging efficiency of $\left(29.9 \pm 0.4\,(stat. + syst.)\right)\%$ determined in the calibration of the flavor tagging algorithms in the measurements of $B^0 \to D^{*-} l^+ \nu_{l^+}$ decays.

The agreement of the mixing frequency measurements and of the estimated effective tagging efficiency provide an additional cross-check for the time-dependent measurements. This

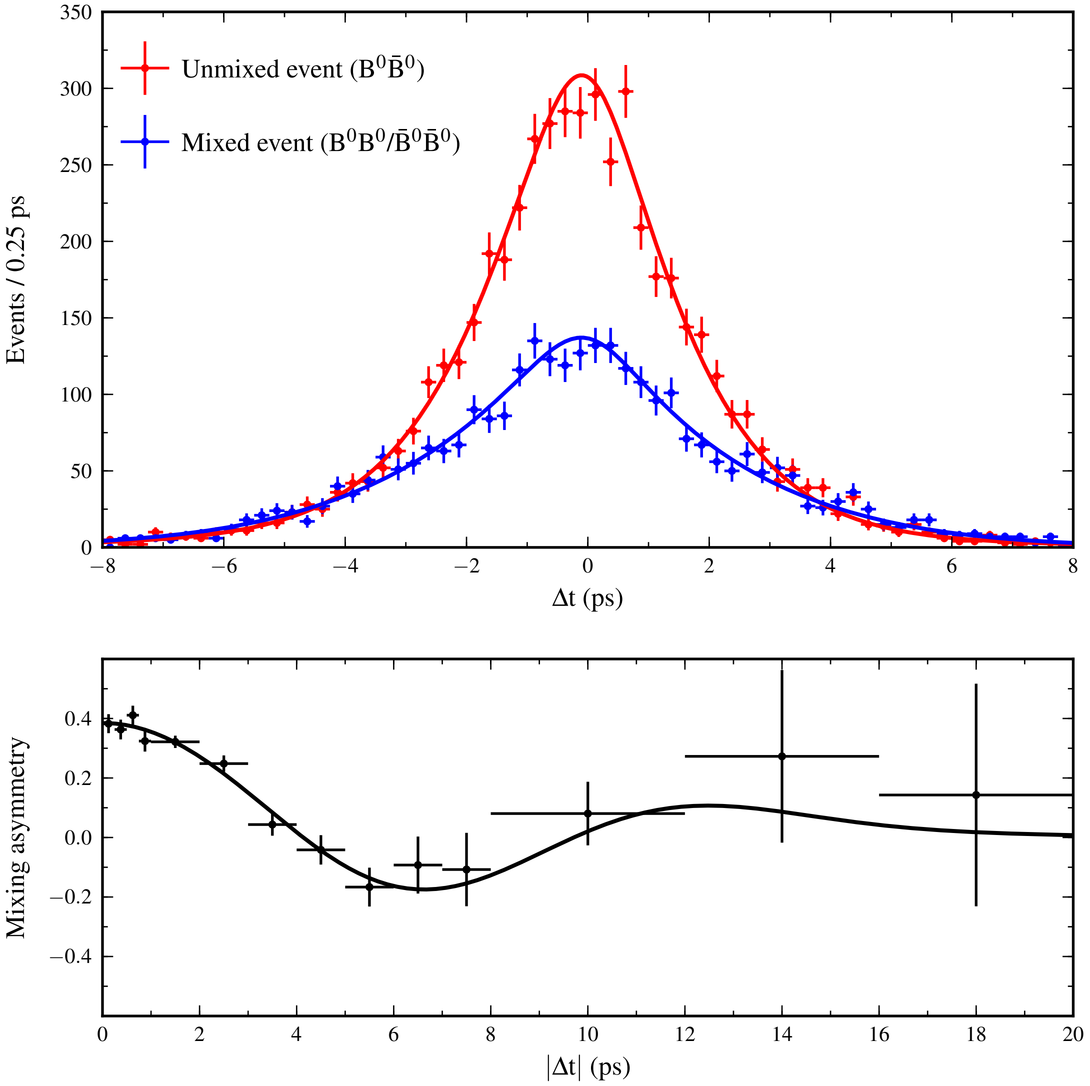

Figure 7.10: Top: Proper decay time difference distributions (data points with error bars) of $B^0 \to D_s^+ D^-$ and $B^0 \to D_s^+ D^{*-}$ candidates. The lines show projections of the simultaneous lifetime and mixing frequency fit. Bottom: The mixing asymmetry obtained from the above distributions and projections.

cross-check is not only sensitive to possible problems in the vertex reconstruction and in the description of the resolution effects, but also tests the flavor tagging algorithms.

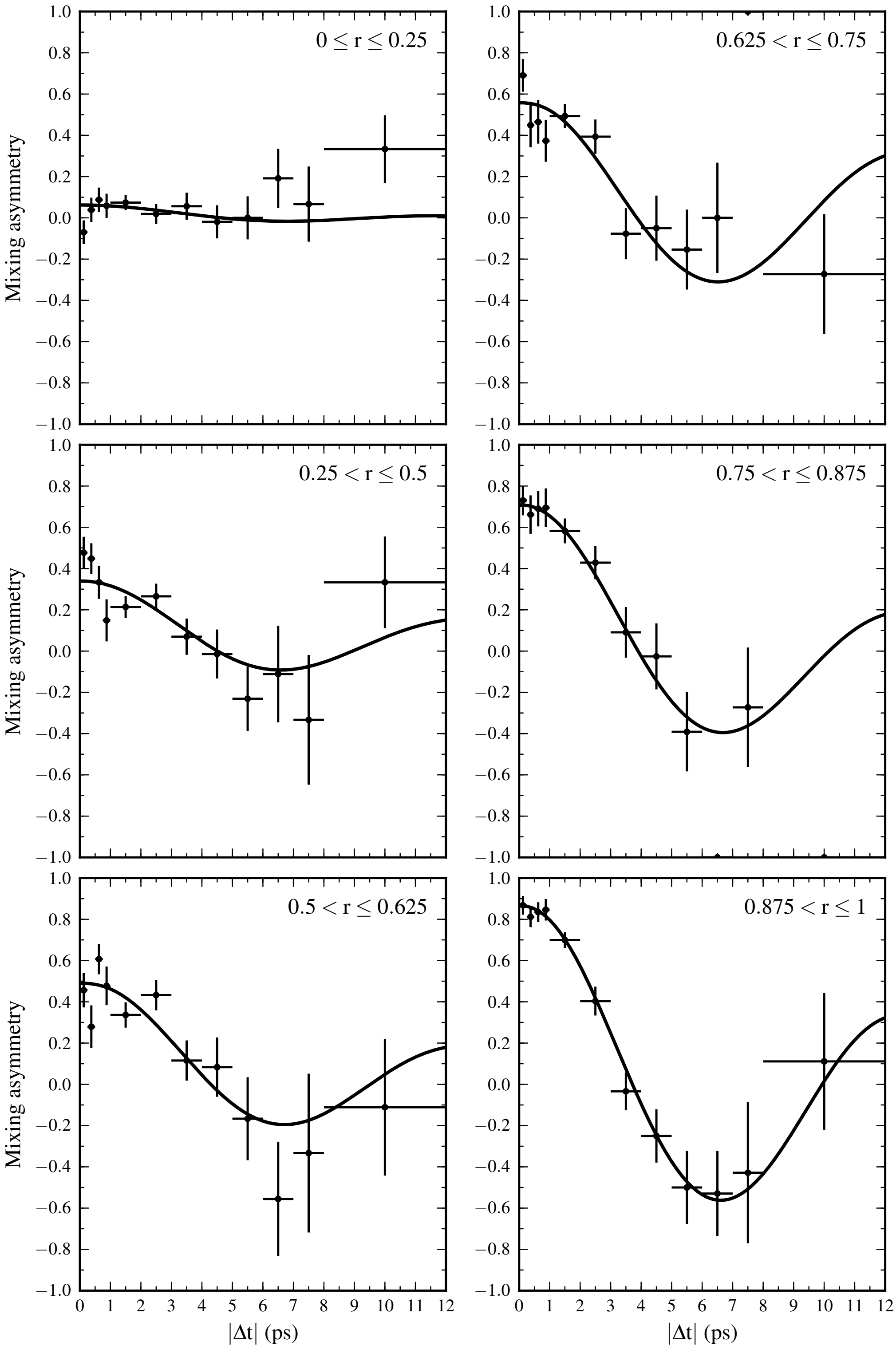

Figure 7.11: The mixing asymmetry from Figure 7.10 in intervals of the flavor tagging quality variable r.

7.2.4 Measurements of CP Violation

The CP violation measurements are performed for the control samples of $\mathrm{B}^0 \to \mathrm{D}_s^+\mathrm{D}^-$ and $\mathrm{B}^0 \to \mathrm{D}_s^+\mathrm{D}^{*-}$ decays by applying the parameterisations for $\mathrm{B}^0 \to \mathrm{D}^{*\pm}\mathrm{D}^{\mp}$ decays defined in Equations 4.41 and 4.42. The proper decay time difference distributions of the flavor-tagged $\mathrm{B}^0 \to \mathrm{D}_s^+\mathrm{D}^-$ and $\mathrm{B}^0 \to \mathrm{D}_s^+\mathrm{D}^{*-}$ decays are shown in Figure 7.12. The results for both parameterisations are summarised in Table 7.8.

Decay mode	$\mathcal{A}_{\mathrm{D_s D^{(*)}}}$	$\mathcal{S}_{\mathrm{D_s^- D^{(*)+}}}$	$\mathcal{C}_{\mathrm{D_s^- D^{(*)+}}}$	$\mathcal{S}_{\mathrm{D_s^+ D^{(*)-}}}$	$\mathcal{C}_{\mathrm{D_s^+ D^{(*)-}}}$
$\mathrm{B}^0 \to \mathrm{D}_s^+\mathrm{D}^-$	-0.01 ± 0.02	-0.05 ± 0.07	-0.94 ± 0.04	-0.06 ± 0.07	$+0.97 \pm 0.04$
$\mathrm{B}^0 \to \mathrm{D}_s^+\mathrm{D}^{*-}$	$+0.01 \pm 0.02$	$+0.06 \pm 0.07$	-0.94 ± 0.04	-0.13 ± 0.07	$+1.05 \pm 0.03$

Decay mode	$\mathcal{A}_{\mathrm{D_s D^{(*)}}}$	$\mathcal{S}_{\mathrm{D_s D^{(*)}}}$	$\mathcal{C}_{\mathrm{D_s D^{(*)}}}$	$\Delta\mathcal{S}_{\mathrm{D_s D^{(*)}}}$	$\Delta\mathcal{C}_{\mathrm{D_s D^{(*)}}}$
$\mathrm{B}^0 \to \mathrm{D}_s^+\mathrm{D}^-$	-0.01 ± 0.02	-0.05 ± 0.05	$+0.01 \pm 0.03$	$+0.01 \pm 0.05$	-0.95 ± 0.03
$\mathrm{B}^0 \to \mathrm{D}_s^+\mathrm{D}^{*-}$	$+0.01 \pm 0.02$	-0.04 ± 0.05	$+0.06 \pm 0.03$	$+0.10 \pm 0.05$	-1.00 ± 0.03

Table 7.8: Result of time-dependent CP violation measurements of $\mathrm{B}^0 \to \mathrm{D}_s^+\mathrm{D}^-$ and $\mathrm{B}^0 \to \mathrm{D}_s^+\mathrm{D}^{*-}$ decays using the parameterisations for $\mathrm{B}^0 \to \mathrm{D}^{*\pm}\mathrm{D}^{\mp}$ decays in Equations 4.41 and 4.42.

The time- and flavor-integrated asymmetry $\mathcal{A}_{\mathrm{D_s D^{(*)}}}$ and the mixing-induced CP violating asymmetries $\mathcal{S}_{\mathrm{D_s^- D^{(*)+}}}$ and $\mathcal{S}_{\mathrm{D_s^+ D^{(*)-}}}$ are consistent with zero indicating no direct and no mixing-induced CP violation in $\mathrm{B}^0 \to \mathrm{D}_s^+\mathrm{D}^-$ and $\mathrm{B}^0 \to \mathrm{D}_s^+\mathrm{D}^{*-}$ decays. The parameters $\mathcal{C}_{\mathrm{D_s^- D^{(*)+}}}$ and $\mathcal{C}_{\mathrm{D_s^+ D^{(*)-}}}$ have maximal values of ±1 and are of opposite sign. The flavor-dependent CP violation $\mathcal{C}_{\mathrm{D_s D^{(*)}}}$ is consistent with zero. The parameter $\Delta\mathcal{C}_{\mathrm{D_s D^{(*)}}}$ measures the asymmetry between the decay rates $\Gamma(\mathrm{B}^0 \to \mathrm{D}^{(*)+}\mathrm{D}_s^-) + \Gamma(\bar{\mathrm{B}}^0 \to \mathrm{D}^{(*)-}\mathrm{D}_s^+)$ and $\Gamma(\mathrm{B}^0 \to \mathrm{D}^{(*)-}\mathrm{D}_s^+) + \Gamma(\bar{\mathrm{B}}^0 \to \mathrm{D}^{(*)+}\mathrm{D}_s^-)$ and is consistent with -1 as it is expected for flavor-specific decays.

In total, the measurements are consistent with the assumption of no CP violation in $\mathrm{B}^0 \to \mathrm{D}_s^+\mathrm{D}^-$ and $\mathrm{B}^0 \to \mathrm{D}_s^+\mathrm{D}^{*-}$ decays. Because the control samples are of high statistics and in many aspects very similar to $\mathrm{B}^0 \to \mathrm{D}^+\mathrm{D}^-$ and $\mathrm{B}^0 \to \mathrm{D}^{*\pm}\mathrm{D}^{\mp}$ decays, the above results provide an important cross-check, that the time-dependent CP violation measurements perform correctly.

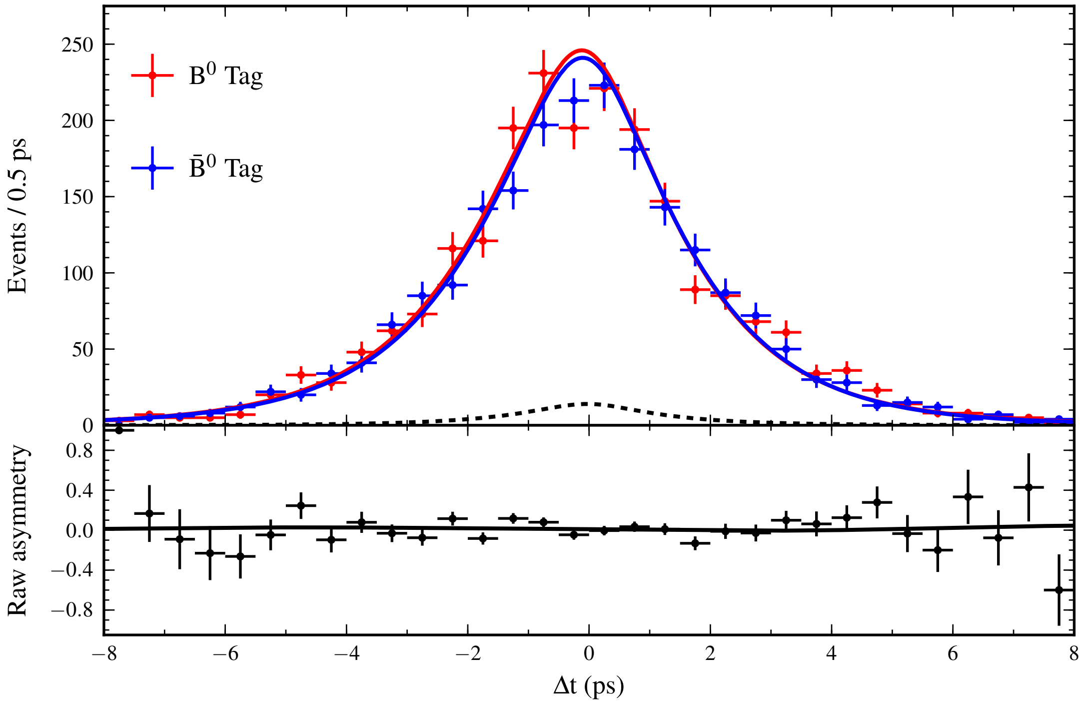

(a) $B^0 \to D_s^+ D^-$

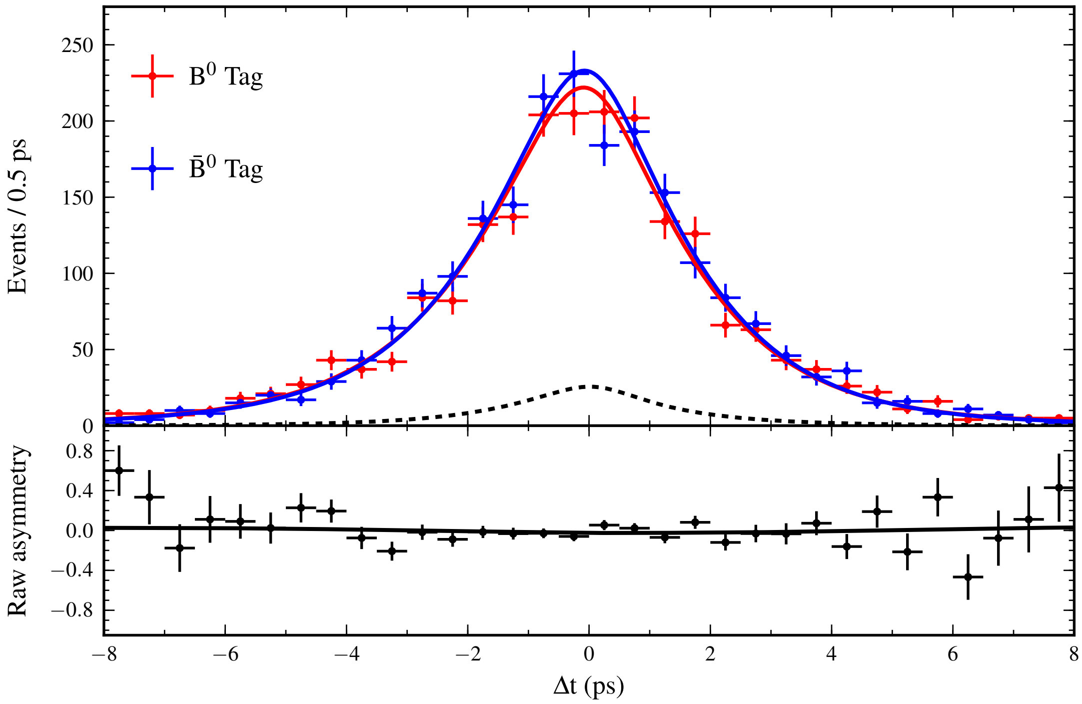

(b) $B^0 \to D_s^+ D^{*-}$

Figure 7.12: Top: Proper decay time difference distributions (data points with error bars) of (a) $B^0 \to D_s^+ D^-$ and (b) $B^0 \to D_s^+ D^{*-}$ candidates. The solid (dashed) lines show projections of all (background) components in the fit. Bottom: The CP asymmetry obtained from the above distributions and projections.

7.3 Time-Dependent Measurements of $B^0 \to D^{(*)\pm}D^{\mp}$ Decays

After the validation of the measurement procedure and passing the described cross-checks, the $B^0 \to D^+D^-$ and $B^0 \to D^{*\pm}D^{\mp}$ data distributions are unblinded and the time-dependent measurements are performed.

7.3.1 Determination of Background Parameters

The parameters of the background probability density function and the corresponding resolution function described in Section 4.5.3 are determined by fits to the data distributions in the $M_{bc} < 5.26\ \mathrm{GeV}/c^2$ sidebands. The proper decay time difference distributions in the sidebands of $B^0 \to D^+D^-$ and $B^0 \to D^{*\pm}D^{\mp}$ decays and the corresponding fit projections are shown in Figure 7.13. The obtained parameters are summarised in Table 7.9. The parameters are consistent with the parameters obtained in the measurements of inclusive Monte Carlo simulation samples in Section 7.1.3. As a cross-check for $B^0 \to D^{*\pm}D^{\mp}$ decays, the background parameters are determined separately for the two charge-configurations of $B^0 \to D^{*+}D^-$ and $B^0 \to D^{*-}D^+$ decays and are found to be consistent.

Parameter	$B^0 \to D^+D^-$	$B^0 \to D^{*\pm}D^{\mp}$
f_δ	0.32 ± 0.06	0.31 ± 0.04
μ_δ (ps)	-0.08 ± 0.06	0.08 ± 0.04
τ_{bkg} (ps)	1.06 ± 0.08	1.03 ± 0.06
μ_τ (ps)	-0.05 ± 0.05	-0.18 ± 0.04
s_{bkg}^{main}	1.32 ± 0.07	1.19 ± 0.04
s_{bkg}^{tail}	6.30 ± 0.85	5.88 ± 1.16
f_{bkg}^{tail}	0.05 ± 0.02	0.06 ± 0.02

Table 7.9: Background parameterisation determined by fits to the proper decay time difference data distributions of $B^0 \to D^+D^-$ and $B^0 \to D^{*\pm}D^{\mp}$ decays in the $M_{bc} < 5.26\ \mathrm{GeV}/c^2$ sidebands. The Δt distributions and projections of the fits to the sidebands are shown in Figure 7.13.

In the following time-dependent measurements of lifetimes and CP violation, the background parameters are fixed to the values determined in the sidebands.

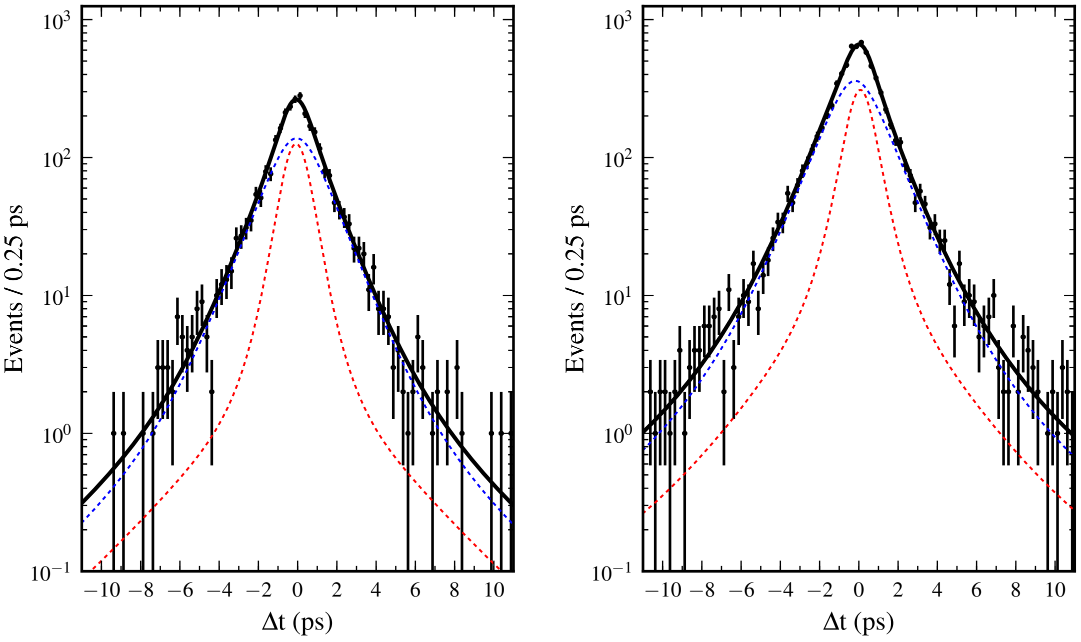

(a) $B^0 \to D^+D^-$

(b) $B^0 \to D^{*\pm}D^{\mp}$

Figure 7.13: Proper decay time difference distributions of (a) $B^0 \to D^+D^-$ and (b) $B^0 \to D^{*\pm}D^{\mp}$ decays in the $M_{bc} < 5.26\ \mathrm{GeV}/c^2$ sidebands. Superimposed are projections of the fits performed for the determination of the background parameters. The blue dashed lines show projections of the lifetime components and the red dashed lines show projections of the prompt components in the fit. The background parameters determined in the fits are summarised in Table 7.9.

7.3.2 Measurements of Lifetime

Prior to unblinding of the data distributions and performing the time-dependent CP violation measurements, the neutral B meson lifetime is determined from the untagged $B^0 \to D^+D^-$ and $B^0 \to D^{*\pm}D^{\mp}$ data samples. In this last cross-check, any deviation from the nominal lifetime would indicate possible problems in the fit procedure, caused e.g. by the calculation of the signal purity, the vertex reconstruction, the resolution functions or the background parameterisation.

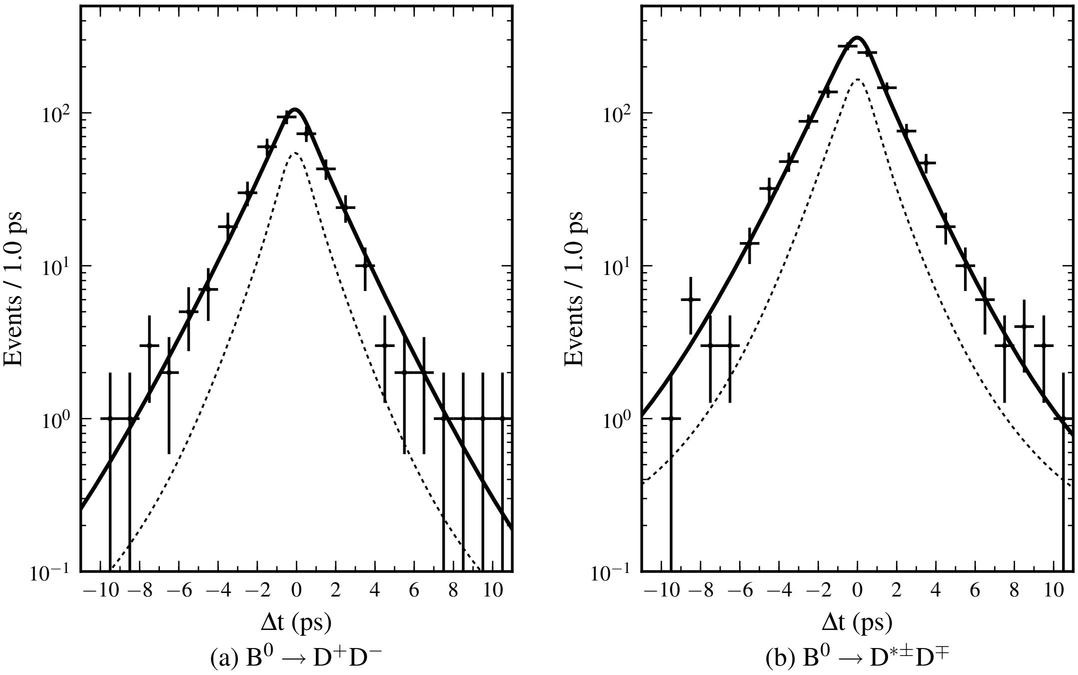

(a) $B^0 \to D^+D^-$ (b) $B^0 \to D^{*\pm}D^{\mp}$

Figure 7.14: Proper decay time difference distributions of untagged (a) $B^0 \to D^+D^-$ and (b) $B^0 \to D^{*\pm}D^{\mp}$ decays and projections of lifetime fits. The dashed lines show projections of the background components in the fits.

The lifetime is extracted by the signal probability density function in Equation 4.33. The background parameterisation is fixed to values determined by fits to the M_{bc} sidebands. The proper decay time difference distributions of the untagged $B^0 \to D^+D^-$ and $B^0 \to D^{*\pm}D^{\mp}$ data samples and projections of the lifetime fits are shown in Figure 7.14.

The following lifetimes are obtained:

$$\begin{aligned} \tau_{B^0\to D^+D^-} &= \left(1.595 \pm 0.134\ (\text{stat.})\right)\ \text{ps} \\ \tau_{B^0\to D^{*\pm}D^{\mp}} &= \left(1.444 \pm 0.082\ (\text{stat.})\right)\ \text{ps} \end{aligned} \qquad (7.4)$$

The lifetimes determined in $B^0 \to D^+D^-$ and $B^0 \to D^{*\pm}D^{\mp}$ deviate by less than 1σ from the current world average of $\tau_{B^0}^{PDG} = \left(1.519 \pm 0.007\right)$ ps [115].

7.3.3 Measurements of CP Violation

After validation of the fit procedure and passing all cross-checks described in the previous sections, the flavor tagged $B^0 \to D^+D^-$ and $B^0 \to D^{*\pm}D^{\mp}$ data distributions are unblinded and the time-dependent CP violation measurements are performed. The CP violation parameters are determined by unbinned maximum likelihood fits to the Δt distributions in the M_{bc} and ΔE signal region. The Δt distributions of the flavor-tagged $B^0 \to D^+D^-$ and $B^0 \to D^{*\pm}D^{\mp}$ data samples and projections of the CP fits are shown in Figure 7.15.

For $B^0 \to D^+D^-$ decays, the CP violation parameters are extracted by the signal probability density function in Equation 4.40. The free parameters in the fit are $\mathcal{S}_{D^+D^-}$ and $\mathcal{C}_{D^+D^-}$. The result is

$$\begin{aligned}
\mathcal{S}_{D^+D^-} &= -1.06\ {}^{+0.21}_{-0.14}\ (\text{stat.}) \pm 0.08\ (\text{syst.}),\\
\mathcal{C}_{D^+D^-} &= -0.43 \pm 0.16\ (\text{stat.}) \pm 0.05\ (\text{syst.}). \qquad (7.5)
\end{aligned}$$

The CP violation parameters are outside of the physical parameter space, defined by $\sqrt{\mathcal{S}^2+\mathcal{C}^2} \leq 1$, and the direct CP violation $\mathcal{C}_{D^+D^-}$ deviates from zero. The statistical uncertainty on $\mathcal{S}_{D^+D^-}$ is asymmetric because of the proximity of the center value to the physical boundary.

For $B^0 \to D^{*\pm}D^{\mp}$ decays, the CP violation parameters are extracted by the signal probability density function in Equation 4.41. The free parameters in the fit are $\mathcal{A}_{D^*D}$ $\mathcal{S}_{D^*D}$, $\mathcal{C}_{D^*D}$, $\Delta\mathcal{S}_{D^*D}$ and $\Delta\mathcal{C}_{D^*D}$. The result is

$$\begin{aligned}
\mathcal{A}_{D^*D} &= +0.06 \pm 0.05\ (\text{stat.}) \pm 0.02\ (\text{syst.}),\\
\mathcal{S}_{D^*D} &= -0.78 \pm 0.15\ (\text{stat.}) \pm 0.05\ (\text{syst.}),\\
\mathcal{C}_{D^*D} &= -0.01 \pm 0.11\ (\text{stat.}) \pm 0.04\ (\text{syst.}),\\
\Delta\mathcal{S}_{D^*D} &= -0.13 \pm 0.15\ (\text{stat.}) \pm 0.04\ (\text{syst.}),\\
\Delta\mathcal{C}_{D^*D} &= +0.12 \pm 0.11\ (\text{stat.}) \pm 0.03\ (\text{syst.}). \qquad (7.6)
\end{aligned}$$

As a cross-check for $B^0 \to D^{*\pm}D^{\mp}$ decays, the CP violation parameters $\mathcal{S}_{D^{*+}D^-}$, $\mathcal{C}_{D^{*+}D^-}$, $\mathcal{S}_{D^{*-}D^+}$ and $\mathcal{C}_{D^{*-}D^+}$ of both charge-configurations, $B^0 \to D^{*+}D^-$ and $B^0 \to D^{*-}D^+$, are determined by the parameterisation in Equation 4.42. The result is

$$\begin{aligned}
\mathcal{A}_{D^*D} &= +0.06 \pm 0.05\ (\text{stat.}),\\
\mathcal{S}_{D^{*+}D^-} &= -0.90 \pm 0.21\ (\text{stat.}),\\
\mathcal{C}_{D^{*+}D^-} &= -0.11 \pm 0.14\ (\text{stat.}),\\
\mathcal{S}_{D^{*-}D^+} &= -0.65 \pm 0.22\ (\text{stat.}),\\
\mathcal{C}_{D^{*-}D^+} &= +0.13 \pm 0.16\ (\text{stat.}). \qquad (7.7)
\end{aligned}$$

The contributions of the above given systematic uncertainties and their evaluation are described in the following Section 7.3.4. The significance of the CP violation measurements in $B^0 \to D^+D^-$ and $B^0 \to D^{*\pm}D^{\mp}$ decays is studied in Section 7.3.5.

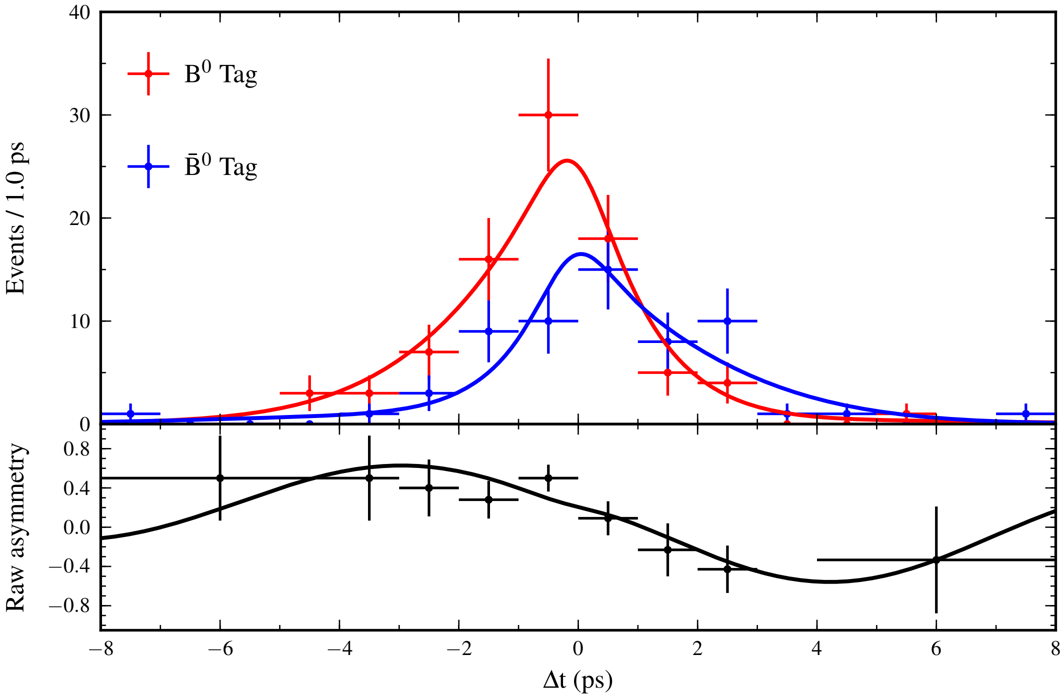

(a) $B^0 \to D^+D^-$

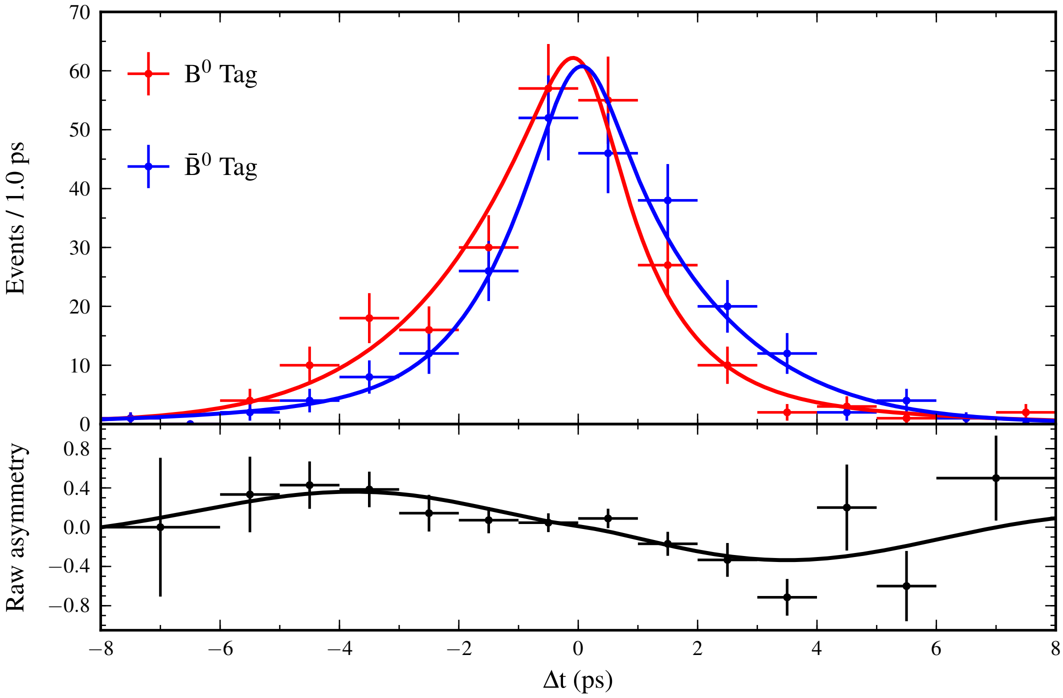

(b) $B^0 \to D^{*\pm}D^{\mp}$

Figure 7.15: Top: Proper decay time difference distributions (data points with error bars) of (a) $B^0 \to D^+D^-$ and (b) $B^0 \to D^{*\pm}D^{\mp}$ candidates associated with high quality flavor tags ($r > 0.5$). The lines show projections of the sum of signal and background components in the fit. The signal purity for $r > 0.5$ is 69% (66%) for $B^0 \to D^+D^-$ ($B^0 \to D^{*\pm}D^{\mp}$). Bottom: The CP asymmetry obtained from the above distributions and projections.

7.3.4 Systematic Uncertainties

The sources of systematic uncertainties on the time-dependent CP violation parameters of $B^0 \to D^+D^-$ and $B^0 \to D^{*\pm}D^{\mp}$ decays and their evaluation are described in the following. The individual contributions are summarised in Table 7.10.

Vertex reconstruction

The following sources contribute to the systematic uncertainty related to the decay vertex reconstruction of B mesons on the reconstruction- and on the tagging-side.

Poor quality vertex rejection

The systematic uncertainty due to the selection requirement on the vertex fit quality indicator h for decay vertices of B mesons on reconstruction- and on tagging-side is estimated by varying the requirement from $h < 50$ to $h < 25$ and $h < 100$.

Δt fit range

The stability of the time-dependent fits with respect to selection requirements on the Δt fit range is studied by varying the fit range from $|\Delta t| < 70$ ps to $|\Delta t| < 40$ ps and $|\Delta t| < 100$ ps.

IP tube constraint in vertex fit

In the vertex fits, B mesons on reconstruction- and on tagging-side are constraint to originate from the IP tube. The IP tube is obtained by smearing the IP profile in the xy-plane to account for the transverse decay lengths of B mesons, compare Section 4.1.2. The systematic uncertainty due to this constraint is estimated by varying the smearing from 21 μm to 11 μm and 41 μm.

Track rejection in B_{tag} vertex fit

In the reconstruction of decay vertices of B mesons on the tagging-side, selection requirements on the impact parameters are applied to remove tracks associated with poor position measurements. The systematic uncertainty is estimated by varying the requirement on the transverse and longitudinal distance of closest approach from < 500 μm to < 400 μm and < 600 μm.

SVD misalignment

The effect of the imperfect alignment between the SVD and CDC detectors on the vertex reconstruction is assumed to be decay mode independent and the systematic uncertainty is taken from Belle's recent $\sin(2\beta)$ measurement in $b \to c\bar{c}s$ transitions [94, 95]. In this measurement the systematic uncertainty is estimated from Monte Carlo simulation samples with artificial misalignment effects.

Δz bias

Biases in Δz measurements are observed in $e^+e \to \mu^+\mu^-$ decays and in control samples. Special correction functions are applied to the vertex fits of B mesons on reconstruction- and on tagging-side. The systematic uncertainty is obtained by taking into account the difference between results of CP violation measurements with and without the corrections applied.

Δt resolution functions

The systematic uncertainties related to the Δt resolution functions are estimated by varying individually every resolution function parameter in Table 4.1 by $\pm 1\sigma$ and repeating the CP violation measurement. For each resolution function parameter, the largest deviation from the result without variation is assigned as systematic uncertainty. The total systematic uncertainty related to the resolution functions is obtained by the quadratic sum of the contributions of all resolution function parameters.

Background Δt parameterisation

The systematic uncertainty due to the background parameterisation is estimated by individual variation of each background parameter in Table 7.9 within its uncertainty. For each parameter, the largest deviation from the result without variation is assigned as systematic uncertainty. The total systematic uncertainty related to the background parameterisation is obtained by the quadratic sum of the contributions of all background parameters.

Signal purity

In the time-dependent CP violation measurements, the signal purity is calculated on an event-by-event basis as a function of the M_{bc} and ΔE observables. The systematic uncertainty related to the signal purity is estimated by individual variation of each parameter of the M_{bc} and ΔE parameterisation within its uncertainty. For each parameter, the largest deviation from the result without variation is assigned as systematic uncertainty. The total systematic uncertainty related to the calculation of the signal purity is obtained by the quadratic sum of the contributions of all background parameters.

Physics parameters τ_{B^0} and Δm

In the CP violation measurements, the B meson lifetime and mass difference are fixed to current world averages $\tau_{B^0} = (1.519 \pm 0.007)$ ps and $\Delta m = (0.507 \pm 0.004)\ \mathrm{ps}^{-1}$ [115]. The systematic uncertainties related to the physics parameters τ_{B^0} and Δm are estimated by variation of each parameter within its uncertainty. For each parameter, the largest deviation from the result without variation is assigned as systematic uncertainty. The total systematic uncertainty related to the physics parameters is obtained by the quadratic sum of the contributions of all background parameters.

Flavor tagging

The systematic uncertainties related to the flavor tagging procedure are estimated by individual variation of the wrong tag fractions and the wrong tag fraction differences in Table 4.2 in each r-interval within their uncertainties. For each parameter, the largest deviation from the result without variation is assigned as systematic uncertainty. The total systematic uncertainty related to the flavor tagging procedure is obtained by the quadratic sum of the contributions of all background parameters.

Possible fit bias

The effect of a possible fit bias in the time-dependent measurements is estimated by large Monte Carlo simulation samples of signal decays. For $B^0 \to D^+D^-$ and $B^0 \to D^{*\pm}D^{\mp}$ decays, 10^6 signal decays are generated each according to the parameters of $\tau_{B^0} = 1.5344\,\mathrm{ps}$, $\Delta m = 0.507\,\mathrm{ps}^{-1}$, $\mathcal{S} = -0.668$ and $\mathcal{C} = 0$. The deviation of the CP fit results from the generator input values are assigned as systematic uncertainties.

Peaking background

The contribution of decays, that have the same final states as the reconstructed $B^0 \to D^+D^-$ and $B^0 \to D^{*\pm}D^{\mp}$ decay modes and that can populate the M_{bc} and ΔE signal region as peaking background, are determined in the branching fraction measurement by fits to the D^- mass sidebands. The $D^- \to K^+\pi^-\pi^-$ mass sidebands are free of peaking background. For $B^0 \to D^+D^-$ ($B^0 \to D^{*\pm}D^{\mp}$) a small contribution of 0.7 ± 1.5 (4.7 ± 2.1) peaking background events is found in the $D^- \to K^0_S\pi^-$ mass sidebands. In the time-dependent fits, these small contributions are neglected.

The effect of the peaking background on the time-dependent CP violation measurements is studied by ensemble tests. For the ensemble tests, Monte Carlo pseudo-experiments containing signal, background and peaking background events are generated according to the data distributions. For the peaking background, different variations of the above yields are generated according to different parameterisations of the proper decay time difference distributions. The peaking background is generated either flavor-blind according to the lifetime distribution in Equation 4.43, or according to the decay rates defined in Equations 4.44 to 4.47. The decay rates introduce an asymmetry to the proper decay time difference distributions and allow for CP violation in the peaking background decays. In the ensemble tests, the nominal fit procedures neglecting the effect of peaking background are applied. The largest systematic biases are assigned as systematic uncertainty for the peaking background.

Tag-side interference

In the time-dependent measurements performed to extract the CP violation parameters, the decay of the B meson on the tagging-side is assumed to be caused by only one decay amplitude and to be flavor-specific. Since the B mesons on the reconstruction-side and on the tagging-side are entangled and evolve coherently, a non-flavor specific decay of the tagging B meson can cause deviations from the standard time evolution, derived in Section 2.5, for the second B meson decaying to a CP eigenstate.

In decays on the tagging-side, for example in $B^0 \to D^-\pi^+$, an interference between Cabibbo-favored $b \to c\bar{u}d$ and suppressed $\bar{b} \to \bar{u}c\bar{d}$ decay amplitudes occurs. This interference, referred to as tag-side interference, can have sizeable effects on the CP violation measurements and results in modified decay rates for the B meson on the reconstruction-side [122, 123]:

$$\begin{aligned}
P_{B^0}(\Delta t) &= \frac{e^{-|\Delta t|/\tau_{B^0}}}{4\tau_{B^0}}\Big[R_{B^0} + \mathcal{S}_{B^0}\sin(\Delta m\Delta t) - \mathcal{C}_{B^0}\cos(\Delta m\Delta t)\Big]\\
P_{\bar{B}^0}(\Delta t) &= \frac{e^{-|\Delta t|/\tau_{B^0}}}{4\tau_{B^0}}\Big[R_{\bar{B}^0} + \mathcal{S}_{\bar{B}^0}\sin(\Delta m\Delta t) - \mathcal{C}_{\bar{B}^0}\cos(\Delta m\Delta t)\Big]\\
R_{B^0[\bar{B}^0]} &= \frac{|\lambda_{CP}|^2 + 1}{2} - 2r'\,\mathrm{Re}(\lambda_{CP})\cos(2\beta + \gamma \mp \delta')\\
\mathcal{S}_{B^0[\bar{B}^0]} &= \pm\,\mathrm{Im}(\lambda_{CP}) + r'\left(1 - |\lambda_{CP}|^2\right)\sin(2\beta + \gamma \mp \delta')\\
\mathcal{C}_{B^0[\bar{B}^0]} &= \mp\,\frac{|\lambda_{CP}|^2 - 1}{2} - 2r'\,\mathrm{Im}(\lambda_{CP})\sin(2\beta + \gamma \mp \delta')
\end{aligned} \tag{7.8}$$

The modified decay rates depend on the CP violation of the reconstructed decay mode expressed by λ_{CP}, the relative weak phases β and γ, the ratio r', and the relative strong phase δ' between Cabibbo-suppressed $\bar{b} \to \bar{u}c\bar{d}$ and favored $b \to c\bar{u}d$ decay amplitudes on the tagging-side.

The quantities $\mathcal{S}_{B^0[\bar{B}^0]} = 2r'\sin(2\beta + \gamma \pm \delta')$ are experimentally accessible in semileptonic $B^0 \to D^{*-}l^+\nu_l$ decays. The results from $B^0 \to D^{*-}l^+\nu_l$ control samples in Belle's recent

$\sin(2\beta)$ measurement in $b \rightarrow c\bar{c}s$ transitions are [94, 95],

$$\begin{aligned} \mathcal{S}_{B^0} &= 2r' \sin(2\beta + \gamma + \delta') = (+0.0096 \pm 0.0073), \\ \mathcal{S}_{\bar{B}^0} &= 2r' \sin(2\beta + \gamma - \delta') = (-0.0067 \pm 0.0107). \end{aligned} \tag{7.9}$$

The effect of the tag-side interference on the CP violation measurements of $B^0 \rightarrow D^+D^-$ and $B^0 \rightarrow D^{*\pm}D^{\mp}$ decays is studied by ensemble tests using pseudo-experiments generated according to the decay rates described above. Input to the generation of the Monte Carlo pseudo-experiments are the $B^0 \rightarrow D^{*-}l^+\nu_l$ control sample results given in Equation 7.9. The parameter λ_{CP} is chosen according to the CP violation results of the measurements in $B^0 \rightarrow D^+D^-$ and $B^0 \rightarrow D^{*\pm}D^{\mp}$ decays and according to the result of the $\sin(2\beta)$ measurement in $b \rightarrow c\bar{c}s$ transitions [94, 95]. The amplitude ratio r' and the relative strong phase δ' are constrained by using the value of $\gamma = (67.3^{+4.2}_{-3.5})^\circ$ provided by the CKMfitter group [46].

The ensemble tests are performed by using pseudo-experiments generated including the effect of tag-side interference. In the ensemble tests, the nominal fit procedures neglecting the effect of tag-side interference are applied. The largest systematic biases on the CP violation parameters are assigned as systematic uncertainties for the tag-side interference.

Source	$\mathcal{S}_{D^+D^-}$	$\mathcal{C}_{D^+D^-}$	$\mathcal{A}_{D^*D}$	$\mathcal{S}_{D^*D}$	$\mathcal{C}_{D^*D}$	$\Delta\mathcal{S}_{D^*D}$	$\Delta\mathcal{C}_{D^*D}$
Vertex reconstruction	3.6	2.2	1.3	2.5	2.3	2.4	2.3
Poor quality vertex rejection	2.6	0.4	0.8	0.6	0.2	1.5	1.1
Δt fit range	0.3	< 0.1	0.1	0.1	< 0.1	< 0.1	< 0.1
IP tube constraint in vertex fit	1.7	0.9	0.5	1.2	1.0	1.7	1.5
Track rejection in B_{tag} vertex fit	1.7	1.4	0.9	1.5	1.8	0.7	0.8
SVD misalignment	0.2	0.4	0.0	0.2	0.4	0.2	0.4
Δz bias	0.6	1.3	< 0.1	1.5	1.0	0.5	0.9
Δt resolution functions	6.5	2.4	0.4	3.5	1.1	1.9	0.6
Background Δt parameterisation	2.7	0.5	0.2	0.7	0.2	0.5	0.1
Signal purity	1.2	1.8	0.2	0.9	0.4	0.3	0.2
Physics parameters τ_{B^0} and Δm	0.7	0.4	< 0.1	0.2	0.1	0.2	< 0.1
Flavor tagging	0.7	0.6	< 0.1	0.4	0.3	0.3	0.2
Possible fit bias	0.8	0.2	0.6	0.8	1.1	0.8	0.5
Peaking background	0.3	0.9	0.4	1.3	0.5	0.8	0.7
Tag-side interference	1.4	3.2	0.2	1.1	3.1	0.9	0.6
Total	8.2	5.1	1.6	4.9	4.3	3.5	2.6

Table 7.10: Summary of systematic uncertainties in the CP violation measurements of $B^0 \to D^+D^-$ and $B^0 \to D^{*\pm}D^{\mp}$ decays (in units of 10^{-2}).

7.3.5 Statistical Significance of the Results

The CP violation measurements are performed by maximising a likelihood function with respect to the parameters $\mathcal{S}_{\mathrm{D^+D^-}}$ and $\mathcal{C}_{\mathrm{D^+D^-}}$ in $\mathrm{B}^0 \to \mathrm{D^+D^-}$ and with respect to the parameters $\mathcal{A}_{\mathrm{D^*D}}$, $\mathcal{S}_{\mathrm{D^*D}}$, $\mathcal{C}_{\mathrm{D^*D}}$, $\Delta\mathcal{S}_{\mathrm{D^*D}}$ and $\Delta\mathcal{C}_{\mathrm{D^*D}}$ in $\mathrm{B}^0 \to \mathrm{D}^{*\pm}\mathrm{D}^{\mp}$. In the measurements, the statistics is large enough to determine central confidence intervals on the CP violation parameters by a likelihood-ratio approach.

In $\mathrm{B}^0 \to \mathrm{D^+D^-}$, the 2-dimensional confidence regions are determined from the shape of the likelihood function $\mathcal{L}$ around its solution given by

$$\ln \mathcal{L}\left(\mathcal{S}_{\mathrm{D^+D^-}}, \mathcal{C}_{\mathrm{D^+D^-}}\right) = \ln \mathcal{L}_{\max}\left(\hat{\mathcal{S}}_{\mathrm{D^+D^-}}, \hat{\mathcal{C}}_{\mathrm{D^+D^-}}\right) - \frac{s^2}{2}, \tag{7.10}$$

where $\mathcal{L}_{\max}$ denotes the extreme value of the likelihood function and $\hat{\mathcal{S}}_{\mathrm{D^+D^-}}$ and $\hat{\mathcal{C}}_{\mathrm{D^+D^-}}$ denote the estimates of the CP violation parameters.

In $\mathrm{B}^0 \to \mathrm{D}^{*\pm}\mathrm{D}^{\mp}$, only three out of the five measured parameters are sensitive to CP violation. In analogy to $\mathrm{B}^0 \to \mathrm{D^+D^-}$, the 3-dimensional confidence regions with respect to these parameters are determined by

$$\ln \mathcal{L}\left(\mathcal{A}_{\mathrm{D^*D}}, \mathcal{S}_{\mathrm{D^*D}}, \mathcal{C}_{\mathrm{D^*D}}\right) = \ln \mathcal{L}_{\max}\left(\hat{\mathcal{A}}_{\mathrm{D^*D}}, \hat{\mathcal{S}}_{\mathrm{D^*D}}, \hat{\mathcal{C}}_{\mathrm{D^*D}}\right) - \frac{s^2}{2}. \tag{7.11}$$

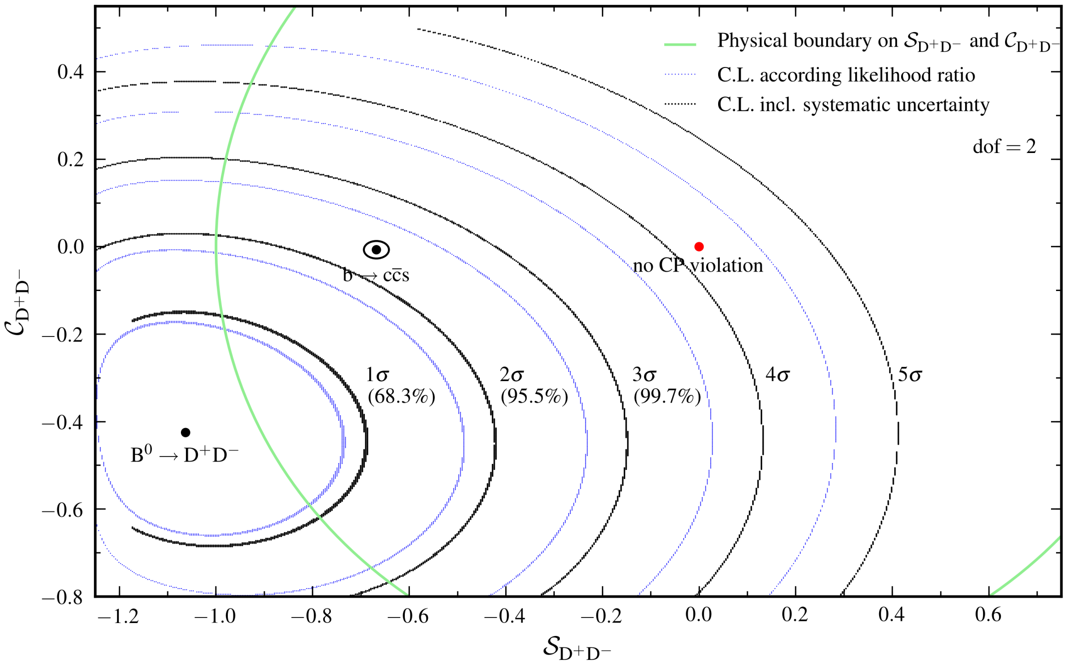

Figure 7.16: Likelihood contours in the $\mathrm{B}^0 \to \mathrm{D^+D^-}$ measurement for different confidence levels according to two degrees of freedom. The blue lines correspond to the likelihood from the fit only. The black lines additionally account for the systematic uncertainties.

The value of the likelihood-ratio $s^2 = -2\ln(\mathcal{L}/\mathcal{L}_{\max})$ can be translated into a probability content by

$$\int_0^{s^2} \chi^2(z, \text{dof})\, dz = 1 - \gamma, \tag{7.12}$$

where s^2 is the quantile of the χ^2 distribution of the order $1-\gamma$ with respect to the particular degrees of freedom (dof) [99, 124].

To determine the confidence regions in the CP violation parameter space associated with a given probability content, the likelihood function is evaluated on a grid of 500×500 points for the parameters $\mathcal{S}_{D^+D^-}$ and $\mathcal{C}_{D^+D^-}$ around the obtained solution in the $B^0 \to D^+D^-$ measurement, and on a grid of $500 \times 500 \times 500$ points for the parameters $\mathcal{A}_{D^*D}$, $\mathcal{S}_{D^*D}$ and $\mathcal{C}_{D^*D}$ around the obtained solution in the $B^0 \to D^{*\pm}D^{\mp}$ measurement. To include the systematic uncertainties in the study of the significance, the likelihood function is additionally convoluted numerically by Gaussian functions with widths chosen according to the systematic uncertainties on the CP violation parameters obtained in Section 7.3.4.

For $B^0 \to D^+D^-$, the confidence regions corresponding to a significance of 1σ to 5σ with respect to two degrees of freedom are shown in Figure 7.16. The parameters $\mathcal{S}_{D^+D^-}$ and $\mathcal{C}_{D^+D^-}$ are correlated at a level of approximately 10%. The measured CP violation parameters are approximately 0.5σ outside of the physical parameter space defined by $\sqrt{\mathcal{S}^2 + \mathcal{C}^2} \leq 1$ and the direct CP violation $\mathcal{C}_{D^+D^-}$ deviates from zero by approximately 2σ. The measurement excludes the conservation of CP symmetry in $B^0 \to D^+D^-$ decays, equivalent to $\mathcal{S}_{D^+D^-} = \mathcal{C}_{D^+D^-} = 0$, at a confidence level of $1 - 2.7 \times 10^{-5}$ corresponding to a significance of 4.2σ.

For $B^0 \to D^{*\pm}D^{\mp}$, the confidence regions corresponding to a significance of 1σ to 5σ with respect to three degrees of freedom are shown in Figure 7.17. The time- and flavor-integrated asymmetry $\mathcal{A}_{D^*D}$ measuring direct CP violation and the parameter $\mathcal{C}_{D^*D}$ measuring flavor-dependent direct CP violation are both consistent with zero. The CP violation in $B^0 \to D^{*\pm}D^{\mp}$ is driven by the mixing induced CP violation $\mathcal{S}_{D^*D}$. The measurement excludes the conservation of CP symmetry in $B^0 \to D^{*\pm}D^{\mp}$ decays, equivalent to $\mathcal{A}_{D^*D} = \mathcal{S}_{D^*D} = \mathcal{C}_{D^*D} = 0$, at a confidence level of $1 - 6.8 \times 10^{-5}$ corresponding to a significance of 4.0σ.

Under the assumption of negligible contributions from penguin amplitudes, the mixing-induced CP violation in $B^0 \to D^+D^-$ and $B^0 \to D^{*\pm}D^{\mp}$ decays is directly related to the angle β of the Unitarity Triangle. The angle β is determined at high precision by measurements of mixing-induced CP violation in $b \to c\bar{c}s$ transitions. The current world average is $\sin(2\beta) = 0.68 \pm 0.02$ [58]. In $B^0 \to D^+D^-$, the mixing-induced CP violation $\mathcal{S}_{D^+D^-}$ deviates by approximately 1.3σ, and in $B^0 \to D^{*\pm}D^{\mp}$, the mixing-induced CP violation $\mathcal{S}_{D^*D}$ deviates by less than 1σ from this value.

The above reported results account for both, the statistical and the systematic uncertainties.

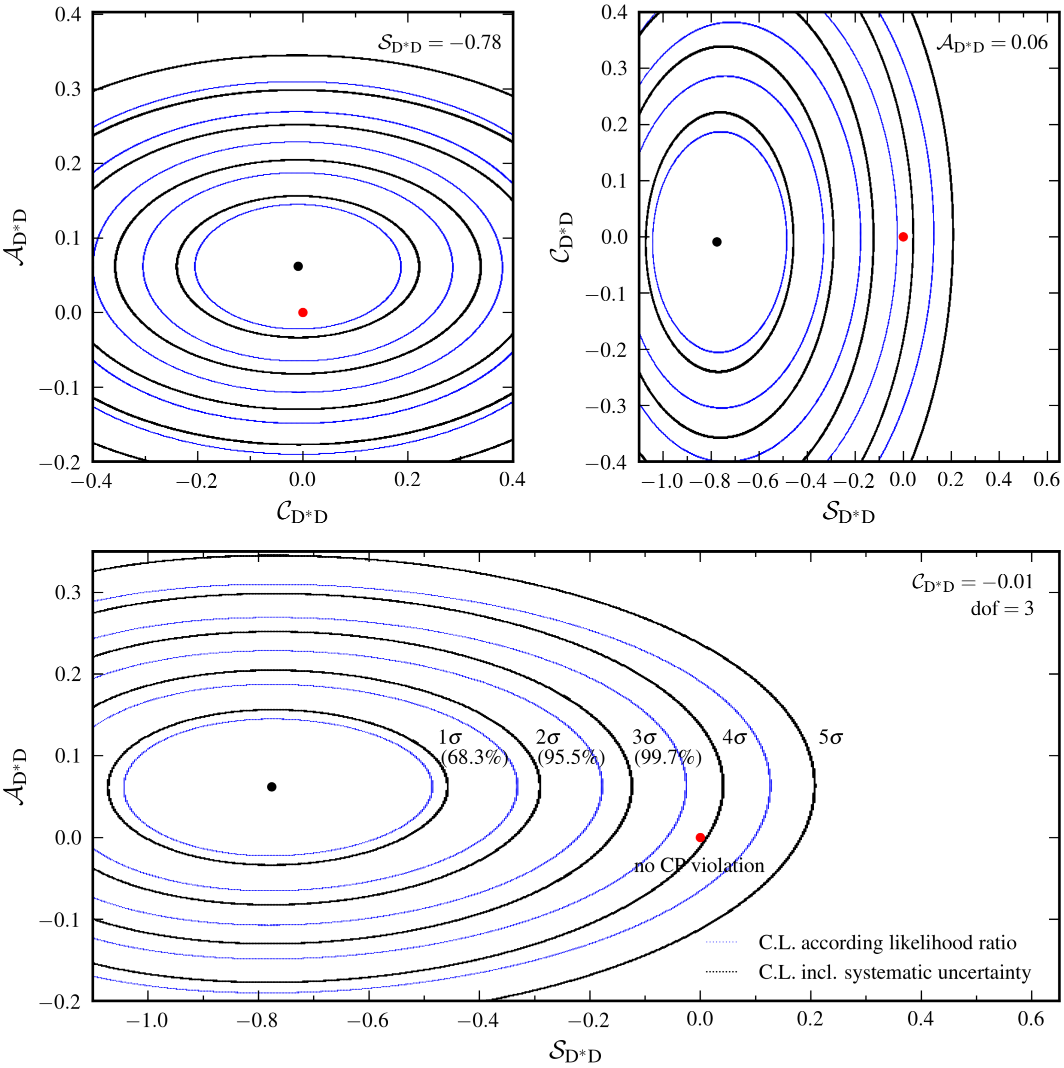

Figure 7.17: Likelihood contours in the $\mathrm{B}^0 \to \mathrm{D}^{*\pm}\mathrm{D}^{\mp}$ measurement for different confidence levels according to three degrees of freedom. The blue lines correspond to the likelihood from the fit only. The black lines additionally account for the systematic uncertainties.

8 Summary and Conclusion

In this thesis, the measurements of branching fractions and time-dependent CP violation in $B^0 \to D^+D^-$ and $B^0 \to D^{*\pm}D^{\mp}$ decays are presented. The measurements are based on the final data set of the Belle experiment containing $(772 \pm 11) \times 10^6$ $B\bar{B}$ pairs collected at the $\Upsilon(4S)$-resonance at the asymmetric-energy KEKB e^+e^--collider.

Compared to previous time-dependent measurements carried out by the Belle Collaboration, the analysis includes several improvements. It makes use of new track finding algorithms, that give rise to higher reconstruction efficiencies, and applies newly developed resolution functions, that allow a decay mode independent modelling of resolution effects related to the vertex reconstruction and consequently bias-free time-dependent measurements. For the $B^0 \to D^+D^-$ measurement, an improved continuum suppression based on neural networks implemented in the NeuroBayes package has been developed. The continuum suppression is realised by a hierarchical arrangement of neural networks that combine information about the event topology. The neural network approach allows to efficiently suppress the background originating from $e^+e^- \to q\bar{q}$ $(q \in \{u,d,s,c\})$ continuum events and has proven to be of superior separation power compared to standard continuum suppression techniques. Due to the above and further improvements in technical details of the analysis, an approximately 80% higher signal yield than in the previous Belle measurement based on a data set containing 535×10^6 $B\bar{B}$ pairs could be achieved in the measurement of $B^0 \to D^+D^-$ decays.

The measurements are performed as blind analyses and are validated by various cross-checks. Prior to unblinding of the $B^0 \to D^+D^-$ and $B^0 \to D^{*\pm}D^{\mp}$ data distributions, the same time-integrated and time-dependent measurements are performed for $B^0 \to D_s^+D^-$ and $B^0 \to D_s^+D^{*-}$ decays. These decays are kinematically very similar and allow to test the analysis procedures on high statistic control samples.

The results of the measurement of branching fractions of the control samples are

$$\mathcal{B}\left(B^0 \to D_s^+D^-\right) = \left(6.62 \pm 0.11 \text{ (stat.)}\right) \times 10^{-3}, \tag{8.1}$$

$$\mathcal{B}\left(B^0 \to D_s^+D^{*-}\right) = \left(7.87 \pm 0.13 \text{ (stat.)}\right) \times 10^{-3}, \tag{8.2}$$

and are consistent with the current wold averages [115].

The results of the time-dependent CP violation measurements of the control samples are

$$\begin{aligned}
\mathcal{A}_{D_sD} &= -0.01 \pm 0.02 \text{ (stat.)},\\
\mathcal{S}_{D_sD} &= -0.05 \pm 0.05 \text{ (stat.)},\\
\mathcal{C}_{D_sD} &= +0.01 \pm 0.03 \text{ (stat.)},\\
\Delta\mathcal{S}_{D_sD} &= +0.01 \pm 0.05 \text{ (stat.)},\\
\Delta\mathcal{C}_{D_sD} &= -0.95 \pm 0.03 \text{ (stat.)},
\end{aligned} \tag{8.3}$$

and

$$\begin{aligned}\mathcal{A}_{D_sD^*} &= +0.01 \pm 0.02 \text{ (stat.)},\\ \mathcal{S}_{D_sD^*} &= -0.04 \pm 0.05 \text{ (stat.)},\\ \mathcal{C}_{D_sD^*} &= +0.06 \pm 0.03 \text{ (stat.)},\\ \Delta\mathcal{S}_{D_sD^*} &= +0.10 \pm 0.05 \text{ (stat.)},\\ \Delta\mathcal{C}_{D_sD^*} &= -1.00 \pm 0.03 \text{ (stat.)}.\end{aligned} \tag{8.4}$$

The results are in agreement with the assumption of no CP violation in $B^0 \to D_s^+D^-$ and $B^0 \to D_s^+D^{*-}$ decays and provide an important confirmation about the validity of the applied fit procedures. Further cross-checks cover the measurements of lifetimes and mixing-frequencies of the control samples and the measurements of the lifetimes of the untagged $B^0 \to D^+D^-$ and $B^0 \to D^{*\pm}D^{\mp}$ decay samples.

In the time-integrated measurements, the yields for $B^0 \to D^+D^-$ decays are 221.4 ± 18.6 signal events in the $(K^-\pi^+\pi^+)(K^+\pi^-\pi^-)$ final state and 48.0 ± 8.9 signal events in the $(K^-\pi^+\pi^+)(K_S^0\pi^-)$ final state. For $B^0 \to D^{*\pm}D^{\mp}$, a yield of 886.8 ± 39.3 signal events is obtained in all reconstructed modes combined. Of these, the yield in modes involving only $D^{*+} \to D^0\pi^-$ decays is 769.2 ± 36.0 signal events.

Decays such as $B^0 \to D^{(*)-}K^{*+}$, $B^0 \to D^{(*)}K^0\pi^+$ and $B^0 \to D^{(*)}\pi^+\pi^+\pi^-$ have the same final states as the reconstructed $B^0 \to D^+D^-$ and $B^0 \to D^{*\pm}D^{\mp}$ decay modes. These decays can possibly populate the M_{bc} and ΔE signal region and are referred to as peaking background. The peaking background contributions are estimated from the D mass sidebands and subtracted from the signal yields given above. Overall the peaking background contributions are found to be small. Following the studies performed by usage of Monte Carlo simulations and data distributions, the $D^- \to K^+\pi^-\pi^-$ sidebands can be considered as free of peaking background. For $B^0 \to D^+D^-$ ($B^0 \to D^{*\pm}D^{\mp}$), a small contribution of 0.7 ± 1.5 (4.7 ± 2.1) peaking background events is found in the $D^- \to K_S^0\pi^-$ sidebands.

The $B^0 \to D^+D^-$ and $B^0 \to D^{*\pm}D^{\mp}$ branching fractions are calculated from the signal yields, the reconstruction efficiencies, the number of $B\bar{B}$ pairs in the data set, and the current world averages of D^0, D^+ and D^{*+} branching fractions [115]. The results are

$$\begin{aligned}\mathcal{B}\left(B^0 \to D^+D^-\right) &= \left(2.12 \pm 0.16 \text{ (stat.)} \pm 0.18 \text{ (syst.)}\right) \times 10^{-4},\\ \mathcal{B}\left(B^0 \to D^{*\pm}D^{\mp}\right) &= \left(6.14 \pm 0.29 \text{ (stat.)} \pm 0.50 \text{ (syst.)}\right) \times 10^{-4}.\end{aligned} \tag{8.5}$$

The precision of the branching fraction measurements is limited by systematic uncertainties. For both decays, the major contributions to the systematic uncertainty originate from the uncertainties on the track reconstruction efficiencies and on the particle identification efficiencies. These contributions are in particular large for $B^0 \to D^+D^-$ and $B^0 \to D^{*\pm}D^{\mp}$ decays, because the reconstructed decay modes contain a high multiplicity of charged tracks in the final states. Furthermore, the world averages of D^0 and D^+ branching fractions are associated with significant uncertainties.

In Figure 8.1, the measured $B^0 \to D^+D^-$ and $B^0 \to D^{*\pm}D^{\mp}$ branching fractions are compared to previous measurements performed by the Belle and BaBar Collaborations [125, 126, 68, 127, 128]. For both decays, the branching fractions are consistent with the results from

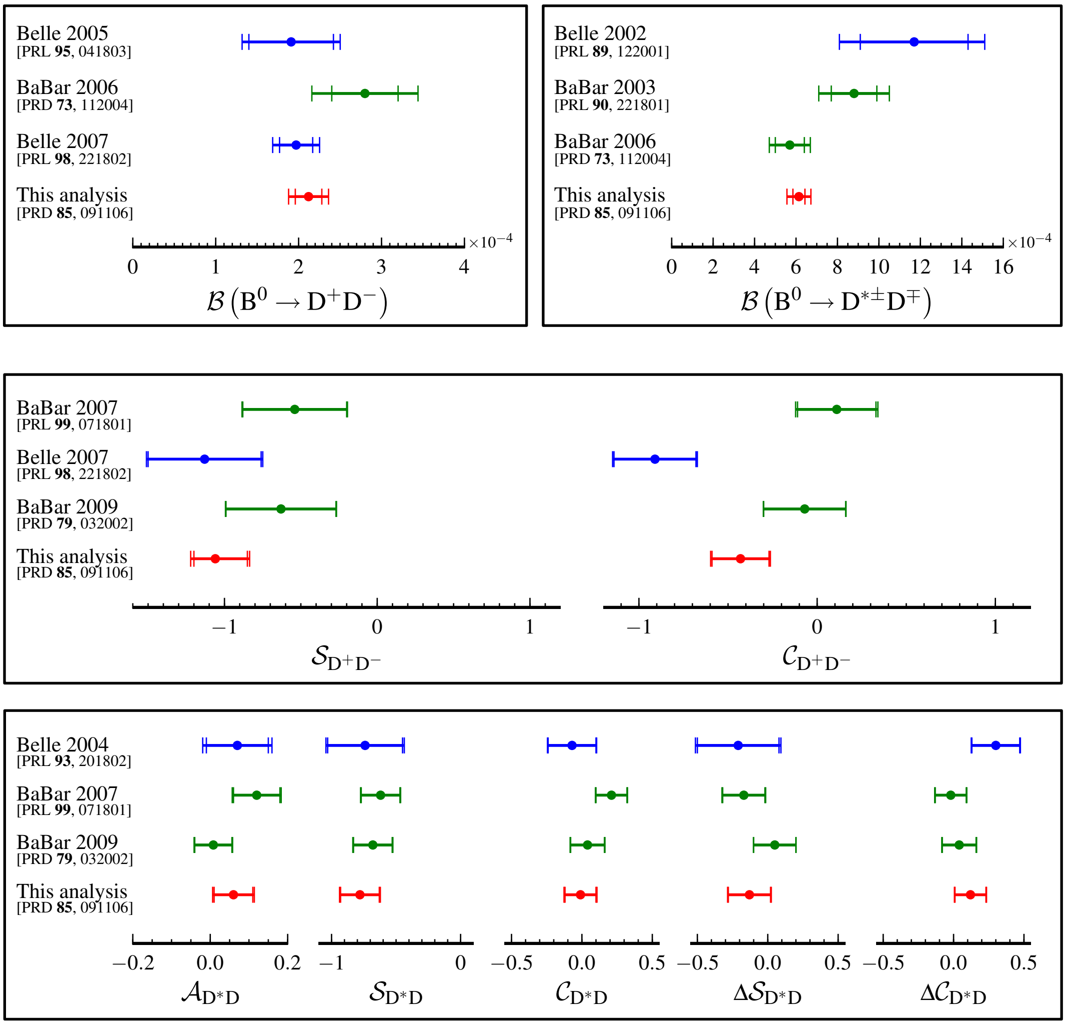

Figure 8.1: Comparison of the results of branching fractions and of time-dependent CP violation parameters to previous measurements in $B^0 \to D^+D^-$ and $B^0 \to D^{*\pm}D^{\mp}$ decays.

previous measurements and exceed them in precision. Regarding the $B^0 \to D^{*\pm}D^{\mp}$ branching fraction, there is one noticeable deviation: the Belle result from 2002 has an approximately two-times larger center value than the present result, but is compatible due to its large uncertainty.

In the time-dependent measurements of $B^0 \to D^+D^-$ decays, the CP violation is determined to

$$\begin{aligned} \mathcal{S}_{\mathrm{D^+D^-}} &= -1.06\ {}^{+0.21}_{-0.14}\ (\text{stat.}) \pm 0.08\ (\text{syst.}), \\ \mathcal{C}_{\mathrm{D^+D^-}} &= -0.43 \pm 0.16\ (\text{stat.}) \pm 0.05\ (\text{syst.}). \end{aligned} \tag{8.6}$$

The measurement excludes the conservation of CP symmetry in $\mathrm{B}^0 \to \mathrm{D}^+\mathrm{D}^-$ decays, equivalent to $\mathcal{S}_{\mathrm{D^+D^-}} = \mathcal{C}_{\mathrm{D^+D^-}} = 0$, at a confidence level of $1 - 2.7 \times 10^{-5}$ corresponding to a significance of 4.2σ.

The CP violation parameters are located approximately 0.5σ outside of the physical parameter space defined by $\sqrt{\mathcal{S}^2 + \mathcal{C}^2} \leq 1$. In the ensemble tests, comparable results are obtained in a significant number of simulated measurements. For Monte Carlo pseudo-experiments, generated according to CP violation close to the Standard Model expectation and with input from the data distributions, the CP fit procedure returns values outside of the physical parameter space in 15% of all simulated measurements.

In Figure 8.1, a comparison with results from previous measurements in $\mathrm{B}^0 \to \mathrm{D}^+\mathrm{D}^-$ decays by the Belle and BaBar Collaborations is shown [129, 68, 69]. Both CP violation parameters, the mixing-induced CP violation $\mathcal{S}$ and the direct CP violation $\mathcal{C}$, are in agreement with the previous measurements and exceed them in precision.

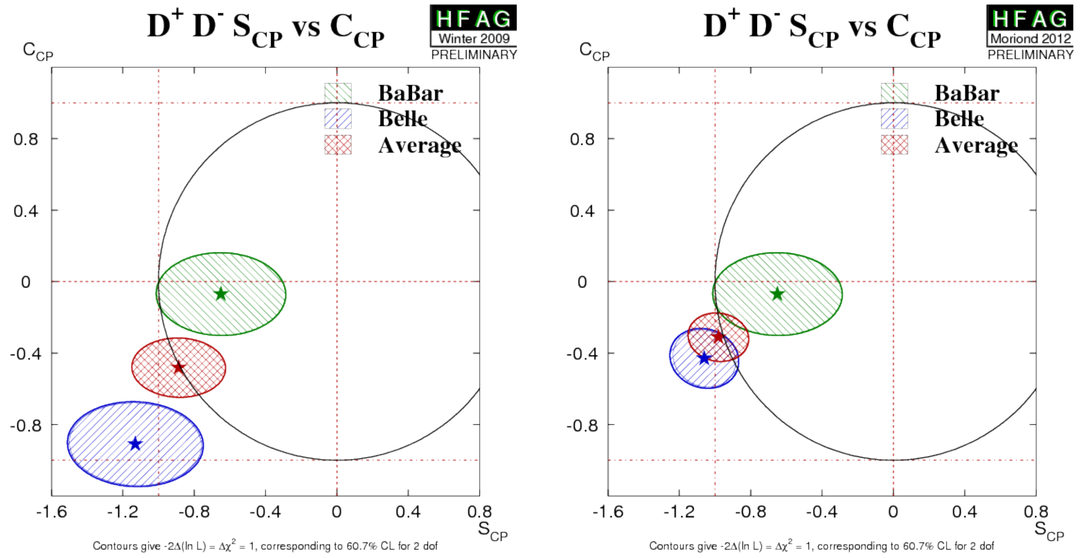

Figure 8.2: Comparison of time-dependent CP violation in $\mathrm{B}^0 \to \mathrm{D}^+\mathrm{D}^-$ decays measured by BaBar and Belle. The Belle result in the left figure is from 2007 [68], and the Belle result in right figure shows the result of the present analysis. The black circles represent the boundary of the physical parameter space defined by $\sqrt{\mathcal{S}^2 + \mathcal{C}^2} \leq 1$. The figure has been provided by the Heavy Flavor Averaging Group [58].

Another comparison provided by the Heavy Flavor Averaging Group is shown in Figure 8.2. In this illustration, the Belle and BaBar measurements are compared in the plane spanned by the CP violation parameters $\mathcal{S}$ and $\mathcal{C}$. The BaBar measurement agrees well with the Standard Model reference given by measurements in $\mathrm{b} \to \mathrm{c\bar{c}s}$ transitions, which suggest $\mathcal{S} = -\sin(2\beta) = -0.68 \pm 0.02$ and $\mathcal{C} = 0$ [58]. In contrast, the Belle measurement from 2007 is located outside of the physical parameter space and shows evidence for a large direct CP violation: $\mathcal{C}_{D^+D^-} = -0.91 \pm 0.23$ (stat.) $\pm\, 0.06$ (syst.) corresponding to a 3.2σ deviation from zero. The measurement of the present analysis includes the data set of the previous measurement and has an approximately 80% higher signal yield. The center value of the direct CP violation reduces by more than half and the significance of the deviation reduces to about 2.0σ. This significant reduction is consistent with the assumption that the large direct CP violation observed in the previous measurement is caused by a statistical fluctuation. On the other hand, the current experimental precision does not allow to provide a statistical significant evidence for a non-zero direct CP violation at small center values.

In the time-dependent measurements of $B^0 \to D^{*\pm}D^{\mp}$ decays, the CP violation parameters are determined to

$$\begin{aligned}
\mathcal{A}_{D^*D} &= +0.06 \pm 0.05 \text{ (stat.)} \pm 0.02 \text{ (syst.)},\\
\mathcal{S}_{D^*D} &= -0.78 \pm 0.15 \text{ (stat.)} \pm 0.05 \text{ (syst.)},\\
\mathcal{C}_{D^*D} &= -0.01 \pm 0.11 \text{ (stat.)} \pm 0.04 \text{ (syst.)},\\
\Delta\mathcal{S}_{D^*D} &= -0.13 \pm 0.15 \text{ (stat.)} \pm 0.04 \text{ (syst.)},\\
\Delta\mathcal{C}_{D^*D} &= +0.12 \pm 0.11 \text{ (stat.)} \pm 0.03 \text{ (syst.)}.
\end{aligned} \tag{8.7}$$

The measurement excludes the conservation of CP symmetry in $B^0 \to D^{*\pm}D^{\mp}$ decays, equivalent to $\mathcal{A}_{D^*D} = \mathcal{S}_{D^*D} = \mathcal{C}_{D^*D} = 0$, at a confidence level of $1 - 6.8 \times 10^{-5}$ corresponding to a significance of 4.0σ.

In Figure 8.1, the $B^0 \to D^{*\pm}D^{\mp}$ result is compared to previous measurements by the Belle and BaBar Collaborations [70, 129, 69]. The measurements agree in all CP violation parameters and indicate no direct CP violation in $B^0 \to D^{*\pm}D^{\mp}$ decays.

If the contribution of penguin amplitudes is negligible, and if the magnitudes of the $B^0 \to D^{*+}D^-$ and $B^0 \to D^{*-}D^+$ decay amplitudes are identical and their relative strong phase is zero, then the parameters $\mathcal{A}_{D^*D}$, $\mathcal{C}_{D^*D}$, $\Delta\mathcal{S}_{D^*D}$ and $\Delta\mathcal{C}_{D^*D}$ vanish and the mixing-induced CP violation $\mathcal{S}_{D^*D}$ is equal to $-\sin(2\beta)$. The results are consistent with the above assumptions, and $\sin(2\beta) = 0.78 \pm 0.15$ (stat.) $\pm\, 0.05$ (syst.) is measured in $B^0 \to D^{*\pm}D^{\mp}$ decays.

In Figure 8.3, the $\sin(2\beta)$ results from measurements of mixing-induced CP violation in $b \to c\bar{c}s$ and in $b \to c\bar{c}d$ transitions are compared. The result of the $B^0 \to D^{*\pm}D^{\mp}$ measurement is is in very good agreement with the current world average of $\sin(2\beta) = 0.68 \pm 0.02$. The result of the $B^0 \to D^+D^-$ measurement deviates by approximately 1.3σ from the current world average.

In summary, the measurements of branching fractions and time-dependent CP violation in $B^0 \to D^+D^-$ and $B^0 \to D^{*\pm}D^{\mp}$ decays have been performed using the final Belle data set of $(772 \pm 11) \times 10^6$ $B\bar{B}$ pairs. The measurements in both decays exclude the conservation of CP symmetry at equal to or greater than 4.0σ significance. In both decays, the CP violation is driven by mixing-induced CP violation according to $\sin(2\beta)$. Compared to the previous $B^0 \to D^+D^-$ measurement by Belle, the direct CP violation reduced significantly and deviates instead of 3.2σ only approximately 2.0σ from zero. In $B^0 \to D^{*\pm}D^{\mp}$, no direct CP violation is

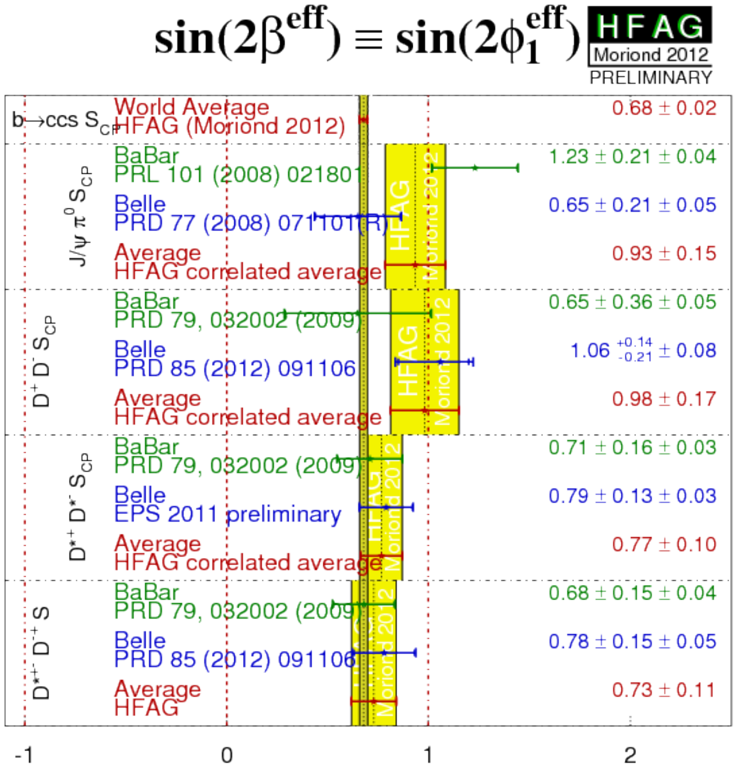

Figure 8.3: Comparison of sin (2β) results from the measurement of mixing-induced CP violation in several different decay modes involving b → c$\bar{c}$s and b → c$\bar{c}$d transitions by BaBar and Belle. The $B^0 \to D^+D^-$ and $B^0 \to D^{*\pm}D^{\mp}$ measurements by Belle are the result of the present analysis. The figure has been provided by the Heavy Flavor Averaging Group [58].

observed suggesting that penguin contributions to the decays are small or possibly negligible. Further experimental efforts are necessary, to probe for small penguin contributions in b → c$\bar{c}$d transitions.

For future measurements performed at B-factory experiments, an integrated luminosity of 50 ab^{-1} will be necessary to achieve the same precision as currently provided by the measurements in b → c$\bar{c}$s transitions. For the year 2015, the commissioning and the start of SuperKEKB and the Belle II experiment is scheduled [130]. The new accelerator and the new detector are designed to operate at an instantaneous luminosity of $8 \times 10^{35}\ \mathrm{cm}^{-2}\mathrm{s}^{-1}$, which is approximately 40-times higher than the peak luminosity reached by KEKB. In the year 2022, an integrated luminosity of 50 ab^{-1} is anticipated.

The presented $B^0 \to D^+D^-$ and $B^0 \to D^{*\pm}D^{\mp}$ measurements supersede previous measurements by Belle [127, 70, 68], and are more precise than all previous measurements performed by the Belle and BaBar Collaborations. The results of the measurements presented in this thesis have been published in Reference [131].

References

[1] J. H. Christenson, J. W. Cronin, V. L. Fitch *et al.* "Evidence for the 2π Decay of the K_2^0 Meson". *Phys. Rev. Lett.*, 13:138–140, 1964.

[2] D. Dorfan, J. Enstrom, D. Raymond *et al.* "Charge Asymmetry in the Muonic Decay of the K_2^0". *Phys. Rev. Lett.*, 19:987–993, 1967.

[3] S. Bennett, D. Nygren, H. Saal *et al.* "Measurement of the Charge Asymmetry in the Decay $K_L^0 \to \pi^\pm + e^\mp + \nu$". *Phys. Rev. Lett.*, 19:993–997, 1967.

[4] M. Kobayashi and T. Maskawa. "CP Violation in the Renormalizable Theory of Weak Interaction". *Progress of Theoretical Physics*, 49(2):652–657, 1973.

[5] S. W. Herb, D. C. Hom, L. M. Lederman *et al.* "Observation of a Dimuon Resonance at 9.5 GeV in 400 GeV Proton-Nucleus Collisions". *Phys. Rev. Lett.*, 39:252–255, 1977.

[6] T. Böhringer, F. Costantini, J. Dobbins *et al.* (CUSB Collaboration). "Observation of Υ, Υ', and Υ'' at the Cornell Electron Storage Ring". *Phys. Rev. Lett.*, 44:1111–1114, 1980.

[7] D. Andrews, K. Berkelman, M. Billing *et al.* (CLEO Collaboration). "Observation of Three Upsilon States". *Phys. Rev. Lett.*, 44:1108–1111, 1980.

[8] D. Andrews, K. Berkelman, R. Cabenda *et al.* (CLEO Collaboration). "Observation of a Fourth Upsilon State in e^+e^- Annihilations". *Phys. Rev. Lett.*, 45:219–221, 1980.

[9] G. Finocchiaro, G. Giannini, J. Lee-Franzini *et al.* (CUSB Collaboration). "Observation of the Υ''' at the Cornell Electron Storage Ring". *Phys. Rev. Lett.*, 45:222–225, 1980.

[10] C. Bebek, J. Haggerty, J. M. Izen *et al.* (CLEO Collaboration). "Evidence for New-Flavor Production at the $\Upsilon(4S)$". *Phys. Rev. Lett.*, 46:84–87, 1981.

[11] L. J. Spencer, G. Fincchiaro, J. Lee-Franzini *et al.* (CUSB Collaboration). "Measurement of B-Meson Semileptonic Decay". *Phys. Rev. Lett.*, 47:771–774, 1981.

[12] E. Fernandez, W. T. Ford, A. L. Read *et al.* (MAC Collaboration). "Lifetime of Particles Containing b Quarks". *Phys. Rev. Lett.*, 51:1022–1025, 1983.

[13] N. S. Lockyer, J. A. Jaros, M. E. Nelson *et al.* (Mark II Collaboration). "Measurement of the Lifetime of Bottom Hadrons". *Phys. Rev. Lett.*, 51:1316–1319, 1983.

[14] H. Albrecht, A. Andam, U. Binder *et al.* (ARGUS Collaboration). "Observation of B^0-$\bar{B}^0$ Mixing". *Physics Letters B*, 192(1-2):245 – 252, 1987.

[15] I. I. Bigi and A. I. Sanda. "CP Violation in Heavy Flavor Decays: Predictions and Search Strategies". *Nuclear Physics B*, 281(1):41–71, 1987.

[16] P. Oddone. *Proceedings of the UCLA Workshop: "Linear Collider $B\bar{B}$ Factory Conceptual Design"*. Edited by D. Stock. World Scientific, p. 243, 1987.

[17] *"PEP-II: An Asymmetric B Factory. Conceptual Design Report"*. SLAC-R-418, Stanford Linear Accelerator Center, 1993.

[18] *"KEKB B-Factory Design Report"*. KEK Report 95-7, High Energy Accelerator Research Organization, Japan, 1995.

[19] D. Boutigny *et al.* (BaBar Collaboration). *"BaBar Technical Design Report"*. SLAC-R-457, Stanford Linear Accelerator Center, 1995.

[20] M. Cheng *et al.* (Belle Collaboration). *"A Study of CP Violation in B Meson Decays: Technical Design Report"*. KEK Report 95-1, High Energy Accelerator Research Organization, Japan, 1995.

[21] K. Abe, R. Abe, I. Adachi *et al.* (Belle Collaboration). "Observation of Large CP Violation in the Neutral B Meson System". *Phys. Rev. Lett.*, 87:091802, 2001.

[22] B. Aubert, D. Boutigny, J.-M. Gaillard *et al.* (BaBar Collaboration). "Observation of CP Violation in the B^0 Meson System". *Phys. Rev. Lett.*, 87:091801, 2001.

[23] Y. Chao, P. Chang, K. Abe *et al.* (Belle Collaboration). "Evidence for Direct CP Violation in $B^0 \rightarrow K^+\pi^-$ Decays". *Phys. Rev. Lett.*, 93:191802, 2004.

[24] B. Aubert, R. Barate, D. Boutigny *et al.* (BaBar Collaboration). "Direct CP Violating Asymmetry in $B^0 \rightarrow K^+\pi^-$ Decays". *Phys. Rev. Lett.*, 93:131801, 2004.

[25] A. Alavi-Harati, I. F. Albuquerque, T. Alexopoulos *et al.* (KTeV Collaboration). "Observation of Direct CP Violation in $K_{S,L} \rightarrow \pi\pi$ Decays". *Phys. Rev. Lett.*, 83:22–27, 1999.

[26] V. Fanti, A. Lai, D. Marras *et al.* (NA48 Collaboration). "A New Measurement of Direct CP Violation in Two Pion Decays of the Neutral Kaon". *Physics Letters B*, 465(1):335–348, 1999.

[27] A. Abulencia, J. Adelman, T. Affolder *et al.* (CDF Collaboration). "Observation of B_s^0-$\overline{B}_s^0$ Oscillations". *Phys. Rev. Lett.*, 97:242003, 2006.

[28] T. Aaltonen, J. Adelman, T. Akimoto *et al.* (CDF Collaboration). "First Flavor-Tagged Determination of Bounds on Mixing-Induced *CP* Violation in $B_s^0 \rightarrow J/\Psi\Phi$ Decays". *Phys. Rev. Lett.*, 100:161802, 2008.

[29] V. M. Abazov, B. Abbott, M. Abolins *et al.* (DØ Collaboration). "Measurement of B_s^0 Mixing Parameters from the Flavor-Tagged Decay $B_s^0 \rightarrow J/\Psi\Phi$". *Phys. Rev. Lett.*, 101: 241801, 2008.

[30] R. Aaij, C. Abellan Beteta, B. Adeva *et al.* (LHCb Collaboration). "Evidence for CP Violation in Time-Integrated $D^0 \rightarrow h^-h^+$ Decay Rates". *Phys. Rev. Lett.*, 108:111602, 2012.

[31] D. N. Spergel, L. Verde, H. V. Peiris *et al.* (WMAP Collaboration). "First-Year Wilkinson Microwave Anisotropy Probe (WMAP) Observations: Determination of Cosmological Parameters". *The Astrophysical Journal Supplement Series*, 148:175–194, 2003.

[32] S. Burles, K. M. Nollett, and M. S. Turner. "Big Bang Nucleosynthesis Predictions for Precision Cosmology". *The Astrophysical Journal*, 552:L1, 2001.

[33] A. D. Sakharov. "Violation of CP Invariance, C Asymmetry and Baryon Asymmetry of the Universe". *JETP Letters*, 5(1):24–27, 1967.

[34] V. Rubakov. "Cosmology and Astrophysics". *Lectures at the European School of High-Energy Physics at Beatenberg (Switzerland) in 2001.*

[35] S. L. Glashow. "Partial-Symmetries of Weak Interactions". *Nuclear Physics*, 22(4): 579–588, 1961.

[36] S. Weinberg. "A Model of Leptons". *Phys. Rev. Lett.*, 19:1264–1266, 1967.

[37] P. Higgs. "Broken Symmetries, Massless Particles and Gauge Fields". *Physics Letters*, 12(2):132–133, 1964.

[38] S. L. Glashow, J. Iliopoulos, and L. Maiani. "Weak Interactions with Lepton-Hadron Symmetry". *Phys. Rev. D*, 2:1285–1292, 1970.

[39] I. I. Bigi and A. I. Sanda. *"CP Violation"*. Cambridge University Press, 2nd edition, 2009.

[40] N. Cabibbo. "Unitary Symmetry and Leptonic Decays". *Phys. Rev. Lett.*, 10:531–533, 1963.

[41] See review on "V_{ud}, V_{us}, the Cabibbo Angle and CKM Unitarity" in Reference [115].

[42] L.-L. Chau and W.-Y. Keung. "Comments on the Parametrization of the Kobayashi-Maskawa Matrix". *Phys. Rev. Lett.*, 53:1802–1805, 1984.

[43] L. Wolfenstein. "Parametrization of the Kobayashi-Maskawa Matrix". *Phys. Rev. Lett.*, 51:1945, 1983.

[44] C. Jarlskog. "Commutator of the Quark Mass Matrices in the Standard Electroweak Model and a Measure of Maximal CP Nonconservation". *Phys. Rev. Lett.*, 55:1039–1042, 1985.

[45] See review on "The CKM Quark-Mixing Matrix" in Reference [115].

[46] J. Charles *et al.* (CKMfitter Group). "CP Violation and the CKM Matrix: Assessing the Impact of the Asymmetric B Factories". *Eur. Phys. J. C*, 41:1–131, 2005.

[47] M. Bona, M. Ciuchini, E. Franco *et al.* (UTfit Collaboration). "The 2004 UTfit Collaboration Report on the Status of the Unitarity Triangle in the Standard Model". *Journal of High Energy Physics*, 2005(07):028, 2005.

[48] V. Weisskopf and E. Wigner. "Berechnung der natürlichen Linienbreite auf Grund der Diracschen Lichttheorie". *Zeitschrift für Physik*, 63:54–73, 1930.

[49] V. Weisskopf and E. Wigner. “Über die natürliche Linienbreite in der Strahlung des harmonischen Oszillators”. *Zeitschrift für Physik*, 65:18–29, 1930.

[50] U. Nierste. “Three Lectures on Meson Mixing and CKM Phenomology”. *Lectures at the Helmholtz International Summer School on “Heavy Quark Physics” at Dubna (Russia) in 2008*.

[51] J. L. Rosner and B. D. Winstein. *“Kaon Physics”*. University of Chicago Press, 1st edition, 2001.

[52] See review on “D^0-$\bar{D}^0$ Mixing” in Reference [115].

[53] See review on “B^0-$\bar{B}^0$ Mixing” in Reference [115].

[54] A. J. Buras, W. Stominski, and H. Steger. “B^0-$\overline{B}^0$ Mixing, CP Violation and the B-Meson Decay”. *Nuclear Physics B*, 245(3):369, 1984.

[55] R. Fleischer. “Flavour Physics and CP Violation”. *Lectures given at the 2003 European School of High-Energy Physics*.

[56] A. Einstein, B. Podolsky, and N. Rosen. “Can Quantum-Mechanical Description of Physical Reality Be Considered Complete?”. *Phys. Rev.*, 47:777–780, 1935.

[57] P. Harrison and H. Quinn. *“The BaBar Physics Book: Physics at an Asymmetric B Factory”*. SLAC-R-504, Stanford Linear Accelerator Center, 1998.

[58] D. Asner, S. Banerjee, R. Bernhard *et al.* (Heavy Flavor Averaging Group). “Averages of b-Hadron, c-Hadron, and τ-Lepton Properties”. arXiv:1010.1589, 2011.

[59] M. Meseck. “Measurement of the CP-odd Fraction in the Decay $B^0 \to D^{*+}D^{*-}$ with the Belle Experiment”. Diploma thesis, Institute for Experimental Nuclear Physics, Karlsruhe Institute of Technology, 2010.

[60] B. Kronenbitter. “Measurement of Polarization and CP Violation in $B^0 \to D^{*+}D^{*-}$ Decays with the Belle Detector”. Diploma thesis, Institute for Experimental Nuclear Physics, Karlsruhe Institute of Technology, 2011.

[61] R. Fleischer. “Exploring CP Violation and Penguin Effects through $B^0_d \to D^+D^-$ and $B^0_s \to D^+_s D^-_s$”. *Eur. Phys. J C*, 51:849–858, 2007.

[62] M. Gronau, J. L. Rosner, and D. Pirjol. “Small Amplitude Effects in $B^0 \to D^+D^-$ and Related Decays”. *Phys. Rev. D*, 78:033011, 2008.

[63] Z.-Z. Xing. “CP Violation in $B_d \to D^+D^-$, $D^{*+}D^-$, D^+D^{*-} and D^+D^- Decays”. *Phys. Rev. D*, 61:014010, 1999.

[64] M. Gronau. “CP Violation in Neutral B Decays to CP Eigenstates”. *Phys. Rev. Lett.*, 63:1451–1454, 1989.

[65] B. Grinstein. “Critical Reanalysis of CP Asymmetries in B^0 Decays to CP Eigenstates”. *Physics Letters B*, 229(3):280–284, 1989.

[66] M. Ciuchini, E. Franco, G. Martinelli *et al.* “CP Violating B Decays in the Standard Model and Supersymmetry”. *Phys. Rev. Lett.*, 79:978–981, 1997.

[67] Y. Grossman and M. P. Worah. “CP Asymmetries in B Decays with New Physics in Decay Amplitudes”. *Physics Letters B*, 395(3):241–249, 1997.

[68] S. Fratina, K. Abe, I. Adachi *et al.* (Belle Collaboration). “Evidence for CP Violation in $B^0 \to D^+D^-$ Decays”. *Phys. Rev. Lett.*, 98:221802, 2007.

[69] B. Aubert, M. Bona, Y. Karyotakis *et al.* (BaBar Collaboration). “Measurements of Time-Dependent CP Asymmetries in $B \to D^{(*)+}D^{(*)-}$ Decays”. *Phys. Rev. D*, 79: 032002, 2009.

[70] T. Aushev, Y. Iwasaki, K. Abe *et al.* (Belle Collaboration). “Search for CP Violation in the Decay $B^0 \to D^{*\pm}D^{\mp}$”. *Phys. Rev. Lett.*, 93:201802, 2004.

[71] K. Vervink, T. Aushev, O. Schneider *et al.* (Belle Collaboration). “Evidence of Time-Dependent CP Violation in the Decay $B^0 \to D^{*+}D^{*-}$”. *Phys. Rev. D*, 80:111104, 2009.

[72] R. Aleksan, I. Dunietz, B. Kayser *et al.* “CP Violation using Non-CP Eigenstate Decays of Neutral B Mesons”. *Nuclear Physics B*, 361(1):141–165, 1991.

[73] B. Aubert, R. Barate, D. Boutigny *et al.* (BaBar Collaboration). “Measurements of Branching Fractions and CP-Violating Asymmetries in $B^0 \to \rho^{\pm}h^{\mp}$ Decays”. *Phys. Rev. Lett.*, 91:201802, 2003.

[74] T. E. Browder and K. Honscheid. “B Mesons”. *Progress in Particle and Nuclear Physics*, 35(0):81–219, 1995.

[75] D. Besson, J. Green, R. Namjoshi *et al.* (CLEO Collaboration). “Observation of New Structure in the e^+e^-- Cross-Section above the $\Upsilon(4S)$”. *Phys. Rev. Lett.*, 54:381–384, 1985.

[76] S. Kurokawa and E. Kikutani. “Overview of the KEKB Accelerators”, and other articles in this volume. *Nuclear Instruments and Methods A*, 499(1):1–7, 2003.

[77] A. Abashian, K. Gotow, N. Morgan *et al.* (Belle Collaboration). “The Belle Detector”. *Nuclear Instruments and Methods A*, 479(1):117–232, 2002.

[78] Y. Ushiroda. “Belle Silicon Vertex Detectors”. *Nuclear Instruments and Methods A*, 511 (1–2):6–10, 2003. Proceedings of the 11th International Workshop on Vertex Detectors.

[79] Z. Natkaniec, H. Aihara, Y. Asano *et al.* “Status of the Belle Silicon Vertex Detector”. *Nuclear Instruments and Methods A*, 560(1):1–4, 2006.

[80] M. Fujikawa. “Measurement of Branching Fraction and Time-dependent CP Asymmetry Parameters in $B^0 \to K^0\pi^0$ Decays”. PhD thesis, Nara Women’s University, 2009.

[81] Belle Tracking Group. “Charged Particle Tracking at Belle”. *Belle Note #327*, 2000.

[82] H. Hirano, M. Akatsu, Y. Fujita *et al.* “A High-resolution Cylindrical Drift Chamber for the KEK B-Factory”. *Nuclear Instruments and Methods A*, 455(2):294–304, 2000.

[83] T. Iijima, I. Adachi, R. Enomoto *et al.* “Aerogel Cherenkov Counter for the Belle Detector”. *Nuclear Instruments and Methods A*, 453(1):321–325, 2000.

[84] H. Kichimi, Y. Yoshimura, T. Browder *et al.* “The Belle TOF System”. *Nuclear Instruments and Methods A*, 453(1):315–320, 2000.

[85] K. Miyabayashi. “Belle Electromagnetic Calorimeter”. *Nuclear Instruments and Methods A*, 494(1):298–302, 2002.

[86] A. Abashian, K. Abe, P. Behera *et al.* “Muon Identification in the Belle Experiment at KEKB”. *Nuclear Instruments and Methods A*, 491(1):69–82, 2002.

[87] Y. Ushiroda, A. Mohapatra, H. Sakamoto *et al.* “Development of the Central Trigger System for the Belle Detector at the KEK B-Factory”. *Nuclear Instruments and Methods A*, 438(2):460–471, 1999.

[88] S. Y. Suzuki, M. Yamauchi, M. Nakao *et al.* “The Belle DAQ System”. *Nuclear Instruments and Methods A*, 453(1):440–444, 2000.

[89] S. Y. Suzuki, R. Itoh, H.-W. Kim *et al.* “Belle DAQ System Upgrade at 2001”. *Nuclear Instruments and Methods A*, 494(1):535–540, 2002.

[90] J. Nocedal and J. W. Stephen. *“Numerical Optimization”*. Springer, 2nd edition, 2006.

[91] P. Avery. “Applied Fitting Theory VI - Formulas for Kinematic Fitting”. *CLEO CBX*, 98(37):1–22, 1999.

[92] T. Tomura. “Study of Time Evolution of B Mesons at the KEKB Factory”. PhD thesis, University of Tokyo, 2002.

[93] H. Tajima, H. Aihara, T. Higuchi *et al.* (Belle Collaboration). “Proper-time Resolution Function for Measurement of Time Evolution of B Mesons at the KEK B-Factory”. *Nuclear Instruments and Methods A*, 533(3):370–386, 2004.

[94] Y. Yosuke and K. Miyabayashi. “Measurement of Time-dependent CP Violation in $\mathrm{B}^0 \to (\mathrm{c}\bar{\mathrm{c}})\mathrm{K}^0$ Decays with $772 \times 10^6 \mathrm{B}\bar{\mathrm{B}}$”. *Belle Note #1149*, 2011.

[95] I. Adachi, I. Aihara, H. Asner *et al.* (Belle Collaboration). “Precise Measurement of the CP Violation Parameter $\sin(2\phi_1)$ in $\mathrm{B}^0 \to \mathrm{c}\bar{\mathrm{c}}\mathrm{K}^0$ Decays”. *Phys. Rev. Lett.*, 108:171802, 2012.

[96] H. Kakuno, K. Hara, B. Casey *et al.* “Neutral B Flavor Tagging for the Measurement of Mixing-induced CP Violation at Belle”. *Nuclear Instruments and Methods A*, 533(3): 516–531, 2004.

[97] H. Albrecht, R. Gläser, G. Harder *et al.* (ARGUS Collaboration). “Search for Hadronic $\mathrm{b} \to \mathrm{u}$ Decays”. *Physics Letters B*, 241(2):278–282, 1990.

[98] J. E. Gaiser. “Charmonium Spectroscopy from Radiative Decays of the J/ψ and ψ'^{*}”. PhD thesis, Stanford Linear Accelerator Center/Stanford University, SLAC-R-255, 1982.

[99] G. Cowan. *“Statistical Data Analysis”*. Oxford University Press, 1st edition, 1998.

[100] E. Farhi. “Quantum Chromodynamics Test for Jets”. *Phys. Rev. Lett.*, 39:1587–1588, 1977.

[101] D. M. Asner, M. Athanas, D. W. Bliss *et al.* (CLEO Collaboration). “Search for Exclusive Charmless Hadronic B Decays”. *Phys. Rev. D*, 53(3):1039–1050, 1996.

[102] K. Barnham, M. Bloch, K. Böckmann *et al.* (Aachen-Bonn-CERN-London-Oxford-Saclay Collaboration). “Spherocity and Thrust Distributions in High Energy Neutrino Interactions”. *Physics Letters B*, 85(2):300 – 303, 1979.

[103] G. C. Fox and S. Wolfram. “Event Shapes in e^-e^+-Annihilation”. *Nuclear Physics B*, 149(3):413 – 496, 1979.

[104] S. H. Lee, K. Suzuki, K. Abe *et al.* (Belle Collaboration). “Evidence for $B^0 \to \pi^0\pi^0$”. *Phys. Rev. Lett.*, 91:261801, 2003.

[105] R. A. Fisher. “The Use of Multiple Measurements in Taxonomic Problems”. *Annals of Eugenics*, 7(2):179–188, 1936.

[106] M. Feindt. “A Neural Bayesian Estimator for Conditional Probability Densities”. arXiv: physics/0402093, 2004.

[107] M. Feindt and U. Kerzel. “The NeuroBayes Neural Network Package”. *Nuclear Instruments and Methods A*, 559:190, 2006.

[108] F. Fang. “Study of $K_S^0 \to \pi^+\pi^-$ Selection”. *Belle Note #323*, 2000.

[109] G. Punzi. “Comments on Likelihood Fits with Variable Resolution”. *In the Proceedings of PHYSTAT2003: Statistical Problems in Particle Physics, Astrophysics and Cosmology*, 2003.

[110] S. Fratina. “Measurement of Time-Dependent CP Violation in $B^0 \to D^+D^-$ Decays”. *Belle Note #935*, 2006.

[111] K. Vervink. “Measurement of Polarization Fraction and Time-dependent CP Asymmetries in $B^0 \to D^{*+}D^{*-}$”. *Belle Note #1007*, 2008.

[112] D. J. Lange. “The EvtGen Particle Decay Simulation Package”. *Nuclear Instruments and Methods A*, 479(1):117–232, 2001.

[113] R. Brun *et al.* “GEANT3 User’s Guide”. *CERN Report*, DD/EE/84-1, 1985.

[114] S. Nishida. “Study of Kaon and Pion Identification Using Inclusive D^* Samples”. *Belle Note #779*, 2005.

[115] K. Nakamura, K. Hagiwara, K. Hikasa *et al.* (Particle Data Group). “Review of Particle Physics”. *J. Phys. G*, 37:075021, 2010.

[116] T. Sjöstrand, P. Edén, C. Friberg *et al.* “High Energy Physics Event Generation with Pythia 6.1”. *Computer Physics Communications*, 135:238, 2001.

[117] P. Koppenburg. “A Measurement of the Track Finding Efficiency Using Partially Reconstructed D^* Decays”. *Belle Note #621*, 2003.

[118] W. Dungel. “Systematic Investigation of the Reconstruction Efficiency of Low Momentum $\pi^\pm$ and π^0”. *Belle Note #1176*, 2011.

[119] E. White. “Determination of K^0_S Systematic Uncertainty and Efficiency”. *Belle Note #1207*, 2011.

[120] S. Lin, P. Chang, and H. Huang. “Update of π^0 Systematics Using Inclusive η (78/fb)”. *Belle Note #645*, 2003.

[121] B. Aubert, Y. Karyotakis, J. P. Lees *et al.* (BaBar Collaboration). “Measurement of Time-dependent CP Asymmetry in $B^0 \to c\bar{c}K^{(*)0}$ Decays”. *Phys. Rev. D*, 79:072009, 2009.

[122] O. Long, M. Baak, R. N. Cahn *et al.* “Impact of Tag-side Interference”. *Phys. Rev. D*, 68:034010, 2003.

[123] K. Hara. “Study of Tag-side Interference Effect in Time-dependent CP Violating Asymmetry Measurements”. *Belle Note #872*, 2006.

[124] F. E. James. *“Statistical Methods in Experimental Physics”*. World Scientific, 2nd edition, 2006.

[125] G. Majumder, K. Abe, I. Adachi *et al.* (Belle Collaboration). “Evidence for $B^0 \to D^+D^-$ and Observation of $B^- \to D^0D^-$ and $B^- \to D^0D^-$ Decays”. *Phys. Rev. Lett.*, 95:041803, 2005.

[126] B. Aubert, R. Barate, M. Bona *et al.* (BaBar Collaboration). “Measurement of Branching Fractions and CP Violating Charge Asymmetries for B Meson Decays to $D^{(*)}\bar{D}^{(*)}$, and Implications for the Cabibbo-Kobayashi-Maskawa Angle γ”. *Phys. Rev. D*, 73: 112004, 2006.

[127] K. Abe, R. Abe, T. Abe *et al.* (Belle Collaboration). “Observation of the Decay $B^0 \to D^\pm D^\mp$”. *Phys. Rev. Lett.*, 89:122001, 2002.

[128] B. Aubert, R. Barate, D. Boutigny *et al.* (BaBar Collaboration). “Measurement of the Branching Fraction and Bounds on the CP Violating Asymmetries of Neutral B Decays to $D^{*\pm}D^\mp$”. *Phys. Rev. Lett.*, 90:221801, 2003.

[129] B. Aubert, M. Bona, D. Boutigny *et al.* (BaBar Collaboration). “Measurement of CP Violating Asymmetries in $B^0 \to D^{(*)\pm}D^\mp$”. *Phys. Rev. Lett.*, 99:071801, 2007.

[130] T. Abe, I. Adachi, K. Adamczyk *et al.* (Belle II Collaboration). *“Belle II Technical Design Report”*. KEK Report 2010-1, High Energy Accelerator Research Organization, Japan, 2010.

[131] M. Röhrken *et al.* (Belle Collaboration). “Measurements of Branching Fractions and Time-Dependent CP Violating Asymmetries in $B^0 \to D^{(*)\pm}D^\mp$ Decays”. *Phys. Rev. D*, 85:091106, 2012.

List of Figures

List of Tables

Danksagungen

Besonders herzlich bedanke ich mich bei Herrn Prof. Dr. Michael Feindt für die Möglichkeit, diese Doktorarbeit durchführen zu können.

Bei Herrn Prof. Dr. Günter Quast bedanke ich mich für die Übernahme des Korreferates.

Für die sehr gute Betreuung in allen Phasen dieser Doktorarbeit bedanke ich mich bei Dr. Thomas Kuhr and Dr. Anže Zupanc.

For the rich scientific programme of the experiment and the pleasant working atmosphere, I would like to thank the coworkers of the Belle Collaboration. In particular, I thank Tagir Aushev, Matthew Barrett, Jeremy Dalseno, Yoshihito Iwasaki, Kenkichi Miyabayashi, Yoshi Sakai and Karim Trabelsi for supporting the performed measurements.

Für die sehr angenehme Arbeitsatmosphäre bedanke ich mich bei allen Mitgliedern der Arbeitsgruppe und bei allen Mitarbeitern des Instituts für Experimentelle Kernphysik.

Ich danke dem Graduiertenkolleg „Hochenergiephysik und Teilchenastrophysik“ und dem Graduiertenkolleg „Elementarteilchenphysik bei höchster Energie und höchster Präzision“ der Deutschen Forschungsgemeinschaft für die Finanzierung dieser Dissertation.

Für die Unterstützung bedanke ich mich bei meiner Mutter, Oma Wilma und der Familie Brümmer aus Langelohe. Mein ganz besonders lieber Dank gilt Anneke.